Advanced Experimental Methods for Noise Research in Nanoscale Electronic Devices

NATO Science Series

A Series presenting the results of scientific meetings supported under the NATO Science Programme.

The Series is published by IOS Press, Amsterdam, and Kluwer Academic Publishers in conjunction with the NATO Scientific Affairs Division

Sub-Series

I. Life and Behavioural Sciences	IOS Press
II. Mathematics, Physics and Chemistry	Kluwer Academic Publishers
III. Computer and Systems Science	IOS Press
IV. Earth and Environmental Sciences	Kluwer Academic Publishers
V. Science and Technology Policy	IOS Press

The NATO Science Series continues the series of books published formerly as the NATO ASI Series.

The NATO Science Programme offers support for collaboration in civil science between scientists of countries of the Euro-Atlantic Partnership Council. The types of scientific meeting generally supported are "Advanced Study Institutes" and "Advanced Research Workshops", although other types of meeting are supported from time to time. The NATO Science Series collects together the results of these meetings. The meetings are co-organized bij scientists from NATO countries and scientists from NATO's Partner countries – countries of the CIS and Central and Eastern Europe.

Advanced Study Institutes are high-level tutorial courses offering in-depth study of latest advances in a field.
Advanced Research Workshops are expert meetings aimed at critical assessment of a field, and identification of directions for future action.

As a consequence of the restructuring of the NATO Science Programme in 1999, the NATO Science Series has been re-organised and there are currently Five Sub-series as noted above. Please consult the following web sites for information on previous volumes published in the Series, as well as details of earlier Sub-series.

http://www.nato.int/science
http://www.wkap.nl
http://www.iospress.nl
http://www.wtv-books.de/nato-pco.htm

Series II: Mathematics, Physics and Chemistry – Vol. 151

Advanced Experimental Methods for Noise Research in Nanoscale Electronic Devices

edited by

Josef Sikula
Brno University of Technology,
Brno, Czech Republic

and

Michael Levinshtein
Ioffe Institute of Russian Academy of Sciences,
St. Petersburg, Russia

KLUWER ACADEMIC PUBLISHERS
NEW YORK, BOSTON, DORDRECHT, LONDON, MOSCOW

eBook ISBN: 1-4020-2170-4
Print ISBN: 1-4020-2169-0

Created in the United States of America

Visit Springer's eBookstore at: http://ebooks.kluweronline.com
and the Springer Global Website Online at: http://www.springeronline.com

CONTENTS

III. Noise Measurement Technique

PREFACE

The NATO Advanced Research Workshop "Advanced Experimental Methods for Noise Research in Nanoscale Electronic Devices" was held in Brno, the Czech Republic, from 14 to 16 August, 2003, being the first event to be held in this country. The Workshop passed off before the 17th International Conference on Noise and Fluctuations – ICNF 2003 that took place at the Charles University Conference Centre, Prague, Czech Republic, from 18 to 22 August, 2003.

The Workshop provided a forum for discussion on recently developed experimental methods for noise research in nanoscale electronic devices. It brought together specialists in the area of transport and stochastic phenomena in nanoscale physics, dealing with systems for future nanoscale electronics. The approach was to create methods for experimental observations of noise sources, their localization and their frequency spectrum, voltage - current and thermal dependences. The present knowledge of measurement methods for mesoscopic devices was summarized, to identify directions for future research, related to downscaling effects.

The directions for future research of fluctuation phenomena in quantum dot and quantum wire devices were specified. Another approach was to emphasize the fact, that nanoscale electronic devices will be the basic components for electronics of the 21st century. From this point of view the signal-to-noise ratio is a very important parameter for the device application. Since the noise is also a quality and reliability indicator, experimental methods will have a wide application in the future.

This ARW promoted and improved links between scientists from NATO and Partner countries and helped also to strengthen the scientific communities in the new NATO countries. The workshop linked the theoretical assessment of the phenomenon of noise with a discussion of the advanced experimental methods. Its main idea was to discuss new results in nanoscale physics and initiate new joint research programmes.

The Workshop was international in scope and included authors from Belgium, Czech Republic, France, German, Italy, Latvia, Lithuania, the Netherlands, Poland, Portugal, Romania, Russia, Slovak Republic, Ukraine, United Kingdom, the United States and Uzbekistan. This Book contains 41 papers providing reviews and recent advances related to noise research in nanoscale electronic devices.

The organizers of the ARW gratefully acknowledge the financial support by the NATO Scientific Committee, Brno University of Technology and VS Technology Brno.

Brno, August 2003 *Josef Sikula*

I. NOISE SOURCES

1/*f* NOISE SOURCES

F.N. Hooge

Department of Electrical Engineering, Eindhoven University of Technology
5600 MB Eindhoven
The Netherlands

Abstract *1/f* noise is a fluctuation in the bulk conductance of semiconductors and metals. This noise could be a fluctuation in the number of the free electrons or in their mobility. Many experimental studies on homogenous layers have proved that the*1/f* noise is a fluctuation in the mobility. There is no theoretical model of mobility *1/f* noise. The McWhorter model for *1/f* noise in MOSTs simply adds generation-recombination spectra from surface states. According to this model, estimates of the noise magnitude give unrealistic values. More important, the McWhorter model is a model on number fluctuations, because GR noise always is a fluctuation in number. There is no experimental proof of number fluctuations in the 1/f noise of MOSTs.

Keywords: noise sources, *1/f* noise, fluctuation in the mobility, number fluctuations

1. Introduction

We present a review of the study of 1/*f* noise in homogenous layers of metals and semiconductors. Homogenous layers are eminently suited to study the basic properties of 1/*f* noise.

Although most work has been done on devices, we will not discuss them because devices are much too complicated to reveal the unknown basic properties of the noise sources. There is one exception, however, the MOST. From the very beginning of noise research this noisy device has been studied extensively.

At first sight, the McWhorter model explains the noise correctly as a summation of generation-recombination from traps in the oxide layer. Because of its simplicity the McWhorter model is still very popular.

First we will demonstrate that experiments on homogenous layers prove that here the McWhorter model does not apply. The 1/f noise turns out to be in the mobility and not in the number of the elections as the result from GR

J. Sikula and M. Levinshtein (eds.),
Advanced Experimental Methods for Noise Research in Nanoscale Electronic Devices (3 - 10)

noise. Whether the McWhorter model does apply to MOSTs, still is an open question.

It is impossible to give a complete survey of all literature on 1/f noise. We restrict ourselves to some important themes that lead to problems still under discussion now. We refer to survey papers [1,2]. We apologize to the original authors of important ideas, who have become invisible in this way. On the other hand the reader should not think that everything presented here was invented in Eindhoven.

2. The empirical relation

1/f noise is a fluctuation in the conductivity of metals and semiconductors. The spectral power density is proportional to 1/f over a wide range of frequencies. The noise can be measured with simple equipment between 10^{-2} Hz and 10^{5} Hz. The slope of the spectrum is $-(1{,}0 \pm 0{,}1)$. Spectra with (sometimes varying) slopes between –0,5 to –1,5 should not be called 1/f spectra

The noise of homogenous layers can be expressed as

$$\frac{S_R}{R^2} = \frac{\alpha}{fN} \tag{1}$$

where S_R is the spectral power density of resistance, R the resistance of the sample, f the frequency at which the noise is measured, N the total number of free electrons, and α is an empirical, dimensionless constant with values usually between 10^{-6} and 10^{-4}. There is no theory behind (1). The relation normalizes the relative noise to 1 electron. The only assumption behind (1) is that, whatever the electrons do, they do it independently. In high-quality material, like epitaxial layers, the α values are in the range 10^{-6} to 10^{-4}. In damaged materials, mechanical damage or radiation damage, the α values are much higher. This could explain why in the old investigations, around 1970, $\alpha=2\text{x}10^{-3}$ seemed a good average. At that time, samples were sawn out of large single crystals.

For measurements on homogenous, ohmic samples one uses

$$\frac{S_R}{R^2} = \frac{S_G}{G^2} = \left(\frac{S_V}{V^2}\right)_{i\,const} = \left(\frac{S_i}{i^2}\right)_{V\,const} = \frac{\alpha}{fN} \tag{2}$$

If one wishes to study the interference of current, temperature doping etc, then the 1/f noise has to be well above the thermal noise 4kTR. In order to avoid heating of the sample, currents should be not too extreme, this sets a limit to N; as a first indication: $N<10^{13}$. This means that for a “good“ 1/f noise metal samples should be smaller than $(10\ \mu\text{m})^3$ and semiconductor

samples (n around 10^{17}cm^{-3}) could be much larger up to (1 mm)^3. The reverse is also true: if one wishes to make samples free of 1/f noise, make them larger than (10 μm)^3 in case of metals and (1 mm)^3 in case of semiconductors.

2.1. Point contacts

Point contacts are notorious for their 1/f noise. A point contact may be homogenous as far as the material is concerned; it is inhomogeneous in the current density. We consider here a contact between two metal spheres. The contact area is a circle with radius a (see Fig. 1).

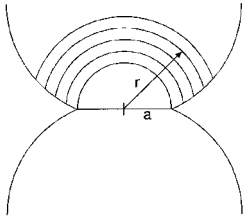

Figure 1. Point contact. $N_{eff} = a^3n$

The spherical shells between the (approximately) equipotential planes are homogenous. We apply (1) and (2) to shell with radius r and thickness dr, and calculate $R(r)$ and $S_R(r)$. Then we integrate from $r = a$ to $r = \infty$, and find an expression like (1). But instead of N we now find

$$N_{eff} = a^3 n \tag{3}$$

where n is the electron density. N_{eff} is the effective number of electrons; it is the number in the contact volume a^3. The radius a of the contact area cannot be measured, but we know the relation between a and R: $R \propto 1/a$.

From this we calculate

$$\frac{S_R}{R^2} = \frac{\alpha}{fna^3} \propto \frac{\alpha}{fn} R^3 \tag{4}$$

The dependence $S_R / R^2 \propto R^3$ is experimentally found in noise measurements in which the pressure on the contact is varied. We have calculated the contact noise from (1) which holds for bulk 1/f noise. Normal α values are experimentally found. So contact noise is bulk 1/f noise.

2.2. Grainy layers

In grainy layers there are many point contacts between the grains. Estimates of the number of contacts and their individual contribution to the noise lead to a relation like (1) with $N_{eff} << N_{total}$. This explains the high noise of grainy layers. One finds extremely high values of α when using the total number of electrons in the sample instead of the number in the contact regions. Superconductors often are in the form of grainy layers. If α is calculated from N_{total}, α is found to be extremely high. Probably this has nothing to do with superconductivity.

3. Mobility noise

Δn or $\Delta\mu$? So far, the empirical relation (1) has been used to describe the conductivity fluctuations in homogenous samples, thin layers and point contacts. The next step is to determine whether the conductivity fluctuates because of fluctuations in the number of the electrons or in their mobility. Number fluctuation was the obvious thing to assume; even today that is what many people do without any discussion.

One cannot decide on Δn or $\Delta\mu$ from measurement on $\Delta\sigma$. One needs an effect where n and μ do not appear as factors in the product $n \times \mu$. Such effects are the Hall effect, thermo e.m.f., hot electron effects, etc. [1,2]. If, for instance, the average effect is proportional to $\mu \ln n$ as in V_{th}, the thermo e.m.f., then we find (6) for the noise

$$V_{th} = C\mu \ln n \tag{5}$$

$$\frac{\Delta V_{th}}{V_{th}} = \frac{\Delta\mu}{\mu} + \frac{\Delta \ln n}{\ln n} = \frac{\Delta\mu}{\mu} + \frac{1}{\ln n}\frac{\Delta n}{n} \tag{6}$$

These voltage fluctuations are compared with resistance fluctuations in the same structure.

$$\frac{\Delta R}{R} = \frac{\Delta\mu}{\mu} + \frac{\Delta n}{n} \tag{7}$$

Mobility fluctuations:

$$\frac{\Delta V_{th}}{V_{th}} = \frac{\Delta R}{R} \tag{8}$$

Number fluctuations:

$$\frac{\Delta V_{th}}{V_{th}} = \frac{1}{\ln n}\frac{\Delta R}{R} < \frac{\Delta R}{R} \tag{9}$$

A nice example is the Hall effect in GaAs [3].

The noise across the Hall contacts is measured in applied magnetic fields, and compared to the noise across the same contacts without magnetic field. The lines for $\Delta\mu$ and Δn in Fig. 2 follow from rigorous, complicated calculations. The experimental points follow the $\Delta\mu$ line, far away from the Δn line. Many more examples of such comparisons are given in the literature. Sometimes there is not much difference between $\Delta\mu$ and Δn lines, but if there is, then Δn is definitely excluded.

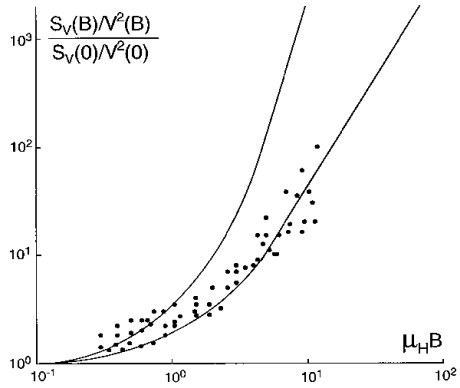

Figure 2. 1/f noise in Hall effect. Epitax n-type GaAs. T=78K [K]. Lines: theory. Points: experimental results

3.1. Lattice scattering

The mobility is determined by scattering of the free electrons. Lattice scattering by acoustic lattice vibrations is always present. Other scattering mechanism might be presented: impurity scattering by charged or neutral centres surface scattering against the crystal boundaries, electron scattering by other electrons. For the study of 1/f noise, materials with two scattering mechanism are of special interest. Let us consider a series of crystals of the same semiconductors material with varying amounts of impurity scattering together with the always present constant lattice scattering. The contribution of the two mechanisms to the resulting mobility μ is given by Matthiessen's rule

$$\frac{1}{\mu} = \frac{1}{\mu_{latt}} + \frac{1}{\mu_{imp}} \tag{10}$$

The observed noise is plotted as $\log\alpha$ versus $\log\mu$.

The $\alpha - \mu$ dependence experimentally found can only be explained by assuming 1/f noise in the lattice scattering whereas the other mechanism is noise free. From (10) follows

$$\frac{1}{\mu}\left(\frac{\Delta\mu}{\mu}\right) = \frac{1}{\mu_{latt}}\left(\frac{\Delta\mu_{latt}}{\mu_{latt}}\right) + 0 \tag{11}$$

$$\alpha = \left(\frac{\mu}{\mu_{latt}}\right)^2 \alpha_{latt} \tag{12}$$

Fig. 3 shows the result for epitaxial n-type GaAs [4], proving that the 1/f noise is in the lattice scattering only.

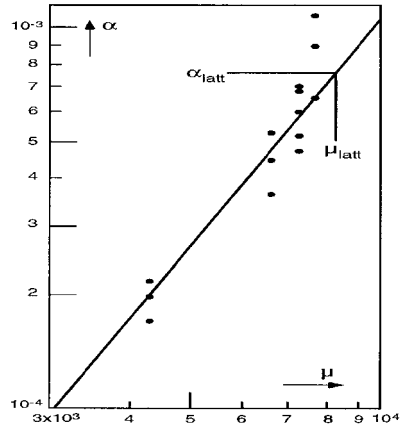

Figure. 3. α versus μ. Epitaxial n-type GaAs T=300K [4]

3.2. Scattered light

Measuring the noise in the intensity of scattered light provides an independent way of proving that the intensity of acoustic lattice modes varies with a 1/f spectrum. Electrons do not play any role in these experiments. Musha [5] designed an experimental set-up in which laser light was scattered in a quartz crystal. See Fig. 4. The spectrum of the scattered light showed peeks left and right of the laser frequency at a distance of the frequency of acoustic mode. The noise in the mode intensity is derived from the correlated part of the noise in the output of the two detectors.

More studies of the optical noise have been performed, also by measuring the transmission of very long glass fibers [6]. The conclusion from this experiment is that the noise spectrum of lattice modes definitively is 1/*f* however; the intensities - related to α- are problematic.

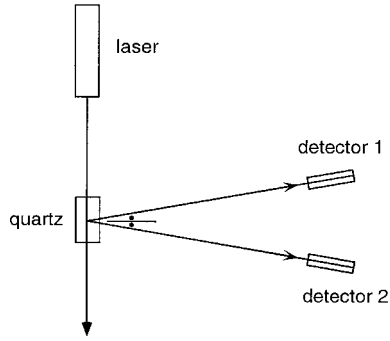

Figure 4. 1/f noise in scattered light. [5]

4. The McWhorter model

The model is based on simple mathematical relations. A GR spectrum corresponds to transitions between the conduction band and a trap with relaxation time τ

$$S(\tau) = \overline{(\Delta N)^2} \frac{4\tau}{1+\omega^2\tau^2} \tag{13}$$

If the different kinds of traps have statistical weights

$$g(\tau)d\tau = \frac{c}{\tau}d\tau \tag{14}$$

Then a 1/f spectrum results by summation of GR spectra

$$S = \int_0^\infty g(\tau)S(\tau)d\tau = \int_0^\infty \frac{c}{\tau}\overline{(\Delta N)^2} \frac{4\tau}{1+\omega^2\tau^2} dr = 4c\overline{(\Delta N)^2} \cdot \frac{1}{f} \tag{15}$$

Finding a physical model is reduced now to finding a trap distribution with the required 1/τ dependence McWhorter proposed a homogenous distribution of traps in an oxide layer in the semiconductor. This model is widely used for the noise in MOSTs. The electrons reach the traps by tunnelling. Therefore, τ depends exponentially on *x*, the distance from the interface.

$$\tau = \tau_0 e^{x/\lambda} \tag{16}$$

where λ is an effective penetrations depth. If the number of traps is T, we find from (16)

$$\frac{dT}{d\tau} = \frac{dT}{dx}\frac{dx}{d\tau} = \frac{dT}{dx}\frac{\lambda}{\tau} \tag{17}$$

The homogenous trap distribution (dT/dx = const.) gives the required statistical weight

This model is simple and therefore, very attractive. However, several assumptions have been made, which are usually passed over:

1. Equal values of $(\Delta N)^2$ in each individual GR spectrum
2. Additivity of the GR spectra
3. GR noise is a Δn fluctuation

Ad 2. Under certain conditions for the numbers of the free and trapped electrons additivity is allowed [7-9]. I shall discus this problem at the Prague conference.

Ad 3. In principle, it could be true that the 1/f noise in MOSTs is of nature different from the noise in homogenous samples, for which we proved experimentally that the 1/f noise is mobility noise. Therefore, we need experimental evidence, that in MOSTs the 1/f noise is a fluctuation in number. Otherwise the McWhorter model is irrelevant.

References

[1] F.N.Hooge, T.G.M Kleinpenning and L.K.J. Vandamme, Rept. Progres. Phys 44,479 (1981)

[2] F.N.Hooge, IEEE Trans El.Dev. 41, 1926 (1994)

[3] L.Ren and J.S.Liberis, Physica B 183,40 (1993)

[4] L.Ren and M.R.Leys, Physica B 172,319 (1991)

[5] T. Musha, G Borbély and M.Shoji, Phys. Rev. Lett 64, 2394 (1990)

[6] F.N.Hooge, Proc. 7th Vilnius Conf. on Fluctuation Phenomena in Physical Systems Palanga 1994 Ed.V.Palenskis. Vilnius Univ. Press 1994. P61

[7] F.N.Hooge, Physica B311, 238 (2002)

[8] F.N.Hooge, Physica B (in Press)

[9] L.K.J.Vandamme and F.N.Hooge, Submitted to Physica B

NOISE SOURCES IN GaN/AlGaN QUANTUM WELLS AND DEVICES

S. Rumyantsev

Rensselaer Polytechnic Institute and Ioffe Institute of Russian Academy of Science, Room 9015, CII, Rensselaer Polytechnic Institute 110 8-th Street, Troy, New York 12180 USA

roumis2@rpi.edu

Abstract We will examine possible sources of generation-recombination and 1/f noise in GaN/AlGaN 2D structures, quantum wells, and devices including contacts, bulk and quantum well itself and show that sources of g-r noise, and most probably of 1/f noise in HFETs are located in GaN or AlGaN layers within some distance from the 2D channel.

Keywords: GaN, AlGaN, 1/f noise, generation-recombination noise, quantum well

1. Introduction

High electron sheet concentration in excess of 10^{13} cm^{-2} on the GaN/AlGaN interface, high breakdown field and high electron peak velocity make GaN/AlGaN 2D structures very attractive for high-temperature, high-power, high frequency, and radiation-hard applications. We will discuss results of the experimental and theoretical investigation of the low-frequency noise (LFN) in GaN/GaAlN heterojunctions and examine possible sources of noise, including contacts, surface and 2D channel itself.

2. Experimental details

The GaN/AlGaN heterostructures were grown by metalorganic chemical vapor deposition (MOCVD) on a semi-insulating 4H-SiC substrate.

J. Sikula and M. Levinshtein (eds.),
Advanced Experimental Methods for Noise Research in Nanoscale Electronic Devices (11 - 18)

They consisted of a 50-nm-thick AlN buffer layer, 0.4-μm-thick undoped GaN layer, followed by $Al_{0.2}Ga_{0.8}N$ barrier layer. As in all our devices, we added traces of indium and carbon to improve materials quality. Transistors and Transmission Line Model (TLM) structures were fabricated on the same wafer. The transistors had the source-drain spacing of 4-5 μm, the gate length, *L*, of 1-1.5 μm, and a gate width, *W,* in the range of 50 -150 μm. The LFN was measured in the common source configuration in the frequency range from 1 Hz to 50 kHz.

3. Location of the noise sources

Many different noise sources in 2D structures might be important including the contact noise, channel noise, surface noise and contribution of the gate leakage current in HFETs (see Review [1] for references).

To evaluate the contribution of the gate leakage current, we measured the gate current fluctuations directly. The appropriate analysis of the results allowed us to calculate the contribution of gate current fluctuations to the output noise. The correlation between the gate and drain current fluctuations were measured and analyzed as well. We found that in the majority of devices the gate current gives only small contribution to the low frequency noise, if any.

To determine the contribution of the contact noise to the measured noise spectra, the noise measurements were performed on the TLM structures. Assuming that the contribution of the contact noise and of the noise from the channel layer are not correlated and taking into account that the contact resistance is much smaller than the channel resistance it easy to find the dependence of noise on the distance *L* between the contact pads. In the limiting case when the contact noise is dominant, the spectral noise density, S_I/I^2, should be proportional to L^{-2}. In the opposite limiting case, we have $S_I/I^2 \sim L^{-1}$. Since the experimental dependence was close to the *1/L* law, we conclude that contacts do not contribute much to the overall noise.

To find the relative contributions to the overall noise from the channel and the surface, we measured the gate voltage dependence of noise in HFETs at a small drain voltage corresponding to the linear regime. We found that depending on the surface preparation, passivation, etc., the open surface might strongly contribute to LFN. For all measurements reported here, we selected transistors with no contribution of the surface noise.

4. Generation-Recombination noise in GaN/AlGaN heterostructures

The generation-recombination (GR) noise in GaN/AlGaN heterostructures was reported for the first time in 1999 in Refs. [2,3]. The temperature dependence of low-frequency noise revealed a contribution from a local level with the activation energy, E_a, of approximately 0.42 eV [2].

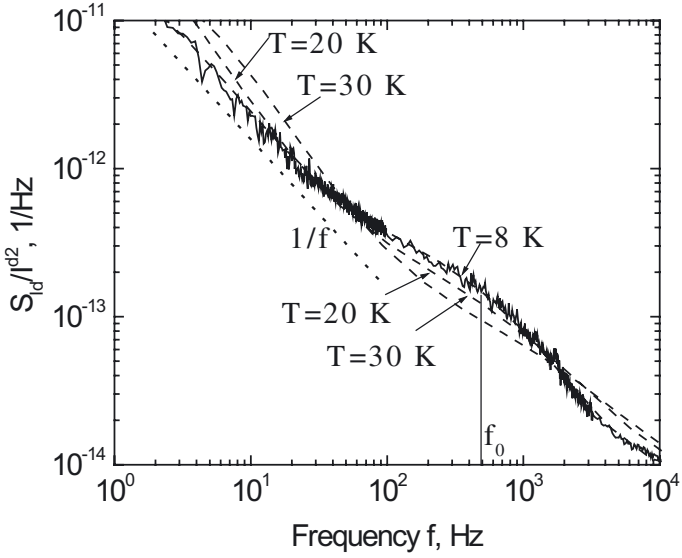

Figure1. Temperature dependence of noise for GaN/AlGaN heterostructure at low temperatures. Temperature dependence of $\tau=1/2\pi f_0$ yields activation energy of E_a=1-3 meV [4].

Since that time a wide spectrum of the local levels have been found within the range of activation energy from 0.2 to 1.0 eV. The smallest activation energy has been measured at low temperatures T<30K in Ref. [4]. Fig.1 shows the noise spectra at three temperatures for the sample exhibited this GR noise. Temperature dependence of characteristic time $\tau=1/2\pi f_0$ gives activation energy of E_a=1-3 meV.

Noise data for the purpose of noise spectroscopy are often presented in the form of temperature dependence of noise at different frequencies f [5,6] (Fig.2).

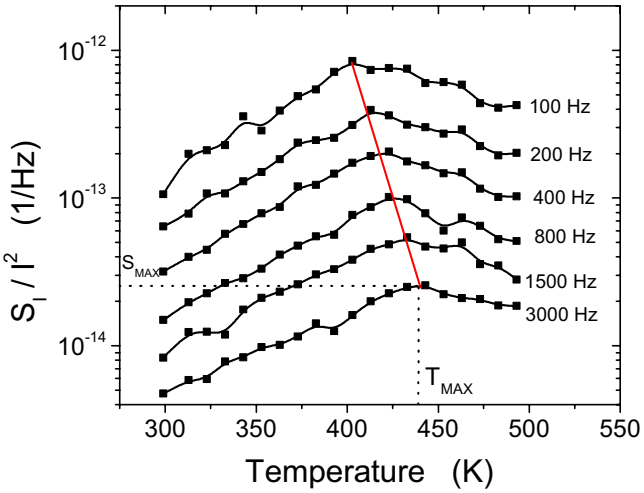

Figure 2. Temperature dependence of low frequency noise in AlGaN/InGaN/GaN quantum well. Arrhenius plot yields the activation energy of 1.6 eV [6].

In this case, τ is taken to be equal to $1/2\pi f$, at the temperature T_{max}, which corresponds to the noise maximum. The slope of the dependence of $ln(f)$ versus $1/T_{max}$ yields the activation energy E_a.

Fig. 2 shows the temperatures dependence of noise for GaN/InGaN/AlGaN quantum wells [6] with the largest activation energy of 1.6 eV ever been found in GaN based devices.

For two dimensional (2D) case, the expression for relative spectral noise density S_I/I^2 generated by the single trap in the 2D channel has the following form:

$$\frac{S_I}{I^2} = \frac{4N_{ts}}{L_0 W n_s^2} \frac{\tau F(1-F)}{1+(\omega\tau)^2}, \qquad (1)$$

where N_{ts} is the trap sheet concentration, L_0 and W are the channel length and width respectively, n_s is the electron sheet concentration, $\omega = 2\pi f$ is the circular frequency, $\tau = \tau_c F$ is the time constant associated with return to equilibrium of the occupation of the level, F is the Fermi - Dirac occupancy function, τ_c is the capture time constant

$$\tau_c = \frac{1}{\sigma n_s v_F}, \qquad (2)$$

where $v_F = \sqrt{2E_F/m}$ is the electron velocity on the Fermi level.

For the 2D degenerate electron gas ($F \approx 1$), with the experimentally found value of τ, the capture cross section is:

$$\sigma \cong \frac{1}{\tau n_s v_F} \tag{3}$$

We found $\sigma \approx 3\times10^{-18}$ cm^2. This value of the capture cross section is too small to be realistic. This result shows that for degenerate 2D gas the source of low frequency generation-recombination noise, with any activation energy, cannot be located directly in the 2D channel.

Another possible location of the traps responsible for generation recombination noise is fully depleted barrier layer including AlGaN surface from the gate side. The GR noise from the traps in the AlGaN layer can be approximately described by Eq. (1), where N_{ts} is replaced with $N_t d$. Here N_t is the volume concentration of traps and d is the thickness of the AlGaN. In this case, the time constant τ is given by the Shockley-Hall-Read theory. Assuming zero free carrier concentration within the depletion region and that the level under consideration is located in the upper half of the forbidden gap, the expression for τ can be written as [7]:

$$\tau = \tau_0 \exp(E_t / kT) \tag{4}$$

where k is Boltzman constant, T is the temperature, $\tau_o = (\sigma_n v_n N_c)^{-1}$, N_c is the density of states in the conduction band.

Hence the slope of the plot of $1/kT_{max}$ against $\ln f$ (Arrhenius plot) yields the level position E_a.

Once E_a is known, the time constant τ_o and electron capture cross section can be found.

Our estimate yields quite reasonable value of capture section $\sigma_n \approx (10^{-12} - 10^{-13})$ cm^2 for all samples.

The trap concentration N_t can be crudely estimated as follows. Assuming that the main contribution to noise comes from the level with occupancy close to 0.5, we find for the trap concentration:

$$N_t = \frac{4\pi f_{max} S_{max} n_s^2 L_0 W}{d} \tag{5}$$

We obtained $N_t \approx 5\times10^{16}$ cm^{-3} for AlGaN/GaN 2D structures and AlGaN/InGaN/GaN quantum wells. Since the doping level of AlGaN barier layer is almost two orders of magnitude higher, this estimate also looks quite reasonable.

Local trap might also locate in GaN layer close to the channel (and close to the Femi level). In this case we have to assume that measured activation

energy fully belongs to the temperature dependence of the capture cross section. The estimate of the of trap concentration in this case yields $N_t \approx 5\times10^{12}$ cm^{-3}.

Measurements of the LFN in GaN films showed that contribution of GR noise is very weak. On the other hand, AlGaN films demonstrated pronounced GR noise with activation energy close to those found in AlGaN/GaN heterostructures. Therefore, we conclude that AlGaN is the most probable source of the GR noise in GaN based 2D structures.

5. 1/f noise

The 1/f noise level in different semiconductor materials and structures is usually characterized by the dimensionless Hooge parameter, $\alpha=(S_I/I^2)f.N$, where N is the total number of the carriers in the sample, f is the frequency, $S_{1/f} = S_I/I^2$ is the relative spectral density of the $1/f$ noise.

In spite of the difference in the absolute values of α, for different samples and structures we found that concentration dependencies $\alpha(n_s)$ are identical for all samples. At low channel concentrations, α decreases with the increase of n_s as $\alpha \sim 1/n_s$, reaches a minimum and then increases with a further increase of n_s (Fig.3). This kind of $\alpha \sim 1/n_s$ dependence was found for both AlGaN/InGaN/GaN quantum wells and GaN/AlGaN heterostructures.

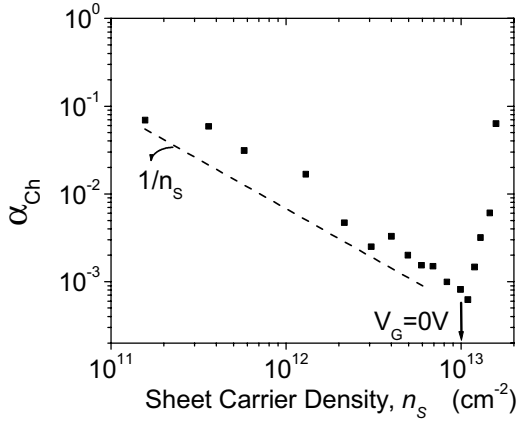

Figure 3. The dependence of Hooge parameter α on 2D sheet carrier concentration n_S for AlGaN/InGaN/GaN quantum wells.

The dependence $\alpha \sim 1/n_s$ indicates that the spectral density S_I does not depend on the channel concentration. Note that such situation is very typical for Si MOSFETs, where the noise arises from the electron tunneling from the semiconductor to traps in the oxide. Hence, the observed $\alpha \sim 1/n_s$ dependence might be linked to the electron tunneling from the 2D gas into the tail states in GaN or AlGaN.

6. Conclusion

Experimental study of the 1/f noise in GaN/AlGaN 2D structures and AlGaN/InGaN/GaN quantum wells showed that in the majority of devices contacts, surface and gate leakage current do not contribute much to noise.

The AlGaN layer is the most probable source of the GR noise in GaN/AlGaN 2D structures. Our estimates yielded a reasonable capture cross-section and concentration of traps located in AlGaN, which might be responsible for the noise.

The dependence of the 1/f noise on electron sheet concentration indicates that the most probable mechanism of the noise is tunneling from 2D channel to the GaN or AlGaN layers.

References

[1] M. E. Levinshtein, A. A. Balandin, S. L. Rumyantsev, and M. S. Shur, Low-frequency noise in GaN-based Field Effect Transistors in: "Noise and Fluctuations Control in Electronic Devices", A. Balandin, ed., American Scientific Publishers (2002)

[2] S. Rumyantsev, M. E. Levinshtein, R. Gaska, M. S. Shur, A. Khan, J. W. Yang, G. Simin, A. Ping and T. Adesida, Low 1/f noise in AlGaN/GaN HEMTs on SiC substrates, Proc. of the Third International Conference on Nitride Semiconductors (ICNS3), Montpellier, France, July 1999, *phys. stat. sol. (a)*, **176** (1999) 201.

[3] A. Balandin, S. Morozov, G. Wijeratne, S. J. Cai, R. Li, K. L. Wang, and C. R. Viswanathan, Effect of channel doping on the low-frequency noise in GaN/AlGaN heterostructure field-effect transistors *Appl. Phys. Lett.* **75** (1999) 2064.

[4] S. L. Rumyantsev, Y. Deng, E. Borovitskaya, A. Dmitriev, W. Knap, N. Pala, M. S. Shur, M. E. Levinshtein, M. Asif Khan, G. Simin, J. Yang, and X. Hu, Low-frequency noise in GaN/AlGaN heterostructure field-effect transistors at cryogenic temperatures, *Journal of Applied Physics* **92** (2002) 4726,

[5] M. E. Levinshtein and S. L. Rumyantsev, Noise spectroscopy of local levels in semiconductors, *Semicond. Sci. and Technol.*, **9** (1994) 1183.

[6] N. Pala, S. Rumyantsev, M. Shur , R. Gaska, X. Hu, J. Yang, G. Simin and M. A. Khan, Low Frequency Noise in AlGaN/InGaN/GaN Double Heterostructure Field Effect Transistors, Solid State Electronics **47** (2003) 1099-1104.

[7] P. O. Lauritzen, Low-frequency generation noise in junction field-effect transistors, *Solid State Electron,* **8** (1965) 58.

1/*f* NOISE IN NANOMATERIALS AND NANOSTRUCTURES: OLD QUESTIONS IN A NEW FASHION

M. N. Mihaila
National Institute of Microtechnology
32B Erou Iancu Nicolae str., 72996 Bucharest
Romania
mihaim@imt.ro

Abstract Some old, perennial questions in the field of low-frequency noise in solid are discussed in the light of some recent achievements concerning the investigation of the noise phenomena in nanomaterials and nanostructures. The main emphasis is placed on the very old yet still hot topic of 1/f noise. Possible new fashion is considered for three longstanding questions: Lorentzian superposition, surface vs. bulk and number vs. mobility fluctuation. Examination of the RTS noise behaviour in meso- and nanostructures does not support its fundamental character in the generation of the 1/f noise. Recent noise measurements on both Single- and Multiple-Walled Carbon Nanotubes (SWNT, MWNT) definitely relax the old dispute whether 1/f noise is a surface or a bulk effect: either surface or bulk or both of them can contribute to 1/f noise. As for the number fluctuation vs. mobility fluctuation controversy, noise measurements in nanomaterials favour mobility fluctuation hypothesis due to phonon scattering as the microscopic source of the 1/f noise.

Keywords: noise, nanomaterials, nanostructures, old questions, new fashion.

1. Introduction

The top down approach in the scaling of electronic devices is at and in some cases beyond the borderline of the nanoworld. Created either by top-down or bottom-up procedures, the newborn nanostructures have fascinating properties. However, the ways to the nanoworld are inexorably accompanied by the increased low-frequency noise level, which is highly detrimental, especially to the nanostructures processing signals. Moreover, below some thresholds, one can encounter intrinsic noise levels comparable with the

J. Sikula and M. Levinshtein (eds.),
Advanced Experimental Methods for Noise Research in Nanoscale Electronic Devices (19-27)

signal these nanostructures have to process. In principle, one can alleviate these difficulties by nanoengineering, except for the situations when the microscopic roots of the unavoidable noise phenomena, which act as fundamental limits are reached. In the bottom-up approach one can, in principle at least, build-up nanostructures with the desired noise properties, therefore noise-oriented design could be of importance in nanoengineering. To do so, one needs principles and rules born out from the fundamental knowledge, which cannot be obtained without finding answers to the longstanding questions in the field of low-frequency noise.

The very old, perennial questions we would like to examine here from the perspective of the nanoscience results are connected with and refer to the well-known issue of 1/f noise. Simply stated, they are:

1. Superposition of Lorentzians. Is the RTS noise the fundamental component of the 1/f noise?
2. A problem of topology: surface vs. bulk;
3. Mobility vs. number fluctuations.

Although vividly debated for many decades, no one of these questions has a definite, "final" answer because they proved extremely intricate so far. In this contribution, we investigate whether the existing experimental noise data for nanomaterials and nanostructures can be used to advance in finding the answers to the above mentioned questions. Due to specific properties of and transport phenomena in nanomaterials and nanostructures, the interpretation of the noise data allows some new approaches in searching for the final answers. New fashion of the old questions is unveiled.

2. Superposition of Lorentzians. Is RTS noise the fundamental component of 1/f noise?

The idea of Lorentzians superposition to obtain a 1/f spectrum has been proposed by Bernamont [1] and Surdin [2] almost 70 years ago. Of course, Lorentzian superposition can mimic a spectrum with a 1/f shape, if the traps are independent [2] and with a $1/\tau$ statistical weight [3], where τ is the trap time constant. In semiconductors and semiconductor devices such a distribution can be associated with the states in the oxide or in the forbidden gap. Starting from this idea, McWhorter [4] proposed his famous microscopic model of carrier tunnelling into oxide states as microscopic source of 1/f noise.

From a theoretical point of view, the superposition has been questioned by famous scientists. For instance, van Kampen [5] considered that, in

general, the superposition “is not a physical explanation, unless one has an explanation for that particular superposition, as in the theory of McWhorter.”, while Hooge [6] deduced the condition of the spectra additivity. When the traps are not independent, the spectra mix and a Lorentz spectrum is found. Moreover, in a very recent paper, van Vliet [7] stated that for discrete traps of small density in the forbidden gap, the spectrum is “a sum of...Lorentzians”, while for “numerous traps” the spectrum is a Lorentzian. For continuously distributed energy range “Our conclusion is that the envelope spectrum for a continuous range of traps is never 1/f over more than 2 decades.” [7], unless band-bending occurs.

The reason why we discuss this topic here is that nanoscience is able to offer a definite answer to this longstanding question. According to McWorther, “a variation of [oxide] thickness from 20Å to 40Å, and a barrier height of one electronvolt, the transition times may vary from 10^{-4} to 10^{4}sec.” [4]. In the case of the MOSFET, the scaling of the channel dimensions requires the reduction of the oxide thickness [8]. Therefore, in the case of a nano-MOSFET working in the ultimate limit of the oxide thickness, which is of the order (12-15)Å corresponding to about four atomic layers, one would expect a reduction of the frequency range spanned by a 1/f spectrum. If the traps are distributed in the whole oxide thickness, a reduction in the oxide thickness will affect the low frequency part of the spectrum, hence below a given frequency one would observe quite an abrupt roll-off in the spectrum. So far, such an effect was not observed, on the contrary, the opposite was apparently found in an experiment done at Bell on MOS transistor with 100 nm gate length and 40 nm gate oxide [9]. In this device, the noise spectrum spanned over several (seven) frequency decades, the corner frequency increases, and the noise intensity is two orders of magnitude more than in a MOSFET with a 0.5 μm gate length. It is as if the number of traps would increase by decreasing the channel length.

The device scaling by the top-down approach in the nanotechnology is accompanied, among other effects, by the occurrence of Random Telegraph Signal (RTS) noise. The phenomenon was observed in different physical systems such as MOSFETs [10-12], quantum point contact [13], metallic nanobridges [14] and others. As in the case of the g-r noise, the spectrum of the RTS noise is also a Lorentzian, therefore the superposition of Lorentzians would give a 1/f spectrum. This was mainly the reason behind the fact that many consider RTS noise as the fundamental source of the 1/f noise. It is also worthwhile mentioning that the similarities between g-r noise and RTS noise are only formal because physically they are very different: while g-r noise is gaussian, RTS noise is strongly nonlinear.

The observation of the RTS noise at low temperature generated by a single fluctuator is the strongest argument put forward in supporting RTS as the fundamental microscopic source of 1/f noise. In this respect, the most

investigated device is the MOS transistor. Reducing the channel dimension in the nanometer range, one can see only a single fluctuator and a corresponding transition from 1/f spectrum to a Lorentzian. Moreover, in some devices the noise level increases by orders of magnitude [15]. Does 1/f noise disappear or its intensity is overwhelmed by Lorentzian? The search for a single fluctuators or even "zero trap" in the channel is a goal followed by some groups [16], which developed nanoMOSFET with cylindrical gate surrounding a few nanometers channel.

However, just observing a single Lorentz spectrum or resolving the spectrum "into a small number of Lorentzians" [17] at low temperature in meso or nanostructures it is not enough to state that RTS noise is the fundamental source of 1/f noise. A necessary condition would be to clean the raw signal by eliminating the RTS and to investigate the spectrum of the background signal. Such experiments performed on microstructures [18] undoubtedly revealed a 1/f spectrum for the background signal, therefore in these cases RTS noise are a "parasitic" noise signal. More important, the RTS noise intensity is almost always orders of magnitude above the "residual" 1/f noise intensity. It is apparent from these facts that by decreasing the temperature, the causes producing 1/f noise do not disappear but considerably diminish. In this respect, it is interesting to note that even in some cases [17], [19] when the fundamental fluctuators are seen, the best theoretical fit to the decomposed spectra is to use Lorentzians plus a "1/f term to account for the small residual 1/f noise" [17]. These observations are also supported by noise measurements in quantum point contacts. For instance, Dekker's results [13] on two quantum point contacts at very low temperature (2K) revealed RTS noise in one of them, while the other featured 1/f noise of intensity orders of magnitude lower. Increasing the temperature, the noise intensity of the Lorentz spectrum associated to RTS noise decreases by orders of magnitude and the shape becomes 1/f at 25K. RTS noise in excess of the 1/f noise has been reported for AlGaAs/GaAs quantum dot single-electron transistor [20]. These results cast some doubts on the RTS as the fundamental ingredient of the 1/f noise.

Another problem could be that only the presence of RTS is not enough to have a 1/f spectrum. As in the case of g-r noise, one needs not only a distribution of time constant but also a $1/\tau$ statistical weight. Especially in the case of a two level RTS it is not clear how a distribution of time constant can be obtained from a single fluctuator. In this respect, recently Belyakov et al. [21] reported that in light emitting diode with quantum dots, the RTS noise intensity is at least an order of magnitude above the 1/f noise intensity of the "residual" signal. In addition, they have found that the current dependence of the characteristic frequency of the RTS spectrum does not vary considerably for about two decades of currents. Therefore, RTS noise cannot be a source of time constant distribution, let alone a $1/\tau$ one.

Seeing the RTS noise as a perturbative phenomenon and not as a fundamental source of the 1/f noise is also considerably supported by the often observed fact that the frequency exponent in the presence of the RTS noise is considerably larger than 1, as in the cases reported for vacuum nanotriode [22] or metallic nanobridges [14]. Sometimes, in small dimensional systems, the two spectra, 1/f and RTS noise, mix (modulate each other) and what is obtained is a $1/f^n$ spectrum, with $n \geq 3$, as in the case of MOS transistors with 100 nm channel length and 25 nm channel width [12]. A $1/f^3$ spectrum occurs when one phenomenon modulates the other. In this case, 1/f noise is hidden in the RTS. These observations do not support the hypothesis of RTS noise as a fundamental source of the 1/f noise.

Introduced as a *Deus ex machina* to circumvent a difficult, maybe a profound physical problem, the idea that RTS noise is the fundamental source of the 1/f noise is a *non sequitur* because, among others arguments, 1/f noise exists both in the absence and in the presence of the RTS noise.

3. A problem of topology: surface vs. bulk

The idea that 1/f noise is a surface effect is a corollary of the McWhorter model. The controversy surface vs. bulk was born out when Hooge [23] observed that 1/f noise intensity is inversely proportional to the total number of carriers in the sample, hence 1/f noise is a bulk effect. It has been long debated and the general belief is that, depending on the situation, there is either surface or bulk 1/f noise or both of them.

By far, the most interesting experiment nanoscience offers to clarify this controversy is the noise measurement on individual carbon nanotubes [24-30]. According to the recent measurements of Collins *et al.* [24], and Postma *et al.* [25] on single-walled carbon nanotubes (SWNTs), 1/f noise cannot be a bulk effect but a surface one. That is because a SWNT is a roled surface which does not have any bulk atom. If the noise is not entirely determined by contacts, it results that in a SWNT 1/f noise is a pure surface effect. Hence, the controversy whether 1/f noise is a surface or a bulk effect came to the end. In any case, since the noise intensity depends quadratically on current, the contacts are ohmic. For a MWCT partially iron-filled, Roumiantsev *et al.* [26] observed nonlinear effects in the noise which were ascribed to a possible nonlinear contact. In two-crossed MWNTs [29], the noise intensity depends superlinearly on current. It has been also explained by the presence of a resistance either at the junction between nanotubes or to nanotube-metal contact.

A very interesting experiment in clarifying this controversy was done recently by Collins and Avouris on MWCTs [30]. Removing the carbon shells one after another by sequential burning, they found that the

contribution of the bulk can be about 90%, while the surface contributes only 10%. There is also a nonlinear component in the noise data of Collins and Avouris [30]. For instance, a close look at the figure 1b from [30] indicates that for current till about 50μA, the noise intensity $S_I \sim I^{1.4}$, which points out to a driven, nonequilibrium 1/f noise mechanism. A transition from nonequilibrium to equilibrium 1/f noise ($S_I \sim I^2$) is observed for I>50μA.

A very important source of 1/f noise has been found to be the interface between carbon nanotubes [27], quantum dots [31] and platinum nanoparticles [32] and the substrate they are sitting on. For highly functional applications of the nanomaterials this could be of great concern.

4. Number vs. mobility fluctuations

The number vs. mobility fluctuation controversy transfers into the validity of the physical mechanisms which support one model or another. The number fluctuation model is based on tunnelling of the carrier into the oxide or interface states. The microscopic mechanism behind the bulk hypothesis [23] is the mobility fluctuation due to phonon scattering [33]. Although the noise measurements on nanomaterials are quite scarce [34-37], some existing results merely support the mobility fluctuation microscopic model instead of the number fluctuation one. For instance, in comparison with a polycrystalline gold film, Ochs et al. [34] observed excess 1/f noise in a gold nanocrystalline film which has been attributed to a higher density of grain boundaries in nanomaterials. But associated to the higher density of grain boundaries in nanomaterials is the excess vibrational density of states observed at both ends of the phonon spectrum [38]. Recently, we have speculated [39] that this excess noise can be the result of the excess phonon density of states. Due to this fundamental property, the nanostructured materials are ideally suited for such a dedicated experiment which is still awaiting.

In carbon nanotubes, the number fluctuation due to carriers tunnelling into interface states does not work at all, therefore, for a physical explanation, one has to look for some other models such as: diffusion or electron-phonon interaction. The last hypothesis is strongly supported by Postma's data [25] on the temperature dependence of 1/f noise in SWNTs which indicates the participation of Umklapp phonons in the 1/f noise.

Rich physical phenomena are encountered in nanoparticle films wherein tunnelling and hopping are fundamental conduction processes. In the experiments of Otten *et al.* [36] on PbS nanoparticle films, the substrate played a fundamental role in carrier transport but only diffusion noise was observed. On the contrary, in the noise measurement of Saminadayar on quantum dots [31] 1/f noise was found. The author attributed this result to

the “free charges moving around the dot” [31], hence to the carriers interaction with the substrate. One can conclude from these experiments that something more is necessary to have 1/f noise in the sense of number fluctuation model, only the interaction with the substrate does not suffice. In a recent experiment [32], nonequilibrium (nonlinear) 1/f-like noise has been found in platinum nanoparticle films, although the measurements were done in the ohmic region of the I-V characteristics. The temperature dependence of the film resistance, performed in the (8-300)K range, revealed a metallic conduction mechanism which is in opposition to the strong nonlinear character of the noise mechanism. Phonon-assisted variable range hopping (VRH) was the only mechanism capable to explain both the noise data and the conduction processes. Moreover, 1/f noise was found only in the (25-300)K temperature range where phonon-assisted VRH dominates the conduction. In the (8-25)K temperature range, where impurity scattering seems to dominate the conduction, there is no 1/f noise [32].

At the atomic scale, Koslowski *et al*. [40] investigated GaAs surface by STM and found that while both Ga and As atoms are “visible”, 1/f noise in the fluctuations of the tunneling current can be observed only when the tip is above the Ga atoms. This observation indicates that tunneling itself is not a source of 1/f noise. The necessary ingredient could be the phonons which inelastically assist the carriers tunneling. In fact, Koslowski *et al*.[39] tentatively attributed 1/f noise to the fluctuation of the surface phonon number. We consider that such an experiment performed on a SWNT would be of fundamental importance for the whole field.

5. Conclusions

Three fundamental longstanding questions in the field of low-frequency noise were discussed in the light of some recent noise measurements in nanomaterials and nanostructures. When possible, the Lorentzian superposition (McWhorther model) can be (in)validated by noise measurements in a nanoMOSFET with an oxide (12-15)Å thick. Analysis of the existing data for quantum point contacts and other small dimensional systems indicates that RTS noise as the fundamental component of the 1/f noise is a *nonsequitur*. The surface origin of the 1/f noise is strongly supported by noise measurements in SW carbon nanotubes, while the noise data for MW carbon nanotubes support both surface and bulk hypothesis. As for the controversy number vs. mobility fluctuations, excess 1/f noise observed in nanocrystalline gold was tentatively associated with the enhanced phonon density of states, specific to nanomaterials. The hypothesis of phonons participation in the 1/f noise is also supported by noise

measurements in platinum nanoparticle films. Certainly, nanoscience already shed much light on the old, still unsolved problems of 1/f noise.

References

[1] J. Bernamont, Ann. Phys. (Paris) 7 (1937) 71.

[2] M. Surdin, J. Phys. Radium, Serie 10 (1939) 188.

[3] A van der Ziel, Physica (Amsterdam) 16 (1950) 359.

[4] A. L. McWhorter, in "Semiconductor Surface Physics", University of Pennsylvania Press, (1957) 207.

[5] N. G. van Kampen, in Noise in Physical Systems, C. M. van Vliet (ed.), World Scientific, (1987) 3..

[6] F. N. Hooge and P. A. Bobbert, Physica B 239 (1997) 223.

[7] C. M. van Vliet, J. Appl. Phys. 93 (2003) 6068.

[8] E. Simoen, C. Claeys, Solid-St. Electron. 43 (1999) 865.

[9] Samuel Martin et al., Bell Labs Technical Journal, 30 (Summer, 1997).

[10] K. S. Ralls et al., Phys. Rev. Lett. 52 (1984) 228.

[11] M. J. Uren et al., Appl. Phys. Lett. 47 (1985) 1195.

[12] H. M. Bu et al., Appl. Phys. A 71 (2000) 133.

[13] C. Dekker et al., Phys. Rev. Lett. 66 (1991) 2148.

[14] K. S. Ralls and R. A. Buhrman, Phys. Rev. B 44 (1991-I) 5800.

[15] G. Ghibaudo et al., Phys. Stat. Sol. (a) 132 (1992) 501.

[16] T.A. Kramer and R. F. W. Pease, http:www.stanford.edu /~tkramer/ ARLSymposium.pdf.

[17] T. Rogers, R. A. Buhrman, Phys. Rev. Lett. 53 (1984) 1272.

[18] U. J. Strasilla and M. J. O. Strutt, Proc. IEEE 62 (1978) 1711.

[19] P. A. M. Holweg et al., Phys. Rev. B 45 (1992-II) 9311..

[20] T. Fujisawa and Y. Hirayama, Appl. Phys. Lett. 77 (2000) 543.

[21] A. V. Belyakov et al., Fluctuation and Noise Letters (in press).

[22] G. Driskill-Smith et al., J. Vac. Sci. Technol. B18 (2000) 3481.

[23] F. N. Hooge, Phys. Lett. A29 (1969) 139.

[24] Philip G. Collins et al., Appl. Phys. Lett. 76 (2000) 894.

[25] H. W. Ch. Postma, Ph. D. Thesis, Univ. of Delft (2001).

[26] S. Roumiantsev et al., Proc. of the 9th Int. Symp. on Nanostructures: Physics and Technology, St. Petersburg, (2001) 418.

[27] L. Roschier et al., Appl. Phys. Lett. 78 (2001) 3295

[28] P.-E. Roche et al., Eur. Phys. J. B 28 (2002) 217.

[29] H. Ouacha, M. Willander et al., Appl. Phys. Lett. 80 (2002) 1055.

[30] P. G. Collins and P. Avouris, ICNF, Prague (2003), in press.

[31] L. Samynadayar, Ph.D thesis, Univ. Paris VI (1997).

[32] M. Mihaila, D. Ursutiu et al., ICNF, Prague (2003), in press.

[33] F. N. Hooge and L. K.J. Vandamme, Phys. Lett. A 66 (1978) 315.

[34] Ochs et al., Phys. Stat. Sol. (a) 168 (1998) R9-R11.

[35] F.Otten et al., Appl. Phys. Lett. 77 (2000) 3421.

[36] Hoel et al., J. Appl. Phys. 91 (2002) 5221-5226.

[37] U. Stuhr et al., Phys. Rev. Lett. 81 (1998) 1449.

[38] M. Mihaila,Low-Frequency Noise in Nanomaterials and Nanostructures, in Noise and Fluctuations Control in Electronic Devices, A.Balandin(editor), American Scientific Publishers,(2002) 367.

[39] B. Koslowski et al., Surf. Sci. 280 (1993) 106.

1/*f* SPECTRA AS A CONSEQUENCE OF THE RANDOMNESS OF VARIANCE

G. Härtler
Gosener Damm 20, 12559 Berlin
Germany
haergis@aol.com

Abstract: It is a general conviction that any measured noise be stochastically continuous and weak stationary. Therefore, standard noise analysis uses the substitution of ensemble averages by time averages, and it considers likewise the autocorrelation function and the sample spectrum as an unbiased and complete characterization of the measured process. However, randomly distributed discontinuities make the constant variance turn into a random one. This contradicts the standard suppositions. We consider the random walk as a typical non-continuous process and derive the influence of the 'variance of variance' on the measured spectrum. In contrast to the standard analysis, sums of squares are no longer proportional to the chi-square-distribution, but to a distribution with a larger variance. When decomposing the data into fixed and random variance components, it can be shown that, despite independent increments, the random variance component produces a positive and time dependent expectation of the covariance. This is the source of the typically shaped non-zero autocorrelation function and the 1/f spectrum. The expectation of the autocorrelation at any given time difference is the product of the random variance component and a factor, which depends only on the total number of data and on the number of sampling intervals between the associated pairs of data. Consequently, the 1/f spectrum is no longer to be understood within the meaning of Parseval' s theorem. The larger the ratio of the random to the fixed variance component, the higher the 1/f increase onset frequency. 'Almost smooth' processes yield an 'almost white' spectrum, larger variance of increments generates a 1/f spectrum over a larger range of frequencies, and if the quotient between random and fixed variance components approaches 1, the 1/f spectrum will appear to extend over the full range of frequencies.

Keywords: Discontinuities, Random variance, 1/f noise.

J. Sikula and M. Levinshtein (eds.),
Advanced Experimental Methods for Noise Research in Nanoscale Electronic Devices (29 - 36)

1. Introduction

Today, it is standard to formulate noise models solely in the frequency domain as a relationship between the measured spectrum and the parameters of possible noise sources. This is correct provided the noise data are stochastically continuous and weak stationary. These standard assumptions are crucial; nevertheless, they are generally taken for granted. They allow to characterize the noise process likewise by the frequency spectrum or by the autocorrelation function, both being non-random functions comprising the complete information on the noise process. The measured spectrum is a statistical estimate with well known properties. As a formal consequence of this standard model we should expect the measured spectra to approach white noise for sufficiently large sampling intervals and measuring times. In contrast, for up-to-now unknown reasons one mostly measures 1/f noise. Commonly, one postulates additional noise sources, e.g. mixtures of processes with distributed time constants. However, the 1/f spectra seem to increase up to *arbitrarily* low frequencies, which can hardly be explained within the paradigm of a standard noise process. Here, we consider an alternative and abandon the standard assumption of stochastic continuity.

In Ref. [1], there were explained some strange 'memory properties' of the observed 1/f noise for fluctuations, which are generated by a randomly indexed random walk, and which are measured at equidistant points in time. This model is the basis of our study, too. We assume the fluctuating variable to be generated by *independent random increments* at *random time points* following the Poisson process. This model seems appropriate for noise processes, e.g., because conductivity fluctuations are fluctuations of the number of free electrons, or because the measured data characterize the instantaneous states of a system that travels randomly through a discrete state space, etc. The randomly indexed random walk is neither stationary nor stochastically continuous. Gut [2] called this process the *stopped random walk* and investigated some of its mathematical properties, e.g., various limit theorems. In our context, the most interesting property is the *randomness of variance*, which for measured 1/f noises was already revealed by Brophy [3]. The source of the random variance is the fluctuating number of increments in time intervals of identical length. With increasing sampling intervals there increase both the average and the variance of the number of increments. Randomness of variance implies the randomness of the autocorrelation function and of the spectrum. It is obvious that in some way the *variance of variance* could influence the sample autocorrelation functions and spectra. The derivation of this influence is the topic of this paper. For the sake of simplicity and in contrast to Ref.[1], we neglect the additional effects of after-effects and of families of Poisson processes.

The meaning of the term 'random variance' is vague if it is used to characterize data that were obtained from a single time domain measurement. There is just a single sequence of data available, which cannot be individually characterized by a 'variance' denoting the 'spread of the distribution'. The standard noise model supposes all data being realizations of *one* random variable, i.e. with *identical* variance. This variance may be estimated by time averaging. The random variance model supposes every value to be the realization of an *individual* random variable with an *individual* variance. It is impossible to estimate the 'variance of variances' from one measurement only. We need lots of them. Here, we study theoretically the influence of the 'variance of variance' for standard estimates of the autocorrelation function and the frequency spectrum. The starting point is the bivariate distribution of the mean squared data and the number of increments. This approach is exemplary of other non-continuous models, e.g., the RTS noise, where one has to apply the corresponding bivariate distribution.

2. The Model

Let $\{X_1, X_2, ..., X_m\}$ and X_t be the record of measured data and the value at time *t*, respectively. The sampling interval, Δ, denotes the time between consecutive measurements. For the sake of simplicity it is put $\Delta = 1$. The random difference between X_t and $X_{t+\Delta}$ is the sum of a random number, *n*, of independent random increments, ε_ν,

$$X_{t+\Delta} - X_t = \sum_{\nu=1}^{n} \varepsilon_\nu \tag{1}$$

Here, it holds $X_0 = 0$. We suppose that the ε_ν 's follow the normal distribution $N(0, \sigma_0)$ with the fixed variance σ_0^2. Hence, the increment of X in one sampling interval Δ follows the normal distribution whose expectation is zero and *random variance,* $n\sigma_0$.

3. Stochastic Properties of the Basic Statistics

The standard spectral estimate, which is obtainable only on a grid of discrete frequencies $\omega_k = 2\pi k / m$, $k = 0,1,2,...,[m/2]$, see e.g. Ref.[4], reads

$$I_m(\omega_k) = 2 \sum_{s=-(m-1)}^{m-1} \left[\frac{1}{m} \sum_{t=1}^{m-|s|} X_t X_{t+|s|} \right] \cos s\omega_k \tag{2}$$

For data following model (1) we need the expectation of the statistic $X_t X_{t+|s|}$ at $t = 1,2,...,m$, and $s = -(m-1),...,(m-1)$.

3.1. Expectation of the random variance

The case *s=0* and *fixed number of increments*, *n*, corresponds to the situation of the common standard model. It is known that the distribution of $(X_{t+\Delta} - X_t)^2$ is proportional to the χ^2-distribution with *n* degrees of freedom. Hence, the expectation and variance of $(X_{t+\Delta} - X_t)^2$ are $n\sigma_0^2$ and $2n\sigma_0^2$, respectively.

In the case of random n, we have to consider the additional influence of the distribution of *n*. The joint distribution of *n* and $(X_{t+\Delta} - X_t)^2$ is a bivariate distribution. Therefore, the expectation and variance of $(X_{t+\Delta} - X_t)^2$ under the influence of the random *n* are obtainable as the expectation and variance of the marginal distribution of $(X_{t+\Delta} - X_t)^2$, which is a weighted sum of all conditional χ^2 - distributions over all possible *n's*. The *n* follows the Poisson distribution

$$p(n) = \frac{\theta^n e^{-\theta}}{n!} , \qquad (3)$$

with θ denoting the intensity of the Poisson process, here defined at $\Delta = 1$. The Poisson distribution is characterized by equality of expectation and variance, both being equal to $N = \theta\Delta$.

According to a theorem of the probability theory one obtains the expectation and variance of the marginal distribution as follows:

1. The expectation of the marginal distribution is the expectation of expectations of all conditional distributions; in our case, it is $\sigma_0^2 N$.
2. The variance of the marginal distribution is the sum of the variance of the conditional distribution at the expectation of *n*, $2N\sigma_0^4$, and the variance of expectations of all conditional distributions, $N\sigma_0^4$.

Hence, for data following the model (1), the variance of $(X_{t+\Delta} - X_t)^2$ is given by $3\sigma_0^4 N$. The distribution of $(X_{t+\Delta} - X_t)^2$ is no longer proportional to the χ^2-distribution. Instead, it follows a marginal distribution with the same expectation and a larger variance.

For the sake of brevity, we replace the 'expectation', 'variance', and 'covariance' terms by operators $E\{...\}$, $Var[...]$, and $Cov[...]$, respectively. Because the model (1) is additive, it follows

$$E\{E[X_t^2]\} = t\sigma_0^2 N, \tag{4}$$

$$E\{Var[X_t^2]\} = 3t\sigma_0^4 N. \tag{5}$$

In Eq. (2), we need the *average* of expectations of all variances

$$\frac{1}{m} E\left\{\sum_{t=1}^{m} X_t^2\right\} = \frac{1}{2}(m+1)\sigma_0^2 N. \tag{6}$$

This corresponds to the variance at the mean time $\frac{m+1}{2}\Delta$ of the measured process, which is an incremental process with an increasing variance.

3.2. Expectation of the random covariance

Next, we need the expectations of all $X_t X_{t+|s|}$ at $|s| = 1,...,(m-1)$. According to the structure of the marginal variance, we decompose every random increment $[X_{t+\Delta} - X_t]$ into the *fixed* and the *random* variance component, $e(\Delta)$ and $a(\Delta)$, respectively. These generate the expectation of the fixed and random variance component, $2N\sigma_0^4$ and $N\sigma_0^4$, respectively. For any t there is $X_t = e_t + a_t$ with $e_t = te(\Delta)$ and $a_t = ta(\Delta)$. Expanding $X_t X_{t+|s|} = (e_t + a_t)(e_{t+|s|} + a_{t+|s|}) = e_t e_{t+|s|} + e_t a_{t+|s|} + a_t e_{t+|s|} + a_t a_{t+|s|}$, $s \neq 0$, we arrive at following implications: Because of the independence of increments, there holds $E[e_t e_{t+|s|}] = 0$, because the increments are independent of the number of increments, there is $E[a_t e_{t+|s|}] = E[a_{t+|s|} e_t] = 0$. The properties of the Poisson process imply $E[a_t a_{t+s}] = E[a^2_{\min[t,t+s]}] = \min[t, t+s]\sigma_0^4 N$, i.e. $E[X_t X_{t+s}] > 0$. In Eq.(2), we need for every $s \neq 0$ *the average* of the expectation of the covariance

$$\frac{1}{m} E\left\{\sum_{t=1}^{m-|s|} X_t X_{t+|s|}\right\} = \frac{(m-|s|)(m-|s|+1)}{2m}\sigma_0^4 N. \tag{7}$$

This is the main result: The random variance component causes a non-zero expectation of the covariance appearing as non-zero 'autocorrelation', and depending on σ_0^4. The general structure of $(m-|s|)(m-|s|+1)/(2m)$ implies that all autocorrelation functions are of similar shape.

4. Expectation of the Random Autocorrelation Function

The expectation of the random autocorrelation function, $Cov(s)$, consists of two parts: At $s = 0$ it corresponds to the average variance, Eq. (6), at $s \neq 0$ it is the expectation of the average covariance, Eq. (7). The latter is proportional to the average number of cases in which the time interval between $t = 0$ and $\min[t, t+s]$ is overlapped.

Figure 1 shows the dependence of $E[Cov(s)]$ on s for $\Delta = 1$, *m=10000*, *N=100*, $E[e(\Delta)] = 1$ and $E[a(\Delta)^2] = 1; 0.9; 0.5; 0.25$. The curves are distinguished by different dashing, where the shorter lines belong to the smaller $E[a(\Delta)^2]$`s. If $E[a(\Delta)^2] < E[e(\Delta)^2]$, $Cov(0)$ has a sharp peak. Here, the case of $E[a(\Delta)^2] > E[e(\Delta)]$ will not be considered.

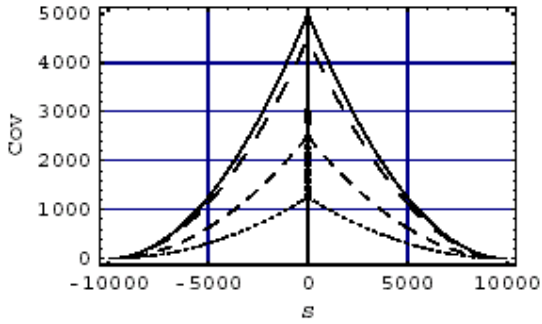

Figure 1. Autocorrelations, $m = 10000$, $E[e(\Delta)] = 1$, $E[a(\Delta)^2] = 1, 0.9, 0.5, 0.25$, top to bottom.

5. Expectation of the Random Sample Spectrum

The expectation of the random spectrum follows from Eq. (2). For the curves of Fig. 1, it is shown in Fig. 2.

The higher the frequency at which the sample spectrum approaches the 1/f behavior, the closer to 1 the ratio of random and fixed variance components. At $E[a(\Delta)^2] / E[a(\Delta)^2] = 1$, the sample spectrum extends over the full range of frequencies like a '1/f' spectrum.

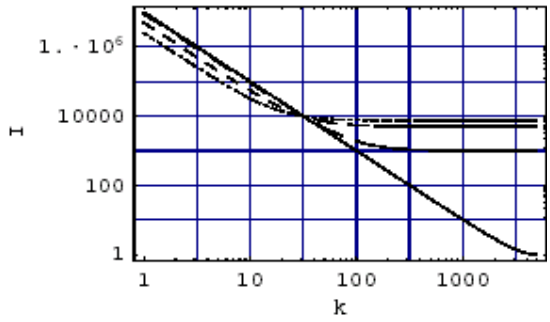

Figure 2. Spectra of curves of Figure 1, $m = 10000$, $E[e(\Delta)] = 1$, $E[a(\Delta)^2] = 1, 0.9, 0.5, 0.25$.

6. Conclusions

Random variance influences both the sample autocorrelation function and the sample spectrum. The reason is simple: Standard noise analysis uses the time averages of $X_t X_{t+|s|}$'s, and the embedded Poisson process yields $E[X_t X_{t+|s|}] = \sigma_0^4 \theta\Delta \min[t, t+s] > 0$. The factor of the random variance term depends only on *m* and $m - |s|$. This explains why sample spectra of random variance processes with the same ratio of random and fixed variance component become similar, and it also implicates that these spectra do not mean 'noise power' in the meaning of Parseval's theorem.

One might express doubts as to the general applicability of the non-continuous model presented here. It was chosen as the simplest prototype of a non-continuous process allowing to show clearly how, despite independent increments, there emerges positive autocorrelation. This model may be linked to theoretic models and adapted to practical situations. For instance, data of typical RTS noise fluctuate during time intervals of random length around non-zero conditional averages. The bivariate distribution of the mean squared deviations and of the probabilities of different conditional averages in one sampling interval yield a marginal distribution, which is no longer a family of simple χ^2-distributions with degrees of freedom following the Poisson distribution.

In the case of our model, the magnitude of the positive autocorrelation depends on σ_0^4. Rather smooth processes, $\sigma_0^2 \to 0$, yield a very small expectation of the covariance, which becomes only detectable at sufficiently large *m* and $\theta\Delta$.

References

[1] G. Härtler, Statistical Explanation for the observation of 1/f noise from basically discrete fluctuations, Fluctuation and Noise Letters, **1** (2001) L139-L146.

[2] J. J. Brophy, Statistics of 1/f noise, Phys.Rev. 166 (1968) 827-831.

[3] A. Gut, Stopped Random Walks, Limit Theorems and Applications, Springer, New York (1988)

[4] M.B. Priestley, Spectral Analysis and Time Series, Academic Press, London, (1981)

QUANTUM PHASE LOCKING, $1/f$ NOISE AND ENTANGLEMENT

M. Planat
Laboratoire de Physique et Métrologie des Oscillateurs du CNRS
32 Avenue de l'Observatoire, 25044 Besançon Cedex
France
planat@lpmo.edu

H. Rosu
Potosinian Institute of Scientific and Technological Research
Apdo Postal 3-74, Tangamanga, San Luis Potosi, SLP
Mexico
hcr@ipicyt.edu.mx

Abstract We develop a new approach of the quantum phase in an Hilbert space of finite dimension which is based on the relation between the physical concept of phase locking and mathematical concepts such as cyclotomy and the Ramanujan sums. As a result phase variability looks quite similar to its classical counterpart, having peaks at dimensions equal to a power of a prime number. Squeezing of that noise is allowed for specific quantum states. The concept of phase entanglement for pairs of phase-locked states is introduced.

Keywords: quantum phase noise, phase locking, phase entanglement, number theory

1. Introduction

Time and phase are not well defined concepts at the quantum level. The present work belongs to a longstanding effort to model phase noise and phase-locking effects that are found in high stability oscillators. It was unambiguously demonstrated that the observed variability, (i.e., the 1/f frequency noise of such oscillators) is related to the finite dynamics of states during the measurement process and to the precise filtering rules that involve continued fraction expansions, prime number decomposition, and hyperbolic geometry [1],[4].

J. Sikula and M. Levinshtein (eds.),
Advanced Experimental Methods for Noise Research in Nanoscale Electronic Devices (37 - 44)

We seek here for a quantum counterpart of these effects by studying the new notions of quantum phase-locking and quantum phase entanglement. The problem of defining quantum phase operators was initiated by Dirac in 1927 [6]. For excellent reviews, see [7]. The starting point is the Pegg and Barnett quantum phase formalism [8] where the calculations are performed in an Hilbert space H_q of finite dimension q. The phase states are defined as superpositions of number states from the so-called quantum Fourier transform (or QFT)

$$|\theta_p\rangle = q^{-1/2} \sum_{n=0}^{q-1} \exp(\frac{2i\pi pn}{q})|n\rangle \ . \tag{1}$$

in which $i^2 = -1$. The states $|\theta_p\rangle$ form an orthonormal set and in addition the projector over the subspace of phase states is $\sum_{p=0}^{q-1} |\theta_p\rangle\langle\theta_p| = 1_q$ where 1_q is the identity operator in H_q. The inverse quantum Fourier transform follows as $|n\rangle = q^{-1/2} \sum_{p=0}^{q-1} \exp(-\frac{2i\pi pn}{q})|\theta_p\rangle$. As the set of number states $|n\rangle$, the set of phase states $|\theta_p\rangle$ is a complete set spanning H_q. In addition the QFT operator is a q by q unitary matrix with matrix elements $\kappa_{pn}^{(q)} = \frac{1}{\sqrt{q}} \exp(2i\pi \frac{pn}{q})$.

From now we emphasize phase states $|\theta'_p\rangle$ satisfying phase-locking properties. We first impose the coprimality condition

$$(p, q) = 1, \tag{2}$$

where (p, q) is the greatest common divisor of p and q. Differently from the phase states (1), the $|\theta'_p\rangle$ form an orthonormal base of a Hilbert space whose dimension is lower, and equals the number of irreducible fractions p/q, which is given by the Euler totient function $\phi(q)$. These states were studied in our recent publication [3].

Guided by the analogy with the classical situation [2] we call these irreducible states the phase-locked quantum states. They generate a cyclotomic lattice L [9] with generator matrix M of matrix elements $\kappa_{pn}^{'(q)}$, (p,q)=1 and of size $\phi(q)$. The corresponding Gram matrix $H = M^\dagger M$ shows matrix elements $h_{n,l}^{(q)} = c_q(n - l)$ which are Ramanujan sums

$$c_q(n) = \sum_p \exp(2i\pi \frac{p}{q} n) = \frac{\mu(q_1)\phi(q)}{\phi(q_1)}, \ \text{ with } \mathrm{q_1 = q/(q, n)}. \tag{3}$$

where the index p means summation from 0 to $q - 1$, and $(p, q) = 1$. Ramanujan sums are thus defined as the sums over the primitive characters $\exp(2i\pi \frac{pn}{q})$, (p,q)=1, of the group $Z_q = Z/qZ$. In the equation above $\mu(q)$ is the Möbius function, which is 0 if the prime number decomposition of q contains a square, 1 if $q = 1$, and $(-1)^k$ if q is the product of k distinct primes [10]. Ramanujan sums are relative integers which are quasiperiodic versus n with quasi period

$\phi(q)$ and aperiodic versus q with a type of variability imposed by the Möbius function. Ramanujan sums were introduced by Ramanujan in the context of Goldbach conjecture.

They are also useful in the context of signal processing as an arithmetical alternative to the discrete Fourier transform [11]. In the discrete Fourier transform the signal processing is performed by using all roots of unity of the form $\exp 2i\pi p/q$ with p from 1 to q and taking their nth power $e_p(n)$ as basis function. We generalized the classical Fourier analysis by using Ramanujan sums $c_q(n)$ as in (3) instead of $e_p(n)$. This type of signal processing is more appropriate for arithmetical functions than is the ordinary discrete Fourier transform, while still preserving the metric and orthogonal properties of the latter. Notable results relating arithmetical functions to each other can be obtained using Ramanujan sums expansion while the discrete Fourier transform would show instead the low frequency tails in the power spectrum.

In this paper we are also interested in pairs of phase-locked states which satisfy the two conditions

$$(p, q) = 1 \ \ and \ \ p\bar{p} = -1(mod\, q). \tag{4}$$

When it exists $\bar{p}$ is uniquely defined from minus the inverse of p modulo q. The two fractions p/q and $\bar{p}/q$ are the ones selected from the partition of the half plane by Ford circles. Ford circles are defined as the set of the images of the horizontal line z=x+i, x real, under all modular transformations in the group of 2×2 matrices $SL(2, Z)$ [4]. Ford circles are tangent to the real axis at a Farey fraction p/q, and are tangent to each other. They have been introduced by Rademacher as an optimum integration path to compute the number of partitions from the Ramanujan's circle method. In that method two circles of indices p/q and $\bar{p}/q$, of the same radius $\frac{1}{2q^2}$ are dual to each other on the integration path.

2. The Quantum Phase Operators

The projection operator over the subset of phase-locked quantum states $|\theta'_p\rangle$ is calculated as

$$P_q^{\text{lock}} = \sum_p |\theta'_p\rangle\langle\theta'_p| = \frac{1}{q}\sum_{n,l} c_q(n-l)|n\rangle\langle l|, \tag{5}$$

where the range of values of n, l is from 0 to $\phi(q)$. Thus the matrix elements of the projection are $q\langle n|P_q|l\rangle = c_q(n-l)$. This sheds light on the equivalence between cyclotomic lattices of algebraic number theory and the quantum theory of phase-locked states.

The projection operator over the subset of pairs of phase-locked quantum states $|\theta'_p\rangle$ is calculated as

$$P_q^{\rm pairs} = \sum_{p,\bar{p}} |\theta'_p\rangle\langle\theta'_{\bar{p}}| = \frac{1}{q}\sum_{n,l} k_q(n,l)|n\rangle\langle l|, \tag{6}$$

where the notation $p, \bar{p}$ means that the summation is applied to such pairs of states satisfying (4). The matrix elements of the projection are $q\langle n|P_q^{\rm pairs}|l\rangle = k_q(n,l)$, which are in the form of so-called Kloosterman sums [5]

$$k_q(n,l) = \sum_{p,\bar{p}} \exp[\frac{2i\pi}{q}(pn - \bar{p}l)], \tag{7}$$

Kloosterman sums $k_q(n,l)$ as well as Ramanujan sums $c_q(n-l)$ are relative integers. They are given below for the two cases of dimension $q = 5(\phi(5) = 4)$ and $q = 6(\phi(6) = 2)$.

$$q = 5: \quad k_5 = \begin{bmatrix} 4 & -1 & -1 & -1 \\ -1 & 4 & -1 & -1 \\ -1 & -1 & 4 & -1 \\ -1 & -1 & -1 & 4 \end{bmatrix}, \quad c_5 = \begin{bmatrix} -1 & -1 & -1 & 4 \\ -1 & 4 & -1 & -1 \\ -1 & -1 & 4 & -1 \\ 4 & -1 & -1 & -1 \end{bmatrix},$$

$$q = 6: \quad k_6 = \begin{bmatrix} 2 & 1 \\ 1 & 2 \end{bmatrix}, \quad c_6 = \begin{bmatrix} -1 & 2 \\ -2 & 1 \end{bmatrix}.$$

One defines the quantum phase-locking operator as

$$\Theta_q^{\rm lock} = \sum_p \theta_p |\theta'_p\rangle\langle\theta'_p| = \pi P_q^{\rm lock} \ \text{ with } \theta_{\rm p} = 2\pi\frac{\rm p}{\rm q}. \tag{8}$$

The Pegg and Barnett operator [8] is obtained by removing the coprimality condition. In such a case it is Hermitian with eigenvalues θ_p. Using the number operator $N_q = \sum_{n=0}^{q-1} n|n\rangle\langle n|$ the authors get a generalization of Dirac's commutator $[\Theta_q, N_q] = -i$.

Similarly one defines the quantum phase operator for pairs as

$$\Theta_q^{\rm pairs} = \sum_{p,\bar{p}} \theta_p |\theta'_p\rangle\langle\theta'_{\bar{p}}| = \pi P_q^{\rm pairs} \ \text{ with } \theta_{\rm p} = 2\pi\frac{\rm p}{\rm q}. \tag{9}$$

The phase number commutator for phase-locked states calculated from (8) is

$$C_q^{\rm lock} = [\Theta_q^{\rm lock}, N_q] = \frac{\pi}{q}\sum_{n,l}(l-n)c_q(n-l)|n\rangle\langle l|, \tag{10}$$

with antisymmetric matrix element $\langle l|C_q^{\rm lock}|n\rangle = \frac{\pi}{q}(l-n)c_q(n-l)$.

For pairs of phase-locked states an antisymmetric commutator $C_q^{\rm pairs}$ similar to (10) is obtained with $k_q(n,l)$ in place of $c_q(n-l)$.

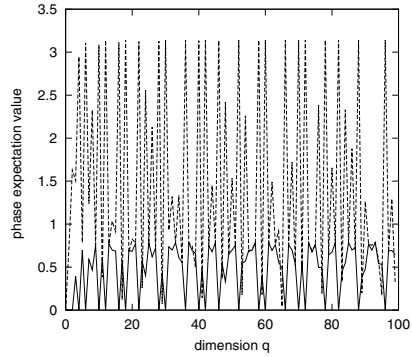

Figure 1. Phase expectation value versus the dimension q of the Hilbert space. Plain lines: $\beta = 0$, Dotted lines: $\beta = 1$.

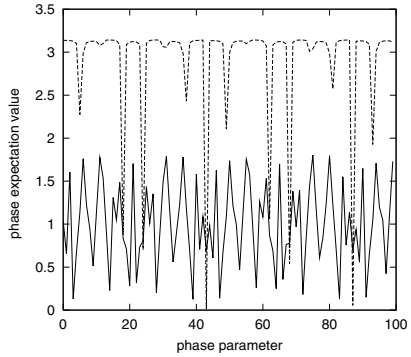

Figure 2. Phase expectation value versus the phase parameter β. Plain lines: $q = 15$. Dotted lines $q = 13$.

3. Phase Expectation Value and Variance

The finite quantum mechanical rules are encoded within expectation values of the phase operator and phase variance.

Rephrasing Pegg and Barnett let consider a pure phase state $|f\rangle = \sum_{n=0}^{q-1} u_n |n\rangle$ having u_n of the form

$$u_n = (1/\sqrt{q}) \exp(in\beta), \tag{11}$$

where β is a real phase parameter. One defines the phase probability distribution $\langle \theta'_p | f \rangle^2$, the phase expectation value $\langle \Theta_q^{\rm lock} \rangle = \sum_p \theta_p \langle \theta'_p | f \rangle^2$, and the phase variance $(\Delta\Theta_q^2)^{\rm lock} = \sum_p (\theta_p - \langle \Theta_q^{\rm lock} \rangle)^2 \langle \theta'_p | f \rangle^2$. One gets

$$\langle \Theta_q^{\rm lock} \rangle = \tfrac{\pi}{q^2} \sum_{n,l} c_q(l-n) \exp[i\beta(n-l)], \tag{12}$$

$$(\Delta\Theta_q^2)^{\rm lock} = 4\langle \tilde{\Theta}_q^{\rm lock} \rangle + \tfrac{\langle \Theta_q \rangle^2}{\pi} (\langle \Theta_q \rangle - 2\pi), \tag{13}$$

with the modified expectation value $\langle \tilde{\Theta}_q^{\rm lock} \rangle = \frac{\pi}{q^2} \sum_{n,l} \tilde{c}_q(l-n) \exp[i\beta(n-l)]$, and the modified Ramanujan sums $\tilde{c}_q(n) = \sum_p (p/q)^2 \exp(2i\pi m \frac{p}{q})$.

Fig. 1 illustrates the phase expectation value versus the dimension q for two different values of the phase parameter β. For $\beta = 1$ they are peaks at dimensions $q = p^r$ which are powers of a prime number p. For $\beta = 0$ the peaks are smoothed out due to the averaging over the Ramanujan sums matrix. Fig. 2 shows the phase expectation value versus the phase parameter β. For the case of the prime number $q = 13$, it is high with absorption like lines at isolated values of β. For the case of the dimension $q = 15$ which is not a prime power the phase expectation value is much lower and much random.

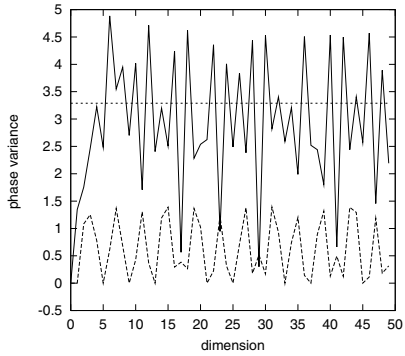

Figure 3. Phase variance versus the dimension q of the Hilbert space. Plain lines: $\beta = 1$. Dotted lines: $\beta = \pi$.

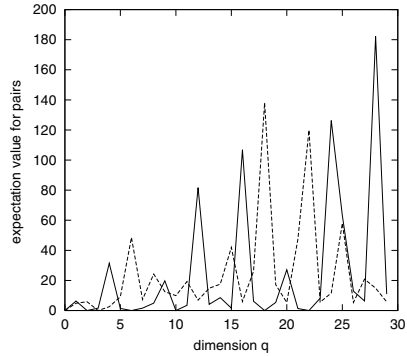

Figure 4. Phase expectation value versus the dimension q for pairs of phase-locked states. Plain lines: $\beta = 0$. Dotted lines: $\beta = 1$.

Fig. 3 illustrates the phase variance versus the dimension q. The case $\beta = 1$ also leads to peaks at prime powers. Like the expectation value in Fig. 1, it is thus reminiscent of the Mangoldt function. Mangoldt function $\Lambda(n)$ is defined as $\ln p$ if n is the power of a prime number p and 0 otherwise. It arises in the frame of prime number theory [1] from the logarithmic derivative of the Riemann zeta function $\zeta(s)$ as $-\frac{\zeta'(s)}{\zeta(s)} = \sum_{n=0}^{\infty} \frac{\Lambda(n)}{n^s}$. Its average value oscillates about 1 with an error term which is explicitely related to the positions of zeros of $\zeta(s)$ on the critical line $s = \frac{1}{2}$. The error term shows a power spectral density close to that of $1/f$ noise [1]. It is stimulating to recover results reminding prime number theory in the new context of quantum phase-locking.

Finally the phase variance is considerably smoothed out for $\beta = \pi$ and is much lower than the classical limit $\pi^2/3$. The parameter β can thus be interpreted as a squeezing parameter since it allows to define quantum phase-locked states having weak phase variance for a whole range of dimensions.

4. Towards Phase Entanglement

The expectation value of quantum phase states can be rewritten from the projection operator of individual phase states $\pi_p = |\theta'_p\rangle\langle\theta'_p|$ as follows

$$\langle\Theta_q^{\text{lock}}\rangle = \sum_p \theta_p \langle f|\theta'_p\rangle\langle\theta'_p|f\rangle = \sum_p \theta_p \langle f|\pi_p|f\rangle. \tag{14}$$

This suggests a definition of expectation values for pairs from the product $\pi_p \pi_{\bar{p}}$ as follows

$$\langle \Theta_q^{\text{pairs}} \rangle = \sum_{p,\bar{p}} \theta_p \langle f | \pi_p \pi_{\bar{p}} | f \rangle. \tag{15}$$

It is inspired by the quantum calculation of correlations in Bell's theorem [12]. Using pure phase states as in (11) we get

$$\langle \Theta_q^{\text{pairs}} \rangle = \frac{2\pi}{q^2} \sum_{n,l} \tilde{k_q}(n,l) \exp[i\beta(n-l)], \tag{16}$$

where we introduced generalized Kloosterman sums
$\tilde{k}_q(n,l) = \sum_{p,\bar{p}} p \exp[\frac{2i\pi}{q}(p-\bar{p})(l-n)]$. These sums are in general complex numbers (and are non Gaussian integers). The expectation value is real as expected. In Fig. 4 it is represented versus the dimension q for two different values $\beta = 0$ and $\beta = 1$. Note that the pair correlation (15) is very much dependant on q and can become quite huge at some values.

This result claims for a detailed study of Bell's type inequalities based on quantum phase-locked states we are looking at, and their relationship to the properties of numbers. Calculations involving fully entangled states

$$|f\rangle = \frac{1}{q} \sum_{p,\bar{p}} |\theta_p, 1\rangle \otimes |\theta_{\bar{p}}, 2\rangle, \tag{17}$$

have to be carried out. This is left for future papers.

5. Conclusion

In conclusion, we pinpoint in this letter several properties resulting from introducing phase-locking in Pegg-Barnett quantum phase formalism. We recall that the idea of quantum teleportation was initially formulated by Bennett et al in finite-dimensional Hilbert space [13], but, yet independently of this, one can conjecture that cyclotomic locking could play an important role in many fundamental tests of quantum mechanics related to quantum entanglement. As a matter of fact, Munro and Milburn [14] have already conjectured that the best way to see the quantum nature of correlations in entangled states is through the measurement of the observable canonically conjugate to photon number, i.e. the quantum phase. Moreover, in their paper dealing with the Greenberger-Horne-Zeilinger quantum correlations, they presented a homodyne scheme requiring discrete phase measurement, which has yet to be experimentally realized in the ultrahigh detector efficiency limit. Nevertheless, a homodyne scheme automatically implies phase-locking measurements with number theory coming into play.The remote phase-locking of atomic clocks is also envisaged [15].

References

[1] M. Planat, $1/f$ noise, the measurement of time and number theory, Fluc. and Noise Lett. 1 (2001) R63–R77.

[2] M. Planat and E. Henry, The arithmetic of $1/f$ noise in a phase-locked loop, Appl. Phys. Lett. 80 (2002) 13–16.

[3] M. Planat and H. Rosu, Cyclotomy and Ramanujan sums in quantum phase locking, Phys. Lett. A (in press), ArXiv quant-ph/0304101.
Some errors and misprints are present in that earlier report. The summation in (3),(5),(7) and (9) should be from 0 to $\phi(q)$. The expectation value $\langle\theta_q^{\rm lock}\rangle$ in (8) should be squared. They are also slight changes in the plots.

[4] M. Planat, Modular functions and Ramanujan sums for the analysis of 1/f noise in electronic circuits, ArXiv hep-th/0209243.

[5] A. Terras, Fourier Analysis on Finite Groups and Applications, Cambridge Press (1999).

[6] P.A.M. Dirac, The quantum theory of the emission and absorption of radiation, Proc. Roy. Soc. London A 114 (1927) 243–265.

[7] R. Lynch, The quantum phase problem: A critical review, Phys. Rep. 256 (1995) 367–436.

[8] D.T. Pegg and S.M. Barnett, Phase properties of the quantized single mode electromagnetic field, Phys. Rev. A39 (1989) 1665-1675.

[9] J.H. Conway and N.J.A. Sloane, Sphere packings, lattices and groups, Springer, New York (1999), p. 227.

[10] G.H. Hardy and E.M. Wright, An introduction to the theory of numbers, Oxford Press, Oxford (1979), p. 237.

[11] M. Planat, Ramanujan sums for signal processing of low frequency noise, Phys. Rev. E 66 (2002) 56128-56135.

[12] M. O. Scully and S. Zubairy, Quantum optics Cambridge Press, (1996), p. 515.

[13] C.H. Bennett et al, Teleporting an unknown quantum state via dual classical and Einstein-Podolsky-Rosen channels Phys., Rev. Lett. 70 (1993) 1895–1899.

[14] W.J. Munro and G.J. Milburn, Characterizing GHZ Correlations in Nondegenerate Parametric Oscillation via Phase Measurements, Phys. Rev. Lett. 81 (1998) 4285–4288.

[15] R. Josza, D. S. Abrams, J. P. Dowling and C.P. Williams, Quantum atomic clock synchronization based on shared prior entanglement, Phys. Rev. Lett. 85 (2000) 2010–2013.

SHOT NOISE IN MESOSCOPIC DEVICES AND QUANTUM DOT NETWORKS

M. Macucci, P. Marconcini, G. Iannaccone, M. Gattobigio, G. Basso, B. Pellegrini

Dipartimento di Ingegneria dell'Informazione
Università degli Studi di Pisa
Via Diotisalvi, 2
I-56122 Pisa, Italy
macucci@mercurio.iet.unipi.it

Abstract We discuss specific noise phenomena in several ballistic mesoscopic structures and in networks of quantum dots or metallic dots interconnected by tunneling barriers, focusing on the techniques used for the numerical simulation and on the physical interpretation of the results.

Keywords: Shot noise suppression, Shot noise enhancement, Nanostructures, Numerical simulation

1. Ballistic structures without magnetic field

For the investigation of transport and noise in structures without magnetic field we use a technique based on the recursive evaluation of the overall Green's function, starting from the analytically computed Green's functions of elementary sections [1, 2]. From the transmission matrix it is then possible to obtain the conductance via the Landauer-Büttiker formula and the Fano factor, i.e. the shot noise suppression or enhancement factor, as will be detailed in the present section.

If we consider a section of the device such that the transverse potential can be considered constant along the direction of electron propagation, there will be no transverse mode mixing in it, thus the Green's function matrix (consisting in a representation over the transverse eigenmodes) will be diagonal and it will be possible to evaluate each element from an analytical expression [1], with the hypothesis of Dirichlet boundary conditions at the section ends. Starting from the semi-infinite section containing the output lead, we keep on

J. Sikula and M. Levinshtein (eds.),
Advanced Experimental Methods for Noise Research in Nanoscale Electronic Devices (45 - 52)

adding the preceding sections, one at a time, introducing a perturbation potential $\hat{V}$ which "opens up" facing section ends and connects them. The Green's function of the perturbed structure (with the two sections joined) can be evaluated from Dyson's equation:

$$\hat{G} = \hat{G}^0 + \hat{G}^0 \hat{V} \hat{G} \,, \tag{1}$$

where $\hat{G}^0$ is the unperturbed Green's function (with the two sections decoupled) and $\hat{G}$ is the perturbed Green's function (with the application of $\hat{V}$). This is an implicit equation, since $\hat{G}$ appears on both sides: with some algebra, considering a representation of the Green's functions on the eigenmodes for the transverse direction and on the sites in real space for the longitudinal direction, it is possible to obtain explicit relationships that can be applied in the recursive procedure [2]. Once the Green's function of the overall structure has been computed, it is straightforward to obtain from it the transmission matrix t, following the procedure outlined in [1].

¿From the transmission matrix t we obtain the conductance of the device via the Landauer-Büttiker formula:

$$G = \frac{2\,e^2}{h} \sum_{n,m} |t_{nm}|^2 \ . \tag{2}$$

The low-frequency noise power spectral density is given by Büttiker [3] as

$$S_I = 4\,\frac{e^3}{h}\,|V| \sum_n w_n \left(1 - w_n\right) \ , \tag{3}$$

where the w_n's are the eigenvalues of the matrix $t\,t^\dagger$, V is the constant externally applied voltage, e is the electron charge, and h is Planck's constant. Since the full shot noise power spectral density is given by Schottky's theorem as $S_{I_{fs}} = 2eI$ (where I is the average value of the current, given by the product of the applied voltage times the conductance), we obtain a simple expression for the ratio γ, usually defined as Fano factor, of the noise power spectral density to that expected for full shot noise:

$$\gamma = \frac{\sum_j w_j \left(1 - w_j\right)}{\sum_{n,m} |t_{nm}|^2} \tag{4}$$

Jalabert *et al.* have shown [4], using Random Matrix Theory, that a ballistic symmetric cavity delimited by apertures that are much smaller than the cavity size (such as the one shown in the inset of Fig. 1) is characterized by a Fano factor of $1/4$. We have applied our numerical techniques to the investigation of shot noise suppression in such cavities in a variety of conditions, which can be treated easily with our approach.

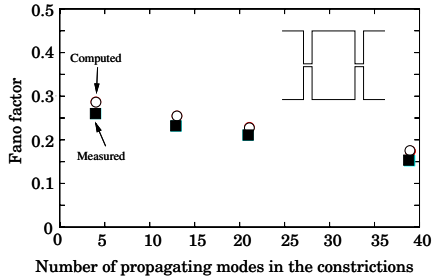

Figure 1. Fano factor in a chaotic cavity with no magnetic field

The Fano factor, which reaches the asymptotic value of $1/4$ for narrow enough and symmetric input and output constrictions, decreases if the constrictions are made wider: in the limiting case of disappearing constrictions (when their width equals that of the wire) the Fano factor is known to drop to zero, since we reach the situation of a perfect, ballistic wire. Results for the Fano factor of a cavity with symmetric apertures as a function of the number of propagating modes in the constrictions are shown in Fig. 1. The width of the cavity is $8\ \mu$m and its length is $5\ \mu$m. Such results, although obtained with a coarse hard wall model, are in rather good agreement with the experimental data published by Oberholzer *et al.* in [5].

Our technique can be readily applied also to cascaded cavities, in particular we focus on identical cascaded cavities, finding that no appreciable variation of the Fano factor is observed with respect to that of a single cavity. Results for 2, 3, and 4 cavities are reported in Fig. 2 as a function of the Fermi energy. This conclusion is in sharp contrast with the analytical conclusion reached by Oberholzer et al. in [6], in which the authors state that the Fano factor for cascaded cavities should tend to the asymptotic limit $1/3$, in analogy with what happens for a series of potential barriers, each of which is orthogonal to the propagation direction. Further investigation is needed to understand the discrepancy between the two approaches, which cannot be explained simply on the basis that our model is fully coherent while that of [6] assumes decoherence between adjacent cavities: the recent literature seems to agree on the irrelevance of the presence or lack of coherence on the noise behavior of mesoscopic devices.

Another interesting structure to be investigated is an antidot lattice inserted in a quantum wire [7]. Let us first examine the noise behavior of a square antidot lattice: we consider a quantum wire $1.2\ \mu$m wide with 7 layers along the longitudinal direction (see the inset of Fig. 3) of square antidots with a side of 24 nm and a distance between antidot centers of 244 nm. The resulting Fano factor is shown in Fig. 3 (solid curve) as a function of the Fermi energy, and it clearly settles around a value of about 0.11. If we increase the size of

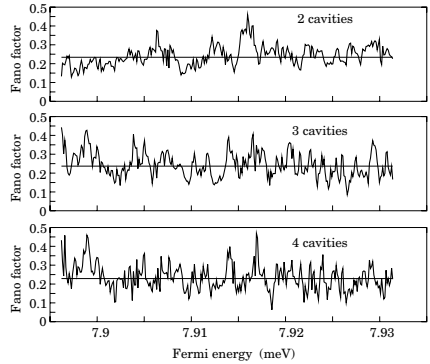

Figure 2. Fano factor for cascaded cavities

the antidots to 48 nm (keeping the same distance between antidot centers as in the previous case), the Fano factor raises to about 0.14, as visible in Fig. 3 (dashed curve). Further increases of the antidot size lead, for a square lattice, to a maximum Fano factor of about 0.15: as the antidot walls get closer along the transverse direction, which tends to increase the Fano factor, they also get closer along the longitudinal direction, thereby approaching the formation of regular, noiseless conduits. The result of these two competing effects is the saturation of the Fano factor to the mentioned limiting value. The dependence of the Fano factor on the number of layers exhibits a saturation, too: for 7 layers we have already reached the asymptotic condition [7].

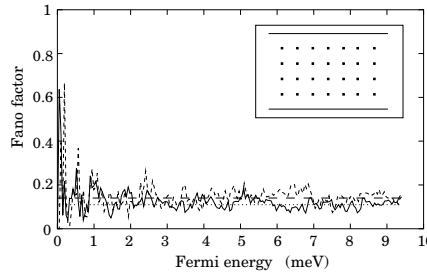

Figure 3. Fano factor for a square antidot lattice

If, instead of a square antidot lattice, we consider a rectangular one, with the longitudinal separation much larger than that along the transverse direction, we have a situation very similar to that of cascaded chaotic cavities, with the only difference that each cavity has multiple input and output apertures instead of a single one: as long as the total width of the resulting apertures is significantly

smaller than that of the wire, we achieve the conditions for shot noise suppression with a Fano factor of 0.25, as typical for chaotic cavities. This is shown in Fig. 4, where the results for shot noise suppression in the case of 188 nm square antidots separated by a distance of 278 nm along the transverse direction and of 1388 nm along the longitudinal direction are reported: the Fano factor settles around a value of about 0.25, as expected for chaotic cavities.

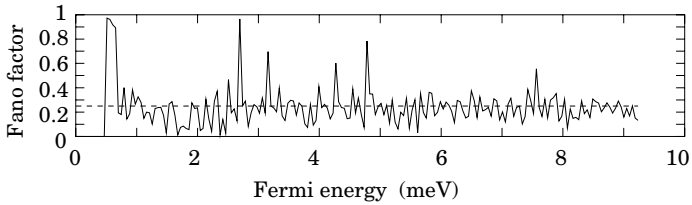

Figure 4. Fano factor for a rectangular antidot lattice

2. Chaotic cavities in a magnetic field

In order to study the behavior of chaotic cavities in the presence of an orthogonal magnetic field, we have selected a scattering matrix approach, which makes treatment of the magnetic field simpler, for several cases, than the formally similar Green's function approach, although being in principle slightly less efficient from the computational point of view.

We have chosen a gauge for the representation of the vector potential with a nonzero component only in the longitudinal direction x ($\vec{A} = [\,-By\ 0\ 0\,]^T$). We subdivide the structure into a number of transverse slices such that inside each of them the scalar and the vector potentials can be considered constant along the longitudinal direction. Then we consider the sections straddling from the middle of a slice to the middle of the following one and, from the transverse eigenfunctions and the longitudinal wave vectors in each slice, we compute the scattering matrix for each section by means of the mode-matching technique. We evaluate the overall scattering matrix of the device by recursively composing the scattering matrices of all of the slices, and, from its properly normalized transmission submatrix, we obtain the actual transmission matrix t. The most challenging task of this calculation is represented by the procedure to compute the transverse eigenfunctions and the longitudinal wave vectors in each slice, which is performed with the technique introduced by Tamura and Ando [8].

We have focused on the investigation of how the Fano factor varies in the presence of a magnetic field in a chaotic cavity. The results of our simulations show that, while for small or zero values of B the Fano factor in a symmetric

chaotic cavity is 0.25, such a value decreases for higher magnetic field values. We wish to point out that this result is independent of the dimensions of the cavity but strongly depends on the width of the constrictions which define it. The Fano factor as a function of magnetic field is shown in Fig. 5 for a few choices of the constriction width: we notice that, as the width is decreased, a larger magnetic field is needed to obtain the same Fano factor. Such a behavior can be explained by comparing the width of the constrictions W_c with the classical cyclotron radius of the electrons $R_c = \sqrt{2m^* E_f}/(eB)$ (where m^* is the effective mass of the electron and E_f is the Fermi energy): in a confined mesoscopic structure in the presence of a magnetic field, edge states form, which can be classically explained as skipping orbits with radius R_c. For values of B such as to make R_c comparable with W_c, the edge states pass through the constrictions and mainly crawl along the walls of the cavity, thereby quenching the chaotic behavior of the cavity and, consequently, the value of the shot noise power spectral density.

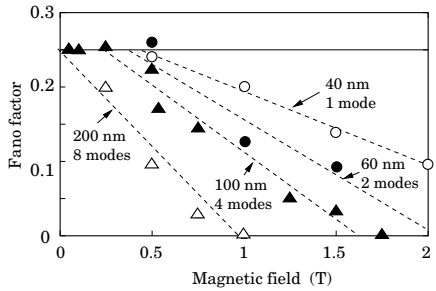

Figure 5. Fano factor as a function of the magnetic field

3. Shot noise suppression and enhancement in networks of metallic dots

Shot noise suppression and, more interestingly, enhancement have been predicted [9] to be observable in single electron circuits based on metallic islands connected by tunnel junctions and capacitors. The particular structure for which we have demonstrated the existence of shot noise enhancement is a Quantum Cellular Automaton cell [10] biased near the point of switching. The cell we have considered is shown in the inset of Fig. 6 and consists of four metal islands: tunneling is possible between the two upper ones or between the lower ones, but not between the upper and lower pairs, which are connected only through standard capacitors. The voltage sources connected to the dots via tunneling junctions make a current flow through the upper and lower pair of

dots, as long as the Coulomb blockade is lifted by adjusting the other voltage sources (which in the following we define bias voltages). In particular, we are interested in the condition in which an excess electron is present on each pair of dots. The Coulomb blockade is lifted when the chemical potentials in a pair of dots are aligned and electrons are therefore allowed to tunnel from one dot to the other.

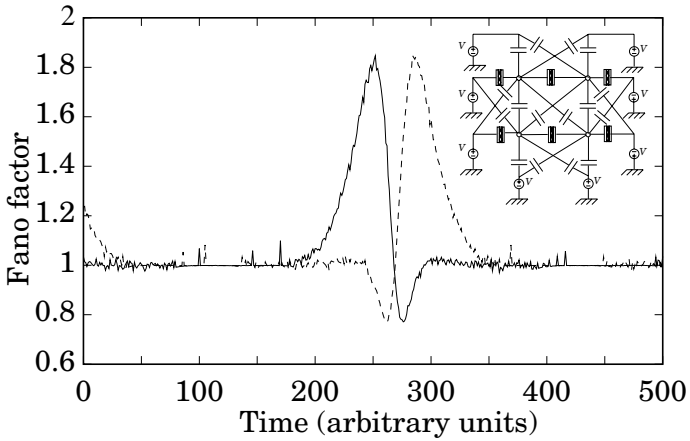

Figure 6. Fano factor for a circuit with 4 coupled dots

We compute the currents and noise in this structure by means of a Monte Carlo simulation, assuming that the bias voltages for each dot pair are varied with two linear ramps of opposite slope, so that at a specific instant the chemical potentials of the two dots line up. A small shift is introduced between the ramps applied to the lower dot pair and those applied to the upper dot pair, so that the Coulomb blockade for the two pairs is lifted at slightly different times. This leads to an interaction between the upper and the lower pair, in which the current through one pair "drives" the other, bringing the other pair closer to the alignment condition. The role of the "driver" and of the "driven" currents are interchanged when the "driven" current becomes larger than the "driver" one. In Fig. 6 we report the behavior of the Fano factor for the two currents as a function of time (and actually of the bias point, since we are considering the application of linear ramps): the driver current (dashed curve in the left part of the plot) exhibits suppressed shot noise, while the driven current (solid curve in the left part of the plot) is characterized by a Fano factor larger than 1. This is a result of positive electron correlations: as an electron tunnels through the dot pair through which the driven current flows, it favors tunneling of an electron in the opposite direction in the other dot pair, whose potentials are thus changed in such a way as to increase the likelihood of a further electron tunneling through the former pair.

4. Conclusion

We have discussed shot noise suppression in several different nanostructures and a case of shot noise enhancement: it is apparent how important an analysis of the noise behavior is for a better understanding of correlations between charge carriers and of transport mechanisms in low dimensional devices. A common value of the Fano factor may hint at deeper analogies between apparently different structures, such as in the case of cascaded chaotic cavities and of transversally dense rectangular antidot lattices. Once again noise is shown to be a more sensitive probe of transport properties than other, more commonly considered, electrical quantities.

Acknowledgments

We gratefully acknowledge financial support from the Italian CNR (National Research Council) through the "5% Nanotecnologie" project and from the cofunding program of the University of Pisa.

References

[1] F. Sols, M. Macucci, U. Ravaioli, and Karl Hess, J. Appl. Phys. 66, (1989) 3892.
[2] M. Macucci, A. Galick, and U. Ravaioli, Phys. Rev. B 52, (1995) 5210.
[3] M. Büttiker, Phys. Rev. Lett. 65, (1990) 2901.
[4] R. A. Jalabert, J.-L. Pichard, and C. W. J. Beenakker, Europhys. Lett. 27, (1994) 255.
[5] S. Oberholzer, E. V. Sukhorukov, and C. Schönenberger, Nature 415 (2002) 765.
[6] S. Oberholzer, E. V. Sukhorukov, C. Strunk, and C. Schönenberger, Phys. Rev. B 66 (2002) 233304.
[7] M. Macucci, Physica B **314** (2002) 494.
[8] H. Tamura and T. Ando, Phys. Rev. B **44** (1991) 1792.
[9] M. Gattobigio, G. Iannaccone, and M. Macucci, Phys. Rev. B 65 (2002) 115337.
[10] C. S. Lent, P. D. Tougaw, and W. Porod, Appl. Phys. Lett. 62, (1993) 714.

SUPER-POISSONIAN NOISE IN NANOSTRUCTURES

Ya. M. Blanter
Department of NanoScience, Delft University of Technology
Lorentzweg 1, 2628CJ Delft
The Netherlands
blanter@tnntw14.tn.tudelft.nl

Abstract We describe the transition from sub-Poissonian to super-Poissonian values of the zero-temperature shot noise power of a resonant double barrier of macroscopic cross-section. This transition occurs for driving voltages which are sufficiently strong to bring the system near an instability threshold. It is shown that interactions in combination with the energy dependence of the tunneling rates dramatically affect the noise level in such a system. Interaction-induced fluctuations of the band bottom of the well contribute to the noise and lead to a new energy in the Fano factor. They can enhance the noise to super-Poissonian values in a voltage range preceding the instability threshold of the system. This mechanism is different from the super-Poissonian enhancement due to the large effective charge.

Keywords: Shot noise, Fano factor, charge accumulation.

1. Introduction

In the last decade, studies of shot noise in mesoscopic conductors [1] have become very popular. This is because they reveal information on transport properties of nanostructures which is not available from conductance measurements. Indeed, according to Landauer formula, the conductance of a mesoscopic system can be expressed via the set of its transmission eigenvalues T_n in a simple way,

$$G = G_Q \sum_n T_n, \quad G_Q = 2_s e^2/2\pi\hbar, \tag{1}$$

where the factor 2_s counts the directions of spin. At the other hand, any process of electron transport is characterized by shot noise, which is a manifestation of randomness of transmission of electrons through the system. At zero tempera-

J. Sikula and M. Levinshtein (eds.),
Advanced Experimental Methods for Noise Research in Nanoscale Electronic Devices (53 - 60)

ture, the (zero-frequency) spectral density shot noise is given by

$$S = 2eG_Q|V|\sum_n T_n(1-T_n). \tag{2}$$

At finite temperature, noise has a more complicated form due to the emergence of equilibrium (Nyquist-Johnson) noise.

We see, indeed, that shot noise measures a different combination of transmission eigenvalues than the conductance and thus contains additional information on the tranmission properties of the system. This is characterized by the Fano factor,

$$F = \frac{S}{2eI} = \frac{\sum_n T_n(1-T_n)}{\sum_n T_n}, \tag{3}$$

with I being the average current through the device. Since the transmission eigenvalues assume the values between zero and one, the Fano factor also varies between zero and one. It equals zero for $T_n = 1$ (ideal transmission) and tends to one when all the eigenvalues are small, $T_n \ll 1$, for instance, for the tunneling barrier. The maximal value of shot noise $S_{max} = 2eI$ corresponds to the random, uncorrelated transmission events and is referred as Poisson value of noise. Shot noise at zero temperature is always suppressed with respect to the Poisson value.

The above considerations refer to non-interacting electrons. A topic of recent interest is whether for interacting electrons shot noise can exceed the Poisson value.

One option is the following. Poissonian noise results from uncorrelated transfer of electrons (with the charge e). Obviously, if the transfer processes are more complicated and involve the transfer of charge Ne, the Fano factor is increased by the factor of N. This is for example what happens for transport between a normal and a superconducting electrodes [2]. For voltages and temperatures below the superconducting gap transfer of electrons into the superconducting electrode is impossible. The transport proceeds by means of Andreev reflection: An electron is reflected back to the normal metal as a hole. Such a process is accompanied by the charge deficit $2e$, which corresponds to the creation of a Cooper pair in the superconductor. Consequently, the Fano factor is multiplied by two. In particular, if the normal metal and the superconductor are separated by the barrier of low transparency, the Fano factor assumes the value of 2 and noise is clearly super-Poissonian. This phenomenon has been recently observed experimentally [3].

A similar idea was used recently in a quite different situation. Safonov et al [4] observed super-Poissonian noise (with the Fano factor up to 1.5) in tunneling via localized states. To explain this enhancement, they suggested an ingenious model of transport controlled by two impurities, say A and B. Each of the impurities can be neutral or charged. For conceptual clarity, we consider

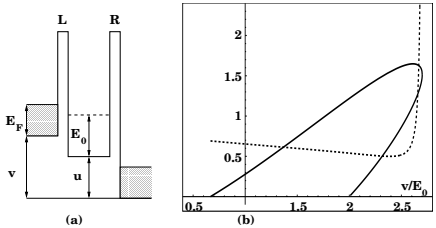

Figure 1. The potential profile of the quantum well (a); current (in units of $c_L E_0^2/e$, solid line) and the Fano factor F (dashed line) as functions of voltage for a particular choice of parameters: $a_L = a_R$, $c_L = c_R$, $E_F = 2E_0/3$, $e^2\nu\mathcal{A} = 10c_L$. For this case $v^* = 2.70E_0$ (b).

the situation when the charging of A shifts the energy level of B above the Fermi surface, so that the current can not flow via B. If, in addition, A changes its state (between charged and neutral) very slowly, it does not contribute to the transport itself, and only modulates the transport via B. This transport appears then to be uncorrelated transfer of N electrons, where $N = T_B/T_A$, with $T_{A,B}$ being the times with the impurity A, B spends in the neutral state. The Fano factor in this situation is enhanced by the factor of N. The analysis on a more qualitative level showed a good agreement with the experimental results.

In this paper, we consider in details a different mechanism of super-Poissonian shot noise enhancement, which originates from an instability in the $I-V$ curve in combination with the charging effects. We present here the classical theory [1]; the quantum theory is also available [5]. The theoretical research was inspired by two experimental studies [6, 7] which observed super-Poissonian enhancement of noise in quantum wells in strongly non-linear regime.

2. Rate equations

We consider the geometry of the quantum well shown in Fig. 1a. The well is extended in x and y directions and has a total area $\mathcal{A}$. In z-direction the motion is quantized, and we assume that there is only one resonant level E_0 (all energies are measured from corresponding band bottoms). The transverse motion is described by a continuum of momenta $p_\perp$. For simplicity we assume also that the Fermi energies E_F in both banks are the same, and $E_0 > E_F$. The distribution functions of electrons in the left and right reservoirs are Fermi functions f_L and f_R, whereas the distribution of electrons inside the well is described by the function $f_w(E_z, p_\perp)$, which remains to be determined. Consequently, the total charge of the well is

$$Q_w = 2_s e \sum_{p_\perp} \int dE_z f_w(E_z, p_\perp)\delta(E_z - E_0). \tag{4}$$

We now introduce the total charges $Q_L(t)$ and $Q_R(t)$ transmitted from the left to the right through the left and the right barriers, respectively, from a reference time $t = 0$ until the time moment t. At any instant of time the charge of the well is $Q_w(t) = Q_L(t) - Q_R(t)$. The time evolution of the charge Q_L is determined by the rate equation,

$$\dot{Q}_L = \frac{2_s e}{\hbar} \sum_{p_\perp} \int dE_z \, \Gamma_L(E_z) \, \delta(E_z - E_0) \left[f_L(E_z + u - v, p_\perp) - f_w(E_z, p_\perp) \right], \tag{5}$$

where v/e and u are the driving voltage and the position of the band bottom of the well, respectively (Fig. 1a). For the energy-dependent tunneling rates $\Gamma_{L,R}$ through the left and right barrier, respectively, we take the specific forms

$$\begin{aligned} \Gamma_L(E_z) &= a_L E_z^{1/2} (E_z + u - v)^{1/2} \theta(E_z) \theta(E_z + u - v); \\ \Gamma_R(E_z) &= a_R E_z^{1/2} (E_z + u)^{1/2} \theta(E_z) \theta(E_z + u), \end{aligned} \tag{6}$$

which correspond to the tunneling through a simple rectangular barrier. For the following, we assume that the tunneling rates are much smaller than all other energy scales, which are u, v, E_0 and E_F. This means that the dimensionless constants a_L and a_R, defined by Eq. (5), are small. Performing the integration and taking Eq. (4) into account, we obtain

$$\begin{aligned} \dot{Q}_L &= \frac{\Gamma_L(E_0)}{\hbar} \left\{ e\nu \mathcal{A}(v + E_F - u - E_0) \theta(v + E_F - u - E_0) \right. \\ &\times \left. \theta(E_0 + u - v) - Q_L + Q_R \right\}, \end{aligned} \tag{7}$$

where ν is the density of transverse states. In the same way, we obtain

$$\dot{Q}_R = \frac{\Gamma_R(E_0)}{\hbar} (Q_L - Q_R). \tag{8}$$

The rate equations (6) and (8) are supplemented by a formula relating the band bottom position u to the total charge of the well $Q_L - Q_R$. Introducing capacitances $c_{L,R}$ of the left (right) barriers, we write

$$e(Q_L - Q_R) = c_L(u - v) + c_R u, \tag{9}$$

which we assume to be valid at any instant of time. Finally, the last equation relates current (which is the sum of particle and displacement currents) across the quantum well to the charges Q_L and Q_R (sometimes cited as Ramo-Shockley theorem),

$$I = \frac{c_L \dot{Q}_R + c_R \dot{Q}_L}{c_L + c_R}. \tag{10}$$

3. Stationary regime. Average current

We study first the average quantities in the stationary regime of the system. Then the band bottom position u is time independent. The average current is $\langle I\rangle = \dot{Q}_L = \dot{Q}_R$.

First, we determine the quantity u. Subtracting Eq. (8) from Eq. (6) and taking Eq. (9) into account, we obtain a closed equation for u,

$$\begin{aligned} & e^2\nu\mathcal{A}\Gamma_L(v+E_F-u-E_0)\theta(v+E_F-u-E_0)\theta(E_0+u-v) \\ - \quad & (\Gamma_L+\Gamma_R)\left[(c_L(u-v)+c_R u\right] = \hbar(c_L+c_R)\dot{u}, \end{aligned} \tag{11}$$

with the notations $\Gamma_{L,R} \equiv \Gamma_{L,R}(E_0)$. Eq. (10) determines the dependence of the energy u on the external bias voltage v. In a certain range of voltages, $v_b \equiv (c_L+c_R)E_0/c_R < v < v^*$, an instability is induced: The equation has three solutions for u, $u_1 < u_2 < u_3$. The solution $u_1 = c_L v/(c_L+c_R)$ corresponds to the charge neutral well, while u_2 and u_3 describe the charged system. It is easily seen from Eqs. (6) and (8) that the solution u_2 is unstable. The instability threshold v^* is determined from the condition $c_L + c_R + c_0[u(v)] = 0$, where $c_0 = -e\partial\bar{Q}/\partial u$ is the response of the charge of the well to an increment of the potential, $\bar{Q} \equiv e\nu\mathcal{A}\Gamma_R(v+E_F-u-E_0)$.

For the average current we find from Eq. (8)

$$\langle I\rangle = \frac{e\nu\mathcal{A}}{\hbar}\frac{\Gamma_L\Gamma_R}{\Gamma_L+\Gamma_R}(v+E_F-u-E_0)\theta(v+E_F-u-E_0)\theta(E_0+u-v), \tag{12}$$

which is an implicit function of voltage if Eq. (10) is taken into account. The current is only nonzero for voltages between $v_a \equiv (c_L+c_R)(E_0-E_F)/c_R$ and v^*. Furthermore, for $v_b < v < v^*$ it is a multi-valued function of the voltage; one of the solutions $\langle I\rangle = 0$ corresponds to the charge neutral well, and the two others (one stable and one unstable) are due to charging. The current-voltage characteristic for this system is shown in Fig. 1b. Due to this multi-stability, the system shows hysteretic behavior: upon increasing voltage, the current stays finite until v^*, and then jumps to the $\langle I\rangle = 0$ branch. When the voltage is decreasing, the current is zero above v_b, and becomes finite for lower voltages. In the real experiment, of course, this hysteretic behavior would be smeared due to the finite value of tunneling rates, and may even totally disappear.

4. Noise

To investigate current fluctuations, one has to include Langevin sources to the right hand side of the rate equations (6) and (8). To make this procedure meaningful, we have to linearize the equations. In the following, we assume that the voltage lies between v_a and v^*. We write $u(t) = u_0(v) + \Delta u(t)$,

where u_0 is the stationary solution. (In the case of several solutions, u_0 always represents the stable one for the charged well, denoted previously by u_3). Linearizing Eqs. (6) and (8) in Δu, we write

$$\begin{aligned} \dot{Q}_L &= \langle I \rangle + \Big[J - e^{-1}\Gamma_L (c_L + c_R + c_0[u_0]) \Big] + \xi_L(t); \\ \dot{Q}_R &= \langle I \rangle + \Big[J + e^{-1}\Gamma_R (c_L + c_R + c_0[u_0]) \Big] + \xi_R(t), \end{aligned} \tag{13}$$

where the u-dependent tunneling rates $\Gamma_{L,R}$ are evaluated for $u = u_0$, and the quantity $J = \partial(\Gamma_R \bar{Q})/\partial u$ (also taken for $u = u_0$) is the response of the average current to the increment of the potential.

On the right hand sides of the rate equations we introduced now the random Langevin forces $\xi_L(t)$ and $\xi_R(t)$. As usual, they vanish on average, $\langle \xi_L \rangle = \langle \xi_R \rangle = 0$. We assume furthermore that fluctuations in different contacts are independent and are correlated according to the classical shot noise rules,

$$\langle \xi_\alpha(t) \xi_\beta(t') \rangle = e \langle I \rangle \delta(t - t') \delta_{\alpha\beta}, \quad \alpha, \beta = L, R. \tag{14}$$

Now, defining the zero-frequency current-current spectral correlation function in a standard way,

$$S = 2 \int d(t - t') \left[\langle I(t) I(t') \rangle - \langle I \rangle^2 \right], \tag{15}$$

after some algebra we obtain the Fano factor,

$$F = \frac{1}{2} + 2 \frac{(\Lambda - \Delta\Gamma)^2}{\Gamma^2}, \quad \Delta\Gamma \equiv (\Gamma_L - \Gamma_R)/2, \quad \Lambda \equiv \frac{J}{c + c_0}. \tag{16}$$

For $v \to v^*$ the denominator $c + c_0$ of the interaction energy $\Lambda(v)$ quite generally diverges as $(v^* - v)^{-1/2}$, while the numerator J stays finite. Thus, the Fano factor diverges according to $(v^* - v)^{-1}$. In particular, close enough to the instability threshold V^* the Fano factor increases above one: The noise becomes *super-Poissonian*. At the onset of current, for $v = v_a$ the Fano factor can be calculated in closed form, and one has $1/2 < F(v_a) < 1$. Thus, we describe the transition from sub-Poissonian to super-Poissonian noise. The minimal possible value of the Fano factor in this theory is $F = 1/2$. It can be shown that the voltage dependence of the Fano factor is peculiar, and, depending on the relative value of the charging effects $e^2 \nu_2 \mathcal{A}/c$, noise may be either suppressed as compared with the non-interacting value for low voltages and enhanced for high voltages ("weak interaction scenario"), or enhanced, then suppressed, and only after that enhanced again ("strong interaction scenario"). The voltage dependence of the Fano factor is illustrated in Fig. 1b. The divergence of noise is clearly seen.

The finite value of the partial decay widths (tunneling rates) smears the singularities, and, in particular, induces a finite value of the Fano factor for

$v = v^*$. Another source of deviations from the experimental results is our linearization procedure. For voltages close to the instability threshold the linear approximation is clearly insufficient, and large fluctuations (transitions between the two states) must be taken into account. These fluctuations also would induce a finite value of noise for $v = v^*$. We do not see any reason, however, why these processes should suppress noise below the Poisson value in the whole range of voltages.

5. Conclusions

We discuss now the following issue. To obtain the super-Poissonian noise enhancement, we needed multi-stable behavior of the I–V curve; in turn, the multi-stability in quantum wells is induced by charging effects. The charging (or, generally, interaction) effects are not required to cause the multi-stability. Indeed, if instead of a voltage controlled experiment, we discuss a current controlled experiment, the I–V characteristics for the uncharged quantum well are multi-stable for *any* external current. For the case of an arbitrary load line there typically exists a finite range of external parameters where multi-stable behavior is developed. However, recent experiments on superlattice tunnel diodes [8] (where one has bistability but no charge accumulation) did not find any traces of noise enhancement. Thus, charging is essential by itself, and this remains an open question.

Usually such bistable systems are discussed from the point of view of telegraph noise, which is due to spontaneous random transitions between the two states. This is a consideration complementary to the one we developed above. Indeed, in the linear approximation the system does not know that it is multi-stable. The shot noise grows indefinitely at the instability threshold only because the state around which we have linearized the system becomes unstable rather than metastable. This is a general feature of linear fluctuation theory. Clearly the divergence of shot noise in the linear approximation must be a general feature of all the systems with multi-stable behavior. Interactions are not the necessary ingredient for this shot noise enhancement. On the other hand, as we have discussed, the transitions between different states, neglected in the linear approximation, will certainly soften the singularity and drive noise to a finite value at the instability threshold. To describe in this way the interplay between shot noise and random telegraph noise remains an open problem.

In conclusion, we described the transition from sub-Poissonian to super-Poissonian values of shot noise of a resonant quantum wells. The super-Poissonian enhancement appears due to the combination of charging, energy dependence of the tunneling rates, and the intrinsic instability induced by these

two factors. This mechanism is different from the previously discussed in the literature super-Poissonian enhancement due to the large effective charge.

References

[1] For review, see Ya. M. Blanter and M. Büttiker, Shot noise in mesoscopic conductors, Phys. Rep. 336 (2000) 1-166.

[2] V. A. Khlus, Current and voltage fluctuations in microjunctions of normal and superconducting metal, Zh. Éksp. Teor. Fiz. 93 (1987) 2179-2190 [Sov. Phys. JETP 66 (1987) 1243-1249]; M. J. M. de Jong and C. W. J. Beenakker, Doubled shot-noise in disordered normal-metal superconductor junctions, Phys. Rev. B 49 (1994) 16070-16073; B. A. Muzykantskii and D. E. Khmelnitskii, Quantum shot-noise in a normal metal - superconductor point contact, Phys. Rev. B 50 (1994) 3982-3987; T. Martin, Wave packet approach to noise in N-S junctions, Phys. Lett. A 220 (1996) 137-142.

[3] X. Jehl, M. Sanquer, R. Calemczuk, and D. Mailly, Detection of doubled shot noise in short normal-metal/superconductor junctions, Nature 405 (2000) 50-53; A. A. Kozhevnikov, R. J. Schoelkopf, L. E. Calvet, M. J. Rooks, and D. E. Prober, Shot noise measurements in diffusive normal metal-superconductor (N-S) junctions, J. Low. Temp. Phys. 118 (2000) 671-678.

[4] S. S. Safonov, A. K. Savchenko, D. A. Bagrets, O. N. Jouravlev, Y. V. Nazarov, E. H. Linfield, and D. A. Ritchie, Enhanced shot noise in resonant tunneling via interacting localized states, Phys. Rev. Lett. (to be published).

[5] Ya. M. Blanter and M. Büttiker, Transition from sub-Poissonian to super-Poissonian shot noise in resonant quantum wells, Phys. Rev. B 59 (1999) 10217-10226.

[6] G. Iannaccone, G. Lombardi, M. Macucci, and B. Pellegrini, Enhanced shot noise in resonant tunneling: Theory and experiment, Phys. Rev. Lett. 80 (1998) 1054-1057.

[7] V. V. Kuznetsov, E. E. Mendez, J. D. Bruno, and J. T. Pham, Shot noise enhancement in resonant-tunneling structures in a magnetic field, Phys. Rev. B 58 (1998) R10159-R10162.

[8] W. Song, E. E. Mendez, V. Kuznetsov, and B. Nielsen, Appl. Phys. Lett. 82 (2003) 1568-1570.

STOCHASTIC AND DETERMINISTIC MODELS OF NOISE

J. Kumičák
Technical University of Košice
Vysokoškolská 4, 042 00 Košice
Slovakia
Juraj.Kumicak@tuke.sk

Abstract The paper describes several models which may be of use for explanation of the origin and properties of experimentally observed types of noise. The stochastic models are analyzed first, including the autoregressive scheme and the moving averages on the *n*-th order. Galton board model and generalized baker map represent deterministic systems with rich set of properties. The results presented in the second half of the paper are intimately connected to the theory of deterministic chaos, and the crucial role is played there by the attractors in phase spaces of the systems.

Keywords: Models of noises, stochastic and deterministic models, generalized baker map

1. Introduction

It is generally admitted that understanding the origin and properties of variety of noises may be aided by mathematical models which are able to generate many different types of noises by changing only a few model parameters. Even if such models will not yield *immediate* physical interpretation, they can help us in our search for physical mechanisms by identifying model components, which critically influence relevant properties of generated processes, such as spectrum.

The models can be subdivided into stochastic and deterministic ones. The former have an appeal of simplicity and plausibility, the latter seem to promise better representation of the physical essence of the problem. One should evidently expect that both approaches will ultimately converge to the same results because conceptually both should represent one and the same physical phenomenon.

J. Sikula and M. Levinshtein (eds.),
Advanced Experimental Methods for Noise Research in Nanoscale Electronic Devices (61 - 68)

Noises observed in physical systems represent paradigmatic stochastic processes and therefore the most natural approach to them relies on their simulation by various types of stochastic mathematical models. Only two such models are analyzed in this context closely, namely the nonlinear generalization of autoregressive scheme of the first order, and the sequence of moving averages with variable order.

Deterministic models of noise may originate in the investigations of irreversibility of simple model systems. At first sight it might seem that this property is not related to the problem of noise, but the contrary is true. Irreversibility is found in systems with sufficiently chaotic dynamics and the latter is at the same time a necessary condition for observing noise in deterministic systems. Preliminary results seem to point to the conclusion that the joint treatment of irreversibility and noise represents the correct direction in which one has to go to arrive at the solution of both problems: the origin and essence of irreversibility, and the characterization of noises appearing in deterministic, microscopically reversible systems, with seemingly irreversible macroscopic behavior.

The paper reflects the author's preferences and experiences with different models and could be considered as a review of his work. The contribution begins with the analysis of stochastic models. One of the simplest is the one based on nonlinear generalization of autoregressive scheme of the first order.

2. Autoregressive scheme

The scheme is described by the iterative prescription

$$y_{k+1} = g(y_k) + \sigma \nu_{k+1}, \tag{1}$$

where $\{\nu_k\}$ denotes the sequence of uncorrelated normally distributed random variables with zero expectation and unit variance. The value σ represents standard deviation of a white noise source. It is evident that for $g(y) \equiv 0$ the scheme (1) will generate the white noise sequence and for $g(y) \equiv y$ the brownian one [1].

For a well defined set of functions $g(y)$ the above scheme was shown to generate noises with $1/f^k$-like spectra with $0 \le k \le 2$. However, the generation of $1/f$ noise using this model did not seem too convincing. Nevertheless, it was able to generate very satisfactory bistable burst noise [2]. To this effect one had to choose $g(y)$ to be a step function $g(y) = a\ \mathrm{sgn}(y)$ with positive constant a. With such a choice of $g(y)$, the waveform generated by the scheme (1) strongly resembled that of the bistable burst noise. The two values $a, -a$ represent evidently its attractors.

Numerical simulations performed for values $\sigma < a$ with samples of the length $1000 \le N \le 10000$ confirmed that the sequences generated by the scheme – and with eliminated white noise component – have Lorentzian spectrum which, at higher frequencies, decays as $1/f^k$ with $k \approx 2$. This result is easy to prove also analytically by demonstrating that the sequence generates random telegraph signal. The proof demonstrated that the latter may be obtained independently by similar simple iteration.

3. Moving averages

It is a well-known fact that any continuous spectrum of a stationary stochastic sequence can be arbitrarily closely approximated by the spectrum of some random sequence of moving averages of order n – or MA(n) for short. We will treat $1/f$ noise as MA(n) with n taken as a *variable* parameter.

Consider a stationary sequence of random variables $\{y_t\}$ having the spectral density $S(\lambda)$ of that of $1/f$ noise. The covariance function $C_n(h)$ of such a sequence is related to its spectrum via the Wiener-Khintchine theorem, which enables to find it as a function of n. Consider now MA(n) generated by coefficients $\{a_k\}$ ($k = 0 \ldots n$) and defined as

$$y_t = \sum_{k=0}^{n} a_k \nu_{t-k}, \tag{2}$$

where $\{\nu_t\}$ is a sequence of totally uncorrelated random variables with unit variance. The covariance function of the sequence $\{y_t\}$ equals

$$R_n(h) = \sum_{k=0}^{n-h} a_k a_{k+h}, \quad h = 0, 1, 2, \ldots, n \tag{3}$$

Choosing now a_k in such a way that $R_n(h) = C_n(h)$, the discretized spectrum of MA(n) will be $1/|\lambda_s|$ ($s = 0 \ldots n$). We are thus facing the problem of finding, for any finite n, the corresponding set $\{a_k\}$. The solution will give us a MA(n) sequence with $1/f$ spectrum for any sample length n.

We have solved the problem numerically [3] using the Seidel iteration method for 12 values of n, ranging from 100 to 10000. The results show that $a_k < 1/\sqrt{k}$ (when counting k from 1), the difference between the left and right hand values being very small for all k except the small vicinity of $k = n$, where a_k falls off quickly.

The results allow the following physical interpretation. The coefficients a_k may be given the meaning of memory terms, or (decaying) correlations. Realistic correlations are nonzero for any k, so that realistic processes should be faithfully simulated by MA(n) with n tending to infinity. Since the infinite sum of a_k^{α} is defined only for $\alpha > 1/2$, this result is amenable to the

interpretation that $1/f$ noise can be viewed as an undefined limit of well defined processes. This behavior represents a phenomenon not unfamiliar in physics and seems to be deeply related to the divergence of $1/f$ spectrum. This may also have some relation to the Fourier invariance of the Fourier (not power) spectrum of $1/f$ noise.

4. Noise in deterministic systems

The deterministic approach to noise is based on the well known fact that many deterministic systems manifest all the features of random processes, so that one can expect various kinds of noise in them. The paradigmatic explanation of this observation relies on the theory of deterministic chaos. The hard problem is, however, how to explain the specific character of fluctuations observed in different systems, expressed usually in the form of spectra, describing the distribution of amplitudes of constituting partial waves over their frequencies.

There are in principle two great groups of dynamical systems which exhibit chaotic behavior – equilibrium and nonequilibrium ones. Archetypal equilibrium systems are conservative and the state of equilibrium is considered a consequence of chaotic motion of phase point representing the state of the system in phase space. There is no problem to analyze equilibrium in deterministic systems if they are sufficiently chaotic. The situation is essentially different with nonequilibrium systems, where the state of nonequilibrium has to be supported by outer influences and the system cannot be therefore isolated: there must be a flow of energy through the system and since this energy should not accumulate in the system, it must be dissipated. The dissipation, however, was until recently considered quite naturally an irreversible process and thus a process not obeying deterministic laws. Only recently a new treatment of dissipation appeared, based on the use of "reversible thermostatting", which enables to study also non-equilibrium reversible deterministic systems.

In the following we will study two very simple models. The first one is the model of a particle moving in a plane among regularly arranged scatterers, the second one is a still simpler model generalizing the standard well-known baker map. The former of the models has a spectrum with power law dependence, the latter one exhibits a different type of noise, but definitely not the power law. Both models have strange attractors in their phase spaces so that their comparison does not confirm our originally favorite hypothesis [4], that the presence of such fractal objects *always* implies $1/f$ noise. We will try to demonstrate under what conditions one can expect such implication to hold.

5. Galton board, or driven Lorentz gas

In an attempt to reconcile time-reversibility of microscopic equations of motion with irreversibility of macroscopic flows, Nosé-Hoover equations of motion began to be studied recently [5]. The aim is a better understanding of explicitly *nonequilibrium* systems driven away from equilibrium by boundary conditions. The latter impose velocity (temperature) gradients on the systems and in such a way cause steady nonequilibrium states. In such systems, which can undergo corresponding *reversible* momentum and energy exchanges with their surroundings, the phase-space states are no more visited with equal probabilities.

The basis of the approach is to introduce heat reservoirs into mechanics implicitly, rather than explicitly, this being done by constraining the kinetic energy of selected "thermostatted" degrees of freedom of a many-body system. This can be achieved with the help of Gauss' principle of least constraint, satisfying also nonholonomic constraints. As a result, additional time-reversible "friction" force appears, which causes the phase flow to collapse onto a strange attractor. Theoretical analysis shows that the systems obeying Nosé-Hoover equations of motion are reversible, ergodic and have negative characteristic Lyapunov exponents.

The typical evolution of such systems is then the following. In the forward direction of time the phase-space hypervolumes shrink very quickly to a fractal object which is stable. Within the zero-volume fractal subspace the motion is chaotic and formally reversible, but the time-reversed trajectory is not stable. The reversed repellor object – differing from attractor just by that the signs of all the momenta and friction coefficients are reversed – is unstable. The lowered fractal dimensionality of the attractors implies the effective loss of degrees of freedom.

Among the models studied in the context of Nosé-Hoover mechanics, there is one which seems to be highly relevant to understanding the properties of some noises. It is the model of externally driven 2-dimensional Lorentz gas, or Galton board [6]. In this model a point mass is driven through an infinite planar lattice of circular elastic scatterers (of radius R) by an external field E (pointing in x direction). The particle would be accelerated by the field, so in order to achieve a stationary nonequilibrium state it is necessary to constrain the kinetic energy which, using the Gauss' principle, leads to the following equations of motion

$$\dot{x} = p_x/m, \quad \dot{y} = p_y/m,$$

$$\dot{p}_x = E - \zeta\, p_x, \quad \dot{p}_y = -\zeta\, p_y, \tag{4}$$

with the thermostat (friction) variable of the form $\zeta = p_x E/\mathbf{p}^2$. Observing the dynamics only at collisions of the particle with the scatterer, one obtains a

Poincaré map in a two dimensional collision space. For non-zero field, measured by the value of $EmR/\mathbf{p}^2$, one observes trajectories approaching strange attractors with fractal structure and with Hausdorff dimension D, for which one finds $1 < D < 2$. The dependence of D on E is not simple but in general D falls with growing E and for $E = 0$ we have, as expected, $D = 2$.

Since the Lorentz gas model has some features distantly reminding motion of charge carriers through lattice of atoms, we suspected that it could exhibit $1/f^k$ spectrum. To verify this conjecture, we analyzed 2000 samples of simulated particle trajectories (suffering 10 000 collisions each) as represented by position vectors and vectors of momenta. Spectra of individual trajectories were analyzed using the standard FFT and subsequently averaged. It turned out that the power spectrum of trajectories in the subspace of positions reminded brownian spectrum, whereas the spectrum of momenta was surprisingly smooth and close to $1/f$. In fact it was of $1/f^k$ type with k exceeding very slightly the value of $k = 1$.

6. Generalized baker map

We conclude by the analysis of generalized baker maps, which are partly contracting and partly dilating, representing thus simple models of reversible and at the same time dissipative evolution [7]. The analysis of the maps has shown that the spectrum of their orbits is white. This seems to demonstrate that the presence of strange attractor alone is not sufficient for appearance of $1/f$ noise, as is sometimes suggested. The example further demonstrates that nonequilibrium states are not necessarily results of global dissipation – local dissipation is quite sufficient to have nonequilibrium steady state.

The model is defined by the transformation B_w denoted as the "generalized baker map" (GBM for short) which preserves the measure globally. The map is piecewise linear and it acts differently to the left and to the right of the vertical line $x = (w - 1)/w$ (dividing line). To the left, i. e. for $0 < x \le (w-1)/w$, we have $B_w(x, y) \equiv L_w(x, y)$, with

$$L_w(x, y) = (xw/(w-1),\ y/w), \tag{5}$$

and to the right, we have $B_w(x, y) \equiv R_w(x, y)$, with

$$R_w(x, y) = (xw - w + 1,\ y + (1 - y)/w). \tag{6}$$

Being piecewise linear, the map represents the simplest nonlinear transformation. The contraction ratio is defined by the parameter $w \ge 1$ such that the area $(w - 1)/w$ of E, to the left of dividing line, is being contracted to $1/w$. For $w = 2$, the map becomes standard baker map, which is measure preserving also locally, and for $w = 1$ it is the linear identity map. For $w \ne 2$,

the local measure preservation does not hold and with growing $w > 2$ the local contraction (of the left part of E) grows. This is the sense in which the model generalizes the classical baker map (hence the name). The consequence of the local contraction is the appearance of an attractor in E: for $w > 2$, any point, or any subset of E approaches (in the forward direction of time) a multifractal object consisting of infinite set of lines parallel to the x-axis. This attractor is self-similar and can be generated by successive applications of B_w to the line $y = 0$ (primary line). Further analysis disclosed that with growing w the information dimension D_1 of the attractor falls from $D_1 = 2$, for $w = 2$, to $D_1 \to 1$, for $w \to \infty$.

The reversibility of the map implies that the analogue to time (velocity) reversal in this model is "rotation" of the "phase" point around the "second diagonal", i.e. around the line $y = 1 - x$. Thus, to any attractor there corresponds a repellor, consisting of lines orthogonal to the lines of the attractor. The specific case of $w = 2$ has also the attractor-repellor pair. The attractor (repellor) consists in this specific case of equidistant horizontal (vertical) lines so that it is "hidden", i. e. macroscopically invisible. The analysis of B_w for arbitrary w has therefore disclosed this hitherto unknown (or at least underestimated) property of the classical baker map.

If we consider E to be a 2-dimensional phase space, then contraction of its subset, induced by B_w, might be interpreted as "cooling", and expansion of the rest as "heating". Then B_w may be thought of as representing a "dynamics" of a system being cooled and heated at opposite sides. Evidently, B_w does not have any causal connection to physically relevant thermostatting – it is just its resulting behavior, which mathematically simulates thermostatting. We can, nevertheless, view this map as an extremely simple model of thermostatting, exactly because under its action one part of E is being contracted and another one expanded, and also because the presence of an attractor demonstrates the existence of a stable nonequilibrium state.

That is why we have analyzed the spectrum of orbits generated by this map. Evidently we could not expect to find $1/f$ noise, if for no other reason, then because the orbits are bounded. Equally bounded are distances between neighboring points on orbits which could be regarded as discrete analogue of velocities, and therefore neither these increments can have $1/f$ noise. If however the model would be endowed with inherent properties able to generate such noise, we should be able to observe at least some signs of such noise. Closer analysis however showed that the spectrum of y-components of orbits was unambiguously white and the spectrum of increments between two neighboring points on an orbit was also white except in a small neighborhood of $f = 0$.

White noise of y-coordinates is quite understandable because the x-coordinates of points on an orbit move chaotically and cover the interval

(0 ; 1] uniformly. We can regard them as "random" values. Their position with respect to dividing line decides whether in the next iteration the y-coordinate of a point will be submitted to the action of L_y or R_y. This means that the sequence of applications of operators L_y, R_y is "random" as well, which immediately implies that the noise of x- and y-coordinates is white. Similar reasonings apply to increments of y between iterations.

To summarize this section we may state that the example of generalized baker map reveals that not every thermostatted system with strange attractor has $1/f^{\,k}$ (k>0) spectrum. It demonstrates further that nonequilibrium states are not necessarily results of global dissipation – local dissipation is quite sufficient to have nonequilibrium steady state. The behavior of spectrum of Galton board then does not represent a situation to be expected everywhere. How typical the Galton board model is for a class of similar systems, deserves further investigation.

Acknowledgements

The author acknowledges the support of the Slovak Grant Agency for Science, VEGA, under the Grant No. 1/0428/03.

References

[1] J. Kumičák, Noises generated by nonlinear autoregression, Ann. Physik **3** (1994) 207–212.

[2] J. Kumičák, Generation of burst noise by nonlinear autoregression, Ann. Physik **4** (1995) 805–808.

[3] J. Kumičák, Modeling $1/f$ noise using moving averages, Czech. J. Phys. **49** (1999) 527–537.

[4] J. Kumičák, Galton board as a model for fluctuations, in: *Unsolved Problems of Noise and Fluctuations*, Eds. D. Abbott and L. B. Kiss, AIP Conference Proceedings No. 511 (AIP, Melville, NY 2000), p. 144–149.

[5] W. G. Hoover, Reversible mechanics and time's arrow, Phys. Rev. **A 37** (1988) 252–257.

[6] J. Kumičák, Driven Lorentz gas with $1/f^k$ noise, Microel. Reliab. **40** (2000) 1799–1802.

[7] J. Kumičák, Character of fluctuations in deterministically thermostatted nonequilibrium systems, Chaos **11** (2001) 624–631.

II. NOISE IN NANOSCALE DEVICES

NOISE IN OPTOELECTRONIC DEVICES

R. Alabedra
Centre d'Electronique de Montpellier
Université Montpellier II – 34095 Montpellier Cedex 5
France
alabedra@cem2.univ-montp2.fr

Abstract In the first part of this paper different kinds of electrical noise in photodiodes are summarized. In the second part electrical and optical noise of laser diodes are presented taking into account the correlation between both noise sources. In the last part some prospective aspects for new research into noise of optical amplifiers are briefly reviewed.

Keywords: Photodiodes, Lasers, Optoelectronic, Noise

1. Noise in photodiodes

1.1. Basic considerations

The photodiodes are light-to-current transducers and, as such, they can detect optical signals. A general behaviour of reverse-biased photodiodes includes basically three processes: carrier generation by absorbed photons, carrier transport without or with multiplication by impact ionization, and interaction of photocurrent with the external circuit to provide the output signal.

Several parameters are required in order to design P.I.N. photodiodes as photodetectors in optical communication systems. These parameters are, for example: a strong electric field to serve to separate the carriers, a narrow space charge to reduce the transit time, nevertheless a wide enough space charge in order to achieve a good quantum efficiency, a small active surface to reduce the capacitance of junction improving the gain-bandwidth product, a high absorption coefficient α_{ab} (expressed in cm^{-1}) at the working wavelength λ, as low dark current as possible, no-tunnelling effect, no 1/f noise in dark current and photocurrent, a good responsivity $\sigma_0(\lambda)$ in A/W.

J. Sikula and M. Levinshtein (eds.),
Advanced Experimental Methods for Noise Research in Nanoscale Electronic Devices (71 - 78)

1.2. Noise in photodiodes

In this section we will divide the noise study into two parts: the noise of the device in the dark and the noise under illumination, because we will distinguish between the dark current and the photocurrent. We will also consider at present only excellent devices which one can find currently in modern systems.

In the dark, for an optimized device without leakage current, as is well known from the classical description [1], the device exhibits a shot noise given by:

$$S_i\,(f)_{dark} = 2\,qI_{dark} \qquad (A^2/Hz) \qquad (1)$$

Of course the shot noise sets a lower limit to the noise in the dark current.

When P.I.N. photodiodes are illuminated by typical light sources (filament lamps or Lambertian sources), the light sources do not bring with their noise sources and the total number of photo-electrons produced during any time interval is much smaller than N atoms, and the individual ionization processes are statistically independent, in other words, the number of photons obeys Poisson statistic. The total noise in this situation will be the shot noise as following :

$$S_i\,(f)_{total} = S_i\,(f)_{dark} + S_i\,(f)_{phot} \qquad (A^2/Hz) \qquad (2)$$

$$S_i\,(f)_{total} = 2\,q[I_{dark} + I_{phot}] \qquad (A^2/Hz) \qquad (3)$$

Here it is assumed that there is no correlation between the photogenerated and thermal generated carriers. The ideal situation is obtained when the dark current is much smaller than the photocurrent. For P.I.N. silicon photodiodes at $\lambda = 0{,}9\ \mu m$ the dark current is about 10^{-11} A and the working photocurrent about 10^{-8} or 10^{-7} A. This is not always the case for infra-red photodiodes designed in narrow-gap materials. Of course the shot noise is the lower limit to the total noise.

When P.I.N. photodiodes are illuminated by laser diodes the beam light can bring a noise source which is characterized by Relative Intensity Noise (RIN.). This term describes the fluctuations of laser diodes optical power by following relation:

$$R.I.N. = \frac{S_{iph} - 2qI_{ph}}{I_{ph}^2} \qquad (Hz^{-1}) \qquad (4)$$

So if the P.I.N. photodiodes are illuminated with a thermal lamp, S_{iph} is equal to shot noise and R.I.N. becomes equal to 0. This optical noise source will be discussed in the second part of this paper.

Finally, recent theoretical analysis [2,3,4] of the squeezing phenomenon and especially the balanced homodyne detection circuit used for its observation, have led to a renewed interest in the shot noise present in the photocurrent and photoelectric detectors. Quantum mechanical description is used as a general expression for noise in the photocurrent even in the case of non-classical states of the radiation. In this case the total noise may actually fall below the shot noise (classical limit), thus indicating the presence of non-classical features of the radiation field such as antihuching or squeezing.

1.3. Noise in avalanche P.I.N. photodiodes

1.3.1. Basic consideration

Avalanche photodiodes are P.I.N. photodiodes which exhibit an internal multiplication of carriers by impact ionization. There devices are strongly reverse-biased in order to obtain a high electric field region between 5.10^4 and 6.10^5 $V.cm^{-1}$ depending on the type of materials. Several theoretical and experimental studies have been reported for various structures [5,6]. In low noise photodetection application only multiplication process at low electric field is very useful in order to obtain a great difference between ionization coefficients $\alpha(E)$ and $\beta(E)$ (in cm^{-1}) of electrons and holes, respectively. Currently there are two groups of A.P.D. structures :

- classical A.P.D. homojunction or heterojunction Separated Absorption Multiplication Avalanche Photodiodes, where the ionization by impact is non-localized.
- Multi Quantum Well Avalanche Photodiode or Superlattice Avalanche detectors, where the impact ionization is localized in stages [7,8].

In brief, the principal theories of impact ionization processes have been developped by Schokley, Wolf, Baraff, Ridley etc. for various values of electric field in order to obtain the expressions of $\alpha(E)$ and $\beta(E)$.

1.3.2. Noise in non-localized multiplication process

It is well known that the A.P.D. noise conventional expression is referred to the PhotoMultiplier Tube (PMT) noise given by :

$$S_i(f) = 2\,qI_{inj}(M)^2 \qquad (A^2/Hz) \qquad (5)$$

Here I_{inj} is the injected current and M the average multiplication factor. Therefore in the A.P.D. , where the multiplication process concerns both carrier types, the noise is given by :

$$S_i(f) = 2\,qI_{inj}(M)^2 \,.\, F(M) \qquad (A^2/Hz) \qquad (6)$$

Here F(M) is called the excess noise factor. The excess noise factor is a useful quantity because it compactly represents the statistical properties of the gain fluctuations that introduce multiplication noise; in all cases F(M) strongly depends from values $\alpha(E)$, $\beta(E)$ or $k = \beta(E)/\alpha(E)$. In the literature several authors have proposed [5,6] various theories relative to the statistical treatment of the avalanche process and the noise in A.P.D. in order to determine F(M). For example the Mc Intyre's theory [5] permits, statistically speaking, all possibilities of the impact ionization compatible with thickness W, the α and β ionization coefficients without any limit for the random impact ionization number given by the probability laws. In the case of Van Vliet theory [6] based on discrete device physics, the M and variance (M) are obtained by means of the recurrent generating function method. In this approach the noise is always lower than the Mc Intyre's limit, the latter being approached to within 5% for gains of the order of 100 or higher and the noise versus (M) shows break points when the regime changes from N to N + 1 possible ionizations per carrier transit.

1.3.3. Noise in multilayer avalanche photodiodes

An essential requirement for low noise avalanche photodiodes is to have a large difference between the ionization coefficients α and β. There are two ways to obtain this large difference.

First: the main method to obtain high k or 1/k materials is to use the III-V or II-VI ternary or quaternary alloys which exhibit a high k for a given value of stoichiometric composition such as $Ga_{1-x}Al_xSb$ APD [9] or $Hg_{1-x}Cd_xTe$ [10]. In this case the ionization coefficients α and β material parameters depend on the semiconductor band structure.

Second: one can obtain high k values by designing new class of APD using the Band Structure Engineering such as Multi Quantum-Well Avalanche Photodiode or Staircase Avalanche Photodiodes [11].

The staircase A.P.D. is a sophisticated structure with a periodical distribution of graded gap wells. We have a ballistic only by electrons ionization process repeated at each stage. The noise approach proposed by Capasso [7] is the same as that for the P.M.T. but the variance of the random gain at each stage is $\delta(\delta-1)$, where δ is the fraction of electrons which do not impact-ionize. Thus the excess noise factor after Capasso is:

$$F(N,\delta) = 1 + \frac{\delta\left(1 - (2-\delta)^{-N}\right)}{(2-\delta)} \qquad (7)$$

where N is the number of stages. A Generalized Excess Noise Factor for Avalanche Photodiodes of Arbitrary Structure is proposed by Hakim Saleh

and Teich [8]. The authors consider a generic multilayer avalanche photodiode model that admits arbitrary variation of the band gap, dark generation rate and ionization coefficients within each stage of the device. Their formalism follows the usual assumption that the ability of a carrier to ionize other carriers is independent of the carrier's history. Their calculations make use of Mc Intyre's general approach and they abandon the restriction that the multiplication shall assume a Bernouilli form with infinitesimal small success probability in the limit of an infinitesimal distance. Their generalized multilayer structure used for their calculation is shown in Fig. 1.

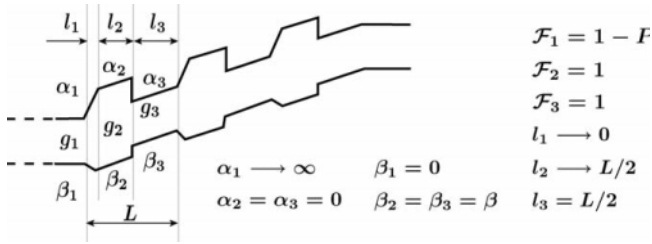

Figure 1. Generic model used for generalized excess noise

This theory is applied to Conventional Avalanche Photodiode APD, MultiQuantum-Well Avalanche Photodiode and Staircase APD, on the assumption that the number of photons at the input of the detector obeys the Poisson distribution. For example, with this theory in the continuous limit, formula (22-d) of 11 is a version of the expression obtained by Mc Intyre[8]. This incorporates both injected and dark generated carriers. The carrier history is taken into account, $\alpha(x)$ and $\beta(x)$ become $\alpha(x,x')$ and $\beta(x,x')$ respectively, to reflect the ionization probabilities for a carrier at the point x when it was generated at the point x'. In this case the authors introduce a "dead space" which prohibits the carrier from multiplying within a certain distance of its birthplace.

2. Electrical and optical noise in laser diodes and their correlation

Several kinds of noise are often generated in semiconductor lasers because of the wideband response characteristics of carrier density fluctuations. 1/f noise, mode hopping noise or mode partition noise are troublesome: these kinds of noise impede attempts to improve optical coherence [12]. Some studies have been made in order to introduce the low and medium frequency noise as a characterization parameter with the fluctuations of the carrier density of lasers. On one hand, the Terminal

Electrical Noise (T.E.N.) is due to the fluctuations of the laser voltage $V_d(t)$ and is given by the voltage noise spectral density S_{Vd} (V^2/Hz). In our case, S_{Vd} can be written as :

$$S_{vd}(f) = 4kTR_s + \left(M\frac{kT}{q} \right)^2 \left\langle \frac{|\Delta n(f)|^2}{n_0^2 \Delta f} \right\rangle \quad (8)$$

$$M = 2 + \frac{n_0}{Vol2\sqrt{2}} \left(\frac{1}{N_V} + \frac{1}{N_c} \right) \quad (9)$$

where N_c ,N_v are the effective conduction and valence band densities, k is the Boltzman's constant, T is the absolute temperature, n_0 is the steady state carrier density, .Δn (f) is the fluctuation of carrier density , Vol is the volume of the active layer and R_s is the series resistance. The first term gives the thermal noise due to the series resistance R_s.

On the other hand, the optical noise is due to the fluctuations of the optical power P_{opt} of the laser, related to the fluctuations of the detected photocurrent $I_{ph}(t)$, and given by the photocurrent spectral density SI_{ph} (A^2/Hz) :

$$S_{Iph} = \sigma^2 \, . \, S_{Popt} \quad (10)$$

In order to analyse the noise behaviour of the laser, we used the experimental set up shown in figure 2.

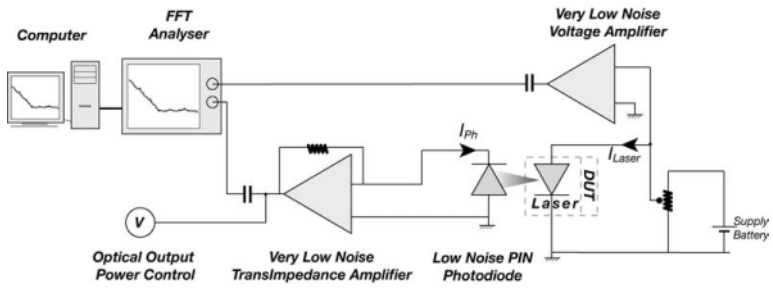

Figure 2. Experimental set-up

In the first channel we measure S_{Vd} thanks to a voltage amplifier, connected in parallel with the laser diode. With the second channel we measure I_{ph} and S_{Iph}, through a standard InGaAs PIN photodiode, or via the DC and AC outputs of a current amplifier. Possible optical feedback due to the second channel is suppressed by an optical isolator when we measure simultaneously the electrical noise S_{Vd} and the photocurrent spectral density S_{IPh}.

3. Noise of optical amplifiers

The amplifier noise model is based on the work by Simon [13] Olsson [14]. The amplifier output spontaneous emission power is given by:

$$P_{sp} = N_{sp}(G-1)h\nu B_0 \tag{12}$$

B_0 is the optical bandwidth, P_{sp} the spontaneous emission power, N_{sp} the spontaneous emission factor, hν the photon energy, G the optical gain. For an ideal amplifier $N_{sp} = 1$, for an Erbium doped fiber amplifier $N_{sp} = 2.2$ and for a semiconductor laser amplifier N_{sp} ranges from 1.4 to 4 depending on both the pumping rate and the operating wavelength. This model is based on a talk given by P.S. Henry [15]. We assume an optical amplifier and a detector with unity quantum efficiency. After square law detection in the receiver, the signal power S is given by:

$$S = (GI_sC_1C_2L)^2 \tag{13}$$

I_s is the photocurrent equivalent of amplifier input power, C_1 – amplifier input coupling efficiency , C_2 – amplifier output coupling efficiency, L – optical losses between amplifier and receiver. The total noise N_{tot} is:

$$N_{tot} = N_{shot} + N_{sp\text{-}sp} + N_{s\text{-}sp} + N_{th} \tag{14}$$

N_{th} is the receiver noise, q is the electronic charge, N_{shot} is the shot noise, $N_{sp\text{-}sp}$ – the spontaneous-spontaneous beat noise, $N_{s\text{-}sp}$ – the signal-spontaneous beat noise. A schematic diagram of the amplifier model is shown in Figure 3.

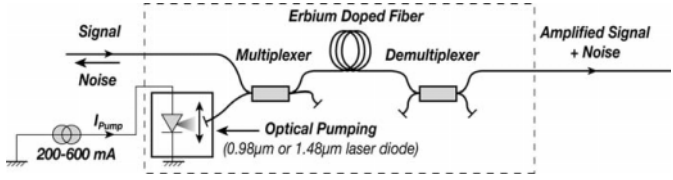

Figure 3. Schematic diagram of an Erbium-doped fiber Amplified Model

One of the most interesting preamplifier applications is the receiver sensitivity dependence of the amplifier gain, noise figure, and optical bandwidth. The application of optical preamplifiers is at very high data rates.

4. Conclusions

Research in photonics and photon-electron interactions, as for example the correlation between electrical noise and optical noise, will become more and more important. Indeed, optics will take place in a very large number of modern systems. For instance, in the case of optical fibre telecommunication networks, noise limits the number of photons per bit which is about 400 photons for a given Bit Error Rate of 10^{-9}, while the theoretical limit is about 40 photons.

References

[1] Van der Ziel, Noise Measurements, Proceeding IEEE **58** (1970) 1178.

[2] Paul H., Shot Noise in Photodiodes and vacuum fluctuations, J. Modern Optics **35** (1988) 1225-1235.

[3] Glauber RJ, Quantum Optics and Electronics, Edited by C. de Witt, A. Blandin and C. Cohen-Tannoudji (N.-Y. : Gordon and Breach) 1965.

[4] Yurke B., Squeezed-coherent-state generation via four-wave mixers and detection via homodyne detectors**,** Phys. Rev. A **35** (1985) 300.

[5] Mc Intyre RJ, Multiplication noise in uniform avalanche photodiodes, IEEE Trans Electronic Device, **ED-13** (1966) 164-168.

[6] Van Vliet K.M. & Rucker L.M., Theory of carrier multiplication and noise in avalanche devices - I - One-carrier processes, IEEE Trans Electron Devices **ED-6** (1979) 746-764.

[7] Capasso F. et al., Staircase solid-state photomultipliers and avalanche photodiodes with enhanced ionization rates ratio, IEEE Trans Electron. Device, **ED-30** (1983) 381-390.

[8] Hakim N.Z., Saleh B.E.A., Teich M.C., Generalized excess noise factor for avalanche photodiodes of arbitrary structure, IEEE Trans electron devices **37**, (1990) 599-610.

[9] Hildebrad O. et al., Ga/sub 1-x/Al/sub x/Sb avalanche photodiodes: resonant impact ionization with very high ratio of ionization coefficients, IEEE J. Quantum Electron. **QE17** (1981) 284

[10] Orsal B., et al., Hg/sub 0.56/ Cd/sub 0.44/ Te 1.6- to 2.5-μm avalanche photodiode and noise study far from resonant impact ionization, IEEE Trans Electron Devices **38** (1991) 1748-1756

[11] Capasso F., Williams G.F., Tsana W.T., Tech. Dig. IEEE Specialist Conf. on Light Emitting Diodes and photodetectors (Ottawa - Hull Canada) (1982) 166-167.

[12] Ohtsu M., Highly Coherent Semiconductor Lasers. Edited by Culshaw, A ; Rogers, H. Taylor. Artech House Inc. Norwood M.A. 02062 U.S.A., (1992).

[13] Simon J.C., GaInAsP semiconductor laser amplifiers for single-mode fiber communications , J. Lightwave Technology **5** (1987) 1286-1295

[14] Olsson N.A., Lightwave systems with optical amplifiers, J. Lightwave Technology **7** (1989) 1071-1082

[15] Henry P.S., Lightwave primer, I.E.E.E., J. Quantum Electron. QE-21 (1985) 1862-1869

FLUCTUATIONS OF OPTICAL AND ELECTRICAL PARAMETERS AND THEIR CORRELATION OF MULTIPLE-QUANTUM-WELL InGaAs/InP LASERS

S. Pralgauskaitė, V. Palenskis and J. Matukas

Departament of Radiophysics, Physics Faculty, Vilnius University

Saulėtekio 9, LT-2040 Vilnius

Lithuania

sandra.pralgauskaite@ff.vu.lt

Abstract Low-frequency noise characteristics of Fabry-Pérot (F-P) and distributed feedback, ridge-waveguide and buried-heterostructures InGaAsP/InP multiple-quantum-well lasers investigation has been carrier out. Mode hopping effect characteristic for F-P laser operation is caused by carrier gathering in barrier and cladding layers, and intensive optical and electrical noise during mode hopping is related with recombination in these layers. Defective laser diodes structures can be revealed by noise characteristic investigation, especially the correlation factor is more informative at threshold.

Keywords: Semiconductor laser, optical noise, electrical noise, correlation factor.

1. Introduction

Nowadays devices with various design quantum structures are of interest in semiconductor laser developing and application areas, because they give such advantages as quantized energy levels and finite density of states, better injected carrier confinement and, thus, lower threshold current, better optical confinement [1, 2]. Improvement of new and modern design laser diode (LD) structures requires detailed investigation of their properties. Noise characteristic investigation can clear up the features and reasons of various effects observed in the semiconductor laser operation. Low-frequency noise indicates various imperfections of material and device [1, 3, 4], and is caused by the same type of defects that also reduce device quality and reliability [3].

The comprehensive study of low-frequency noise characteristics of various design semiconductor lasers is presented in this paper. The basic

J. Sikula and M. Levinshtein (eds.),
Advanced Experimental Methods for Noise Research in Nanoscale Electronic Devices (79 - 88)

purpose of the investigation was to clear up the noise origin and features characteristic for InGaAsP/InP multiple-quantum-well different structure laser diodes, to elucidate the reasons and nature of processes that take part during mode hopping effect in Fabry-Pérot laser operation.

2. Noise Measurement Technique and Investigated Devices

In the optoelectronic devices investigation it is important to know characteristics of both optical (laser output power fluctuations) and electrical (laser diode terminal voltage or current fluctuations) noises, and correlation between optical and electrical fluctuation characteristics. In Fig. 1, there is presented measurement circuit for simultaneous optical and electrical noise signals measurement and evaluation of their correlation factor.

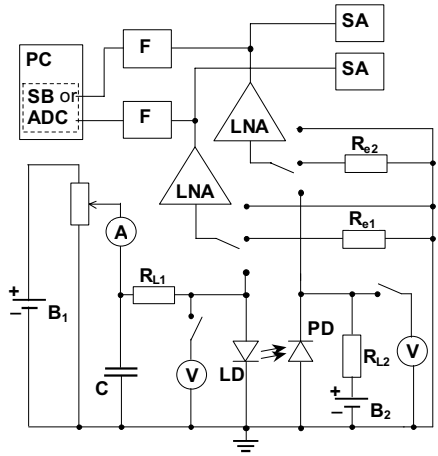

Figure 1. Experiment circuit: LD – laser diode, PD – photodetector, R_{L1}, R_{L2} - load resistances, R_{e1}, R_{e2} – standard resistances, B_1 and B_2 – storage batteries, LNA – low-noise amplifier, F – filter system, SB – soundboard, ADC – analogue-to-digital converter, PC – personal computer, SA – spectrum analyzer.

Laser diode emitted light power and its fluctuations are detected by the specially selected Ge photodiode, which own noise spectrum was inversely proportional to the frequency, and noise intensity remained about two decades lower than LD optical noise in all lasing current region. Therefore, the optical noise is photodiode voltage fluctuations due to LD output power fluctuations.

Both noise signals were amplified by low-noise amplifiers (LNA). Standard soundboard that limits signal in the frequency range from 20 Hz to

20 kHz can be used as analogue-to-digital converter. Using data acquisition board and/or spectrum analyzers the frequency range was broadened from 0.1 Hz to 35 MHz .The noise spectral density, S_V, is valuated by comparing with the thermal noise of standard resistor R_e

The investigated lasers were fabricated on the ground of material $In_{1-x}Ga_xAs_yP_{1-y}$. Fabry-Pérot (F-P) lasers with ridge-waveguide (RWG) radiating around 1.33 μm wavelength and DFB lasers with RWG and buried-heterostructure (BH) radiating around 1.55 μm have been investigated. All samples have graded-index separate-confinement-heterostructure (GRINSCH) with multiple quantum well (MQW) active layer (Fig. 2) grown by metal-organic vapor deposition [5, 6].

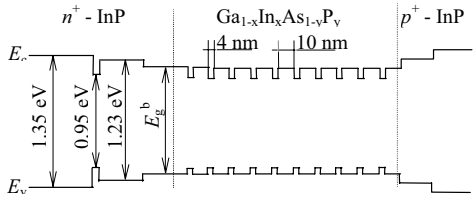

Figure 2. Schematic energy band diagram of the laser MQW active region within GRINSCH (E_g^b - barrier layer energy band-gap).

F-P laser active region contains ten 4 nm thick compressively strained (0.7 %) InGaAsP quantum wells (QWs) separated by 10 nm thick *p*-doped InGaAsP/InP barriers lattice matched to InP (Fig. 2). DFB RWG laser diode active layer consists of 4 QWs , and DFB lasers with thyristor-type current-blocking layers (BH) active region contains six 5.5 nm thick compressively strained QWs.

3. Semiconductor Laser Noise Characteristics

Optical and electrical laser diode noise spectra and correlation factor between optical and electrical fluctuations investigation has been carried out in the frequency range from 1 Hz to 1 MHz at wide laser current and temperature regions. Typical LD noise characteristics are presented in Fig. 3. At the lasing operation region (above threshold) optical and electrical noise intensity slowly increases with laser current. In the investigated frequency range optical and electrical noise spectral density vs. frequency dependencies

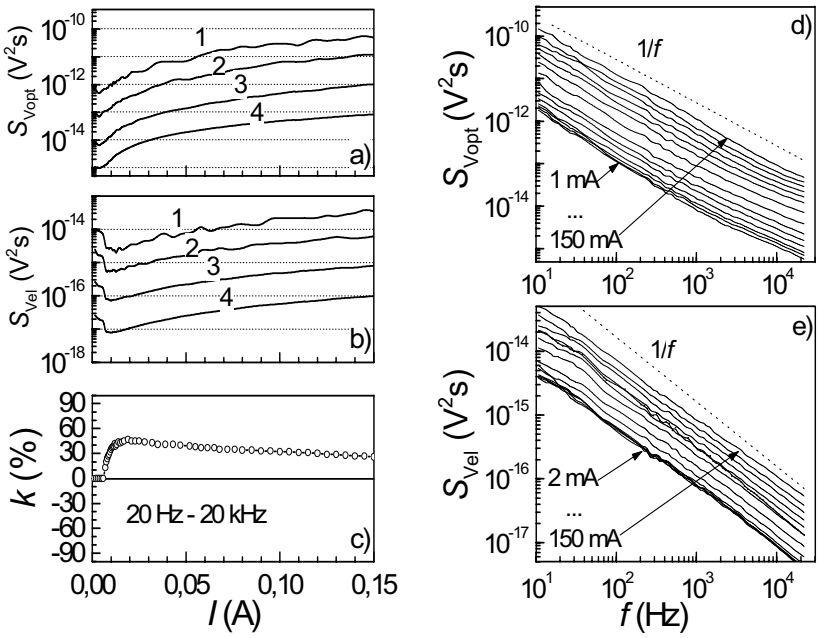

Figure 3. DFB laser optical (a) and electrical (b) noise spectral density (1- 22 Hz, 2- 108 Hz, 3- 1 kHz, 4- 10 kHz) and correlation factor (c; 20 Hz – 20 kHz) dependencies on laser current; optical (d) and electrical (e) noise spectra at different currents (T=290 K).

are $1/f^{\gamma}$ type, where γ changes from 0.95 to 1.43 (graphs d) and e) Fig. 3). This type of noise is characteristic for all (F-P and DFB) investigated samples at the stable operation (when there is no mode hopping), and does not change with laser current or temperature. Origin of the $1/f$ noise in laser diode, as in many semiconductor devices [3, 4], is a superposition of fluctuations due to charge carrier capture and emission processes in localized states with different capture cross-sections caused by various defects and impurities. Correlation factor between optical and electrical fluctuations at the lasing region changes in the range (10-60)%, mostly is positive, and has tendency slowly decrease with laser current increasing (graph c) in Fig. 3). Thus, at the lasing operation there are active some defects, that randomly modulate free charge carrier number in the active layer and, as a consequence, lead to the photon number fluctuations that have the same phase as LD terminal voltage fluctuations and $1/f$ type spectra.

3.1. Mode hopping effect in Fabry-Pérot laser operation

At defined forward currents and temperatures F-P laser diodes have very large and strongly correlated (up to 98 %) Lorentzian type optical and electrical noises (Fig. 4). These noise peaks are related with mode hopping effect. It is found, that for some mode hopping peaks positive correlation factor is observed, and for others – negative one (Fig. 4). Different noise

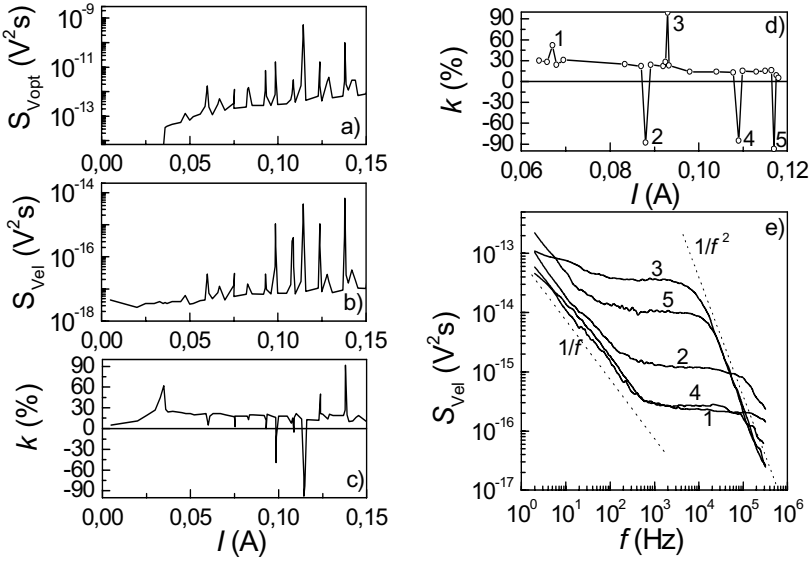

Figure 4. F-P laser optical (a) and electrical (b) noise spectral density (at 10 kHz) and correlation factor (c; 1 Hz – 1 kHz) dependencies on laser current; correlation factor (d) and electrical noise spectra (e) at mode hopping regions (T=290 K).

characteristics (positive or negative correlation, different cut-off frequency of Lorentzian type noise spectra: characteristic time ranges from 1 μs to 1 ms (graph e) in Fig. 4)) at the mode hopping indicate various possible processes during mode hopping as noise origin. Thus, there is more than one reason for mode hopping effect appearing.

The measured charge carrier lifetime in the active region (2.2 ns [7]) that corresponds to the spontaneous recombination time is much shorter than the observed relaxation times of processes related with Lorentzian type noise during mode hopping (Fig. 4). So, mode hopping noise is not related with charge carrier spontaneous recombination in the quantum wells.

Fig. 5 illustrates the mode hopping noise correlation dependencies on both laser current and temperature. Logarithm of the peak center current dependency on the inverse temperature is linear and has the same slope (thus

the process activation energy is the same) independently on correlation factor sign. The activation energy has been evaluated to be 0.53 eV, what is very close to the half of the barrier and cladding layers band-gap energy (0.54 eV). This indicates that mode hopping noise is related to the recombination processes in the barrier or cladding layers. So, mode hopping effect causes the radiating mode instability due to the presence of injected charge carriers in the barrier or cladding layers. Back-reflected light influences charge carrier and photon redistribution in the active region. It is shown that F-P LD facet coating by antireflection layer (decreasing of the resonator quality) substantial suppresses mode hopping effect with only a small change of the light output power (Fig. 6).

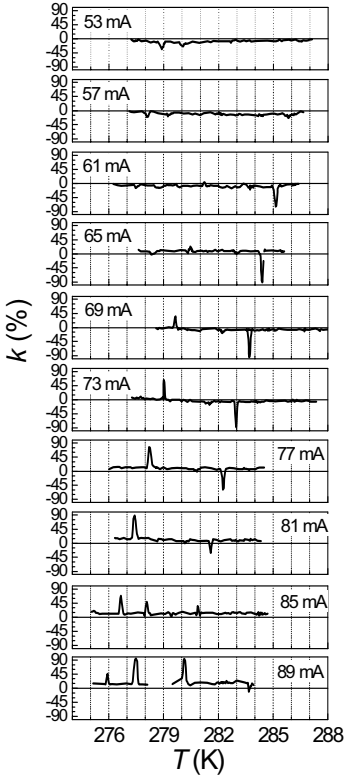

Figure 5. F-P laser noise correlation factor (1 Hz–1 kHz) dependencies on temperature and laser current at mode hopping regions.

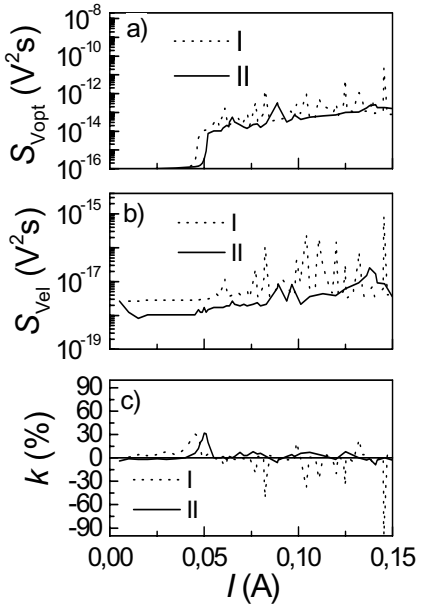

Figure 6. F-P laser optical (a) and electrical (b) noise spectral density (at 10 kHz) and correlation factor (c; 1 Hz–1 kHz) dependencies on laser current without (I) and with (II) facet coating (T=290 K).

3.2. Ridge-waveguide and buried-heterostructure laser noise characteristics

Better charge carrier and photon confinement in the active layer is achieved in buried-heterostructure laser diodes thanks to the thyristor-type current-blocking layers ensure the lower threshold current and higher efficiency of BH lasers in comparing with ridge-waveguide ones.

Noise characteristic features at the lasing operation of BH and RWG lasers are quite similar (Fig. 7): optical and electrical noise intensities increase approximately proportional to the laser current. Noise intensity for different samples varies no more than an order of magnitude and noise spectra are $1/f$ type. Correlation factor between optical and electrical fluctuations is positive and varies in the range of (0-60) %.

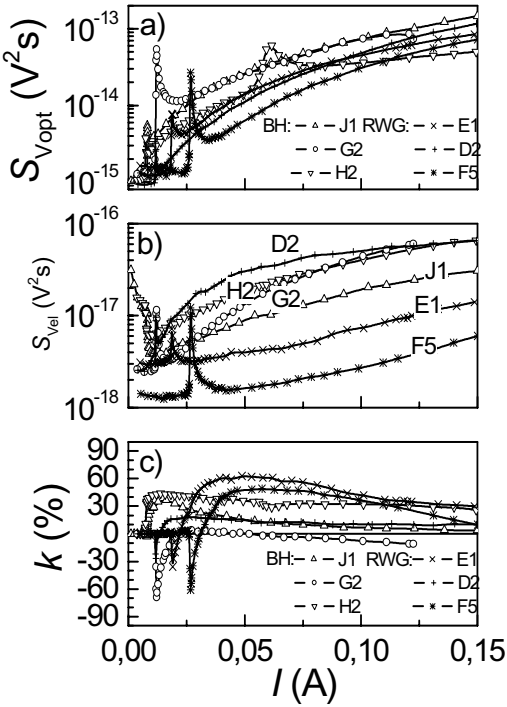

Figure 7. Comparison of optical (a) and electrical (b) noise spectral density (at 10 kHz), correlation factor between optical and electrical fluctuations (c; 20 Hz-20 kHz) dependencies on laser current for ridge-waveguide (D2, E1, and F5) and BH (G2, H2, and J1) lasers at room temperature

BH lasers have better operation characteristics, but growth of current blocking layers introduces additional defects into laser diode structure that could lead to a moderate noise increase: BH sample optical noise intensity is about a half order of magnitude larger than ridge-waveguide laser (graph a) in Fig. 8). Regardless of larger optical noise and due to higher efficiency, the BH laser signal-to-noise ratio is larger than for RWG samples.

Defects at the active region interface with current-blocking layers and non-optimal current-blocking layer position with respect to the active region can lead to a large leakage current and in particular cases to the thyristor (that is formed from current-blocking layers in BH) turn-on at comparatively low current. Low-frequency noise characteristic features (optical and electrical noise spectral densities are about 1-2 order of magnitude larger than for the BH lasers without the thyristor turn-on effect) suggest that in the "thyristor" case, the active region surface of the BH laser contains additional defects that cause non-uniform current flow and its leakage to the current-blocking layers.

Threshold region is peculiar laser operation region where stimulated emission starts to dominate over spontaneous one. It is turned out that noise characteristics at the threshold are the most sensitive to the structure defectiveness and device quality. As it is seen in Fig. 8, optical and electrical noise at the threshold has additional very intensive Lorentzian type noise with characteristic negative correlation factor. The Lorentzian noise intensity, correlation sign and magnitude at the threshold are different for different investigated samples and are related with the defective nature of the surface or interface of the laser active layer [8]. Noise characteristics, especially correlation between optical and electrical fluctuations factor, investigation could help to evaluate LD quality and lifetime without aging experiments.

4. Conclusions

Optical and electrical noises of semiconductor lasers at stable operation regions are $1/f$ type, and are caused by the inherent material defects and defects created during the device formation. Positive correlation ((10-60) %) is characteristic for $1/f$ optical and electrical noise at the lasing operation.

Optical and electrical fluctuations due to mode hopping observed in F-P laser operation are strongly correlated and have Lorentzian type spectra. It is shown that there are more than one different process that take place during mode hopping. Mode hopping effect arises due to charge carrier gathering in the barrier and cladding layers, and noise during mode hopping is related with recombination processes in these layers.

Buried-heterostructure lasers have better operation characteristics in comparing with ridge-waveguide diodes, but formation of current-blocking layers introduces additional defects at the active region surface, what increases leakage currents and, in exceptional cases, can lead to the thyristor turn-on effect at low currents.

Carried out experimental investigations have shown that noise characteristics (especially correlation factor) are more informative on the physical processes in semiconductor laser structure related with operation characteristics and laser quality. Threshold noise characteristic investigation could be used for laser diode quality and reliability prediction.

Acknowledgments

The authors would like to thank the Center for Electrophotonic Materials and Devices of McMaster University and Nortel Networks Optical Components in Canada for providing the devices.

References

[1] A. Dandridge and H. F. Taylor, Correlation o flow-frequency intensity and frequency fluctuations in GaAlAs lasers, IEEE J. Quant. Electron. **QE-18** (1982) 1738-1750.

[2] P. J. A. Thijs, L. F. Tiemeijer, J. J. M. Binsma, and T. van Dongen, Progress in long-wavelenght strained-layer InGaAs(P) quantum-well semiconductor lasers and amplifiers, IEEE J. Quant. Electron. **30** (1994) 477-499.

[3] B. K. Jones, Electrical noise as a measure of quality and reliability in electronic devices, Adv. electron. electron phys. **87** (1994) 201-257.

[4] J. Matukas and V. Palenskis, Low-frequency noise of the metal-gallium arsenide contact at various treatment of semiconductor surface, Lith. Phys. J. **36** (1996) 39-48.

[5] J. F. Hazell, J. G. Simmons, J. D. Evans, and C. Blaauw, The effect of varying barrier height on the operational characteristics of 1.3 μm strained-layer MQW lasers, IEEE J. Quant. Electron. **34** (1998) 2358-2363.

[6] B. B. Elenkrig, S. Smetona, J. G. Simmons, T. Makino, and J. D. Evans, Maximum operating power of 1.3 μm strained layer multiple quantum well InGaAsP lasers, J. Appl. Phys. **85** (1999) 2367-2370.

[7] J. Matukas, V. Palenskis, Č. Pavasaris, E. Šermukšnis, J. Vyšniauskas, S. Pralgauskaitė, G. Letal, S. Smetona, J. G. Simmons, and R. Sobiestijanskas, Optical and electrical characteristics of InGaAsP MQW BH DFB laser diodes, Material science forum **384-385** (2002) 91-94.

[8] G. Letal, S. Smetona, R. Mallard, J. Matukas, V. Palenskis, and S. Pralgauskaitė, Reliability and Low-Frequency Noise Measurements of InGaAsP MQW Buried-Heterostructure Lasers, J. Vac. Sci. Technol. **A20** (2002) 1061–1066.

MICROWAVE NOISE AND FAST/ULTRAFAST ELECTRONIC PROCESSES IN NITRIDE 2DEG CHANNELS

A. Matulionis

Semiconductor Physics Institute
Vilnius
Lithuania

e-mail: matulionis@pfi.lt

Abstract Microwave noise technique is applied to study ultrafast correlations in AlGaN/GaN and AlN/GaN two-dimensional electron gas (2DEG) channels subjected to a strong electric field applied in the plane of electron confinement. The experimental data are discussed in terms of hot-electron-energy dissipation on phonons, longitudinal-optical (LO) phonon conversion into other phonon modes, and hot-electron deconfinement. At high electric fields, the hot-electron energy relaxation is limited by the LO-phonon conversion. The LO-phonon conversion lifetime is estimated to be 350 fs in AlGaN/GaN channel. The lifetime is a useful parameter for extrapolation of hot-electron temperature beyond the field range where it is available from microwave noise experiments. The extrapolated hot-electron temperature is used to discuss hot-electron deconfinement noise.

Keywords: microwave noise, hot electrons, hot phonons, fast and ultrafast processes, two-dimensional electron gas channels, nitride heterostructures

1. Introduction

A two-dimensional electron gas (2DEG) channel supports excellent performance of a field-effect transistor at microwave frequencies. Nitride 2DEG transistors are high-power devices: a single transistor can generate a 10 W power at a 10 GHz [1]; the cutoff frequency of a nanometer-gate device exceeds 80 GHz [2]. Investigation of power–speed tradeoff requires a better understanding of hot-electron energy dissipation and other ultrafast processes in a biased nitride 2DEG channel. The required information can be obtained through experiments on microwave fluctuations [3,4].

J. Sikula and M. Levinshtein (eds.),
Advanced Experimental Methods for Noise Research in Nanoscale Electronic Devices (89 - 96)

At a high bias, spontaneous emission of optical phonons by high-energy electrons is the main mechanism for electron energy dissipation [5–7]. Conversion of the emitted optical phonons into other phonon modes is a bottleneck of the dissipation process in nitride channels [8,9]. The bottleneck causes accumulation of nonequilibrium longitudinal-optical (LO) phonons, termed hot phonons [10]. Hot phonons limit electron drift velocity [11,12] and support electron deconfinement at a reduced bias [13]. Because of high electron density in nitride 2DEG channels for high-power applications, the hot-phonon effects are strong and deserve special attention at a high bias.

The standard electric characterization—measurement of electron mobility and sheet density—does not provide with sufficient data for considering hot-phonon effects. Time-resolved anti-Stokes Raman light scattering technique has been applied to investigate hot-phonon effects in bulk semiconductors and multi-quantum-well structures [10], but this technique has never been used for measuring LO-phonon conversion lifetime in a single-quantum-well nitride 2DEG channel. The microwave noise technique has demonstrated its potential for studying hot phonons in biased AlGaN/GaN, AlN/GaN, and AlGaN/AlN/GaN 2DEG channels [8, 9, 14–16].

The aim of this paper is to report on advances of microwave noise technique for characterization of electronic and phononic processes in a biased nitride 2DEG channel.

2. Experimental

Most experiments were carried out on two-electrode 2DEG channels prepared from nominally undoped nitride heterostructures grown in laboratories of Cornell University (Ithaca) and the University of Michigan (Ann Arbor). A channel was subjected to a strong electric field applied in the plane of electron confinement. Hot-electron noise was measured in the bias direction at a microwave frequency, usually near 10 GHz, where generation–recombination, flicker, and other low-frequency sources of noise are of negligible intensity. Pulsed bias was applied in order to minimize channel self-heating. The noise temperature was measured during the voltage pulse with a gated modulation-type radiometer of microwave noise power in the way described elsewhere [3–5].

Fig. 1 illustrates bias dependence of the longitudinal excess noise temperature (open circles) [14]. Several ranges of electric field can be resolved. In range A, the transport and dissipation parameters are independent of electric field. As a result, the noise temperature equals the electron temperature and increases proportional to the squared electric field. In range B, spontaneous emission of optical phonons becomes important for non-ohmic transport and energy dissipation. Additional noise is caused by

fluctuations δT_e in hot-electron temperature, and the noise temperature T_n exceeds the electron temperature T_e in this range [6]. Noise due to hot-electron deconfinement appears in range C [4,5,13,14]. The hot-electron noise is thermally quenched due to lattice heating in range D.

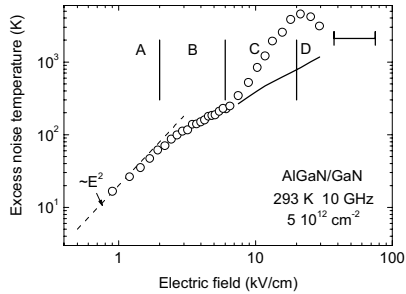

Figure 1. Field-dependent excess noise temperature $T_n - T_L$ at T_L = 293 K (open circles) [14] and excess hot-electron temperature $T_e - T_L$: solid line—from Eq. (3) with F = 1 and τ_{ph} = 350 fs ; horizontal H bar stands for hot-electron luminescence data [20].

It has been shown for a high-density 2DEG [6,17] that the noise temperature is expressible in terms of the electron temperature and the conductivity tensor components. This holds in the field range where the electron deconfinement is negligible. The estimation for nitride channels shows [6,14] that one can assume $T_n = T_e$ in ranges A and B (Fig. 1).

3. Hot-electron energy relaxation time

Once the electron temperature is available from the noise experiment, hot-electron energy relaxation time τ_ε can be determined according to:

$$\tau_\varepsilon = k_B(T_e - T_L) / (UI/N_{el}) \qquad (1)$$

where T_L is the lattice temperature—the temperature of all phonons except for those involved in the electron–LO-phonon interaction, N_{el} is the electron number, U is the applied voltage, I is the current.

Squares in Fig. 2 illustrate the results for AlGaN/GaN at two lattice temperatures. The relaxation time decreases as the field increases because the LO-phonon emission becomes increasingly important.

This expectation is confirmed by a modified Arrhenius plot (Fig. 3). Triangles in Fig. 3 stand for the supplied electric power per electron as a function of the reciprocal noise temperature in the field range where $T_n = T_e$. The results at T_L = 80 K can be fitted with the exponential dependence

$UI/N_{el} = \Delta\varepsilon/\tau_{ph} \exp(-\Delta\varepsilon/k_B T_n)$ where the activation energy $\Delta\varepsilon$ approximately equals the LO-phonon energy in GaN: $\Delta\varepsilon = \hbar\omega = 0.092$ eV. This result confirms that the supplied power is dissipated on LO phonons.

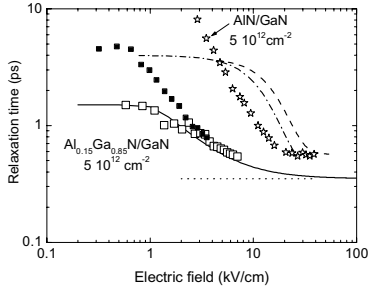

Figure 2. Field-dependent electron energy relaxation time: AlGaN/GaN at 303 K (open squares) [16], at 80 K (closed squares) [6]; AlN/GaN at 80 K (stars) [8]. Electron deconfinement relaxation time in AlGaN/GaN: 303 K (dash) [16], 80 K (dash–dot) [14].

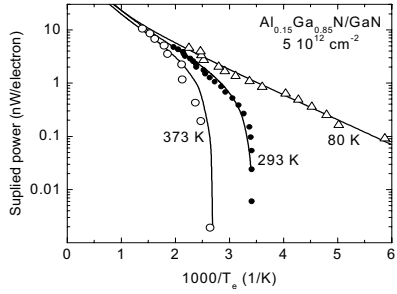

Figure 3. Supplied electric power per electron against reciprocal electron temperature for AlGaN/GaN channel at different temperatures T_L: 373 K [18] (open circles), 293 K [9] (bullets), and 80 K [9] (triangles). Solid lines stand for dissipated power due to LO-phonon conversion (r.h.s. of Eq. (3), $\hbar\omega = 0.092$ eV, $\tau_{ph} = 350$ fs, $F = 1$). $N_{el} = 7.2\ 10^7$.

4. LO-phonon lifetime

Let us introduce the LO-phonon lifetime τ_{ph} with respect to LO-phonon conversion into other phonon modes. The conversion rate is assumed proportional to the excess occupancy $N_{ph} - N_{ph}(T_L)$ of the LO-phonon states:

$$dN_{ph}/dt = -[N_{ph} - N_{ph}(T_L)]/\tau_{ph} \qquad (2)$$

where $N_{ph}(T_L)$ is the occupancy at thermal equilibrium.

For strong electron–LO-phonon coupling the hot-electron temperature T_e approximately equals the hot-phonon temperature T_{ph} [9]. Thus, the power balance equation can be written as:

$$UI/N_{el} = F\,(N_{ph}/N_{el})\,(\hbar\omega/\tau_{ph})\,[N_{ph}(T_e) - N_{ph}(T_L)] \qquad (3)$$

where $F = N_{ph}/N_{el}$ is the form factor, N_{ph} is the number of involved LO-phonon states, $\hbar\omega$ is the LO-phonon energy, $N_{ph}(T_e)$ is the nonequilibrium occupancy of these states when $T_{ph} = T_e$. Monte Carlo simulation shows that Eq. (3) is acceptable at moderate electron temperatures [18,19].

Solid lines in Fig. 3 illustrate the r.h.s. of Eq. (3) for $\tau_{ph} = 350$ fs and $F = 1$ at different lattice temperatures T_L. A reasonable interpretation of the experimental data (symbols) is obtained. At low temperatures, $T_L < T_e << \hbar\omega/k_B$, Eq. (3) reduces to $UI/N_{el} = \hbar\omega/\tau_{ph}\,\exp(-\hbar\omega/k_B T_e)$.

The balance equation (3) can be solved with respect to τ_{ph}. Now, the experimental data of Fig. 3 lead to the results illustrated in Fig. 4. The obtained mean LO-phonon lifetime seems to be independent of the lattice temperature. No systematic dependence on the electric field is found.

Let us use the value $\tau_{ph} = 350$ fs for extrapolation of $T_e(E)$ dependence beyond the range where it can be measured through the noise experiment. For this, the balance equation (3) is solved with respect to T_e, and the results are plotted in Fig. 1 (solid line). The estimated electron temperature is in a reasonable agreement with the temperature T_e obtained from the spectrum of hot-electron luminescence emitted from the gate–drain region of a biased AlGaN/GaN transistor channel (Fig. 1, horizontal bar H)[20].

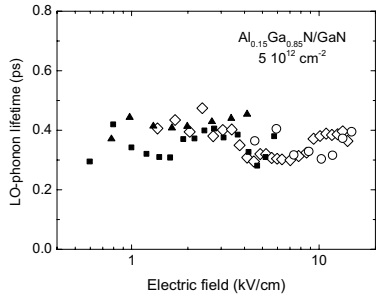

Figure 4. LO-phonon conversion lifetime for AlGaN/GaN 2DEG channel at different electric field and ambient temperature: 80 K—squares [9] and triangles [14], 303 K—diamonds [16], 373 K—circles [18].

When the electron temperature is known, the electron energy relaxation time can be estimated according to Eq. (1) (Fig. 2, solid line). Open squares

stand for the experimental data in the field range where the energy relaxation time can be measured directly. Solid line tends to the constant high-field value and merges with the extrapolated LO-phonon lifetime (Fig. 2, dots). A 0.55 ps field-independent value for the electron energy relaxation time has been observed at high fields [8] for AlN/GaN channels (Fig. 2, stars). Similar values of 0.5 ps have been obtained for GaN bulk samples during femtosecond optical pump–probe experiments [21, 22].

5. Electron deconfinement

The extrapolated field-dependence of the electron temperature $T_e(E)$ for AlGaN/GaN can be used for considering electron redistribution among subbands. Since the envelope wave function penetrates into AlGaN layer when the electron occupies the high-energy subband, the adjacent GaN and AlGaN layers share the high-energy electrons. The subband model [11] provides with the shared electron density as a function of the electron temperature, $n_{sh}(T_e)$ [13]. The dependence $n_{sh}(T_e)$ [13], together with the $T_e(E)$ dependence (Fig. 1, dashes), provides with the field dependence of the shared electron density, $n_{sh}(E)$.

Within a two-level model, the product of the shared and the confined electron densities $n_{sh}n_{cf}$ is the measure of spectral intensity of the occupancy fluctuations. The product has the maximum in the field range where the spectral intensity of current fluctuations has the maximum [13,14,16]. The ratio n_{sh}/n_{cf} enters the expression for the relaxation time of the occupancy fluctuations [14, 16]. The fitted dependence of the relaxation time on electric field is illustrated in Fig. 2.

6. Conclusion

Microwave noise technique can be used for estimation of relaxation time constants and the LO-phonon conversion lifetime in nitride 2DEG channels. The LO-phonon lifetime is a useful parameter that decides hot-electron energy dissipation and electron deconfinement at high electric fields.

Acknowledgements

Partial support from USA ONR Grant No N00014-03-1-0558 and from NATO Grant No PST ARW 979380 is acknowledged.

References

[1] L. F Eastman, V. Tilak, V. Kaper, J. Smart, R. Thompson, B. Green, J. R. Shealy, and T. Prunty, Progress in high-power, high frequency AlGaN/GaN HEMT's, phys. stat. sol. (a) **194** (2002) 433–438.

[2] A. Vertiatchikh, H. Kim, W. J. Schaff, L. F. Eastman, R. Thompson, V. Kaper, and R. Shealy, Bias dependent frequency response of AlGaN/GaN HEMT, in Proc. 27th Workshop on Compound Semiconductor Devices and Integrated Circuits held in Europe 2003, ed. W. Bachtold, pp. 41–42.

[3] H. Hartnagel, R. Katilius, and A. Matulionis, *Microwave Noise in Semiconductor Devices*, Wiley, New York (2001).

[4] A. Matulionis, I. Matulionienė, Hot-electron noise in III–V semiconductor structures for ultrafast devices, in: "*Noise and Fluctuations Control in Electronic Devices*", Ed. A. Balandin, American Sci. Publishers (2002) pp. 249–266.

[5] A. Matulionis, J. Liberis, L. Ardaravičius, M. Ramonas, I. Matulionienė, and J. Smart, Hot-electron energy relaxation time in AlGaN/GaN, Semicond. Sci. Technol. **17** (2002) L9–L14.

[6] A. Matulionis, R. Katilius, J. Liberis, L. Ardaravičius, L. F. Eastman, J. R. Shealy, and J. Smart, Hot-electron-temperature relaxation time in a two-dimensional electron gas: AlGaN/GaN at 80 K, J. Appl. Phys. **92** (2002) 4490–4497.

[7] N. Balkan, M. C. Arikan, S. Gokden, V. Tilak, B. Schaff, and R. J. Shealy, Energy and momentum relaxation of hot electrons in GaN/AlGaN, J. Phys.: Condens. Matter. **14** (2002) 3457–3468.

[8] A. Matulionis, J. Liberis, L. Ardaravičius, J. Smart, D. Pavlidis, S. Hubbard, and L. F. Eastman, Hot-phonon limited electron energy relaxation in AlN/GaN, Intern. J. High Speed Electronics and Systems **12** (2002) 253–262.

[9] A. Matulionis, J. Liberis, I. Matulionienė, L. F. Eastman, J. R. Shealy, V. Tilak, A. Vertiatchikh, Hot-phonon lifetime in a biased AlGaN/GaN channel, Phys. Rev. B **68**, (2003), 035338-1–7.

[10] J. A. Kash, and J. C. Tsang, Nonequilibrium phonons in semiconductors, 1992 in: *Spectroscopy of Nonequilibrium Electrons and Phonons*, C. V. Shank and B. P. Zakharchenya, eds., Modern Problems in Condensed Matter Sci. Vol. **35**, North-Holland, Amsterdam (1992) pp. 113–167.

[11] M. Ramonas, A. Matulionis, and L. Rota, Monte Carlo simulation of hot-phonon and degeneracy effects in the AlGaN/GaN two-

dimensional electron gas channel, Semicond.Sci.Technol.**18** (2003) 118–123.

[12] S. Gokden, N. Balkan, and B. K. Ridley, Effect of non-drifting hot phonons on high-field drift velocity in GaN/AlGaN, Semicond. Sci. Technol. **18** (2003) 206–211.

[13] A. Matulionis, J. Liberis, L. Ardaravičius, M. Ramonas, T. Zubkutė, I. Matulionienė, L. F. Eastman, J. R. Shealy, J. Smart, D. Pavlidis, and S. Hubbard, Fast and ultrafast processes in AlGaN/GaN, phys. stat. sol. (b) **234** (2002) 826–829.

[14] A. Matulionis, Fast and ultra-fast dissipation and fluctuations in two-dimensional channels for nitride and arsenide FETs, in: Proc. of SPIE *Noise in Devices and Circuits*, Vol. **5113** (2003) 237–251.

[15] A. Matulionis, J. Liberis, I. Matulionienė, L. F. Eastman, J. R. Shealy, J. Smart, V. Tilak, and A. Vertiatchikh, Estimation of hot-phonon temperature and lifetime from microwave noise measurements, Proc. *17th International Conference on Noise and Fluctuations ICNF 2003*, Ed. J. Sikula, Brno University of Technology (2003) pp. 251–254.

[16] J. Liberis and A. Matulionis, Hot-electron noise in nitride 2DEG channels, in: Proc. *17th International Conference on Noise and Fluctuations ICNF 2003*, Ed. J. Sikula, Brno University of Technology (2003) pp.241–246.

[17] R. Katilius, Kinetic theory of fluctuations in a biased degenerate two- or three-dimensional electron gas, in: Proc. *17th International Conference on Noise and Fluctuations ICNF 2003*, Ed. J. Sikula, Brno University of Technology (2003) pp.25–30.

[18] M. Ramonas, and A. Matulionis, Monte Carlo simulation of hot-phonon effects in a biased AlGaN/GaN channel, Semicond. Sci. Technol. (2004) (accepted).

[19] A. Matulionis, J. Liberis, L. Ardaravičius, L. F. Eastman, J. R. Shealy, and A. Vertiatchikh, Hot-phonon lifetime in AlGaN/GaN at an elevated lattice temperature, Semicond. Sci. Technol. (2004).

[20] N. Shigekawa, K. Shiojima, and T. Suemitsu, Optical study of high-biased AlGaN/GaN high-electron-mobility transistors, J. Appl. Phys. **92** (2002) 531–535.

[21] C.-K. Sun, Y.-L. Huang, S. Keller, U. K. Mishra, and S. P. DenBaars, Ultra-fast electron dynamics study of GaN, Phys. Rev. B **59** (1999) 13535–13538.

[22] H. Ye, G. W. Wicks, and P. M. Fauchet, Hot electron relaxation time in GaN, Appl. Phys. Lett. **74** (1999) 711–713.

NOISE OF HIGH TEMPERATURE SUPERCONDUCTING BOLOMETERS

I.A. Khrebtov

S.I. Vavilov State Optical Institute
199034 St.Petersburg
Russia
iiakhrebtov@yahoo.com

Abstract The review describes the noise properties of the high-T_c superconducting *(HTS*) bolometers developed for applications in optical electronic devices of infrared and submillimeter wavelengths. The principle of bolometer operation and its noise theory are considered. The published results of bolometer noise modeling are discussed. Various sources of the excess 1/*f*-noise in *HTS* films are reviewed. Comparative analysis of noise characteristics of the most developed *HTS* bolometers for application is carried out.

Keywords: noise, bolometer, film, high temperature superconductivity

1. Introduction

After the discovery of high-T_c superconductivity (*HTS*) it has become obvious that one of the most promising applications of *HTS* materials is the development of high-sensitivity bolometers [1-4]. The operating temperature close to 77 K, thin film technology, sharp temperature dependence of resistance in the superconducting transition region provide the high responsivity and small response time. The sensitivity of the *HTS* bolometer is limited by various noise sources due to the thermodynamic origin, the nature of high-T_c superconducting and *HTS* films technology. It should be noted that in spite of the evident progress of the manufacturing *HTS* bolometers the excess 1/*f*-noise problem is of primary importance [4].

2. Some Questions of Bolometer Noise Theory

The operating principle of the *HTS* bolometer is illustrated by Fig. 1.

J. Sikula and M. Levinshtein (eds.),
Advanced Experimental Methods for Noise Research in Nanoscale Electronic Devices (97 - 107)

The radiation is absorbed by a *HTS* film on a substrate with a heat capacity C [J/K], which is weakly coupled to a heat sink through thermal conductance G [W/K]. The absorbed radiation heats the *HTS* film, operating at the temperature T_b to change its resistance R_b proportionally to the temperature coefficient of resistance $\beta = 1/R_b \times dR/dT$ [1/K]. The constant bias current I_b or voltage V_b are applied to the bolometer and an output voltage or current signals are measured with readout electronics.

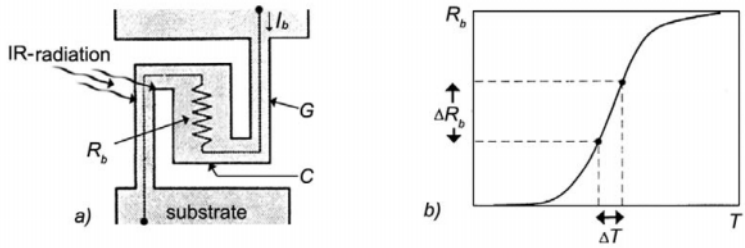

Figure 1. a) Schematic design of bolometer; b) Change of the resistance R_b in the superconducting transition region due to the absorbed *IR* radiation.

The ultimate sensitivity is determined by both the noise equivalent power {*NEP)* and the specific detectivity (*D*)*, at bandwidth $\Delta f = 1$Hz, equal to:

$$NEP = \frac{V_n}{S_V}, \text{ [W/Hz}^{1/2}\text{]}, \tag{1}$$

$$D^* = \frac{A^{1/2}}{NEP}, \text{ [cmHz}^{1/2}\text{/W]}, \tag{2}$$

where V_n is the total noise as composed of a sum of various independent noise sources, A is the bolometer area, S_V is the voltage responsivity [3]:

$$S_V = \frac{\varepsilon L_0}{I_b \left(1 - L_0\right)\left(1 + \omega^2 \tau_e^2\right)^{1/2}}, \text{ [V/W]}, \tag{3}$$

where: $L_0 = \beta P_b / G$ is the electrothermal feedback (*ETF*) gain coefficient, $P_b = I_b^2 R_b$ is the bias power, $\omega = 2\pi f$ is the circle frequency, f is the operating frequency, L_0 is positive value at the constant bias current (*CCM*) operation and L_0 is negative one at constant bias voltage (*CVM*) operation. Accordingly, the effective thermal time constant is $\tau_e = \tau/(1-L_0)$ for *CCM* and $\tau_e = \tau/(1+L_0)$ for *CVM,* τ is the intrinsic thermal time constant.

Theoretical value of the detectivity of *HTS* bolometer, limited by only the photon noise in the background radiation, is equal to $D^*_{phot}=2.8\times10^{10}$ cmHz$^{1/2}$/W at $T_{phot}=300$ K and $T_b=77$ K. Note that in the practice the *NEP* of *HTS* bolometers is due to other noise sources and, therefore, the resulting *NEP,* which is the same for both positive and negative *ETF* operations, is rewritten as [3-5]:

$$NEP_{V,I}=\left\langle \frac{4\kappa {T_b}^2 G}{\varepsilon^2}+\left(\frac{4\kappa T_b G^2}{\varepsilon^2\beta^2 P_b}+\frac{G^2\alpha}{\varepsilon^2\beta^2 NAtf^a}\right)\left[1+\omega^2\tau^2\right]\right\rangle^{1/2}, \qquad (4)$$

where: the 1-st term is due to the phonon noise caused by the random energy exchange between the bolometer element and the heat sink through G at bolometer T_b, the 2-nd term is due to Johnson noise of *HTS* film resistance, the 3-rd component is due to excess current 1/*f*-noise of *HTS* film.

Excess 1/*f*-noise component of *NEP* is obtained from the empirical formula of Hooge [6], where α_H is the film quality-dependent parameter for *HTS* film, N is the density of charge carriers in the film, set at 10^{21} cm^{-3} [7], A is the area and t is the thickness of the film, the coefficient a at f is close to 1. Usually, the Hooge parameter α_H in the normal state is used for the noise characterization of *HTS* films**.**

It should also be noted that according to "(4)" NEP_R and $NEP_{1/f}$ depend on the thermal time constant τ, but not τ_e as for S_V "(3)". This factor is explained by taking into account the effect of *ETF* on Johnson and flicker noise contributions. In case of *CVM* operation P_b can be larger than for *CCM* operation, so according to "(4)" Johnson contribution is suppressed with an increasing P_b.

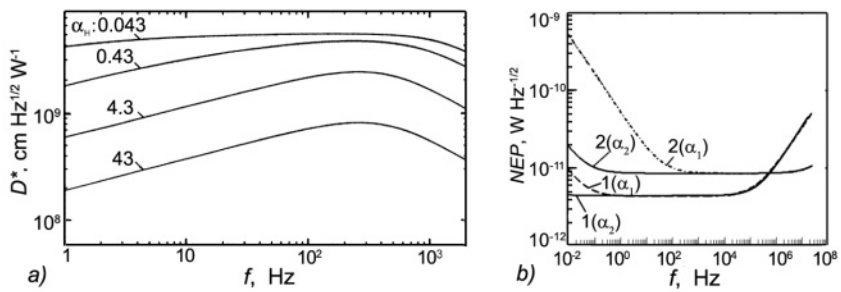

Figure2. Calculated noise performance of different *HTS* bolometers.*a)* The detectivity D^* of *GdBaCuO* bolometer on *YSZ/Si* membrane *versus* frequency for various Hooge-parameter α_H [2, 8]. *b)* The *NEP* of *YBaCuO* bolometers on $SrTiO_3$ substrates *versus* frequency for various α_H ($\alpha_1 = 2\cdot10^{-3}$, $\alpha_2 = 2\cdot10^{-6}$) [10]: 1-membrane bolometer, $A = 50\times50$ μm^2, $R_b = 200$ Ω, G = $4\cdot10^{-5}$ W/K, $\tau = 62$ μs; 2-microbolometer on solid substrate, $A = 1\times10$ μm^2, $R_b = 25$ Ω, G = $1.6\cdot10^{-4}$ W/K, $\tau = 0.25$ μs.

Modeling of noise parameters of *HTS* bolometers of various designs was reported in [3-5, 8-11]. The calculated analysis of the noise behavior of *GdBaCuO* bolometer on *YSZ/Si* membrane [2] at *f*-range of 1 Hz – 10 kHz was carried out using the experimental data on *G* and $\alpha_H = 0.043\text{-}43$ [8].

Fig. 2a shows that with increasing α_H and, thus, degrading film quality, *D**-value decreases. At the maximum, the achievable *D** will be about 80% of the possible phonon noise limit of $5 \cdot 10^9$ cmHz$^{1/2}$/W for Hooge-parameter of *HTS* film at the transition midpoint of α_H = 1–2, and the optical absorption $\varepsilon = 0.26$ [2].

Fig. 1b shows an estimate of *NEP* for bolometers using *YBaCuO* on $SrTiO_3$ substrates having a record-low α_H [10]. For slow membrane bolometer, a *NEP* value, which is limited only by phonon noise, can be achieved at low modulating frequencies < 0.01 Hz ($\alpha_H = 2 \cdot 10^{-6}$). At high $f > 10^4$ Hz the increase of *NEP* is explained by the effect of the Johnson noise. The fast microbolometer on solid substrate with a higher *G* operates at a higher bias current, therefore the excess 1/*f*-noise begins to dominate at $f <$ 0.1 Hz ($\alpha_H = 2 \times 10^{-6}$). Thus, at $\alpha_H = 2 \times 10^{-6}$ the microbolometer will operate at the phonon limit in frequency region of 0.1 Hz–10 MHz.

3. Excess 1/*f*-Noise in *HTS* films for Bolometers

The problem of noise in the *HTS* material prospective for new microelectronic devices, operating at 77 K, was first discussed in the review [7]. Here we consider the results of 1/*f*-noise study in *HTS* films prepared on substrates of various materials suitable for bolometric application. Noise characteristics of the test *HTS* film samples of meander-type (m) and bridge-type (b), fabricated by magnetron sputtering (M) or laser ablation (L), are presented in Tab. 1. All film structure changes should be attributed only to the two main sources: (i) the change of the substrate material, (ii) the difference in substrate quality (mosaic spread). The last source is obvious– the better the mosaic spread of substrate, the better epitaxial *HTS* film may be manufactured. This effect is especially distinct for substrates with good coincidence site lattice conditions ($SrTiO_3$, $NdGaO_3$) with $\Delta\omega$ smaller than 0.3 deg. for which its mosaic spread is negligible.

Typical behavior of 1/*f* noise for epitaxial *YBaCuO* films is shown in *Fig. 3* [12]. The study of critical current and noise behavior showed the films with high structural perfection had the most and sharpest critical current density $j_c(T)$, low 1/*f*-noise in normal state and the absence of magneto-dependent peak noise in the transition “tail” region [12].

Table 1. Noise characteristics of *HTS* films using for bolometers.

No., Ref.	Substrate, deposition method		Film size, mm×mm×μm		R_N, Ω	Δω, deg.	β, K^{-1}	α_N at R_N
1[12]	$SrTiO_3$,	L	0.31×0.02×0.2,	b	55	0.3	0.7	$3\cdot10^{-4}$
2[12]	$NdGaO_3$,	L	0.33×0.010×0.2,	b	86	0.2	1.5	$2\cdot10^{-4}$
3[12]	*MgO*,	L	0.51×0.047×0.2,	b	21	0.6	0.7	0.014
4[12]	Al_2O_3,	L	0.52×0.037×0.2,	b	64	1.7	0.7	0.09
6[10]	$SrTiO_3$,	L	0.5×0.006×0.2,	b	252	0.1	5.8	$2\cdot10^{-6}$
7[8]	**YSZ/Si,*	M	10×0.05×0.05,	m	9700		0.6	0.01
9[3]	**YSZ/Si/SiN*,	M	17×0.025×0.06,	m	20000		5.8	1.0

In Table: **GdBaCuO* film, others-*YBaCuO* films, RN is the resistance in the normal state, Δω is the half of film (005) rocking curve from X-ray measurements.. The critical temperatures of superconducting transition were in the region of 85−92 K.

A few models were proposed to interpret the origin of the noise peak. These include the vortex motion [13], thermodynamic phase transition of the vortex state [14] and critical current fluctuations of weak links [15]. Investigation of critical current behavior in *YBaCuO* films allows one to think that the factor, due to vortex motion, dominates in structural perfect films. The factor of weak links dominates in films of granular type. In most cases the experimenters deal with films of average quality and then both factors affect simultaneously.

A percolation model of 1/*f*-noise in superconductors was proposed to describe the noise behavior in a wide temperature region from normal state down to superconducting state [7]. In this model the superconductors are considered as a resistance network whose elements are grain boundary junctions. The total network resistance is a function of the fraction of superconducting junctions p and the resistance fluctuations arise from random switching of the junctions (p-noise). Noise behavior of granular and epitaxial films is in good agreement with that percolation model. The percolation also explains the noise peak as a 3*D*/2*D*-crossover of the percolation.

There is a confidence, that the excess 1/*f*-noise in the normal phase is caused by the structural fluctuation processes in the vicinity of the extended structural defects. The intrinsic deformation fluctuations <e>, due to the matching of the substrate and *HTS* film with the lattice parameters and the temperature expansion coefficient, lead to the relaxation of substrate disorder and 1/*f*-noise in the normal phase [16].

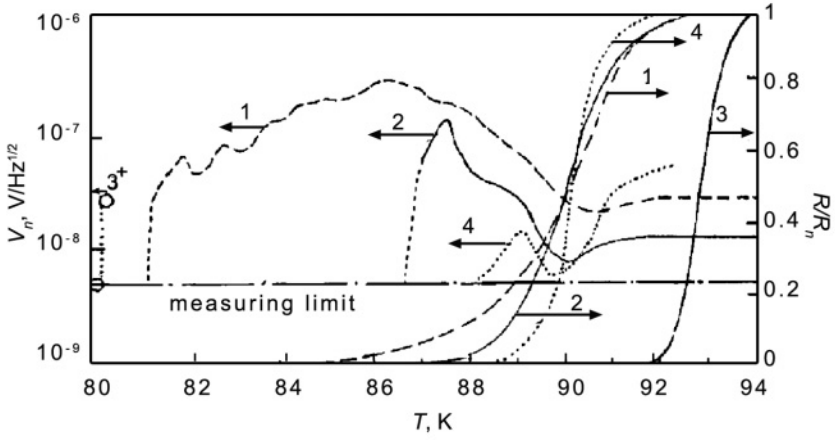

Figure 3. Noise voltage V_n and resistance R/R_N *versus* temperature for *YBaCuO* films on various substrates. 1 – Al_2O_3, $j = 1.4 \cdot 10^5$ A/cm^2, 2 – *MgO*, $j = 1.1 \cdot 10^5$ A/cm^2, 3$^+$ – $NdGaO_3$, $j = 1.1 \cdot 10^6$ A/cm^2, 3 – $NdGaO_3$, $j = 1.1 \cdot 10^4$ A/cm^2, 4 – $SrTiO_3$, $j = 1.1 \cdot 10^4$ A/cm^2 [12].

4. Experimental Noise Study of *HTS* Bolometers

4.1. Noise of bolometers on micromachined silicon technology

At present, *HTS* bolometers fabricated by micromachined silicon membrane technology are considered as the most prospective high performance infrared detectors [1-4, 8-9, 11-12, 17]. However, in spite of large advantages of this technology there is a problem of the excess flicker noise in *HTS* films on silicon substrates.

The structural quality of films is affected by some mechanisms: (i) through the large lattice mismatch between the buffer layer and the *HTS* film on top, (ii) through the large difference of the temperature dependent expansion coefficients within the layer system, (iii) through the interdiffusion along grain boundaries and the resulting chemical reactions. Thus, during thermal cycling, microcracks formation is observed in the system. It may result in affecting the bolometer parameters, especially, noise. The influence of microcracks formation in *GdBaCuO* film on *Si*-membrane on noise and degradation of characteristics had been investigated in [8]. The results of SEM image and noise spectral measuring, showed in Fig. 4a, confirm it.

Fig. 4a shows that at $f < 10$ Hz flicker noise is dominant and the V_n^2 line strictly follows the 1/*f*-dependence, with $V_n^2 \sim f^{(0.8\text{-}1.0)}$. The V_n^2 measured at

operating T, where the bolometric signal is maximum, typically revealed a plateau at $10 < f < 200$ Hz, due to phonon noise. At frequencies > 10 Hz $1/f$-noise decreases, while the phonon noise is invariable up to 200 Hz. Further the phonon noise begins to decrease as $V_n^2 \sim 1/f^2$, i.e., more than flicker noise. As result, the noise at high frequencies is due to the Johnson noise. Such behavior of noise agrees with calculation [8].

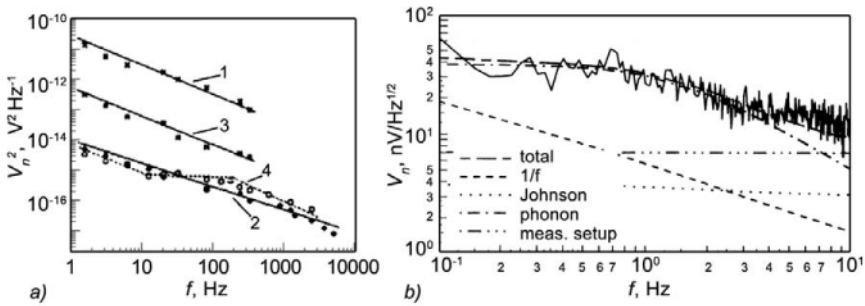

Figure. 4. a) Noise spectrum $V_n^2(f)$ of *GdBaCuO* bolometers on *YSZ/Si* membrane in CCM operation [2, 8]. Virgin sample No. 1: 1 – I_b = 0.24 mA, T = 300 K, 2 – I_b = 1.1 mA, $R_b = 0.001R_N$; virgin sample No. 2 (data of No. 2 are shown in Tab. 2): 4 — I_b = 0.24 mA, $R_b = 0.3R_N$; aged sample No. 2: 3 – I_b = 0.24 mA, R_b=0.5R_N. b) Noise spectrum of one from *GdBaCuO* bolometers on *YSZ/Si/Si₃N₄* membrane at T = 89.5 K [3]. The phonon noise was calculated using following parameters: I_b = 17.8 μA, R_b = 1.9 kΩ, β = 5.8 1/K, G = 18 μW/K, L_0 = 0.19, τ_e = 95 ms, S_V = 8.4 kV/W (electrical one at ε = 1) at $f = 1/2\pi\tau_e$.

Fig. 4b shows a frequency dependence of V_n (f) of *GdBaCuO* bolometer on an *YSZ/Si/Si₃N₄* membrane. The bolometer differs from the previous *Si*-membrane bolometer by a low thermal conductance and, accordingly, low response time, but higher responsivity (see Tab. 2, No. 3). It can be seen that between 0.2 and 3 Hz the measured spectrum is also fully due to the calculated phonon noise. Note, the samples No. 2 [17] and No. 4 [9] show the possibility of manufacturing *HTS* microbolometer arrays with high performance.

Table 2. Noise characteristics of *HTS* bolometers based on *Si*-micromachined technology.

No Ref	Membrane	A/t, μm²/μm	R_b, Ω	α_H	G, mW/K	τ, ms	S_V, kV/W	NEP, pW/Hz$^{1/2}$	D^*, cmHz$^{1/2}$/W
1[2]	**YSZ/Si*	$72\cdot10^4/1$	6400	0.01	0.3	0.58	0.85	22.0	$3.8\cdot10^9$
2[17]	*YSZ*	8000/0.07	8000	3.6	$8.5\cdot10^{-5}$	110	32	1.5	$8\cdot10^9$
3[3]	**YSZ/Si/SiN*	$95\cdot10^4/1$	3600	1.0	$1.5\cdot10^{-2}$	115	4.76	5.5	$1.8\cdot10^{10}$
4[9]	*CeO_2/YSZ*	$10^4/0.08$	-	-	$6.2\cdot10^{-4}$	0.56	12	4.0	$2.5\cdot10^9$

In *Table*: * – *GdBaCuO* films, others-*YBaCuO* film; t is the thickness of the membrane; S_V, *NEP and D** are obtained from optical measurements.

4.2. Noise of antenna-couple *HTS* microbolometers

One of the prospective applications of *HTS* films is the antenna-couple microbolometers, operating in far infrared and submillimeter wavelength regions [1, 4, 12, 18-22]. In such detectors, an *HTS* microbridge, connected to the output of receiving metal film antenna, is used as a thermal converter of high-frequency power generated by the antenna into a comparatively low-frequency output signal. The small size of *HTS* element of about some μm^2 provides a fast response and, when operating at high frequencies, allows one to operate near to phonon noise limit [12, 19, 22]. However, because of the element contact with substrate having high thermal conductivity, high bias current density is used in these microbolometers. Thus, current 1/*f*-noise has a stronger effect on their *NEP* at low operating frequencies (see Fig. 6).

In addition to their very small size, the local defects can influence the noise properties of such detectors, therefore, very narrow temperature-dependent noise peaks at transition tail would be observed in the microbolometers [20]. Fig. 5a shows that the intensity of narrow peak noise in the range of $T << T_c$ for *YBaCuO* microbolometer is very sensitive to small variations of magnetic field. Noise spectra (*Fig. 5b*) at the maximum (a) and (b) are of $V_n^2 \sim 1/f^2$ type, while at the minimum (c) the frequency noise dependence is close to the Lorentzian form with frequency cut-off $f_{\text{cut-off}} \sim 5$ kHz. However, the noise peak, proportional to dR/dT has a typical $V_n^2 \sim 1/f$ dependence.

Using the LTSEM technique, the noise origin of the single peak for *YBaCuO* meander film on *MgO* substrate was localized, and it was established that the noise peak was related to a single weak link on a microcrack blocking the path of current percolation [23]. This noise has the character of random telegraph signals and may arise from the Abrikosov vortex motion resulting in the fluctuations of the phase difference across the weak link which leads to the fluctuations of its critical current [23].

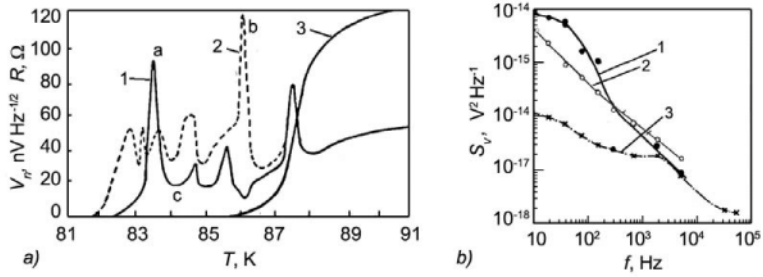

Figure 5. Noise characteristics of *YBaCuO* microbolometer ($3\times35\times0.15$ μm^3) on *YSZ* substrate [20]. a) Temperature dependencies of noise V_n (1, 2) at $f = 10$ Hz , $I = 0.98$ mA and resistance (3) for at various magnetic fields: 1 -$B = 0$; 2 – B ($\perp$) = 8 mT. b) Noise spectrum V_n^2 (f): 1 – $T = 83.5$ K, $B = 0$; 2 – $T = 87.6$ K, dR/dT (max), $B = 0$; 3 – $T = 84.1$ K, B = 0.

Note that for microbolometers 1/*f*-noise at $T < T_c$ is less dangerous than the noise peak proportional to d*R*/d*T* in the transition middle, which has been observed for *YBaCuO* microbolometer on *YSZ* substrate [20].

Tab. 3 and Fig. 6 show the results of experimental investigation of antenna-couple *YBaCuO* microbolometers on various substrates [12, 21, 22]. Fig. 6 shows the noise characteristics of the microbolometer on a $NdGaO_3$ substrate (No. 3, Tab. 3) that was patterned and provided by an *Au* bow-tie antenna. The noise and microbolometer response in a high frequency range have similar temperature dependencies in the transition region. The noise voltage in the maximum is close to that calculated from a phonon noise, furthermore, its coincidence with the signal dependence confirms that the observed noise is a phonon one. Nevertheless, the excess noise restricts the sensitivity of a detector up to ~1 kHz, which is seen on Fig. 6 [12].

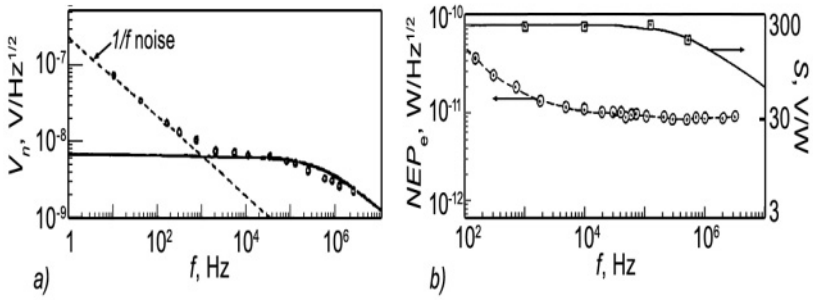

Figure 6. a) Frequency dependence of the noise voltage V_n for *YBaCuO* microbolometer on a $NdGaO_3$ substrate (No. 3, Tab. 3). Solid line is the calculated phonon noise. b) Experimental frequency dependencies of the electrical responsivity S_e and noise equivalent power NEP_e.

The frequency dependence of the experimental noise and calculated phonon noise beyond 10 kHz also agree. It is seen that the best antenna microbolometers have electrical NEP_e, limited only by phonon noise, within the frequency range of (0.001–3) MHz for $NdGaO_3$ substrate and 100 Hz-30MHz for $LaAlO_3$ substrate. Note that the optical *NEP* and *D** depend on the efficiency of film antenna and the wavelength of radiation [18].

Table 3. Noise characteristics of antenna-coupled *YBaCuO* microbolometers

No., Ref.	Substrate material	*YBaCuO* film size,μm^2	R_b, Ω	α_N	G, mW/K	τ, ns	S_e, kV/W	NEP_e, pW/Hz$^{1/2}$
1[20]	*YSZ*	13×6	40	0.4	0.036	$2\cdot10^4$	0.48	4.5
2[19]	*YSZ* membr.	10×5	75	0.13	0.003	10^4	*2.9	*9
3[12]	$NdGaO_3$	14×2	24	$2\cdot10^{-2}$	0.3	$3\cdot10^2$	0.24	16
4[18]	$LaAlO_3$	1×0.7	20	$1.4\cdot10^{-4}$	0.005	30	1.7	1.5

in Table: * – measured optical *S* and *NEP*.

References

[1] P. L. Richards, Bolometers for infrared and millimeter waves, J. Appl. Phys. **76** (1994) 1–24.

[2] H. Neff, J. Laukemper, I. A. Khrebtov et al, Sensitive high-T_c transition edge bolometer on micromachined silicon membrane, Appl. Phys. Lett. **66** (1995) 2421–2423.

[3] de M. J. M. E Nivelle, M. P. Bruijn, de R. Vries et al, Low noise high-T_c superconducting bolometers on silicon nitride membranes for far-infrared detection, J. Appl. Phys. **82** (1997) 4719–4726.

[4] I.A. Khrebtov, Noise properties of high temperature superconducting bolometers. Fluctuation and Noise Letters, **2** No.2 (2002) R51-R70.

[5] A. T. Lee, J. M. Gildemeister, S-F. Lee and P. L. Richards, Voltage-biased high-T_c superconducting infrared bolometers with strong electrothermal feedback, IEEE Trans. Appl. Supercond. **7** (1997) 2378–2381.

[6] F. N. Hooge, T. G. Kleinpenning and L. K. Vandamme, Experimental studies of 1/f noise, Rep. Prog. Phys. **44** (1981) 479–532.

[7] L. B. Kiss and P. Svedlindh, Noise in high T_c superconductors, IEEE Trans. Electron. Devices **41** (1994) 2112–2122.

[8] H. Neff, I. A. Khrebtov, A. D. Tkachenko et al, Noise bolometric performance and aging of thin high T_c superconducting films on silicon membranes, Thin Solid Films **324** (1998) 230–238.

[9] L. Mechin, J. Villegier and D. Bloyet, Suspended epitaxial YBaCuO microbolometers fabricated by silicon micromachining: Modeling and measurements, J. Appl. Phys. **81** (1997) 7039–7047.

[10] I. A. Khrebtov, B. Dam, A. D. Tkachenko et al, YBCO films on $SrTiO_3$ substrates with recordly low 1/f noise for bolometer applications, Proc. of 4th European Workshop on Low Temperature Electronics, ESA **WPP-171** (2000) 335–339.

[11] S. Verghese, P. L. Richards, K. Char et al, Feasibility of infrared imaging arrays using high-T_c superconducting bolometers, J. Appl. Phys. **71** (1992) 2491–2498.

[12] I. A. Khrebtov, V. N. Leonov, A. D. Tkachenko et al, Noise of high-T_c superconducting films and bolometers, J. Phys. IV France **8 Pr3** (1998) 293–296.

[13] G. Jung, M. Bonaldi, S. Vitale and J. Konopka, One the origin of low frequency noise in HTSC thin films, Physica C **180** (1991) 276–279.

[14] D. G. Steel, D. H. Kim, K. E. Gray et al, Electrical-noise signatures of possible vortex transitions in epitaxial $YBa_2Cu_3O_7$ thin films, Physica C **248** (1995) 55–60.

[15] D. V. Shantsev, A. V. Bobyl, M. E. Gaevskii et al, Noise properties of inhomogeneous non-linear medium: application to high-Tc superconductors, in Noise in Physical Systems and 1/f Fluctuations, Proc. 14th Int. Conf., eds. C. Clayes and E. Simoen, Leuven (1997), 321–324.

[16] A. V. Bobyl, M. E. Gaevskii, S. F. Karmanenko et al, Intrinsic microstrains and normal-phase flicker noise in $YBa_2Cu_3O_7$ epitaxial films grown on various substrates, J. Appl. Phys. **82** (1997) 1274–1280

[17] B. R. Johnson, M. C. Foote, H. A. Marsh and B. D. Hunt, Epitaxial $YBa_2Cu_3O_7$ superconducting infrared microbolometers on silicon, Proc. SPIE **2267** (1994) 24–30.

[18] V. N. Leonov and I. A. Khrebtov, Antenna-coupled thermal radiation detectors (Review), Instr. Exp. Techn. **36** (1993) 501–520.

[19] M. Nahum, Q. Hu, P. L. Richards et al, Fabrication and measurement of a high-T_c superconducting microbolometer, IEEE Trans. Magn. **MAG-27** (1991) 3081–3085.

[20] V. N. Leonov and I. A. Khrebtov, Noise of YBaCuO microbolometers, Superconductivity: Phys. Chem. Techn. **4** (1991) 1260–1266.

[21] I. R. Rice, E. N. Grossman and D. A. Rudman, Antenna-coupled high-T_c air bridge microbolometer on silicon, Appl. Phys. Lett. **65** (1994) 773–775.

[22] S. F. Karmanenko, A. A. Semenov, I. A. Khrebtov et al, Fabrication process and noise properties of antenna-coupled microbolometers based on superconducting YBCO films, Supercond. Sci. Technol. **13** (2000) 273–286.

[23] A. V. Bobyl, M. E. Gaevski, S. F. Karmanenko et al, Magneto-depending noise of a single latent weak link in $YBa_2Cu_3O_{7-x}$ film, Physica C **266** (1996) 32–40.

1/*f* NOISE IN MOSTs: FASTER IS NOISIER

L.K.J. Vandamme

Eindhoven University of Technology, Department of Electrical Engineering EH 9.13

5600MB Eindhoven

The Netherlands

L.K.J.Vandamme@tue.nl

Abstract Circuit-simulation-oriented equations (SPICE and BSIM3) for the 1/*f* noise are discussed and their fitting parameters are translated in the 1/*f* noise parameter α. The effect of scaling down on the 1/*f* noise is studied in the ohmic region as well as in saturation and sub-threshold. A prospective for scaling down is given for channel length L < 0.12 μm where velocity saturation becomes dominant. A relation is proposed between the 1/*f* noise corner frequency f_c, where the 1/*f* noise is equal to the thermal noise, and the unit current gain frequency f_T. Faster devices (with higher f_T) are inherently noisier considering f_c. Approximately holds, $10^{-4} f_T < f_c < 10^{-3} f_T$.

Keywords: MOST, 1/*f* noise, thermal noise, f_T, unit current gain frequency, SPICE, BSIM

1. Introduction

The majority of 1/*f* noise results obtained on homogeneous semiconductors and *p*-MOSTs can be described by Hooge's empirical relation [1] considering the 1/*f* noise [2-4] as a volume effect

$$\frac{S_I}{I^2} = \frac{S_V}{V^2} = \frac{S_R}{R^2} = \frac{S_G}{G^2} = \frac{\alpha}{Nf} \qquad (1)$$

α, the 1/*f* noise parameter is not a constant [2] but volume and device-length independent [3, 5] with values between 10^{-6} and 10^{-3} for metals and semiconductors. A systematic study [4, 5] of flicker noise in CMOSTs shows that for modern *p*-and *n*-channel devices holds $10^{-6} < \alpha < 10^{-4}$. N is the total number of free charge carriers in a homogeneous sample with perfect contacts. N must be replaced by a well-defined reduced number in samples submitted to non-homogeneous fields [6] as is often the case in contacts. Often technology recipes are described to achieve low 1/*f* noise devices

J. Sikula and M. Levinshtein (eds.),
Advanced Experimental Methods for Noise Research in Nanoscale Electronic Devices (109 - 120)

without being specific about what is low. For sake of comparison the α-parameter can be used. α is a quantitative figure of merit for the $1/f$ noise. The usefulness of Eq. (1) lays in the fact that a comparison in $1/f$ noise in α-values is made independent of bias, frequency and size of the device. It expresses the relative noise in the conductivity for one carrier at 1 Hz in a single very specific value. The larger the amount of carriers in the sample the lower is the amount of relative noise in the resistance. The misuse of the empirical relation (1) to calculate α values from experimental results by overlooking either noisy series resistances or the non-uniform current densities on a microscopic scale, e.g., by replacing $1/N$ by $q\mu R/L^2$, always leads to overestimation in terms of apparent α-values [2, 3, 6, 7] The equation $1/N = q\mu R/L^2$ with q the elementary charge, μ the mobility, R the sample resistance and L the length between the contacts, only holds for homogeneous fields in homogeneous samples. The $1/f$ noise of n-MOSTs has been described successfully by carrier-number fluctuations ΔN, which are thought to be caused by tunnelling of free-charge carriers into oxide traps close to the Si-SiO_2 interface [7]. Classical arguments in favour of the McWhorter model are the observed proportionality between trap density and $1/f$ noise [8, 9]. In chapter 2, we discuss the geometry and bias dependence of $1/f$ noise in MOSFETs. Table 1 shows some $1/f$ noise relations for MOSFETs based on the empirical relation. Table 2 shows some circuit-simulation-oriented equations (SPICE and BSIM3) for the $1/f$ noise in MOSTs with the fitting parameters translated in α-values. In chapter 3 we demonstrate that faster devices are inherently noisier. In Table 3 the relations for thermal noise and corner frequency are shown. In Table 4 the calculated $1/f$ noise, thermal noise and f_c, f_T is shown for 5 devices from 3 different technologies.

2. Geometry-, and Bias-Dependence in α- and SPICE-parameters

The study of geometry and bias dependence of the $1/f$ noise in sub-micron MOSTs is a powerful diagnostic tool to discriminate between channel and series resistances noise [10, 11]. Only if series resistance contributions can be ignored, the straightforward circuit-simulation-oriented equations can be applied. The $1/f$ noise parameter α is used in our analysis as a figure of merit. Its value is gate-length independent at least if the channel length is larger than the mean free path of carriers [5]. For the sake of simplicity we assume no series resistance or edge current problems. This results in a generally accepted dependence between the $1/f$ noise in MOSTs and the channel area [7, 8]; however, the dependence on oxide thickness is

still under discussion. We start from the empirical relation (1) and suggest that even in the MOSTFET the 1/f noise is a bulk phenomenon with $\Delta\mu$ fluctuations due to electron-lattice interactions in the bulk. If experimental results are at variance with this hypothesis, which is sometimes the case for surface-channel n-MOSTs, we find $\alpha \propto 1/V_G^*$ for kT/q < V_G^* <1V. Then all derived equations are still applicable. In Table 1 a number of simple equations is described in order to be able to analyze and compare experimental results expressed in different ways in literature.

Table 1. 1/*f* noise relations for MOSFETs, based on the empirical relation, geometry and bias dependencies [5] [7] [9] [12] [14]

Bias condition	Equations
Ohmic (below saturation) $V_D \le V_G^*$ $V_G^* = V_G - V_T > 0$	$\frac{S_I}{I^2} = \frac{\alpha q \mu R}{l^2 f} = \frac{\alpha q \mu V_D}{Il^2 f} = \frac{\alpha q}{C_{ox} V_G^* Wlf}$ $S_I = \frac{\alpha q \mu V_D I}{l^2 f} = \frac{\alpha q \mu^2 C_{ox} V_G^* V_D^2 W}{fl^3}$ $S_{Veq0} = \frac{\alpha q V_G^*}{WlC_{ox} f}$
Saturation $V_D \ge V_G^*$ a) $v_d < v_{sat}$	$S_{I_S} = \frac{2\alpha I_S^2}{Nf} = \frac{\alpha q \mu^2 C_{ox} V_G^{*3} W}{2fl^3}$ $S_{I_S}(I_s) = \frac{\sqrt{2}\alpha q \mu^{1/2} I_s^{3/2}}{W^{1/2} C_{ox}^{1/2} fl^{3/2}}$ $S_{Veq}(V_G^*) = \frac{\alpha q V_G^*}{2WlC_{ox} f}$ $S_{Veq}(I_s) = \frac{\alpha q I_s^{1/2}}{\sqrt{2}(WC_{ox})^{3/2} (l\mu)^{1/2} f}$
b) $v_d = v_{sat}$ (l < 0.15μm)	$S_{I_S} = \frac{\alpha q W C_{ox} V_G^* v_{sat}^2}{lf}$ $S_{Veq} = \frac{\alpha q V_G^*}{C_{ox} Wlf}$
Weak inversion Sub threshold [12]	$\frac{S_{Isub}}{I_{sub}^2} = \frac{\alpha}{(N+N_0)f} \approx \frac{\alpha}{N_0 f} = \frac{\alpha q^2}{kTC_{ox} Wlf}$

With $N = C_{ox} V_G^* WL/q$ with $V_G^* = V_{GS} - V_T$ and the simple current-voltage

Eq. (2) (3), we find the 1/*f* noise relations [7, 12]. Ignoring the α dependence on scattering others than lattice scattering we find in Table 1 the relations for the ohmic, saturation and sub-threshold region [5, 7, 9, 12]. At fixed V_G^* compared to the ohmic region ($V_d \to 0$) we find in saturation a reduced free carrier number. For the thermal current noise holds in first approximation a factor 2/3 between the current noise of a MOST biased in saturation and in ohmic region at the same gate voltage [13]. For the 1/*f* noise holds a factor 2 [14]. For the ratio between the relative 1/*f* noise in the saturation and in the ohmic region at the same gate voltage holds (S_{Isat} / I_{sat}^2) / (S_I / I^2) = 2. Ignoring the series resistance, velocity saturation and body effect, we expect for the saturation current and transconductance in first order approximation

$$I_S = (W/L)\mu C_{ox} V_G^{*2} / 2 \text{ and } g_{m_s} = \partial I_S / \partial V_G^* = (W/L)\mu C_{ox} V_G^* = 2I_S / V_G^* \quad (2)$$

For deep sub-micron ($L < 0.12$ μm) the simple equations (2) for current and transconductance are no more valid when the devices are biased at drain and gate voltages of about 1 V. Current density is given by $J = qnv_d$ and under velocity saturation conditions the drift velocity v_d has to be replaced by a field independent saturation velocity $v_s \approx 10^7$cm/s for silicon. For a 2-dimensional description J is in A/cm and n is the concentration of carriers per unit area (cm^{-2}). Hence the current and the transconductance become:

$$I_{sat} = WC_{ox} V_G^* v_{sat} \text{ and } g_m = WC_{ox} v_{sat} = I_s / V_G^* \quad (3)$$

The 1/*f* fluctuations and the α-value under hot carrier conditions at velocity saturation are reduced compared to the values at low fields [1].

Table 2. HSPICE level: 0, 1, 2, 3 and BSIM3-parameters translated in α-values [5] [7]

SPICE		Saturation $\frac{S_{I_s}}{I_s^2} = \frac{2\alpha}{Nf}$ with $N = WlC_{ox}V_G^*/q \quad V_{ds} \geq V_G^*$	
	NLEV=0	$S_{I_s} = \frac{KF0 I_s^{AF}}{C_{ox} l^2 f}$	AF = 1; $KF0 = \alpha q V_G^* \mu C_{ox}$ AF=3/2; $KF0 = \alpha q (2\mu C_{ox} l / W)^{1/2}$
	NLEV=1	$S_{I_s} = \frac{KF1 I_s^{AF}}{C_{ox} l W f}$	AF = 1; $KF1 = \alpha q V_G^* \mu C_{ox} (W/l)$ AF=3/2; $KF1 = \alpha q (2\mu C_{ox} (W/l))^{1/2}$
	NLEV=2, 3 BSIM3v2	$S_{I_s} = \frac{KF2 g_m^2}{C_{ox} l W f}$	$KF2 = \alpha q V_G^* / 2$

In Table 2 we show some pragmatic circuit-simulation oriented noise equations in order to be able to calculate α-values from results in literature given in KF0, KF1, KF2 values. The fourth column in Table 2, bridge the

gap between the parameters used by circuit designers and the α-value characterizing the relative 1/*f* noise at 1Hz per carrier. The disadvantage of the K-values is that they often are geometry and bias dependent except for KF2, applied to surface-channel *n*- MOSTs if αV_G^* is constant.

3. The Faster the MOSFET, the Higher the 1/f Noise

The corner frequency, f_c , where the 1/*f* noise equals the thermal noise is a figure of merit for the low frequency noise, while the unit current gain frequency or the so-called transition frequency, f_T, is used as a characterization of the high frequency behaviour of MOSTs. In Table 3 a new relation shows that the higher f_T will be, the higher f_c will be, or faster is noisier. In order to calculate the intersection between thermal and 1/*f* noise we need the expressions for 1/*f* and thermal noise of MOSFETs [7, 9, 13, 14]. The thermal noise and f_c are summarized in Table 3.

Table 3. Thermal noise $S_{I_{th}}$, $S_{Veq_{th}}$ and frequency f_c, geometry and bias dependence [9]

Bias condition	Thermal noise equations: $S_{I_{th}}$; $S_{Veq_{th}}$ versus V_G^* and I_s	$f_c(V_G^*), f_c(I_s)$
Ohmic $\upsilon = V_D / V_G^*$ $\upsilon < 1$	$S_{Veq_{th}} = \frac{4kTR_0}{\upsilon^2}\left(\frac{1-\upsilon+\upsilon^2/3}{1-\upsilon/2}\right)$ $S_{I_{th}} = \frac{4kT}{R_0}\left(\frac{1-\upsilon+\upsilon^2/3}{1-\upsilon/2}\right)$	$\frac{\alpha q \upsilon^2 (1-\upsilon/2)^2 \mu V_G^{*2}}{4kTl^2(1-\upsilon+\upsilon^2/3)} = f_c$
$V_D \geq V_G^*$ $\upsilon = 1$	$S_{I_{th}}(V_G^*) = \frac{2}{3} 4kT \frac{W}{l} \mu C_{ox} \lvert V_G^* \rvert$ $S_{Veq_{th}}(V_G^*) = \frac{2}{3}\frac{4kT}{g_{ms}} = \frac{2}{3}\frac{4kTl}{W\mu C_{ox}\lvert V_G^*\rvert}$	$f_c = \frac{3\alpha q V_G^{*2} \mu}{16kTl^2}$
	$S_{I_{th}}(I_s) = \frac{\sqrt{2}}{3} 8kT \left(\frac{W}{l} \mu \ C_{ox} I_{sat}\right)^{1/2}$ $S_{Veq_{th}}(I_s) = \frac{\sqrt{2}}{3}\frac{4kTl^{1/2}}{W^{1/2}\mu^{1/2}C_{ox}^{1/2}I_{sat}^{1/2}}$	$f_c = \frac{3\alpha q I_s}{8kTWlC_{ox}}$

The equivalent input noise S_{Veqth} counting for the Brownian motion of the carriers in the channel in Table 3 is obtained from $S_{I_{Sth}} / g_{ms}^2$ and expressed as a function of V_G^* or I_s. For $\upsilon \rightarrow 0$, by $V_D \rightarrow 0$, $g_m \rightarrow 0$, the S_{Veqth} becomes

divergent. This has no physical meaning. The thermal equivalent input voltage noise is proportional to l/W and $1/V_G^*$, and S_{Is} has the opposite dependence. For the 1/*f* noise S_{Veqth} and S_{Is} holds that both increase with bias, but with different dependencies (see Table 1). The corner frequency f_c is obtained from $S_{th} = S_{1/f}$ and is the same for the equivalent input noise voltage or the current noise. Now we calculate in Table 4, as a function of geometry and bias, f_c, f_T, f_c / f_T and S_{Veq} and S_{Is}, together with the integrated noise represented by $<\Delta V_{eq}^2>$ and $<\Delta I_S^2>$, respectively. From the expressions in Tables 1 and 3 we obtain for MOSTs biased in saturation f_c (V_G^*) and f_c (I_S) respectively [9].

$$f_c(V_G^*) = \frac{3\alpha q V_G^{*2}\mu}{16kTl^2} = \frac{3\alpha q V_G^* g_{ms}}{16kTWlC_{ox}} \text{ and } f_c(I_S) = \frac{3\alpha q I_S}{8kTWlC_{ox}} \quad (4)$$

We must emphasize that f_c is a relative figure of merit and not an absolute one. A low value for f_c does not mean a low value for the integrated noise in the device. Comparing two devices with the same channel length *l*, bias voltage V_G^* at the same temperature, but with different widths (W/l ratios) will show the same f_c value, but the widest device will have the lowest 1/*f* and thermal noise expressed in S_{Veq}.

The unit current gain frequency f_T of a MOSFET is defined as:

$$f_T = \frac{g_{ms}}{2\pi C_{ox} lW} = \frac{\mu V_G^*}{2\pi l^2} \propto \frac{\mu V_G^*}{l^2} \quad (5)$$

The highest frequency for applications is about $f_h = f_T/5$. Both frequencies f_c and f_T are proportional to $1/l^2$; hence the ratio f_c/f_T becomes independent of channel length as can be seen in the ratio:

$$\frac{f_c}{f_T} = \frac{3\pi\alpha q V_G^*}{8kT} \quad (6)$$

At room temperature, with $\alpha = 2\text{x}10^{-5}$ and $V_G^* = 1\text{V}$ holds that $f_c = 10^{-3} f_T$. The ratio is independent of geometry. The α- values are technology dependent, with high values (10^{-4}) for oxide implanted substrates or other lattice damage in the current path of the inversion layer. f_c and f_T increase with V_G^*; however, for *n*-channel MOSFETs sometimes holds that αV_G^* is constant and then f_c/f_T is even independent of bias.

The integrated noise (variance in a bandwidth f_h-f_l) also is considered as a figure of merit. $S_{Veq}(f)$, $<\Delta V_{eq}^2>$ and $S_{I_S}(f)$, $<\Delta I_S^2>$ can be written as:

$$S_{Veq}(f) = a + b/f \text{ and } <\Delta V_{eq}^2> = a(f_h - f_L) + b\ln(f_h / f_L), \quad (7)$$

$$S_{I_S}(f) = c + d/f \text{ and } <\Delta I_S^2> = c(f_h - f_L) + d\ln(f_h / f_L),$$

where a and c represent the thermal noise contributions as given in Table 3 and b and d represent the $1/f$ part of the spectrum with values as given in Table 1. The following simple relations hold between a, b, c and d:

$$f_c = b/a = d/c \text{ and } g_{ms}^2 = c/a = d/b \quad (8)$$

The integrated $1/f$ noise (f_L=1 Hz) can be ignored compared to the integrated thermal noise if $f_c/f_T < 10^{-2}$, which is often the case in broadband applications. The condition for an integrated thermal noise equal to the variance of the $1/f$ noise contribution leads to:

$$a(f_h - f_L) = b\ln(f_h / f_L) \text{ or } (f_h - f_L) = f_C \ln(f_h / f_L) \quad (9)$$

For $f_h >> f_L$ and taking into account that the highest frequency applied in the MOST is related to f_T as $f_h = f_T/p$ (often with $p \approx 5$), we find for Eq. (9):

$$\frac{f_T}{p} = f_C \ln(f_T / pf_L) \text{ or } \frac{f_T}{f_C} = p\ln(f_T / pf_L) \quad (10)$$

At room temperature, even with $p \leq 5$ (as in broadband applications) and $\alpha < 10^{-4}$ (healthy technology), we find that $<\Delta V_{eq}^2>$ or $<\Delta I_S^2>$ always are dominated by the thermal noise contribution. For $f_h = f_T$ and $f_L << f_h$ we find the surprising result that $<\Delta V_{eq}^2>$ is independent of bias and mobility and inversely proportional to the total gate capacitance. Smaller is noisier.

$$<\Delta V_{eq}^2> \approx <\Delta V_{eq_{th}}^2> = \frac{4kT}{3\pi WlC_{ox}}, \quad (11)$$

The spectral value $S_{Veq_{th}}$ and f_T are proportioned to $1/V_G^*$ and V_G^*, respectively. The result in Eq. (11) is similar to the variance of the thermal noise across a resistor in parallel with a capacitance C, there too we have $<\Delta V^2> = kT/C$. In order to illustrate the complex trade off between device size, current density, power consumption, low integrated noise and speed in advanced submicron technologies, five simulation examples are shown in Table 4 and in Fig. 1a in $S_{Veq}(f)$ and Fig. 1b in $S_{I_S}(f)$ values .

Table 4. Calculated f_c, f_T, $S_{Veq}(f)$, $S_{I_S}(f)$, $<\Delta V_{eq}^2>^{1/2}$ and $<\Delta I_S^2>^{1/2}$ (with $f_h = f_T/5$) and current density (I_s/W) for different technologies, geometries and bias conditions. Devices I, II, IV belong to a 0.15 μm technology with t_{ox}=3nm, Device II is a 1.5 μm technology with t_{ox}=30nm and device V a 15 μm technology with t_{ox} = 300nm. All devices have and $\alpha = 10^{-5}$ and are at T= 320 K and devices I, II, III, IV have a μ= 300 cm^2/Vs and device V a μ= 600 cm^2/Vs.

No	W/l μm/ μm	V_G^* (V)	I_S/W (A/ μm)	I_S (A)	g_{ms} (A/V)	f_c (Hz)	f_T (Hz)	$S_{Veq} = a + \frac{b}{f}$ (V^2/Hz)	$<\Delta V_{eq}^2>^{\frac{1}{2}}$ (V)	$S_{I_S} = c + \frac{d}{f}$ (A^2/Hz)	$<\Delta I_S^2>^{\frac{1}{2}}$ (A)	$f_c/f_T \approx$
I	1/0.15	0.466	2.5×10^{-4}	2.5×10^{-4}	1.1×10^{-3}	1.96×10^{7}	9.9×10^{10}	$1.1\times10^{-17}+2.16\times10^{-10}/f$	4.7×10^{-4}	$1.3\times10^{-23}+2.5\times10^{-16}/f$	5×10^{-7}	2×10^{-4}
II	10/1.5	0.093	10^{-6}	10^{-5}	2.15×10^{-4}	7.9×10^{3}	2×10^{8}	$5.5\times10^{-17}+4.3\times10^{-13}/f$	4.7×10^{-5}	$2.5\times10^{-24}+2\times10^{-20}/f$	10^{-8}	4×10^{-5}
III	10/1.5	0.294	10^{-6}	10^{-5}	6.77×10^{-5}	7.9×10^{4}	6.3×10^{8}	$1.7\times10^{-16}+1.36\times10^{-11}/f$	1.5×10^{-4}	$7.97\times10^{-25}+6.2\times10^{-20}/f$	10^{-8}	1.2×10^{-4}
IV	10/1.5	0.466	2.5×10^{-5}	2.5×10^{-4}	1.1×10^{-3}	1.97×10^{5}	9.9×10^{8}	$1.1\times10^{-17}+2.1\times10^{-12}/f$	4.7×10^{-5}	$1.3\times10^{-23}+2.5\times10^{-18}/f$	5×10^{-8}	2×10^{-4}
V	10^3/15	2	9.2×10^{-7}	9.2×10^{-4}	9.2×10^{-4}	7.25×10^{4}	8.4×10^{7}	$1.3\times10^{-17}+9.27\times10^{-13}/f$	1.5×10^{-5}	$1.1\times10^{-23}+7.8\times10^{-19}/f$	1.35×10^{-8}	8.6×10^{-4}

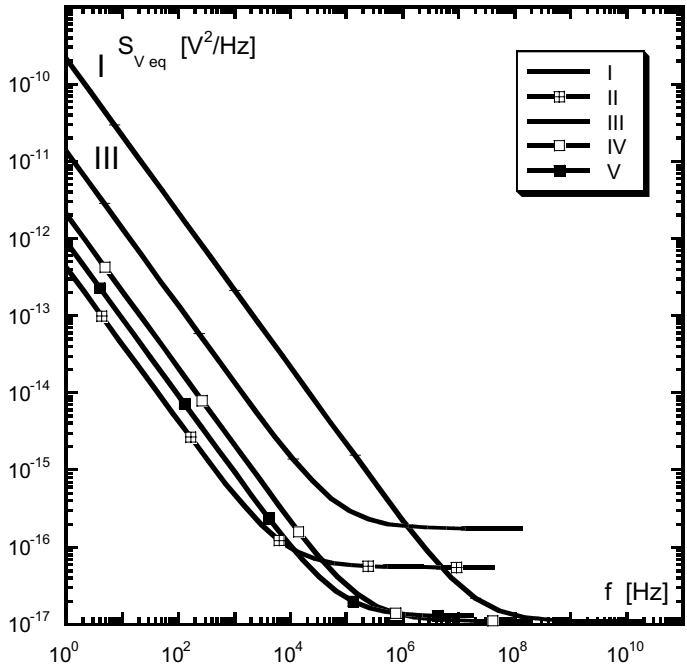

Figure. 1a. Calculated spectra of 5 different devices from 3 different technologies as given in Table 4 and calculated with equations from Table 1 and 3 for 1 Hz $< f < f_T$ /5

Device I is the shortest, fastest, noisiest and smallest one. Device II has the same W/l ratio as device I but an area that is 10^2 times larger. Device II is slower and is weakly biased to have a low current density in the channel in order to have the lowest 1/*f* noise. Device III has the same area, current density and W/l ratio as device II, but it is an older technology (1.5μm technology with t_{ox} = 30nm in stead of t_{ox} = 3nm for I, II and IV). Device IV can be compared to I, same technology, same W/l and bias, same transconductance, but channel length and width are 10 times higher. This shows the benefits of a low noise design by increasing dimensions in an advanced submicron technology at the expense of lower f_T. Lower 1/*f* and thermal noise is possible at the expense of a larger channel area and a lower f_T, e.g., comparing device I and IV. Device V is a 35-year-old technology with L = 15μm, t_{ox} = 300nm and μ = 600cm^2/Vs.

High mobility MOSFETs are realized in Si/SiGe. Such devices will show compared to a reference device with lower mobility, and the same α, for the

same effective bias condition (V_G^*) and the same W and l a higher g_m, f_T and f_c but the same ratio f_c/f_T and a lower S_{Veqth}. However, the integrated noise over the full bandwidth remains constant (see Eq. 11).

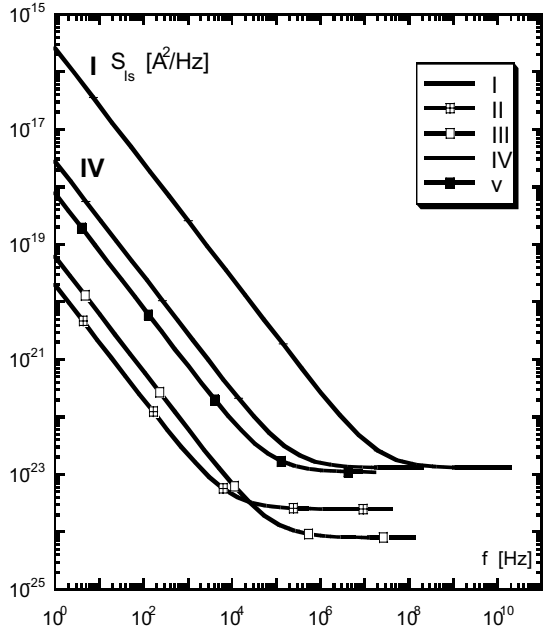

Figure 1b. Calculated spectra of 5 different devices from 3 different technologies as given in Table 4 and calculated with equations from Table 1 and 3 for 1 Hz < f < f_T /5

4. Conclusions, α-values, and t_{ox} dependence

Geometry dependence is well understood; there is debate only on the t_{ox} dependence. The width, length and V_G^* dependence can be used as a diagnostic tool to trace series resistance and edge current contributions in sub-micron devices.

The 1/*f* noise parameter α is a perfect figure of merit to describe the 1/*f* noise in a comparative study of CMOS transistors [4, 5]. In this way we better can compare different technologies in a quantitative way and study the change in noise source through degradation independent of geometry, frequency and current passed through the sample. A review over several technologies shows:

(i) The α-parameter scatters over the usual 2-orders of magnitude just like in bulk semiconductors ($10^{-6} < \alpha < 10^{-4}$). We observed $\alpha \approx 3\times10^{-7}$ which is

among the lowest values ever observed for bulk *p*-MOSTs, while for *n*-MOSTs holds $3\times10^{-5}\text{V}<\alpha V_G^{*}<3\times10^{-4}\text{V}$, with $\alpha \propto V_G^{*-1}$ [8]. This means that for *n*-MOSTs α at V_G^{*} = 1V is between $3\times10^{-5} < \alpha < 3\times10^{-4}$ and the proportionality $\alpha < V_G^{*-1}$ often holds for 0.1 V < V_G^{*} < 1 V.

(ii) High quality wafers with epitaxial layers on top and in situ doping instead of implanting and buried channels are the right precautions to reduce α-values and to realize ultra low 1/*f* noise MOSFETs. Not well-annealed implantations leave some crystal damage in the current path and will probably cause a generation-recombination noise on top of the 1/*f* noise. If there is a single trap at the Fermi level positions and $N < 1/\alpha$ [15] it becomes an RTS contribution on top of the 1/*f* noise.

(iii) The recent [16] and old results [9] show $S_{Veq} \propto t_{ox}$ and not $S_{Veq} \propto t_{ox}^2$ as expected from the ΔN model. The α-values are at least not a function of t_{ox}^2 or t_{ox} and $S_{Veq} \propto t_{ox}$ for 2nm < t_{ox} < 600nm is an indication against the ΔN origin for the 1/*f* noise in MOSFETs. The devices with t_{ox}=600nm are designed as sensors for ionising radiation.

The difference between *n*- and *p*-MOSTs expressed in α becomes smaller if: *n*-MOSTs are compared with surface channel *p*-MOSTs (p^+ polysilicon gate) or bulk *n*-MOSTs are compared with bulk *p*-type MOSFETs. Surface channel *n*-MOSTs are easier to interpret in the straightforward ΔN formalism, while low-noise *p*-MOSTs follow the straightforward $\Delta\mu$ formalism.

The equations in Table 2 show that the simulation oriented parameters are geometry and bias dependent at least for *p*-type MOSFETs that make the noise prediction rather difficult. Considering the typical $\alpha \propto 1/V_G^{*}$ proportionality for surface *n*-MOSFETs, NLEV2, 3 is very useful, because the KF2 is geometry independent. For *p*-type MOSFETs, α-values are in general V_G^{*} independent.

Acknowledgements

The NATO Project Science for Peace (SfP-973799) has financially supported part of this work

References

[1] F.N.Hooge, T.G.M.Kleinpenning, and L.K.J.Vandamme, Experimental studies on 1/f noise, Rep. on Prog. in Phys. **44** (1981) 479-532.

[2] L.K.J. Vandamme, Is the 1/f noise parameter α a constant?, Proc. 7th Int. Conf. on Noise in Physical Systems May 17-20 (1983) Montpellier. eds. Savelli M et. al. (1983) 183-192 Elsevier

[3] L.K.J. Vandamme, Noise as a Diagnostic Tool for Quality and Reliability of Electronic Devices, IEEE Trans. Elect. Dev. **41** (1994) 2176-2187.

[4] J. Chang, A.A. Abidi, and C.R. Viswanathan, Flicker noise in CMOS transistors from sub threshold to strong inversion at various temperatures, IEEE Trans. Elect. Dev. **41** (1994) 1965-1971.

[5] L.K.J. Vandamme, 1/f noise in CMOS transistors, Proc. 10th Inter. Conf. on Noise in Physical Systems, Budapest Aug. 21 - 25 (1989) ed. Ambrozy A. pp. 491-494, 1990 Akademiai Kiado. Budapest.

[6] E.P. Vandamme and L.K.J. Vandamme, Current crowding and its effect on 1/f noise and 3rd-harmonic distortion, Microelectronics and Reliability **40** (2000) 1847-1853.

[7] L.K.J. Vandamme, X. Li, and D. Rigaud, 1/f noise in MOS devices, mobility or number fluctuations? IEEE Trans. Elect. Dev. **41** (1994) 1936-1945.

[8] F.M. Klaassen, Characterization of low 1/f noise in MOS transistors IEEE Trans. Elect. Dev. **ED-18** (1971) 887-891.

[9] L.K.J. Vandamme and R.G.M. Penning de Vries, Correlation between MOST 1/f noise and CCD transfer inefficiency, Solid-State Electr. **28** (1985) 1049-1056.

[10] X. Li and L.K.J. Vandamme, 1/f noise in series resistance of LDD MOSTs, Solid-State Electr. **35** (1992) 1471-1475.

[11] X. Li and L.K.J. Vandamme, 1/f noise in MOSFET as a diagnostic tool,Solid-State Electr. **35** (1992) 1477-1481.

[12] E.P. Vandamme and L.K.J. Vandamme, Unsolved Problems on 1/f Noise in MOSFETs and Possible Solutions, Proc. of the 2nd Inter. Conf. on Unsolved Problems of Noise and Fluctuations (UPoN '99) in Adelaide, 11th - 15th July 1999 ed. Abbott D (1999) 481-486

[13] A.G. Jordan and N.A. Jordan, Theory of noise in metal oxide semi - conductor devices, IEEE Trans. Elect. Dev. **ED-12** (1965) 148-156.

[14] L.K.J. Vandamme and H.M.M. de Werd, 1/f noise model for MOSTs biased in nonohmic region, Solid-State Electr. **23 (**1980) 325-329.

[15] L.K.J. Vandamme, D. Sodini, and Z. Gingl, On the anomalous behaviour of the relative amplitude of RTS noise, Solid-State Electr. **42** (1998) 901-905.

[16] P. Fantini, L. Vendrame, and D. Riccardi, Low frequency noise in CMOS transistors: an experimental and comparative study on different technologies, FNL **1** (2001) L233-L238

EXPERIMENTAL ASSESSMENT OF QUANTUM EFFECTS IN THE LOW-FREQUENCY NOISE AND RTS OF DEEP SUBMICRON MOSFETs

E. Simoen[1] and A. Mercha
IMEC
Kapeldreef 75, B-3001 Leuven
Belgium

C. Claeys
E.E. Dept
KU Leuven
Belgium

[1]simoen@imec.be

Abstract The down-scaling of MOSFETs brings about inversion-layer quantization. Another consequence is the enhancement of the direct tunneling current through the gate, which is a source of parasitic leakage and noise. While these effects are accounted for in the DC characteristics, so far, little attention has been paid to the impact on the low-frequency noise. In this work, the focus will be on the assessment of these quantum noise effects. It is shown that appropriate test structures are required, while more detailed information can be obtained by changing the vertical field, i.e., through a change in the bulk bias. It will also be pointed out that beside experimental data, there is a growing need for accurate noise models, which go beyond the generally accepted correlated mobility fluctuations approach.

Keywords: Low-frequency noise; silicon MOSFETs; quantum effects

1. Introduction

One of the consequences of technology scaling is that several types of quantum effects need to be considered in the charge transport through a silicon MOSFET. For present-day commercial technologies in the 90-130 nm node, one can still use the classical graded-channel approach in the lateral direction, if proper account is made for the short channel effects. This

J. Sikula and M. Levinshtein (eds.),
Advanced Experimental Methods for Noise Research in Nanoscale Electronic Devices (121 - 128)

is, however, no longer true for the vertical direction, where both the shrinking of the physical gate dielectric thickness (t_{ox}) and the increase of the substrate doping density N_{sub} contribute to an increase of the transverse electric field F_s. This has two serious effects: one, the inversion layer becomes quantized and behaves like a two-dimensional electron (or hole) gas (2DEG). This is schematically represented in Fig. 1. Second, when t_{ox} becomes smaller than the direct tunneling limit of ~ 3 nm, carriers can tunnel from gate to substrate, thereby generating a non-negligible gate leakage current I_G.

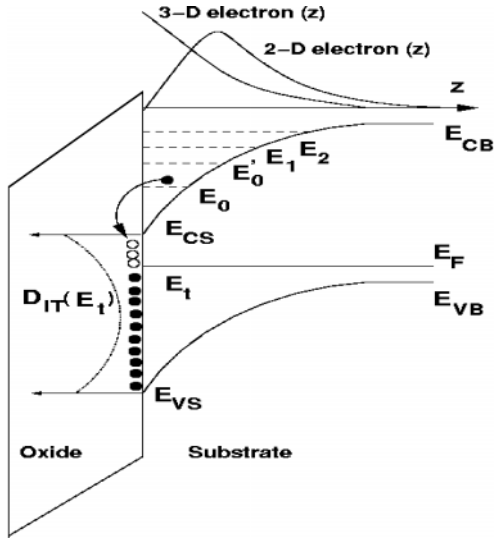

Figure 1. Schematic description of the Si/SiO_2 system showing the discrete energy levels and the spatial extent of the inversion layer in both cases of a quantized inversion layer (2-D) and a classical one (3-D).

These quantum effects (QEs) have a strong impact on the steady-state transport characteristics of deep submicron MOSFETs. However, it is only recently that one recognizes that also the fluctuations, giving rise to low-frequency (LF) noise are subjected to QEs [1-7]. Note that this was already the case before in III-V heterojunction devices, relying on conduction in a 2DEG [8]. Here, a brief overview will be given on the impact of QEs on the DC and LF noise behavior of deep submicron silicon MOSFETs and how these should be experimentally assessed.

2. Impact of quantization on the static characteristics

As sketched in Fig. 1, the high vertical electric field generates a splitting of the inversion layer into subbands, with energies E_0, E_0‘, E_1, E_2,… In addition, an offset ΔE_c is generated in the conduction band minimum (E_{CS}) at the surface, which affects the intrinsic carrier concentration. Moreover, the density of states changes from a 3-dimensional (3-D) bulk one to a 2-dimensional (2-D) distribution. As a result, the carrier density and current in the 2DEG becomes smaller than in the classical case [9, 10]. Another consequence, illustrated in Fig. 1 is that the carrier distribution drastically changes. Inversion-layer quantization results in a peaked profile, with a maximum occurring at a distance z_{av} from the interface, which is determined by F_s. The calculated offset for n- and p-MOSFETs, belonging to a 0.13 µm CMOS technology with a physical t_{ox}=2 nm is shown in Fig. 2a [9, 10]. Due to this inversion-layer offset, the electrical or effective oxide thickness t_{oxeff} becomes larger than the physical one and can be approximated by:

$$t_{oxeff} = t_{ox} + \frac{1}{3} z_{av} . \qquad (1)$$

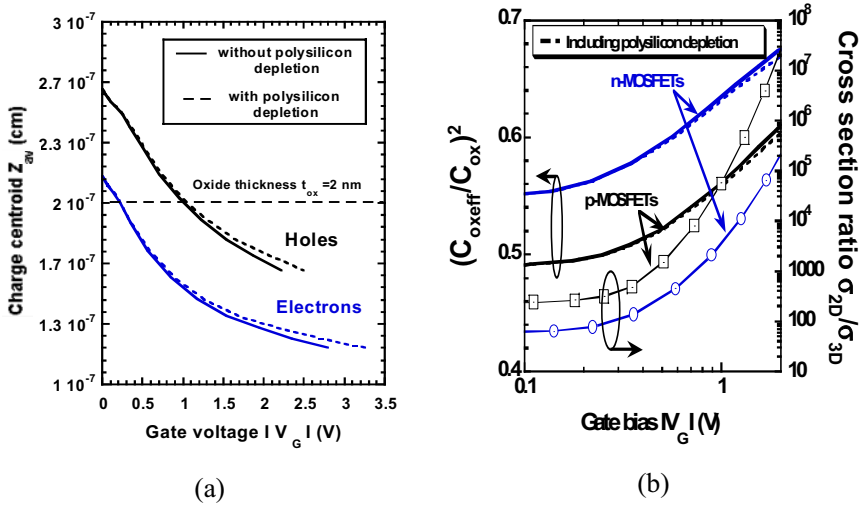

Figure 2. (a) Charge centroid mean position for both holes and electrons taking into account or neglecting the impact of polysilicon gate depletion. (b) Calculated gate capacitance ratio and the cross section ratio versus the absolute value of the gate bias V_G for n- and p-channel devices belonging to a 0.13 µm CMOS technology, with t_{ox}=2 nm (after [9, 10]).

This becomes clear when measuring the capacitance-voltage (C-V) characteristics of a thin-gate MOS capacitor, from which an empirical value for t_{oxeff} can be derived [9, 10]. In fact, combining C-V characteristics with a 1-D quantum-mechanical (QM) numerical fitting procedure provides the necessary input for a QM-based device modeling. As shown in Fig. 2b, the measured capacitance density C_{oxeff} is considerably smaller than the one based on the physical t_{ox}. This has also consequences for the interpretation of 1/f noise in deep submicron MOSFETs, which is discussed below.

3. Impact of quantization on RTS

Historically, QEs have first been assessed experimentally for so-called Random Telegraph Signals (RTSs) [3-5], which are believed to be one of the fundamental components of 1/f noise in MOSFETs. This is not so surprising since RTSs can be considered as local probes for the microscopic charge environment at the Si/SiO_2 interface, lending themselves for the fundamental study of the physics of carrier-trap interactions [6]. One of the fingerprints of QEs is the sensitivity of the RTS parameters (amplitude, characteristic time constant τ) on the applied vertical electric field, which is illustrated by Fig. 3. The latter can easily be varied at constant drain current I_D by changing the substrate bias, in case of a bulk transistor. The inversion-layer charge density, the charge centroid position and the vertical electric field in Fig. 3 have been calculated from the analytical model reported in [11]. Using these parameters enables to derive the Coulomb blockade energy ΔE of the charged oxide trap from the measured capture time constant (τ_c), according to [3]:

$$\Delta E = kT \ln(\tau_c C_n n_s) . \qquad (2)$$

In Eq. (2), k is Boltzmann's constant, T the absolute temperature, n_s the volume carrier density and C_n the capture coefficient, defined as the product of the trap capture cross section and the carrier thermal velocity. In this respect, it should be remarked that an RTS can also be viewed as a kind of natural single electron capacitor existing at the Si/SiO_2 interface [12]. The charging of the trap by a carrier will locally enhance the Fermi level E_F by Coulombic repulsion with an amount ΔE. It is clear from Eq. (2) that for a proper derivation of ΔE, one should derive n_s from the 2DEG density of states and not from the classical one, if inversion-layer quantization prevails [3-5]. In the assumption that RTS is a fundamental component of the 1/f noise found inevitably in large-are transistors, one is led to the conclusion that QEs will also appear in its behavior.

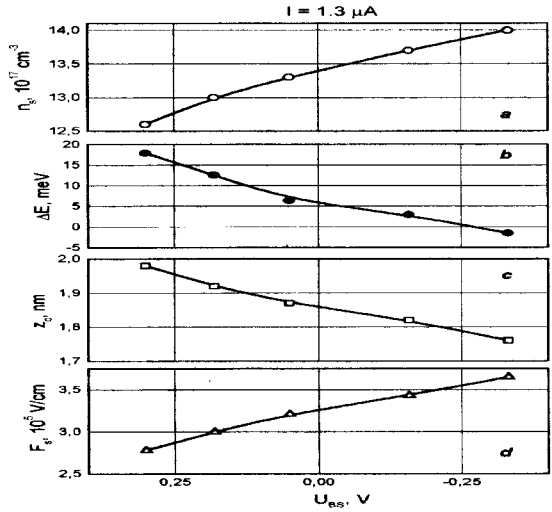

Figure 3. Inversion-layer carrier density n_s (a), Coulomb repulsion energy ΔE (b), average charge centroid (z_c) (c) and vertical electric field F_s (d) as a function of the substrate bias U_{BS}, for an RTS in an L=0.55 μm and t_{ox}=7 nm n-MOSFET. The transistor is operated in the linear regime. A constant drain current of 1.3 μA was applied (after [3]).

4. Impact of quantization on 1/f noise

Although for a long time, the fundamental origin of 1/f noise has been and still is a matter of strong debate, in the engineering community a concensus has grown that the experimental behavior in silicon MOSFETs can be described on the basis of the so-called correlated mobility fluctuations model [13, 14], whereby the origin of the fluctuations is ascribed to interactions of channel carriers with traps residing in the vicinity of the Si/SiO_2 interface. In that framework, the input-referred noise is often approximated by:

$$S_{VG} = \frac{q^2 kT\lambda N_{ot}}{WLC_{ox}^2 f} \tag{3}$$

an expression that is valid in weak inversion and ohmic operation. In Eq. (3), N_{ot} is the density of oxide traps, generating the number fluctuations, WL is the transistor area, $C_{ox}=\varepsilon_{ox}/t_{ox}$ is the capacitance density (ε_{ox} the permittivity of SiO_2) and λ is a tunneling parameter on the order of 0.1 nm. Based on Eq.(3), a density of oxide traps can be extracted, which is often considered a figure of merit of the gate dielectric.

From the foregoing, it is immediately clear that in order to calculate a meaningful trap density, one should replace C_{ox} by C_{oxeff} in Eq. (3) when inversion-layer quantization takes place [9, 10]. Neglecting this will result in an overestimation of N_{ot}, which amounts to 50 % (see Fig. 2b). Another modeling problem becomes obvious when considering the gate voltage dependence of S_{VG} in the linear regime [9, 10]. Standard correlated mobility fluctuations theory predicts a quadratic dependence [13, 14], wherefrom a scattering coefficient can be derived. However, a much stronger variation with $|V_G|$ is often found for deep submicron MOSFETs that cannot be explained by this engineering approach. Considering, on the other hand, the impact of inversion-layer quantization on the 2-D capture cross section (σ_{2D}) of oxide traps, depicted in Fig. 2b, reveals a similar strong variation with $|V_G|$ or with the vertical field. The calculation of the σ_{2D}/σ_{3D} ratio, with σ_{3D} the constant 3-D capture cross section, includes the band offset and the density of states in the 2DEG, following the approach proposed in [11]. Based on these results, an improved semi-empirical expression has been developed, replacing Eq. (3) for the case of a quantized inversion layer by [9, 10]:

$$S_{VG} = \frac{q^2 kT\lambda N_{ot}\sigma_{2D}/\sigma_{3D}}{WLC_{oxeff}^2 f} \tag{4}$$

In Eq. (4), all quantities can be extracted from combined C-V and noise measurements, the only fitting parameter being N_{ot}. Using this approach, reasonable trap densities have been extracted from the noise data in weak inversion [9, 10].

5. Impact of gate tunneling current

Gate leakage and the associated LF noise is of concern for state-of-the-art deep submicron devices [7]. Beside the direct gate tunneling current, a second leakage component can be generated at a sufficiently large V_G, which is related to the so-called Electron Valence-Band (EVB) tunneling [10]. EVB tunneling not only increases the gate current but also generates a flow of majority carriers in the bulk of the transistor. For Silicon-on-Insulator (SOI) transistors operating with a floating body, this will induce a kink effect in the linear drain current I_D [10]. As a result, a second peak in the transconductance g_m versus V_G curve will be observed like in Fig. 4, obtained for a bulk p-MOSFET with a 10 GΩ resistor connected to the well contact. The latter simulates a floating substrate. Contrary to the case of SOI, no strong increase in the LF noise, due to an excess Lorentzian, is observed.

Only a shift of the 1/f noise is found, which reflects the second g_m maximum.

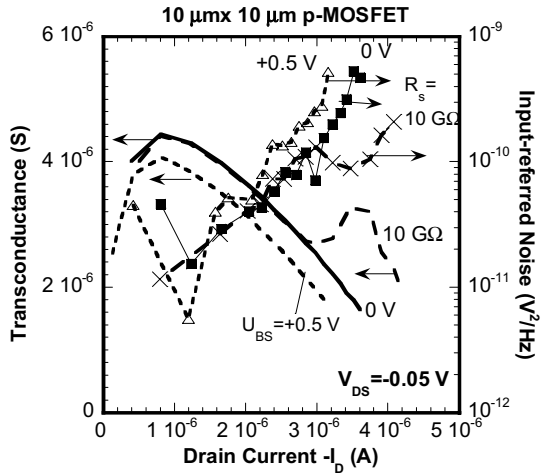

Figure 4. Input referred noise spectral density at 1 Hz for a L=10 µm p-MOSFET versus drain current, with and without a 10 GΩ series resistance connected to the substrate. The third set of curves corresponds to a substrate bias of +0.5 V.

Acknowledgements

The Authors would like to acknowledge stimulating discussions with many Colleagues, in particular with N. Lukyanchikova.

References

[1] A. Palma, A. Godoy, J.A. Jiménez-Tejada, J.E. Carceller and J.A. López-Villanueva, Quantum two-dimensional calculation of time constants of random telegraph signals in metal-oxide-semiconductor structures, Phys. Rev. B **56** (1997) 9565-9574.

[2] A. Pacelli, S. Villa, A.L. Lacaita and L. M. Perron, Quantum effects on the extraction of MOS oxide traps by 1/f noise measurements, IEEE Trans. Electron Devices **46** (1999) 1029-1035.

[3] N.B. Lukyanchikova, M.V. Petrichuk, N.P. Garbar, E. Simoen and C. Claeys, Influence of the substrate voltage on the random telegraph signal parameters in submicron n-channel metal-oxide-semiconductor field-effect transistors under a constant inversion charge density, Appl. Phys. A **70** (2000) 345-353.

[4] Z. Çelik-Butler and F. Wang, Effects of quantization on random telegraph signals observed in deep-submicron MOSFETs, Microelectron. Reliab. **40** (2000) 1823-1831.

[5] N.V. Amarasinghe, Z. Çelik-Butler and A. Keshavarz, Extraction of oxide trap properties using temperature dependence of random telegraph signals in submicron metal-oxide-semiconductor field-effect transistors, J. Appl. Phys. **89** (2001) 5526-5532.

[6] E. Simoen and C. Claeys, Random Telegraph Signal: a local probe for single point defect studies in solid-state devices, Mat. Sci. Eng. B**91-92** (2002) 136-143.

[7] J. Lee, G. Bosman, K.R. Green and D. Ladwig, Model and analysis of gate leakage current in ultrathin nitrided oxide MOSFETs, IEEE Trans. Electron Devices **49** (2002) 1232-1241.

[8] M.A. Py and H.-J. Buehlmann, Evidence for screening effects on the 1/f current noise in GaAs/AlGaAs modulation doped field effect transistors, J. Appl. Phys. **80** (1996) 1583-1593.

[9] A. Mercha, E. Simoen, G. Richardson and C. Claeys, Inversion layer quantization impact on the interpretation of 1/f noise in deep submicron CMOS transistors, In: Proc. 32nd ESSDERC, Eds G. Baccarani, E. Gnani and M. Rudan, University of Bologna (Italy) (2002) 79-82.

[10] A. Mercha, E. Simoen and C. Claeys, Impact of the high vertical electric field on low frequency noise in deep submicron MOSFETs, accepted for publication in IEEE Trans. Electron Devices.

[11] R.R. Siergiej, M.H. White and N.S. Saks, Theory and measurement of quantization effects on Si-SiO_2 interface trap modeling, Solid-St. Electron. **35** (1992) 843-854.

[12] M. Schulz, Coulomb energy of traps in semiconductor space-charge regions, J. Appl. Phys. **74** (1993) 2649-2657.

[13] G. Ghibaudo, O. Roux, Ch. Nguyen-Duc, F. Balestra and J. Brini, Improved analysis of low frequency noise in field-effect MOS transistors, Phys. Stat. Sol. (a) **124** (1991) 571-581.

[14] K.K. Hung, P.K. Ko, C. Hu and Y.C. Cheng, A physics-based MOSFET noise model for circuit simulators, IEEE Trans. Electron Devices **37** (1990) 1323-1333.

NOISE AND TUNNELING THROUGH THE 2.5 nm GATE OXIDE IN SOI MOSFETs

N. Lukyanchikova[1]
Institute of Semiconductor Physics
Prospect Nauki 45, 03028 Kiev
Ukraine

E. Simoen[2] and A. Mercha
IMEC
Kapeldreef 75, B-3001 Leuven
Belgium

C. Claeys
E.E. Dept
KU Leuven
Belgium

[1] natali@isp.kiev.ua ; [2] simoen@imec.be

Abstract It is shown that some peculiar features are typical for the drain current noise spectra of SOI MOSFETs with 2.5 nm gate oxide. In the frequency range 0.7 Hz≤f≤50 Hz a drain current spectral density is observed which follows a $1/f^{1.7}$ law for a broad range of operation conditions. It is demonstrated that this noise is only found in the front-channel current and is observed both in SOI and bulk MOSFETs. The model proposed considers this noise as being generated by carriers tunneling between the front channel and traps associated with the polysilicon gate/oxide interface and situated sufficiently close to the channel in the case of an ultra-thin gate oxide.

When the absolute value of the gate voltage is equal or higher than 1 V, a Lorentzian component appears in the noise spectra measured in the linear regime. It is shown that the Lorentzian amplitude $S_I(0)$ can be described by the formula $S_I(0)=B\tau(V_{DS})^2/L^3$ where B is a coefficient, τ is the Lorentzian time constant that decreases exponentially with increasing gate voltage, V_{DS} is the drain voltage and L is the channel length. The mechanism proposed for this noise is based on the idea that it originates from the filtered shot noise induced by majority carriers which are injected in the floating body of the transistor by electron valence-band tunneling across the ultra-thin gate oxide. Therefore, the appearance of both noise components can be regarded as thin-oxide noise effects.

Keywords: SOI, ultra-thin gate oxide, low-frequency noise, Lorentzian noise

J. Sikula and M. Levinshtein (eds.),
Advanced Experimental Methods for Noise Research in Nanoscale Electronic Devices (129 - 136)

1. Introduction

The paper considers two noise components connected with electron tunneling through the 2.5 nm gate oxide in SOI MOSFETs. The first one called "$1/f^{1.7}$ noise" has been detected in the frequency range 0.7 Hz ≤ f ≤ 50 Hz. For this component the noise power spectral density follows a $1/f^n$ law with n≈1.7 for a broad range of operation conditions [1, 2]. The second one is the excess Lorentzian noise which appears in the noise spectra measured in the linear regime at 1 V≤$|V_G|$≤1.5 V where V_G is the gate voltage [3]. The typical behavior of these noise components and the models proposed are described below.

2. Experimental

The SOI MOSFETs studied have been fabricated in a 0.1 μm technology on UNIBOND wafers. The gate stack consists of a 2.5 nm nitrided oxide and a 150 nm polysilicon layer. The devices come from two wafer splits, one without HALO and another with a high-dose HALO implantation. The channel width Z was 10 μm while the channel length L varied from 10 μm to 0.22 μm. The noise spectra $S_I(f)$ of the drain current I were measured in the frequency (f) range from 0.7 Hz to 100 kHz. The measurements were carried out at low drain voltage V_{DS} corresponding to the linear regime.

3. Results and discussion

3.1. The $1/f^{1.7}$ noise

The main properties of the $1/f^{1.7}$ noise are the following. First of all, it has been found that only the front-channel current shows the $1/f^{1.7}$ noise (Fig. 1a) whereas such a noise is absent in the back-channel current (Fig. 1b).

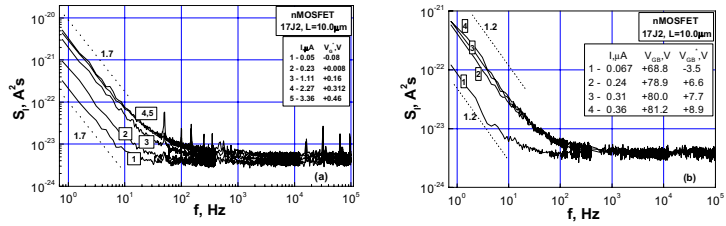

Figure 1. Noise spectra of the front-channel (a) and back-channel (b) current measured in the same nMOSFET at different overdrive voltages $V_G^* = V_G - V_{th}$ where V_{th} is the threshold voltage

This noise is also absent in the gate current [1, 2]. Therefore, the $1/f^{1.7}$ noise is a peculiar feature of the front-channel current.

Secondly, the $1/f^{1.7}$ behavior has also been observed in a split batch of bulk devices processed simultaneously with the SOI devices and having the same gate oxide (Fig. 2a). Moreover, the dependences $S_I(V_G^*)$, with V_G^* the gate overdrive voltage, for the $1/f^{1.7}$ noise measured at a given f in the bulk and SOI devices fall on a single line (Fig. 2b). Therefore, the $1/f^{1.7}$ noise is not SOI related.

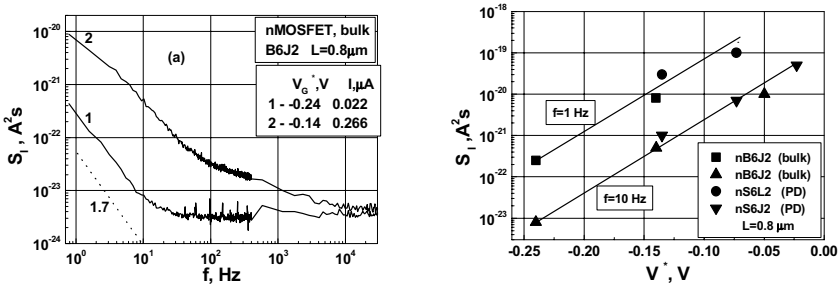

Figure 2. The $1/f^{1.7}$ component in the noise spectra of the bulk nMOSFET (a) and the dependences of S_I on V_G^* measured at f=1 Hz and f=10 Hz in the bulk and SOI nMOSFETs (b)

Thirdly, the $1/f^{1.7}$ noise is not observed in devices with a 3.5 nm gate oxide [4]. This suggests that the $1/f^{1.7}$ noise decreases with increasing oxide thickness.

Fourthly, the dependences of the $1/f^{1.7}$ noise level on V_G and L are typical for the McWhorter (surface) noise, namely: (i) S_I increases with increasing gate voltage in weak inversion and saturates in strong inversion; (ii) in weak inversion S_I/I^2 is independent of V_G^* and decreases as L^{-1} with increasing L; (iii) in strong inversion $S_I=S_I^{sat}\sim L^{-3}$ where S_I^{sat} is the value of S_I measured in saturation; (iv) the equivalent gate voltage noise S_{VG} does not depend on V_G^* and decreases as L^{-1} with increasing L so that the value of $(S_{VG}L)$ is constant for devices of different L and at different V_G^*. This suggests that the $1/f^{1.7}$ noise is of a surface origin.

The following model has been proposed for the $1/f^{1.7}$ noise [1, 2]. The traps responsible for this noise are associated with the polysilicon gate/oxide interface and show a steep concentration profile over a small depth range (Fig. 3a). Some properties of such traps are described in [5]. The $1/f^{1.7}$ noise considered is determined by electron tunneling between these traps and the channel. As is seen from Fig. 3a, the corresponding concentration N_{tg} is supposed to be much higher than the concentration of the slow oxide traps N_{to} (responsible for the 1/f noise observed at f>50 Hz) up to some distance x_g from the polysilicon gate/oxide interface while N_{tg} decreases steeply with increasing distance x from that interface at $x>x_g$. This distribution can be

described as follows: $N_t=N_{to}$ at $x \geq x_g+\Delta x$ and $N_t=N_{tg}+N_{to} \approx N_{tg} >> N_{to}$ at $x \leq x_g$ where the distance Δx is sufficiently small. Therefore, a sharp increase of N_t with increasing distance from the Si/SiO_2 interface takes place near $x=x_g$. The energy levels of the gate-related traps are considered to be distributed homogeneously over the oxide band gap.

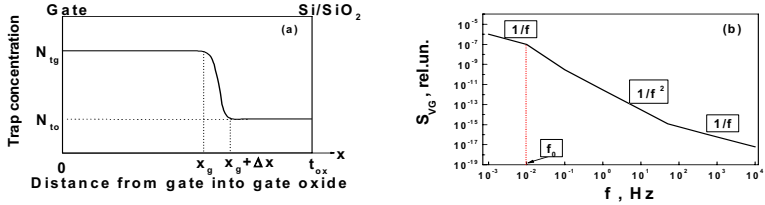

Figure 3. Distribution of the trap concentration in the gate oxide considered in the model of the $1/f^{1.7}$ noise (a) and the shape of the noise spectrum corresponding to such traps distribution (b); x=0 corresponds with the polysilicon gate

By introducing such a distribution $N_t(x)$ into Eqs. (11) and (4) of [6], the conclusion can be drawn that the corresponding noise spectrum is of the following shape (Fig. 3b). It consists of the 1/f portion at $f<f_0=(2\pi\tau)^{-1}$ followed by the $1/f^n$ portion at $f>f_0$ where $1<n<2$ and f_0 is the turn-over frequency determined by the relaxation time τ of charge fluctuations at the gate-related traps located at $x=x_g$. The case n=2 should be observed if the decrease of N_{tg} with increasing x in the region Δx is sufficiently steep. The case n<2 (for example, n=1.7 as in our experiments) will occur if some tail in the distribution $N_t(x)$ takes place at $x>x_g$ so that the decrease of N_t with increasing x at $x>x_g$ is not ideally sharp. The "high-frequency" 1/f noise shown in Fig. 3b is due to slow oxide traps of concentration N_{to}. The following formulae have been derived for the case where n=2:

$$S_I^{sat}(f > f_0) = \frac{q^2 kTN_{tg} x_g^2 Z\mu_{n,p}^2 V_{DS}^2}{L^3 \tau(2\pi f)^2 t_{ox}^2 \alpha} \tag{1}$$

$$S_{VG}(f > f_0) = \frac{q^2 kTN_{tg} x_g^2}{LZC_0^2 \tau(2\pi f)^2 t_{ox}^2 \alpha} \tag{2}$$

$$\tau = \tau_0 exp[(\alpha(t_{ox}-x_g+Z_C)] \tag{3}$$

where q is the electron charge, k is the Boltzmann constant, T is the temperature, N_{tg} is the density of the gate/oxide traps in units $cm^{-3}(eV)^{-1}$, $\mu_{n,p}$ is the charge carrier mobility in the inversion channel, $\alpha=10^8 cm^{-1}$ is a tunneling parameter [6], C_0 is the oxide capacitance per cm^2, $\tau_0=10^{-10}s$ is the minimal trapping time for tunneling exchange of the oxide traps with the channel [6] and Z_C is the distance of the centroid of the inversion layer from

the Si/SiO_2 interface due to the inversion-layer quantization [7]. From Eq. (3) follows that the value of τ decreases with decreasing t_{ox}. Therefore, the level of the noise described by Eqs. (1) and (2) increases very rapidly with decreasing t_{ox}.

When applying Eqs (1) and (2) to the experimental results, the following values of N_{tg} and x_g have been found [2]: $x_g<1.36$ nm, $N_{tg}>2\times10^{20}cm^{-3}(eV)^{-1}$. Note that the values $N_{to}<3\times10^{18}$ $cm^{-3}(eV)^{-1}$ and $N_{to}<2.5\times10^{19}$ $cm^{-3}(eV)^{-1}$ have been found for the concentrations of the slow traps responsible for the 1/f noise in sub-micron n-channel and p-channel MOSFETs with nitrided gate oxide, respectively [8]. Therefore the N_{tg} obtained here satisfies the inequality $N_{tg}>N_{to}$ which is of basic importance for the model proposed.

3.2. The Lorentzian noise at $|V_G|>1$ V

The Lorentzian noise observed at $V_G\geq1$ V in the linear regime shows the following features. It has been found that $S_I(0)\sim\tau$ and $S_I(0)\sim1/L^3$ at $L>0.5$ μm where $S_I(0)$ corresponds to the low-frequency plateau of a Lorentzian spectrum and τ is the Lorentzian time constant which decreases exponentially with increasing $|V_G|$ [9].

Figures 4a and 4b show the behaviour of the Lorentzian noise parameters with changing V_{DS}. As is seen from Fig. 4a, curves 1 and 2, an increase of τ and $S_I(0)$ with increasing drain voltage takes place in the linear regime. As a result, the low-frequency Lorentzian plateau in the noise spectra becomes shorter and higher (Fig. 4b). However, the value of $S_I(0)/\tau(V_{DS})^2$ does not change with changing V_{DS} (Fig. 4a, curve 3).Therefore, $S_I(0)$ can be described by the formula $S_I(0)=B\tau(V_{DS})^2/L^3$ where B is a coefficient.

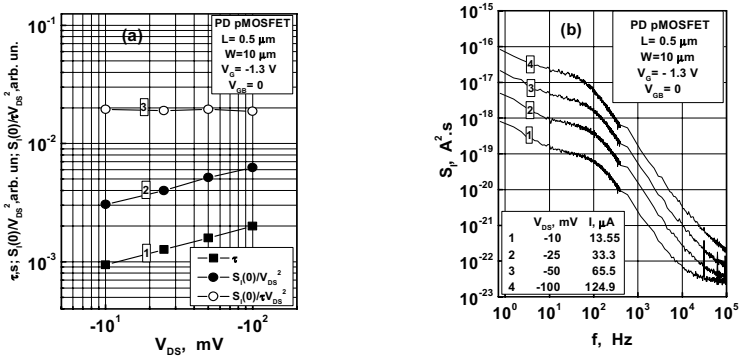

Figure 4. Influence of the drain voltage on Lorentzian noise parameters in a linear regime (a) and the noise spectra measured at V_G=-1.3 V and 10 mV≤$|V_{DS}|$≤100 mV in the PD pMOSFET

The value of B appears to be different in devices of different types. This is shown in Fig. 5. As is seen, the PD nMOSFETs are characterized by higher values of B than the PD pMOSFETs and Fully Depleted (FD) nMOSFETs, namely: $(B_n)_{PD}$=(2 to 3)×10^{-25} S^2cm^3; $(B_p)_{PD}$=1×10^{-25} S^2cm^3 (Fig. 5a) and $(B_n)_{FD}$=(0.7 to 2)×10^{-25} S^2cm^3(Fig. 5b). It is also derived from Fig. 5b that for FD devices, B increases when applying an accumulation back-gate voltage.

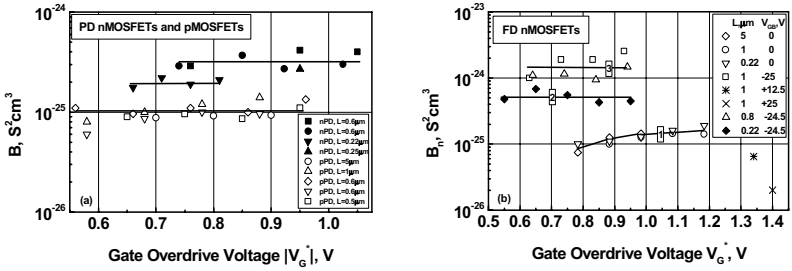

Figure 5. Coefficient B in function of V_G^* for PD n- and pMOSFETs (a) and FD nMOSFETs (b)

It has been revealed that the overdrive voltage is the important factor determining the value of τ. The dependences of τ on V_G^* can be experimentally described by τ~exp(-γ|V_G^*|) where γ=(12 to 14) V^{-1}. This is demonstrated in Fig. 6. It follows from Fig. 6 that another important feature of τ is that its values measured at a given overdrive voltage in the different device types are different, namely: $(\tau_n)_{PD} \approx (\tau_n)_{FD} > [(\tau_n)_{FD}]_{ac} \geq (\tau_p)_{PD}$ where $[(\tau_n)_{FD}]_{ac}$ refers to FD nMOSFETs with the back interface in accumulation.

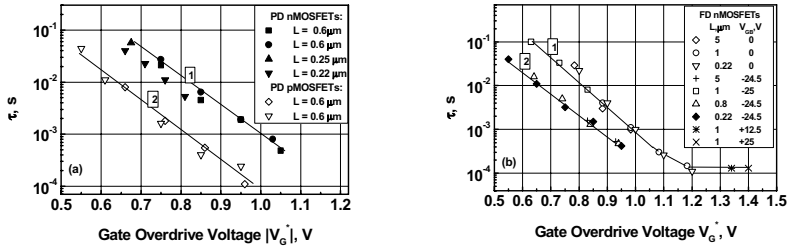

Figure 6. Lorentzian time constant τ vs overdrive voltage for the PD n- and pMOSFETs (a) and FD nMOSFETs (b)

From the above it can be concluded that the Lorentzian noise considered correlates very well with the linear kink effect (LKE) in the transconductance [3]. Both effects occur in the same gate voltage range and

are more pronounced in PD than in FD devices where both effects are enhanced by an accumulation voltage at the back gate. Such a correlation suggests that the electron valence-band (EVB) tunneling through the thin gate oxide starting at $|V_G| \approx 1$ V and giving rise to a majority carrier current I_T into the silicon film is responsible for both the LKE and the Lorentzian noise considered.

In the model proposed it is assumed that the shot noise associated with the injection of majority carriers in the body generates fluctuations in the body potential V_{BS} across the dynamic resistance of the forward biased source-body junction [9]. This will in turn lead to fluctuations in the threshold voltage and finally in the channel current, by taking account of the transconductance. In other words: $S_I=(\partial I/\partial V_{th})^2(\partial V_{th}/\partial V_{BS})^2 S_{VBS}=(g_m\beta)^2 S_{VBS}$ where $\beta=\partial V_{th}/\partial V_{BS}$ and S_{VBS} is the spectral density of the body potential fluctuations. Due to the impedance of the source-body junction, the resulting spectrum of the shot noise is Lorentzian with a time constant τ determined by the parallel connection of the differential resistance r_j of the source-body junction and the equivalent capacitance C of the order of the gate capacitance: $\tau=r_jC$ where $r_j=(mkT/qI_T)$, $C=ZLC_0$, $I_T=WLj_T$ where m is the ideality factor of the gated source-film junction, j_T is the density of current due to the EVB tunneling through the gate oxide. Combining this, one has:

$$\tau=(mkT/qj_T)C_0 \tag{4}$$

$$S_I(0)=2qI_T(r_j)^2\beta^2(g_m)^2=2\tau mkTC_0Z(\mu_{n,p})^2\beta^2(V_{DS})^2m_g^2/L^3 \tag{5}$$

where $g_m= m_g[\mu_{n,p}ZC_0V_{DS}/L]$ is used where the coefficient $m_g>1$ is introduced to take into account the linear kink effect.

Since j_T enhances with increasing gate voltage, the value of τ described by Eq. (4) has to decrease with increasing $|V_G|$. Exactly such a behaviour of τ with $|V_G|$ is observed in our experiments.

As is seen, Eq. (5) explains the dependences of $S_I(0)$ on τ, L and V_{DS} observed experimentally. It can also be shown that the values of $S_I(0)$ predicted by Eq. (5) are in reasonable agreement with the experimental data observed in PD MOSFETs. Therefore, the model based on EVB tunneling through the thin gate oxide gives a good explanation of the main experimental results.

4. Conclusions

The reason for both noise components considered above is the ultra-small thickness of the gate oxide. The fact that in such a case the traps associated with the polysilicon gate/oxide interface are sufficiently close to the channel (so that electron tunneling between those traps and the channel is effective) is responsible for the low-frequency $1/f^{1.7}$ noise component. EVB

tunneling through an ultra-thin gate oxide gives rise to a Lorentzian noise component. Therefore, the $1/f^{1.7}$ noise and the Lorentzian noise described can be regarded as thin-oxide noise effects.

References

[1] N. Lukyanchikova, M. Petrichuk, N. Garbar, E. Simoen, A. Mercha, H. van Meer, K. De Meyer and C. Claeys, On the origin of the $1/f^{1.7}$noise in deep submicron partially depleted SOI transistors, Proc. ESSDERC 2002, eds. G. Baccarani, E. Gnani and M. Rudan, The University of Bologna (Italy) (2002) 75-78.

[2] N. Lukyanchikova, M. Petrichuk, N. Garbar, E. Simoen, A. Mercha, C. Claeys, H. van Meer and K. De Meyer, The $1/f^{1.7}$ noise in submicron SOI MOSFETs with 2.5 nm nitrided gate oxide, IEEE Trans. Electron Devices **49** (2002) 2367-2370.

[3] A. Mercha, J. M. Rafi, E. Simoen, C. Claeys, N. Lukyanchikova, M. Petrichuk, N. Garbar, Evidence for a "linear kink effect" in ultra-thin gate oxide SOI n-MOSFETs, in Proc. of the Eleventh Int. Symposium on Silicon-on-Insulator Technology and Devices XI, Eds S. Cristoloveanu, G. K. Celler, J. G. Fossum, F. Gamiz, K. Izumi and Y.-W. Kim, The Electrochem. Soc. Ser. PV **2003-05** (2003) 319-324.

[4] E. Simoen, M. Da Rold, C. Claeys, N. Lukyanchikova, M. Petrichuk and N. Garbar, Flicker noise in submicron MOSFETs with 3.5 nm nitrided gate oxide, in Proc. ICNF '2001, Ed. G. Bosman, World Scientific (Singapore) (2001) 177-180.

[5] K. M. Chang, Y. H. Chung, T. C. Lee and Y. L. Sun, A method to characterize n^+-polysilicon/oxide interface traps in ultrathin oxides, Electrochem. and Solid-State Letters **4** (2001) G47-G49.

[6] R. Jayaraman and C. G. Sodini, A 1/f noise technique to extract the oxide trap density near the conduction band edge of silicon, IEEE Trans. Electron Devices **36** (1989) 1773-1782.

[7] R. R. Siergiej, M. H. White, and N. S. Saks, Theory and measurement of quantization effects on Si-SiO_2 interface trap modeling, Solid-St. Electron., 35 (1992) 843-854.

[8] E. Simoen and C. Claeys, On the flicker noise in submicron silicon MOSFETs, Solid-St.Electron. **43** (1999) 865-882.

[9] N. B. Lukyanchikova, M. V. Petrichuk, N. Garbar, A. Mercha, E. Simoen and C. Claeys, Electron Valence Band tunneling-induced Lorentzian noise in deep submicron Silicon-on-Insulator Metal-Oxide-Semiconductor Field-Effect Transistors, J. Appl. Phys., **94** (2003) 4461-4469.

LOW FREQUENCY NOISE STUDIES OF Si NANO-CRYSTAL EFFECTS IN MOS TRANSISTORS AND CAPACITORS

S. Ferraton[1], L. Montès, I. Ionica and J. Zimmermann

Institut de Microélectronique Electromagnétisme et Photonique,
UMR CNRS 5130, ENSERG-INPG,
23 rue des Martyrs, BP 257, 38016 Grenoble Cedex 1
France

J. A. Chroboczek[2]

DTS/LETI CEA-Grenoble,
17 rue des Martyrs, 38054 Grenoble Cedex 9
France

[1] ferraton@enserg.fr

[2] Jan.chroboczek@cea.fr

Abstract Recent developments in the novel generation of Non Volatile Memories (NVM) containing a plane of Si nano-crystals (Si-nc), embedded in the gate oxide MOS transistors, created a need for a better understanding of the basic physics of the charge/release phenomena on the Si-nc's. Such studies are also important because the expected retention time is interesting for practical memory applications. Here, for the first time to our knowledge, low frequency noise (LFN) studies on MOS capacitors and transistors with the Si-nc's are presented. The results obtained in the structures with and without Si-nc's are compared. The implication of the Si-nc's in the LFN generation and charge dynamics in the devices are discussed.

Keywords: Non Volatile Memory, MOS Transistors, Si Nano-Crystals, LF noise

1. Introduction

Physical limitations for the scaling of CMOS devices below 10 nm create a need for research on novel structures of even smaller dimensions. The single electron transistor, SET, is one example of such devices. In this

J. Sikula and M. Levinshtein (eds.),
Advanced Experimental Methods for Noise Research in Nanoscale Electronic Devices (137 - 144)

paper we discuss MOS transistors and capacitors with oxides containing a 2D layer of silicon nano-crystals, Si-nc's, acting as nodes for charge retention in the non volatile memory, NVM, devices [1]. The objective of this work is to use low frequency noise, LFN, technique for studying the dynamics of electric charge/release phenomena on Si-nc's. Although these devices have already been studied [2,3], to our knowledge, no results on their LFN properties have been reported.

2. Devices

The devices studied are MOS capacitors and FETs with a 2D layer of Si-nc's in the dielectric. Control samples without Si-nc are also used as a reference. The devices have been fabricated in the framework of the PLATO technological platform at the LETI-CEA in Grenoble. The Si-nc's were fabricated by Low Pressure Chemical Vapor Deposition (LPCVD) over a variety of thin, tunnel thermal oxides (0.8 to 2.5 nm thick), grown on B-doped ($3\text{-}4\times10^{17}\text{cm}^{-3}$) substrates. The Si-nc layer were then encapsulated with a non-annealed LPCVD High Thermal Oxide (HTO). An N^+ poly-Si gate was then deposited over the HTO. The typical size of the Si-nc's was 5nm (with a dispersion of 1 nm) and their density about $4\times10^{11}\text{cm}^{-2}$ [1].

3. Studies of MOS Capacitors

3.1. Experiments

In the case of the capacitors, the power spectral densities, PSD, of fluctuations in the current, I, passing across the capacitor (leakage current) was measured with an HP 35665A analyzer. The measurements were carried out at the room temperature. In order to obtain an evaluation of the average quadratic current fluctuations $<\Delta I^2>$ in the capacitor, we integrated the PSD in the frequency range used, and then normalized the result by dividing it by I^2. The number of noise generating centers, N, active in the frequency range involved, is then

$$N = \frac{I^2}{\langle \Delta I^2 \rangle} \tag{1}$$

3.2. Results and discussion

The measurements were carried out on the devices with and without Si-nc's and compared. An example of such a comparison is shown in Fig. 1. The fluctuations measured on the capacitor leakage current was analysed in a rather low frequency range, $0.0625\text{Hz} < f < 25$ Hz. The PSD spectra follow the

$1/f^{\alpha}$ with $0.65<\alpha<0.75$ in the structures with Si-nc's, whereas in the structures without Si-nc $1.03<\alpha<1.36$. Figure 1 shows that, at sufficiently high currents, the PSD of current fluctuations varies as I^2.

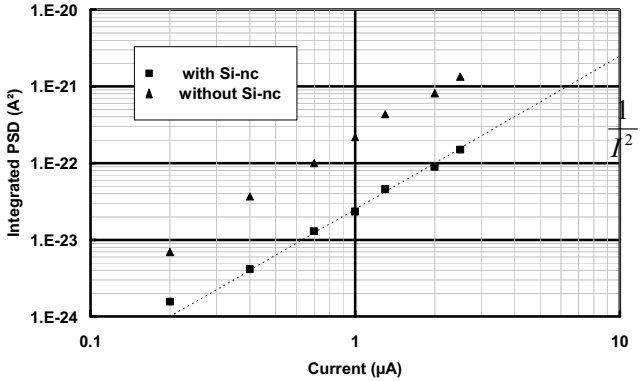

Figure 1. Comparison of average quadratic noise current fluctuations in capacitors with (squares) and without (triangles) Si-nc's. Device area is 0.24 mm^2.

The 1/f general behaviour revealed in the spectra and the proportionality of the PSD to I^2 imply that the noise is generated by a large number of evenly distributed centres with rather slow response times. At f=100Hz or higher, depending on the current, the measured PSD was observed to deviate from the 1/f-type dependence. This issue is still under study. Supposing that the active centres are independent of each other, the number of the active centres in the frequency range of interest, can be calculated using Eq. (1). The result is shown in Fig. 2, as a function of I.

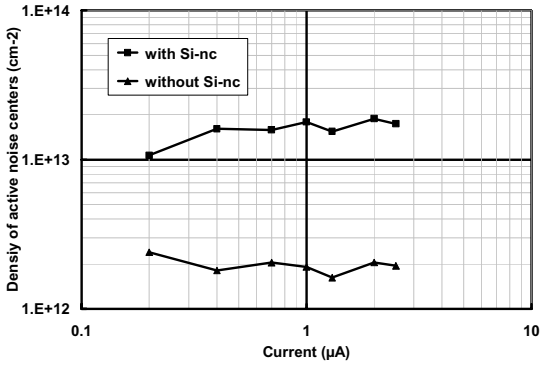

Figure 2. Density of active noise centers in capacitors with (squares) and without (triangles) Si-nc's.

The difference between the results obtained on control devices and those with Si-nc's is significant. In fact, the large number of noise centres is

attributed to high density of traps present in the non-annealed HTO layer and at the interface between the thermal oxide and the HTO. The presence of Si-nc's at this interface increases the number of traps by a factor of 5 to 10.

As the fluctuations are analyzed in a leakage current flowing through both oxides and the Si-nc's, the response incorporates all the effects of all the traps present, including the contributions due to Si-nc's. However, the main contribution comes from the traps located in the HTO cap layer.

4. Studies of NMOS Transistors

4.1. Experiments

We studied MOSFETs with the gate area (L×W)=1x10 μm^2 and 0.8nm - thick tunnel thermal oxide, T1, using the frequency range between 1Hz and 5kHz. The PSD of the drain current, I_d, fluctuations was measured at V_D=50mV, as a function of the gate voltage, V_g. In this study, experiments were performed on devices with and without Si-nc's, using an automatic LFN measuring system [4].

4.2. Results and discussion

The PSD of I_d fluctuations was found to follow the 1/f dependence in both types of devices. In Fig. 3 we plot the PSD extracted at 10Hz, normalized by I_d^2 *versus* I_d. The data for both types of devices could be interpreted using Eq. (2) based on McWhorter [5] approach. The term in parentheses is derived assuming that the charge fluctuation in the insulator can also induce a fluctuation in the mobility of the inversion layer carriers and thus a fluctuation of the drain current (correlated LFN).

$$\frac{S_{id}}{Id^2} = \left(1 + \alpha_c \mu_0 Cox \frac{Id}{g_m}\right)^2 \frac{{g_m}^2}{Id^2} S_{V_{FB}} \qquad (2)$$

The parameters α_c and Sv_{FB} are adjusted to fit of the experimental data. Sv_{FB} contains the bulk density of the active noise centers, N_t. Using the McWhorter's expression for Sv_{FB} and the tunneling constant λ=0.1nm, we calculate the N_t values for both types of devices. We find $N_{t1}=1.2\times10^{18}$/eV/cm^3 for devices with Si-nc's and $N_{t2}=4.8\times10^{17}$/eV/cm^3 for devices without the Si-nc's. The surface density of the Si-nc's is then of the order of magnitude of $(N_{t1})^{2/3}-(N_{t2})^{2/3}= 5\times10^{11}$/eV/cm^2. This value is in a good agreement with those estimated previously by the SEM (Scanning Electrical Microscopy) and electrical measurements [2,3].

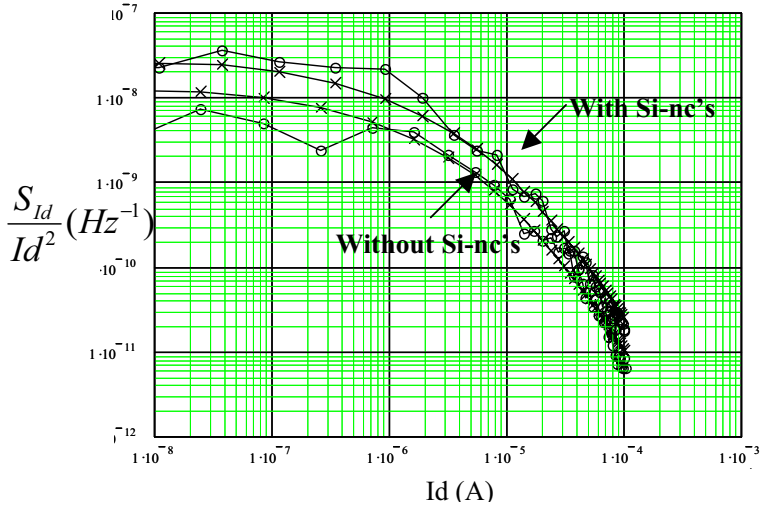

Figure 3. Comparisons theory-experiment: Sid/Id^2 vs. Id for devices with and without Si-nc's (experiment: circles, theory: crosses), T1=0.8nm

5. 1/f$^{\alpha}$ noise dependence (α >1.2) for "Si-nc devices" with a higher tunnel oxide thickness

5.1. Results and discussions

Experiments similar to those described in §4 were carried out on devices with a tunnel thermal oxide thickness of 1.5nm. Figure 4 shows the PSD of the drain current measured on devices with and without Si-nc's for I_d = 60µA.

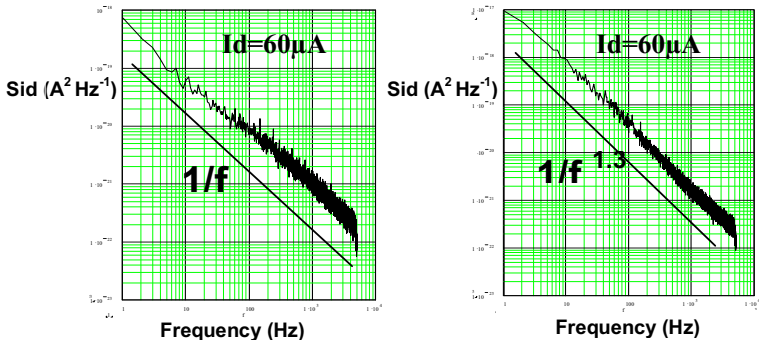

Figure 4. PSD of the drain current for devices without Si-nc's (left) and with Si-nc's (right) T1=1.5nm; Id=60µA

In the devices without Si-nc's, the PSD varies like 1/f in the frequency range defined above, whereas for the devices with Si-nc's a significant deviation from 1/f behavior is observed. In the structure with Si-nc's, the PSD behaves like $1/f^{\alpha}$ with α=1.3. For this reason, the analysis involving the Mc Whorter's formalism was not possible. We also observed an increase of S_{Id}/I_d^2, extracted at 10Hz for higher drain current values (see Fig. 5). Similarly, in devices with Si-nc's, deposited on a 2nm thick thermal oxide, we observed that PSD followed the $1/f^{1.5}$ dependence for 1Hz ≥f ≥100Hz at comparable I_d values. For higher frequencies, up to 5kHz, PSD decreased as 1/f. On the other hand, all reference samples showed the 1/f behavior in the entire frequency range explored.

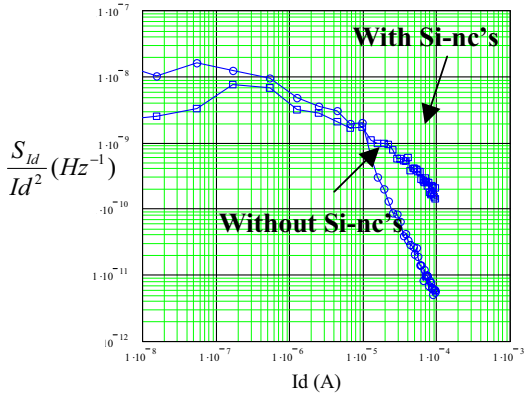

Figure 5. Sid/Id^2 vs. Id for devices with (squares) and without (circles) Si-nc's; T1=1.5nm

6. Discussion

In this work we studied devices with Si-nc's located at a relatively small distance form the interface, 0.8nm and larger, 1.5 nm. For the former, a standard approach, assuming a uniform distribution of background traps and Si-nc was possible and the results were interpreted in terms of the McWhorter theory [5]. The Si-nc's densities thus estimated were close to the values obtained from the SEM observations. However, when the thermal oxide separating the channel from the Si-nc's layer was thicker, we observed $1/f^{\alpha}$ dependence, with $\alpha \geq 1.2$. One can propose various explanations for such a behavior, related to the non-uniform volume or energy distribution of noise generating centers. For instance, the size dispersion of the Si-nc's, estimated to be 1 nm (around 5 nm) affects the energy level structure inside the Si-nc's that may lead to a non-uniform energy distribution, in which case, the

resulting LF noise PSD would behave like $1/f^{\alpha}$ [6]. A non-uniform energy distribution may also originate from a random crystallographic orientation of the Si-nc's. Furthermore, as the Si-nc's are not uniformly distributed in the oxide, having an almost planar distribution, deviations from the 1/f type spectral dependence are expected [7]. For example, the $1/f^{\alpha}$ dependence is obtained, with $1<\alpha<2$, when the trap density increases exponentially with the distance from the interface. In the devices without Si-nc, the traps responsible for the LF noise should have a more uniform energy and spatial distribution. In that case LF noise PSD would be closer to 1/f ; this is what we observed. As a matter of fact, special models need to be developed. A possible starting point for tackling the problem is illustrated in Fig. 6.

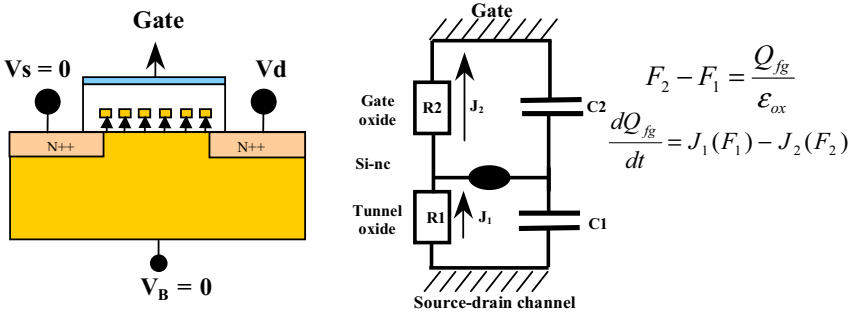

Figure 6. Cross sectional schematic view of a TMOS containing 2D layer of Si-nc's and the associated equivalent electrical circuit.

The set of the two equations in Fig. 6, (Gauss's law and current continuity) is now commonly used in the domain of floating gate memory analysis [8]. The charging/release of the Si-nc's by electrons flowing from/to the substrate generate the fluctuations in the current J_1, inducing fluctuations in I_d. A closer examination of time recordings of I_d at various gate voltages lead us to the conclusion that the signal is stationary. Therefore, the time derivative in Fig. 6 vanishes for the average current density, but not for the fluctuations. As J_1 is a tunnel current and thus depends exponentially on the electric field in the oxide and on the oxide thickness, it may induce significant fluctuations of the flat band voltage. However, more work is needed to develop this approach in detail.

In conclusion, comparing the LF noise data taken on MOS transistors and capacitors, with and without Si-nc's, we could identify the features originating from the presence of the Si-nc's in the structures. This study, being the first in this domain, is rather qualitative. More data, on improved structures (annealed HTO, and devices with varied Si-nc's densities) should provide a better understanding of the physics of the charging/release

phenomena on Si-nc's and lead to a more qualitative description of the device functioning.

Acknowledgements

This research was carried at the Centre de Projets en Microélectronique Avancée located at PLATO-LETI, CEA of Grenoble. Financial support from the Région Rhône-Alpes is also acknowledged.

References

[1] T. Baron, F. Martin, P. Mur, C. Wyon and M. Dupuis, Silicon Quantum Dot Nucleation on Si_3N_4, SiO_2 and SiO_xN_y Substrates for Nanoelectronic Devices, J. Crystal Growth, **290** (2000) 1004-1008.

[2] S. Ferraton, L. Montès, J. Zimmermann and A. Souifi, Evidence of charging effect in silicon nano-crystals using a feedback charge method with metal oxide-semiconductor capacitors, Nanotechnology **14** (2003) 633-636.

[3] S. Ferraton, L. Montès, A. Souifi and J. Zimmermann, Evidence of Room Temperature Charging Effects in Discrete Floating Gate Single Electron Memory Using the Feedback Charge Method, Microelectronic Engineering **67-68** (2003) 858-864.

[4] J.A. Chroboczek, Automatic, Wafer-level, Low Frequency Noise Measurements for the Interface Slow Trap Density Evaluation, in ICMTS-2003 Technical Digest p. 95, IEEE. No. 03CH37417.

[5] A. L. McWhorter, in 1/f noise and Ge Surface Properties, R.H. Kingston, Edit. (1957), p. 207ff.

[6] Z. Celik-Butler and T.Y. Hsiang, Spectral Dependence of $1/f^{\gamma}$ Noise On Gate Bias in N-MOSFET, Solid-State Electronics, **30** (4) (1987) 419-423.

[7] F. Berz, Theory of Low Frequency Noise In Si MOST'S, Solid-State Electronics, **13** (1969) 631-647

[8] B. De Salvo, G. Ghibaudo, G. Pananakakis, P. Masson, T. Baron, N. Buffet, A. Fernandes, B. Guillaumot, Experimental and theoretical investigation of nano-crystal and nitride-trap memory devices, IEEE Trans. Electron Devices, **48** (2001) 1789-1799.

NOISE MODELLING IN LOW DIMENSIONAL ELECTRONIC STRUCTURES

L. REGGIANI
INFM - NNL, Dipartimento di Ingegneria dell' Innovazione
Universitá di Lecce, Via Arnesano s/n, 73100 Lecce
Italy
lino.reggiani@unile.it

V.Ya ALESHKIN
Department Semiconductor Physics, Institute for Physics of Microstructures
603950, Nizhny Novgorod, GSP-105
Russia
aleshkin@ipm.sci-nnov.ru

A. REKLAITIS
Semiconductor Physics Institute
Goshtauto 11, LT2600 Vilnius
Lithuania
reklaitis@uj.pfi.lt

Abstract We investigate electron transport and shot noise in single and double barrier GaAs/GaAlAs semiconductor structures. Both structures evidence shot noise enhancement and suppression. The enhanced mechanism is due solely to the positive feedback between tunneling and space charge, and it is a precursor of current instability. Concerning the suppression mechanism, the standard sequential tunneling model does not explain a suppression with a Fano factor below 0.5, which is found in several experiments. By contrast the coherent tunneling model predicts shot noise suppression below 0.5 because of Pauli principle and/or Coulomb interaction in agreement with experiments. We conclude that shot noise suppression below one-half of the full Poissonian value is a signature of coherent tunnelling against sequential tunneling in double barrier resonant diodes.

Keywords: Coherent tunneling, Fano factor, heterostructure, mesoscopic, Monte Carlo, resonant tunneling, shot noise.

J. Sikula and M. Levinshtein (eds.),
Advanced Experimental Methods for Noise Research in Nanoscale Electronic Devices (145 - 152)

1. Introduction

Shot-noise is the electrical fluctuation due to the discreteness of the charge that provides direct information on the correlation of different current pulses crossing a device. As such, its determination is of basic complement to a current voltage (I-V) measurement. A convenient analysis of shot-noise is usually performed through the Fano factor $\gamma \geq 0$ defined as $\gamma = S_I(0)/(2qI)$, $S_I(0)$ being the spectral density of current fluctuations at low frequency, and q the elementary quantum of charge determining I (For a recent review see Ref. [1]. In the absence of correlation between current pulses it is $\gamma = 1$, and this case

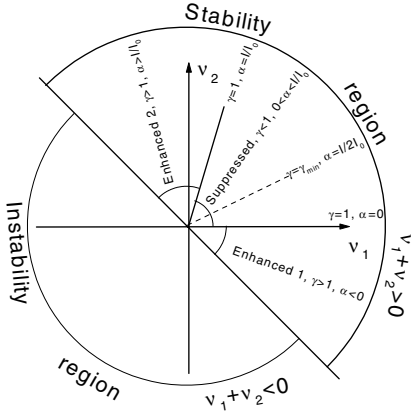

Figure 1. Lifetime plane of different transport regimes and shot-noise behaviors of a two terminal device with current controlled by number of particles in it under high voltages when $g_2 = 0$. I_0 is the emitter injection current.

corresponds to full shot-noise. Deviations from this ideal case is a signature of existing correlations between different pulses and the two possibilities of suppressed (i.e. $\gamma < 1$) and enhanced (i.e. $\gamma > 1$) shot-noise are possible, as confirmed by experiments. Here we present recent theoretical investigations concerning shot noise suppression and enhancement in single and multiple barrier diodes made by semiconductor heterostructures [2, 3, 4, **?**, 6]. The results are obtained by different approaches based on sequential and coherent tunneling models as well as Monte Carlo (MC) simulations.

2. Sequential tunneling approach

In this approach the steady current is governed by four rates, denoted as $g_{1,2}$, $r_{1,2}$, describing the income or generation (outcome or recombination) of

carriers from the contacts into (out) the active region of the device under test (DUT) as (henceforth CGS system and unit contact area is used):

$$I = -q(g_1 - r_1) = -q(r_2 - g_2) \tag{1}$$

From the above four rates, two differential rates, denoted as $\nu_{1,2}$, can be constructed. These describe the decay of the carrier number fluctuations in the DUT through the contact interfaces 1 and 2. We note that the g, r are positive definite quantities, while the ν can be positive (damping of fluctuation) or negative (enhancement of fluctuation). The spectral density of current fluctuations at low frequency takes the form:

$$S_I = 2q^2 \frac{[\nu_2^2(g_1 + r_1) + \nu_1^2(g_2 + r_2)]}{(\nu_1 + \nu_2)^2} \tag{2}$$

When the applied voltage is high enough to neglect g_2, so that shot noise regime is achievable, by defining $\alpha = \nu_2/(\nu_2 + \nu_1)$, the Fano factor becomes:

$$\gamma = 1 - 2\alpha + 2\alpha^2 \frac{g_1}{r_2} \tag{3}$$

The scenario for the values of the Fano factor is illustrated in Fig. 1.

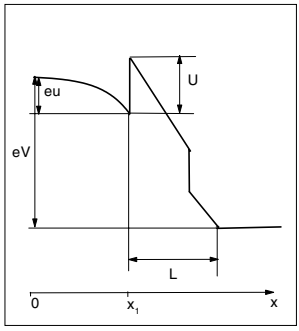

Figure 2. Sketch of the band diagram of the single barrier structure considered here. Contact resistance at the terminals is neglected for simplicity.

Let us consider a single barrier structure, as depicted in Fig. 2. The theory concerns with a model material (GaAs like) of static dielectric constant $\kappa = 12.95$ and parabolic conduction band with effective mass $m = 0.067$. For a given temperature T and voltage V the theory is based on three parameters, respectively the contact carrier concentration n_b, the probability of non-scattering β associated with the motion of ballistic particles from the emitter, and the length of the DUT L.

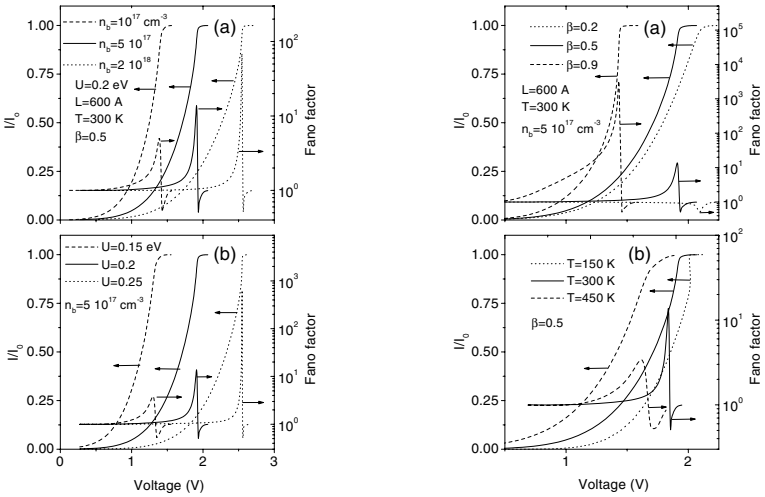

Figure 3. Left part (lp) - Current voltage characteristics and Fano factors for the barrier structure in Fig. 3 for different n_b (a) and different U (b). Right part (rp) - Current voltage characteristics and Fano factors for the barrier structure in Fig. 3 for different β (a) and for different T (b).

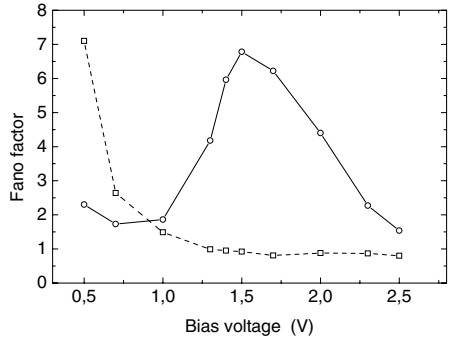

Figure 4. Fano factor vs bias voltage for the diode in Fig. 3. Continous (dashed) curves refer to a dynamic (static) Poisson solver simulation.

The typical I-V characteristic and the corresponding Fano factor is presented in Fig. 3. The current exhibits a strong super-Ohmic behavior due to tunneling processes and saturates at the injected value. Concerning the Fano factor, enhanced shot noise is related to $\nu_2 < 0$, while suppressed shot noise to the condition $\nu_1 = \nu_2 > 0$. The realistic modelling of enhanced shot noise was provided by MC simulations performed on a structure consisting of: a GaAs emitter and collector (n-doped with $n_b = 5 \times 10^{18}\ cm^{-3}$), a GaAs well

(50 nm long and n-doped with $n = 10^{16}\ cm^{-3}$), an Al(0.25)Ga(0.75)As barrier (50 nm long and undoped), and a GaAs layer (10 nm long and n-doped with $n = 10^{16}\ cm^{-3}$). Figure 4 reports the Fano factor as a function of the applied voltage. To analyze the effects of the space-charge on tunneling, calculations are performed with a dynamic (static) Poisson solver and are reported as continuous and circles (dashed and squares) curves. For the dynamic case, we found that at low voltages ($0.7 < U < 1\ V$), being the barrier transparency $D \ll 1$, very few carriers can tunnel the barrier thus the tunneling space-charge feedback is negligible and $\gamma \to 1$ as expected by simple partition noise. At intermediate voltages ($1 < U < 2\ V$) the positive feedback between space-charge and tunneling provides a systematic enhancement of shot-noise up to a maximum of $\gamma \simeq 7$ at a bias of $1.5\ V$.

For the standard symmetric double well we consider the structure reported in Fig. 5. As typical values we take the thickness of each barrier $d = 100$ Å, the energy of the resonant level as measured from the center of the potential well $\varepsilon_r = 50\ meV$ with the partial width of the resonant level due to the tunnelling through the left and right barriers $\Gamma = \Gamma_L + \Gamma_R = 5\ meV$. The case of a low temperature of $4.2\ K$ is reported in Figs. 6. Figure 6(lp) shows the current and Fig. (6rp) the Fano factor as function of the applied voltage. Practically, in the whole region of applied voltages the current is found to be determined by the flow of injected particle from the emitter, g_1. Concerning the Fano factor, we find that at the lowest voltages ($qV/k_BT < 1$) the transition from thermal to shot noise is evidenced. Then, at increasing voltages ($qV/k_BT > 1$) we find two separate regions of shot noise suppression matched by a region of full shot noise, and one region of shot noise enhancement just before. the instability condition. In Figs. 6(rp) we present a detailed analysis of the different param-

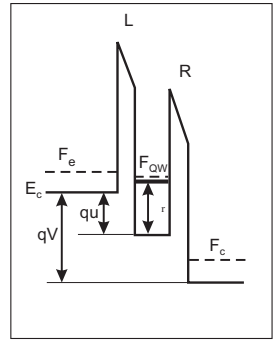

Figure 5. Sketch of the band profile of the double barrier structure considered here under typical operation conditions. Here F_e, F_{QW}, F_e are the electrochemical potential in the emitter, the quantum well and the collector regions.

eters entering the definition of γ. Figure 6 (rpa) reports α and the normalized current $I/(qg_1)$ vs the applied voltage. Figure 6 (rpb) reports the dependencies of $\nu_{1,2}$ on voltage. We can see that ν_1 exhibits a complicate structure at increasing voltages with two positive peaks in the positive differential conductance (PDC) region and one negative peak in the bistable region. By contrast, ν_2 is constant at almost all voltages implying that sooner or later tunneling from the resonant state to the collector will occur. At the smallest voltages, ν_2 decreases due to Pauli principle. At increasing voltages, the condition $\nu_1 = \nu_2$ gives $\gamma = 0.5$ in analogy with the general model of two equal resistors with shot noise sources in series. From Fig. 6(rpa) we argue that all peculiarities of the Fano factor in essence are controlled by the behavior of ν_1.

3. Coherent tunneling approach

The structure here investigated is the same double well reported in Fig. 5 with the double barrier transparency $D(\varepsilon_z)$ given by:

$$D(\varepsilon_z) = \frac{\Gamma^2/4}{(\varepsilon_z - \varepsilon_r + qu)^2 + \Gamma^2/4} \tag{4}$$

where $\varepsilon_{z,\perp}$ are the energies for electron motion perpendicular and along barriers. For the steady current it is:

$$I = -\frac{qm}{2\pi^2\hbar^3}\int_0^\infty d\varepsilon_z d\varepsilon_\perp D(\varepsilon_z)\left[f_L(\varepsilon) - f_R(\varepsilon)\right] \tag{5}$$

with $f_{L,R}$ the electron distribution in the emitter (L) and collector (R) contacts, respectively. For the spectral density of current fluctuations we found:

$$S_I = \frac{q^2 m}{\pi^2\hbar^3}\int_0^\infty d\varepsilon_\perp d\varepsilon_z \{D[q_+^2 f_L(1-f_R) + q_-^2 f_R(1-f_L)] - D^2(f_L - f_R)^2\} \tag{6}$$

with $q_\pm$ taking values in the range $\pm\infty$ the dimensionless effective charge accounting for the self-consistent potential.

Figure 7 reports the current (Fig. 7(a)) and the Fano factor (Fig. 7(b)) at $T = 0$ as function of dimensionless voltage $\xi = 2(qu - \varepsilon_r)/\Gamma$ for different values of dimensionless chemical potential $f = 2F_L/\Gamma$. Curves labelled 1, 2, and 3 correspond to $f = 1$, 15 and ∞ respectively. The current exhibits the well known peaked behavior reducing to zero at the highest voltages because we neglect resonant states above thefirst one. Of interest is the behavior of the Fano factor. The common features of all curves is the presence of a minimum of γ near to the current peak and the evidence of full shot noise in regions where the current becomes relatively small. Remarkably, the minimum value of the Fano factor is found to be always less than 0.5, taking the value 0.391

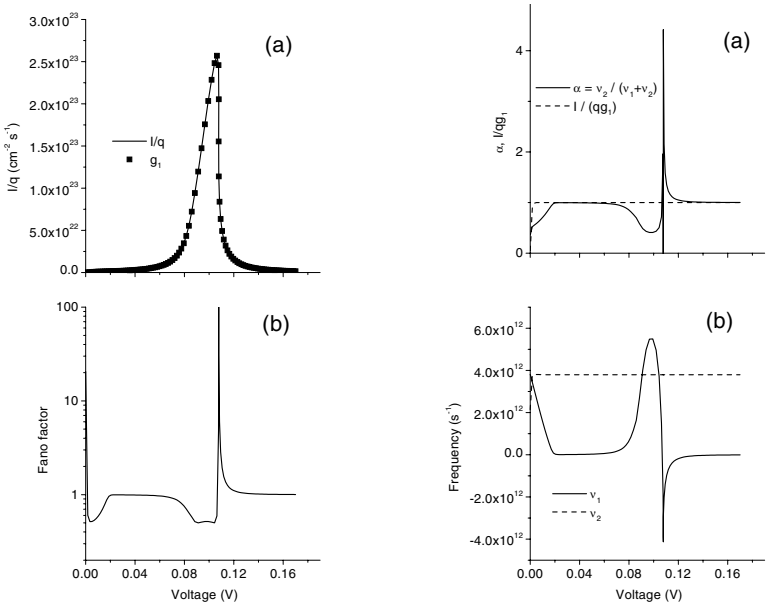

Figure 6. Left part (lp) - Current (a) and Fano factor (b) as functions of the applied voltage at $T = 4.2\ K$ and $n = 5 \times 10^{16}\ cm^{-3}$ for the barrier structure in Fig. 5. Right part (rp) - Normalized rate α and normalized current (a), and ν_1 and ν_2 (b) as functions of the applied voltage at $T = 4.2\ K$ and $n = 5 \times 1^{16}\ cm^{-3}$ for the barrier structure in Fig. 5.

at $\xi = -0.801$ for $f = \infty$ and being systematically lower than this value at decreasing value of f.

4. Conclusions

We have presented a theoretical analysis of electron transport and shot noise in ultra-short single and double barrier semiconductor structures. The mechanism of suppression can be due to Pauli principle and/or to Coulomb correlation. The mechanism of enhancement is due solely to the positive feedback between tunneling and space charge.

For coherent tunneling, we have found that around zero temperature shot noise is suppressed because of Pauli principle alone with a Fano factor minimum of 0.391 near the current peak in agreement with experiments. This giant suppression is also confirmed at 77 and 300 K. Thus, shot noise suppression below one-half of the full Poissonian value is taken as a signature of coherent tunneling against sequential tunneling in double barrier resonant diodes.

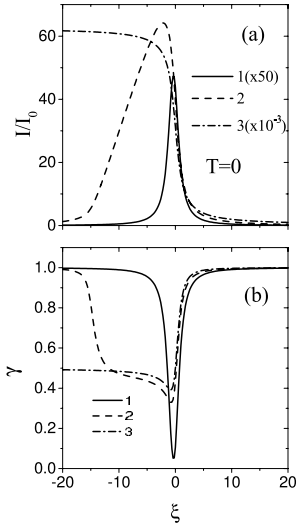

Figure 7. Dependence of current (a) and Fano factor (b) on applied voltage in a typical symmetric DBRD at zero temperature. For convenience dimensionless current and voltages are used. Here $I_0 = qm\Gamma_L\Gamma_R/(2\pi^2\hbar^3)$ and . $\xi = 2/(qu - \varepsilon_r)\Gamma$. Curves labelled as 1, 2, 3 correspond to values of the dimensionless electrochemical potentials: $f = 1,\ 15,\ \infty$ ($f = 2F_L/\Gamma$) respectively.

Acknowledgments

Partial support from the Italian Ministry of Foreign Affairs through the Volta Landau Center (the fellowship of V.Ya.A.), and the SPOT-NOSED project IST-2001-38899 of the EC is gratefully acknowledged.

References

[1] Y. M. Blanter and M. Büttiker, Phys. Rep. **336**, 1-161 (2000).
[2] A. Reklaitis and L. Reggiani, Phys. Rev. **B60**, 11683-11693 (1999).
[3] V. Aleshkin, L. Reggiani and A. Reklaitis, Semicond. Sci. Technol., **15**, 1045-1048 (2000).
[4] A. Reklaitis and L. Reggiani, Phys. Rev. **B62**, 16773-16776 (2000).
[5] V. Aleshkin, L. Reggiani and A. Reklaitis, Phys. Rev. **B63**, 085302 1-11 (2001).
[6] V. Ya. Aleshkin and L. Reggiani, Phys. Rev. **B64**, 245333 1-11 (2001).

CORRELATION NOISE MEASUREMENTS AND MODELING OF NANOSCALE MOSFETs

J. Lee and G. Bosman

Department of Electrical and Computer Engineering, University of Florida

585 NEB Gainesville, FL 32611

USA

bosman@ece.ufl.edu

Abstract A detailed study of low frequency noise drain-gate correlation in the presence of significant gate leakage current will be presented for ultrathin oxide MOSFETs. Measurements and a physical model for the correlation coefficient will be discussed. The correlation coefficient between the drain and the gate is derived on the basis of partition noise theory and the BSIM4 gate leakage current model with source-drain partition, and is in good agreement with correlation noise measurements as a function of the gate to the drain current ratio.

Keywords: MOSFET, noise correlation, low frequency

1. Introduction

Correlation noise measurements at low frequencies have been previously presented for bipolar transistors [1], and the influence of the gate leakage current on the high frequency noise performance was investigated for MESFET's and MODFETs [2]. To date, no detailed study of low frequency correlation and noise performance in the presence of gate leakage current has been given for ultrathin oxide MOSFETs.

In this paper, a comprehensive noise characterization at low frequencies is presented. The correlation coefficient is derived on the basis of partition noise theory [3] and the BSIM4 gate leakage current model with the source-drain partition [4], and is compared with correlation noise measurements carried out as a function of the gate to drain current ratio. It is shown that accurate modeling and understanding of the physical noise sources at low frequencies are indispensable for optimum designs of ultrathin oxide MOS devices and circuits.

J. Sikula and M. Levinshtein (eds.),
Advanced Experimental Methods for Noise Research in Nanoscale Electronic Devices (153 - 160)

2. Theory

In a direct tunneling gate oxide MOSFET, a gate leakage current component I_g exists besides the drain current component I_d. The ratio of gate leakage current to drain current, I_g/I_d, decreases approximately in proportion to the square of channel length, L^2 and typically lies between 1 and 10^{-6}, depending on channel length [5]. As shown in Fig. 1, the source current I_s is partitioned into I_d flowing to the drain with a partition factor λ, and I_g flowing to the gate with a partition factor (1- λ). The average value of the partition factor λ represents the probability that electrons arrive at the drain. The drain current noise $S_{I_d}^{LF}(f)$, the gate leakage current noise $S_{I_g}^{LF}(f)$ and the cross noise spectrum $S_{I_dI_g}^{LF}(f)$ at low frequencies are given by [3]

$$S_{I_d}^{LF}(f)=\left(\frac{1}{1+\lambda_p}\right)^2\cdot S_{I_s}^{LF}(f)+\left(\frac{1}{1+\lambda_p}\right)\cdot S_{I_g}^{LF}(f) \tag{1a}$$

$$S_{I_g}^{LF}(f)=\left(\frac{\lambda_p}{1+\lambda_p}\right)^2\cdot S_{I_s}^{LF}(f)+\left(\frac{1}{1+\lambda_p}\right)\cdot S_{I_g}^{LF}(f) \tag{1b}$$

$$S_{I_dI_g}^{LF}(f)=\frac{\lambda_p}{(1+\lambda_p)^2}\cdot S_{I_s}^{LF}(f)+\left(\frac{1}{1+\lambda_p}\right)\cdot S_{I_g}^{LF}(f) \tag{1c}$$

with

$$S_{I_s}^{LF}(f)=\frac{1+\lambda_p}{1-\lambda_p}\left[S_{I_d}^{LF}(f)-S_{I_g}^{LF}(f)\right] \quad \text{and} \quad \lambda_p=\frac{I_g}{I_d}=\frac{1-\lambda}{\lambda} \tag{2}$$

where $S_{I_s}^{LF}(f)$ is the source current noise before partitioning into the drain and the gate.

The cross correlation coefficient at low frequencies between the drain and the gate current noise is defined as

$$C^{LF}(f)=\frac{S_{I_dI_g}^{LF}(f)}{\sqrt{S_{I_d}^{LF}(f)\cdot S_{I_g}^{LF}(f)}} \tag{3}$$

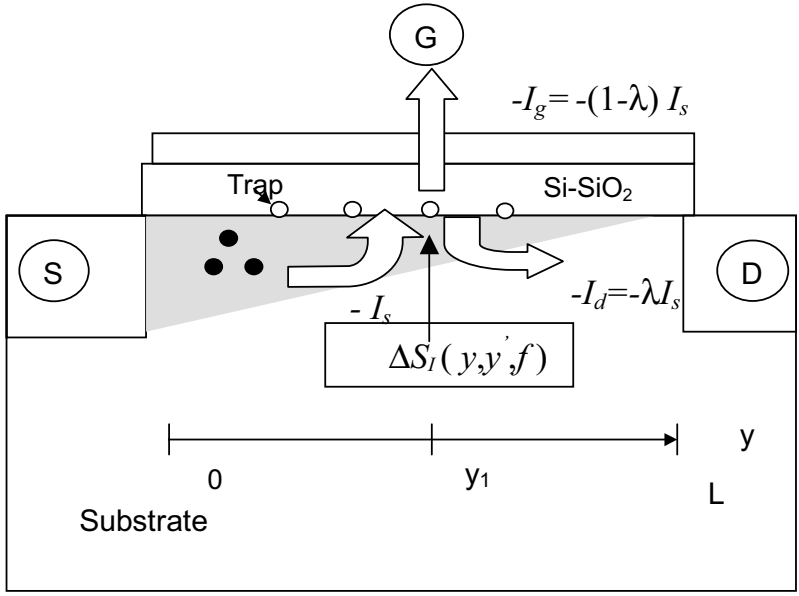

Figure 1. Noise current components in an ultrathin oxide MOSFET. I_s is partitioned into I_d with a partition factor λ, and into I_g with a partition factor (1- λ).

For the evaluation of the correlation function at low frequencies, it is necessary to obtain a physical model for the spectral densities. Under the assumption that at low frequencies both the drain and gate noise are caused by a random trapping-detrapping of carriers in localized trap states near the Si-SiO_2 interface, we can use the Klaassen's formula for the $1/f^{\gamma}$ noise current generator at y and y' along the channel [6]

$$\Delta S_{I_{d,g}}^{LF}(y, y', f) = H^{d,g}(y) \cdot \frac{I^2}{f^{\gamma_{d,g}}\, g(V_i(y))}\, \delta(y - y') \qquad \text{for} \quad i = 0,1 \qquad (4)$$

where δ(y) is a delta function, H(y) the local noise source modeling the trap efficiency, $g(V_i)$ the channel conductance per unit length at y, $V_0(y)$ the channel voltage at y, and $V_1(y)$ the perturbation voltage induced by the gate leakage current ($V_0(y) >> V_1(y)$). If the noise source is distributed uniformly over the range $0 < y < y_1$, the noise spectrum ratio may be represented by

$$\frac{S_{I_g}^{LF}(f)}{S_{I_d}^{LF}(f)} = \frac{\frac{1}{L^2}\int_0^{y_1}\int_0^{y_1} H^g(y)\frac{I_g^2}{f^{\gamma_g} g(V_1(y))}\delta(y-y')dydy'}{\frac{1}{L^2}\int_0^{y_1}\int_0^{y_1} H^d(y)\frac{I_d^2}{f^{\gamma_d} g(V_0(y))}\delta(y-y')dydy'} \quad (5)$$

where L is the effective channel length. Assuming $H^g(y) = H^d(y)$ and carrying out the integration [7],

$$\frac{S_{I_g}^{LF}(f)}{S_{I_d}^{LF}(f)} = \lambda_p \cdot \frac{V_1(y_1)}{V_0(y_1)} \cdot f^{(\gamma_d - \gamma_g)} \quad (6)$$

3. Measurements

The MOS transistors studied were fabricated using a manufacturable remote plasma nitrided oxide (RPNO) process. About 2.0 – 2.5 *nm* of gate oxide was grown with rapid-thermal based processes. N_2-plasma nitridation was performed at room-temperature by exposing the gate oxide to a remote helicon-based nitrogen discharge, and then followed by post-nitridation annealing. Devices were fabricated with standard processing techniques on p-Si substrate with n^+ poly-Si gates, using LOCOS isolation to define the active regions. A 270 nm undoped poly-Si gate layer was deposited and P was implanted (5.0×10^{15} cm^{-2}, 45 keV) for n^+ gates.

Prior to noise correlation measurements, all devices were examined for the drain and gate leakage current by measurements of *I-V* characteristics. The gate leakage current in the direct tunneling regime is not negligible, and the ratio of gate current to drain current ranges from ~ 10^{-4} to ~ 10^{-2} for nMOSFETs with $W = 10$ μm, $L = 10$ μm, and $t_{ox} = 2.2$ nm.

Noise correlation measurements were performed using a HP3582A double channel spectrum analyzer in the frequency range 1 Hz to 25 kHz. Brookdeal 5004 low-noise voltage amplifiers were used for both the drain and gate current noise measurement. The voltage noise at the gate and the drain of MOS transistors in a common-source configuration are simultaneously obtained, allowing cross correlation noise acquisition. The drain current noise $S_{I_d}(f)$ and gate current noise $S_{I_g}(f)$ are directly measured at the drain and gate of the device, and the cross noise spectrum $S_{I_d I_g}(f)$ is determined from the cross correlation coefficient and noise measurements. Fig. 2 shows a typical drain, gate, and their cross noise spectrum measured at $I_d = 9.0\times10^{-5}$ A and $I_g = 6.5\times10^{-7}$ A.

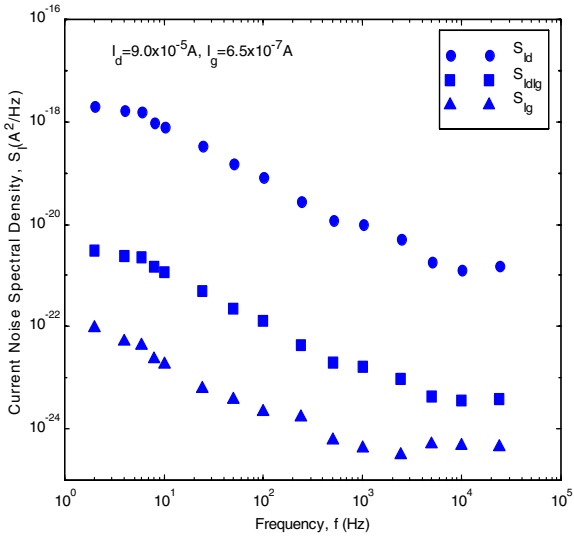

Figure 2. Measured drain, gate, and their cross noise spectrum as a function of frequency f for a nMOSFET with W = 10 µm, L = 10 µm, and t_{ox} = 2.2 nm

The noise spectra clearly show a $1/f^{\gamma}$ frequency dependence with the spectral power factor γ close to unity. As shown in Fig. 3, we observe that a partial correlation between the drain and the gate current noise sources exists and varies with the current ratio. In the 10 Hz – 1 kHz frequency range, the existence of correlation effects is probably caused by common noise sources which, we assume, are the occupancy fluctuations of the slow trap states available for trap-assisted tunneling.

4. Simulation Results

The variations of measured noise ratio $S_{I_g}(f)/S_{I_d}(f)$ and correlation coefficient $C^{LF}(f)$ with current ratio I_g/I_d are plotted in Fig. 4 and 5, respectively. These values are compared with those calculated for a nMOSFETs biased at V_{gs} = 0.8 - 2.0 V and V_{ds} = 0.3 V with W = 10 µm, L = 10 µm, t_{ox} = 2.2 nm, µ = 300 cm^2/V-s, m = 1.2, V_T = 0.2 V, ϕ_b = 3.1 eV, and m_{ox} = 0.4 m_0, and $\gamma_d - \gamma_g$ = 0.5, where γ_d and γ_g are the spectral density frequency exponents of the drain and gate low frequency noise, respectively and other symbols have their usual meaning. Good agreement is obtained for the noise ratio at f = 100 Hz and for the correlation coefficient at f = 10 Hz and f = 100 Hz.

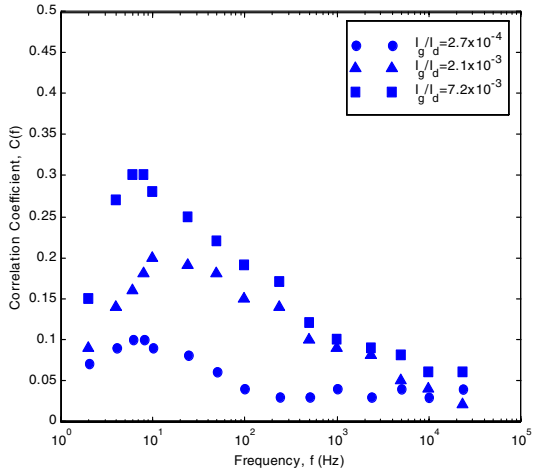

Figure 3. Measured correlation coefficient between drain and gate as a function of frequency f for a nMOSFETs with W = 10 µm, L = 10 µm, and t_{ox} = 2.2 nm

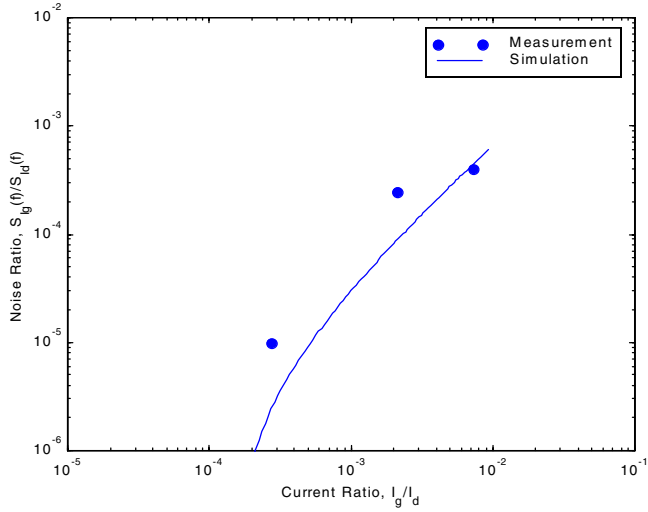

Figure 4. Comparison of measured data and simulation results of the noise ratio between the gate and the drain (f = 100 Hz) as a function of current ratio I_g/I_d for a nMOSFETs biased at V_{gs} = 0.8 - 2.0 V and V_{ds} = 0.3 V.

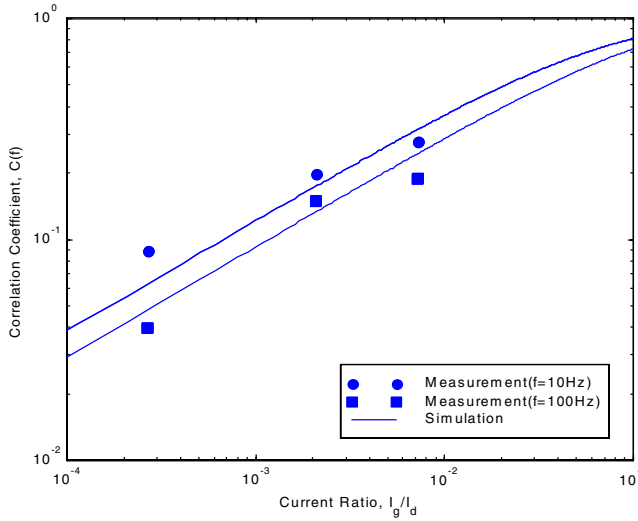

Figure 5. Comparison of measured data and simulation results of the correlation coefficient as a function of current ratio I_g/I_d for nMOSFETs biased at V_{gs} = 0.8 - 2.0 V and V_{ds} = 0.3 V.

5. Conclusions

Measurements and compact model simulations of the low frequency noise performance of ultrathin gate oxide MOSFETs were presented. For a comprehensive evaluation of noise performance, the compact model was formulated accounting for the gate leakage current and the cross correlation between the drain and the gate low frequency noise. For the physical modeling of the correlation coefficient at low frequencies, intrinsic noise sources were taken into account, with the help of partition noise theory and the BSIM4 partition current model. The correlation characteristics were verified by correlation noise measurements.

Acknowledgements

This research was sponsored by the Semiconductor Research Corporation.

References

[1] Y.Mourier, S.Jarrix, C.Delseny, F.Pascal, A.Penarier, D.Gasquet. Characterization of polysilicon bipolar transistors by low-frequency noise and correlation noise measurements. Semicond. Sci. Technol. 2001; 16: 233-238.

[2] L.K.J.Vandamme, D.Rigaud, J.M.Peransin. Coherence between gate- and drain-current fluctuations in MESFET's and MODFET's biased in the ohmic region. IEEE Trans. Electron Devices 1992; 39(10): 2377-2382.

[3] D.Rigaud, M.Valenza. Correlation measurement of carrier multiplication noise sources in MOS transistors at low frequencies. IEEE Trans. Electron Devices 1994; 41(11): 2076-2081.

[4] K.M.Cao, W.C.Lee, W.Liu, X.Jin, P.Su, S.K.H.Fung, J.X.An, B.Yu, C.Hu. BSIM4 gate leakage model including source-drain partition. IEDM Tech. Dig. 2000; 815-818.

[5] H.S.Momose, M.Ono, T.Yoshitomi, T.Ohguro, S.Nakamura, M.Saito, H.Iwai. A study of flicker noise in n- and p-MOSFETs with ultrathin gate oxide in the direct-tunneling regime. IEDM Tech. Dig. 1998; 923-926.

[6] F.M.Klaassen. Characterization of low 1/*f* noise in MOS transistors. IEEE Trans. Electron Devices 1971; 18(10): 887-891.

[7] J. – H. Lee, Comprehensive compact noise modeling of nanoscale CMOS devices, Ph. D. Dissertation, University of Florida, 2003.

TUNNELING EFFECTS AND LOW FREQUENCY NOISE OF GaN/GaAlN HFETs

M. Levinshtein[1]

Solid State Electronics Division,
The Ioffe Physical-Technical Institute of Russian Academy of Sciences,
194021, ul. Politekhnichskaya 26, St. Petersburg,
Russia

S. Rumyantsev and M. S. Shur[2]

Department of ECSE and Broadband, Rensselaer Polytechnic Institute, USA
110 8-th Street, Troy, New York 12180-3590
USA

[1] melev@nimis.ioffe.rssi.ru

[2] shurm@rpi.edu

Abstract Attempts to explain the nature of the 1/f noise in AlGaN/GaN HFETs have involved three different mechanisms: occupancy fluctuations of the tail states near the band edges, fluctuations in the space charge regions surrounding dislocations, and electron tunneling from the 2D gas into adjacent GaN or AlGaN layers. Our experimental data favor the third mechanism. Three main arguments support this tunneling mechanism: (i) the observed temperature dependence of noise in the doped channel of AlGaN/GaN HFETs, which is explained by the tunneling model, (ii) a very weak temperature dependence of the 1/f noise in the temperature interval from 8 K to 300 K, (iii) the concentration dependence of the Hooge parameter typical for noise caused by the electron tunneling..

Keywords: 1/f noise, GaN/GaAlN HFETs, tunneling

1. Introduction

Gallium nitride and gallium-aluminum nitride based electronic devices, especially AlGaN/GaN HFETs, are now in the forefront of the semiconductor research. They have excellent potential for high power, high frequency, and radiation hard applications. The level of the low frequency

J. Sikula and M. Levinshtein (eds.),
Advanced Experimental Methods for Noise Research in Nanoscale Electronic Devices (161 - 168)

noise (in the frequency range 10^0 Hz - 10^4 Hz) is one of the most important characteristics of devices used in microwave (10^9 Hz - 10^{12} Hz) and optical (10^{13} Hz - 10^{15} Hz) communication systems. The low-frequency noise level upconverts into phase noise that limits performance of oscillators, mixers, and other electronic systems.

The level of the 1/f noise in HFETs is much smaller than that in GaN epi-layers. The low frequency noise level in thin (~ 0.1 – 3 μm) n-GaN epi-layers is characterized by the Hooge constant, α, ranging from ~10^{-3} to 10 [1]. As usual, the level of noise is strongly correlated with the structural imperfection of the samples. Unlike GaN films, GaN/GaAlN HFETs are characterized by a rather low level of the 1/f noise with α values of ~10^{-4} ÷10^{-5} [2]. (These values of α are comparable with those for GaAs/GaAlAs HFETs.) Hence, it is obvious that the mechanism responsible for 1/f noise in thin GaN layers is suppressed in the GaN/GaAlN HFETs. In contrast, GaAs epi-layers of average quality have the values of α within the range $10^{-4} < \alpha < 10^{-5}$ (comparable to the values of α for AlGaAs/GaAs HFETs.

Two mechanisms of the 1/f noise suppression in the HFETs channels have been discussed. In Ref. [3], it was suggested that the 1/f noise in the HFETs channels is caused by the fluctuations of the occupancy of the tail states near the band edges. Then, for degenerate semiconductors, the noise caused by the tail states decreases with an increase in the degeneracy as $exp\ ((E_F - E_c)/kT)$ [4]. Hence, a high degree of degeneracy in GaN/GaAlN HFET channels might explain this drastic noise reduction.

Another mechanism links the 1/f noise in GaN films and GaN/GaAlN HFETs to the fluctuations in the space charge regions surrounding the dislocations [5]. This mechanism relates a high level of the 1/f noise in GaN films to a very large dislocation density in thin GaN layers (~ 10^8-10^{10} cm^{-2}). The suppression of the 1/f noise in the GaN/GaAlN HFET channels is explained by effective screening of the dislocations by the 2D gas. (Reference [5] gives only qualitative discussion of this mechanism).

We believe that both these mechanisms of the 1/f noise (or at least the dominant on) are suppressed due to the large sheet density of the 2D gas.

Our experimental data show that in the channels of GaN/GaAlN HFETs, tunneling from the 2D gas into the traps in the adjacent GaN or AlGaN layers becomes the main source of the 1/f noise.

2. Experimental Details

The sample fabrication was described in detail in References [6,7]. The AlGaN/GaN heterostructures were grown by low-pressure MOCVD on SiC substrates. A 150nm AlN layer grown on SiC substrate was followed by the deposition of a 1 μm nominally undoped GaN layer. In some cases, a 50 nm

n-GaN layer with estimated doping level of 2×10^{17} cm^{-3} was introduced between undoped GaN layer and 15 – 40 nm $Al_xGa_{1-x}N$ barrier layer with $0.15 < x < 0.2$. The Hall measurements yield 2D electron sheet concentration n_s in the range from $\sim1.0\times10^{13}cm^{-2}$ to $\sim1.3\times10^{13}cm^{-2}$and Hall electron mobility 1000 - 1500 cm^2/Vs. The HFETs with gate lengths L_g from 1 μm to 100 μm have been used for measurements. The gate widths W ranged from 50 to 200 μm. The devices were wire-bonded and placed into the chamber of a closed cycle Helium cryostat. A low frequency noise was measured in the frequency range from 1 Hz to 10 kHz in the temperature interval from 8 K to 300K. The drain voltage fluctuations were measured in common source configuration in linear and saturated regimes.

3. Results and discussion

The measurements of the current - voltage characteristics showed that the threshold voltage in AlGaN/GaN HFETs is only weakly dependent on temperature across the entire temperature range 8-300 K. The electron sheet concentration also changed little with temperature. The channel resistance under the gate at $V_g = 0$ (extracted from the current-voltage characteristics) decreased monotonically with temperature manifesting a mobility increase. The electron mobility increased approximately three times with temperature decrease from 330 to 8 K.

Measurements of noise on TLM structures using the technique described in Ref. [6] showed that contacts did not contribute much to output noise.

Fig. 1 shows the temperature dependencies of noise at different frequencies in the sample with Si-doped GaN layer. Within the temperature range from 50 K to 150 K, broad maxima were observed in the noise temperature dependencies [7]. Although these temperature dependencies look somewhat similar to those typical for GR noise, the observed noise cannot be attributed to the simple GR noise for two main reasons: (I) the position of the maxima practically does not depend on frequency, (II) the frequency dependence of noise at all temperatures $T > 50$K is close to that typical for the 1/f noise.

The model, which explains the observed temperature dependence of noise by the electron tunneling from the 2D electron gas AlGaN/GaN HFETs, has been developed in Reference [7]. This McWorter-like model predicts the $1/f$ spectrum with the amplitude and the position of the noise maximum in the noise temperature dependence in good agreement with the experiment data (Fig. 2).

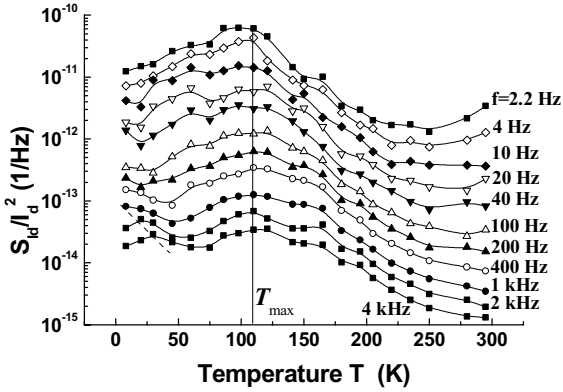

Figure1. Temperature dependencies of noise at different frequencies. The sample with Si-doped layer between AlGaN barrier and undoped GaN layer. Linear regime [7].

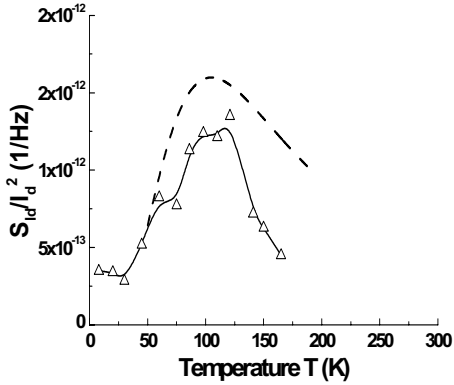

Figure 2. Experimental (solid line) and calculated (dashed line) temperature dependencies of noise at frequency f = 100Hz. Dashed curve has been calculated in the frame of the phonon assisted tunneling model [7].

Fig. 3 shows the noise spectra at three temperatures for the transistor with undoped GaN layer. As seen from the figure, these dependencies have the form of the $1/f^{\gamma}$ noise with the exponent γ being close to unity and only weakly dependent on temperature. The noise amplitude also depends on temperature rather weakly [8]. A weak temperature dependence of the measured noise is a signature of the tunneling mechanism of noise.

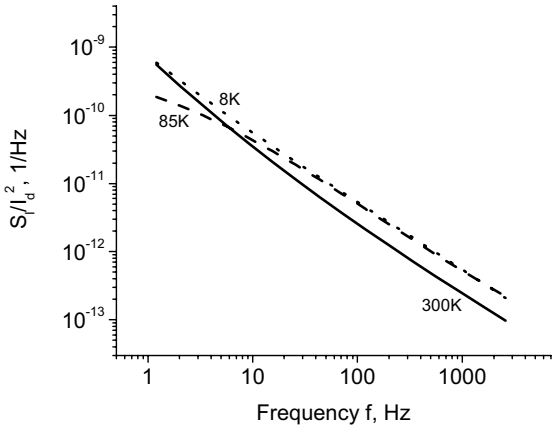

Figure 3. The frequency dependencies of the relative short circuit drain current fluctuations at temperatures 8 K, 85 K, and 300 K. Gate voltage $V_g = 0$. Linear regime [8].

Fig. 4 shows concentration dependencies of the 1/f noise in the channel of AlGaN/GaN HFETs [7,9].

As seen, at low channel concentrations, when the channel under the gate makes the main contribution to noise, α decreases with the increase of n_s as $\alpha \sim 1/n_s$. The dependence $\alpha \sim 1/n_s$ is often observed in n-channel Si MOSFETs. It is generally accepted that the most probable mechanism for such dependence is the electron tunneling from the channel to the oxide (McWhorter mechanism). According to this mechanism, the spectral noise density of number of carrier fluctuations depends only on the trap density near the Fermi level and does not depend on the electron concentration in the channel. In this case, the Hooge parameter $\alpha \sim 1/n_s$ [10]. Since we found the same behavior for in AlGaN/GaN HFETs, the noise observed might be linked to the similar noise mechanism: electron tunneling from the 2D gas into the traps in GaN or AlGaN.

The dependencies shown in Fig. 4 have been extracted from the noise dependencies on the normalized gate voltage $V_{gn} = (V_g - V_{th})/|V_{th}|$ [11]. Such dependencies were studied in the temperature range from 8 K to 300 K in Ref [8] (Fig. 5).

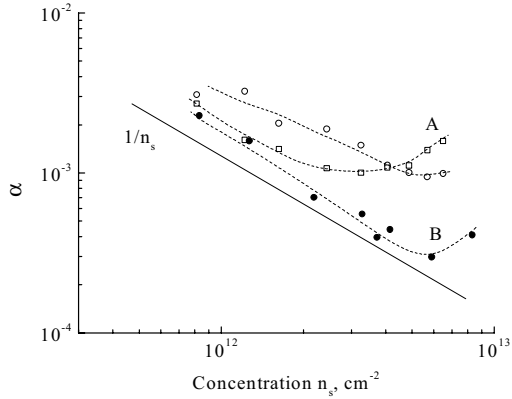

Figure 4. The dependencies of the Hooge parameter α on 2D sheet channel concentration n_s for *A* and *B* GaN/GaAlN HFETs. Different symbols represent the data for different samples [9].

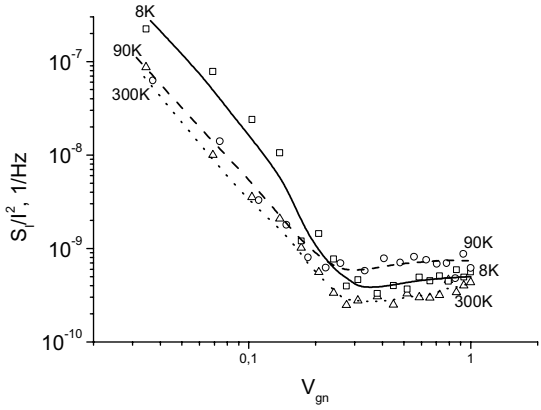

Figure 5. The dependencies of the relative spectral noise density S_{Id}/I_d^2 on reduced gate voltage V_{gn} at three temperatures: the highest temperature T = 300 K, the lowest T = 8 K, and T = 90 K. Linear regime. Frequency of analysis f = 1 Hz [8].

As seen, from Fig. 5, at small values V_{gn} (large negative gate voltage close to the threshold voltage), the spectral noise density S_I/I^2 decreases with V_{gn} approximately as V_{gn}^{-2} at all temperatures. In accordance with the analysis presented in Refs. [9,11], it means that Hooge constant α_H is inversely proportional to the sheet carrier concentration in the channel (See Fig. 4).

The slope of $S_{Id}/I_d^2(V_{gn})$ dependencies is nearly the same for all temperatures. Moreover, the value of the relative spectral noise density depends on temperature very slightly: the change in background 1/f noise magnitude does not exceed a factor of three with temperature variation from 8 K to 300 K. Such weak temperature dependence of the noise provides an additional argument in favor of the tunneling mechanism of the 1/f noise in the channel of GaN/AlGaN HFETs.

4. Conclusion

Our experimental data on the temperature dependence of noise in the doped channel of AlGaN/GaN HFETs in the temperature interval from 50 K to 150 K, a very weak temperature dependence of the 1/f noise level in wide temperature region, and the concentration dependence of the Hooge parameter, show that the 1/f noise in the channel of AlGaN/GaN might be linked to the electron tunneling from the 2D gas into the traps in GaN or AlGaN.

Acknowledgements

The work at RPI was supported by the Office of Naval Research (Project Monitor Dr. Harry Dietrich). The work at Ioffe Physico-Technical Institute was supported by Russian Foundation for Basic Research (grant N 02-02-17619).

References

[1] M. E. Levinshtein, S. L. Rumyantsev, M. S. Shur, R. Gaska, and M. Asif Khan, Low frequency and 1/f noise in wide gap semiconductors: Silicon Carbide and Gallium Nitride" IEE Proceedings Circuits, Devices and Systems (Special Issue "Selected Topics on noise in semiconductor devices") **149** (2002) 32-39.

[2] M. E. Levinshtein, A. A. Balandin, S. L. Rumyantsev, and M. S. Shur, Low-frequency noise in GaN-based Field Effect Transistors, in: "Noise and Fluctuations Control in Electronic Devices", A. Balandin, ed., American Scientific Publishers (2002)

[3] M. E. Levinshtein, F. Pascal, S. Contreras, W. Knap, S. L. Rumyantsev, R. Gaska, J. W. Yang, and M. S. Shur, Low-frequency noise in GaN/GaAlN heterojunctions, Appl. Phys. Lett. **72** (1998) 3053-3055

[4] A. P. Dmitriev, E. Borovitskaya, M. E. Levinshtein, S. L. Rumyantsev, and M. S. Shur, Low Frequency Noise in Degenerate Semiconductors J. Appl. Phys. **90** (2001) 301-305

[5] J. A. Garrido, B. E. Foutz, J. A Smart, J. R. Shealy, M. J. Murphy, W. J. Schaff, and L. F. Eastman, Low-frequency noise and mobility fluctuations in AlGaN/GaN heterostructure field-effect transistors Appl. Phys. Lett, **76** (2000) 3442-3444

[6] S. L. Rumyantsev,; N. Pala,; M. S. Shur,; R. Gaska,; M. E. Levinshtein, M. A. Khan, G. Simin,; X Hu, and J. Yang, Low frequency noise in GaN metal semiconductor and metal oxide semiconductor field effect transistors. J. Appl. Phys., **90** (2001) 310-314

[7] S. L. Rumyantsev, Y. Deng, E. Borovitskaya, A. Dmitriev, W. Knap, N. Pala, M. S. Shur, M. E. Levinshtein, M. Asif Khan, G. Simin, J. Yang, and X. Hu, Low-frequency noise in GaN/AlGaN heterostructure field-effect transistors at cryogenic temperatures, J. Appl. Phys. 92 (2002) 4726-4730

[8] S. L. Rumyantsev, Y. Deng, M. S. Shur, M. E. Levinshtein, M. Asif Khan, G. Simin, J. Yang, X. Hu and R. Gaska, On the Low Frequency Noise Mechanisms in GaN/AlGaN HFETs Semicond. Sci. Techn.**18** (2003) 589-593

[9] S. L. Rumyantsev, N. Pala, M. S. Shur, R. Gaska, M. E. Levinshtein, P. A. Ivanov, M. Asif Khan, G. Simin, X. Hu, and J. Yang, Concentration dependence of the 1/f noise in AlGaN/GaN Heterostructure Field Effect Transistors, Semicond. Sci. Technol. **17** (2002) 476-479

[10] L. K. J. Vandamme and R.G.M. Penning de Vries, Correlation between MOST 1/f noise and CCD transfer inefficiency", Solid State Electron., **28** (1985) 1049-1056

[11] J-M. Peransin, P. Vignaud, D. Rigaud and L K J Vandamme, 1/f noise in MODFETs at low drain bias, IEEE Trans Electron Devices **37** (1990) 2250-2253

HIGH FREQUENCY NOISE SOURCES EXTRACTION IN NANOMETIQUE MOSFETs

F. Danneville, G. Pailloncy and G. Dambrine
IEMN, UMR CNRS 8520
Cité Scientifique, Avenue Poincaré, BP 69
59652 Villeneuve d'Ascq Cédex
France
Francois.danneville@iemn.univ-lille1.fr

Abstract The continuing down-scaling of MOSFET's make their noise properties to be more and more fundamentals, for some difficulties may happen when considering high frequency applications. Indeed, though the intrinsic noise performances of MOSFET's are very promising, the technological process inherent to such devices when the device is scaling down makes de facto parasitic elements (such overlap capacitances, gate resistances) to limit greatly the f_{max} (maximum oscillation frequency) and then the noise performances of the device. Also, potential mismatch in Low Noise Amplifiers (LNA) along with the use of high losses Silicon Substrate may increase greatly the noise figure of the LNA, that will be much higher than the minimum noise figure of the stand alone device. As a general trend, the decrease of device's dimensions along with the decrease of the DC supply voltage will require in the future to have the availability of more and more accurate thermal (and related diffusion) noise models. These noise models can be issued from device physics models but also can be extracted from experimental noise measurements ; in such a case, one wants to perform accurate measurements of the noise parameters F_{min}, R_n *and* Γ_{opt} of the Device Under Test (DUT). A lot of methods are available in the literature, we will focus here upon the one used in routine in our laboratory, which is based on noise figure measurements in a 50 Ω environment and physical considerations. The presentation of the NF_{50} method will be re-called prior describing the problems related to an accurate extraction of the noise sources. These problems will address, by the use of a physical noise modeling, a discussion related to the theoretical assumption (uncorrelated noise sources) made to extract the four noise parameters from the NF_{50} data versus frequency. Due to the low resistivity silicon wafers used for such characterization, we will also pay attention towards the specific de-embedding noise procedure which needs to be used.

Keywords: NF_{50} Method, MOSFET's, High Frequency Noise

J. Sikula and M. Levinshtein (eds.),
Advanced Experimental Methods for Noise Research in Nanoscale Electronic Devices (169 - 176)

1. The NF_{50} Method

This method was first developed for III-V devices [1] prior being used in MOSFET's. The method lies upon the physical noise behavior of MOSFET's, using a current-current representation (Fig. 1), taking into account of the frequency variation of the noise sources.

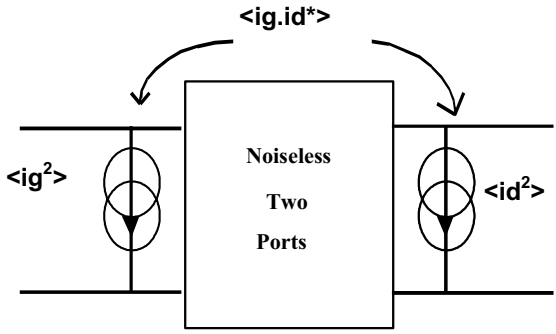

Figure. 1. Noise representation of a Two-Ports MOSFET's using a current-current representation

Let's get interest in the expression of the noise figure when a particular conductance $G_s = G_0 = 20\ mS$ associated to the noise source is presented to the device. The expression of the noise figure in such a case is called NF_{50}:

$$NF_{50} = \left(1 + R_n G_0\right) + \frac{R_n}{G_0}\left(2G_0 G_{cor} + \left|Y_{opt}\right|^2\right) \tag{1}$$

In this expression, R_n is the equivalent noisy resistance, Y_{opt} $(= G_{opt} + j\ B_{opt})$ the optimum noise admittance and F_{min} the minimum noise figure. In a first step, we will describe the frequency variations of each element involved in (1), starting with R_n expressed by:

$$R_n = \frac{\overline{i_d}^2}{4kT_0\left|Y_{21}\right|^2 \Delta f} \tag{2}$$

R_n depends on the drain noise source $\overline{i_d}^2$ which is frequency independent ("white noise"). The modulus of Y_{21} (strongly related to the transconductance) is also frequency independent over a wide frequency range, leading the extrinsic value of R_n to be not sensitive to the frequency,

as long as a gate inductor L_g may be neglected (which holds in the case of on-wafer measurements).

Secondly, let us consider the expression of the noise correlation conductance G_{cor} :

$$G_{cor} = \Re\left(Y_{11} - \frac{\overline{i_g i_d}^*}{\overline{i_d}^2} Y_{21} \right) \tag{3}$$

In this equation, $<i_g.i_d^*>$ is essentially imaginary while Y_{21} is essentially real, leading G_{cor} to be close to the real part of Y_{11}. As a consequence, G_{cor} presents a linear dependence as a function of the square frequency :

$$G_{cor} \approx G_{11} \approx R_i C_{gs}{}^2 \omega^2 \tag{4}$$

Finally, we can discuss about the term $\left|Y_{opt}\right|^2$ which is given by the following expression :

$$\left|Y_{opt}\right|^2 = \frac{1}{4kT_0 R_n \Delta f}\left[\overline{i_g}^2 + \left|\frac{Y_{11}}{Y_{21}}\right|^2 \overline{i_d}^2 - 2\Re\left(\frac{Y_{11}}{Y_{21}} \overline{i_d i_g}^* \right) \right] \tag{5}$$

with :

- $\overline{i_d}^2$ and R_n frequency independent
- $\overline{i_g}^2$ square frequency dependent
- $\overline{i_g.i_d^*}$ linear versus frequency
- $\left|Y_{11}\right|$ almost linear versus frequency
- $\left|Y_{21}\right|$ almost frequency independent

From (5), we deduce that $\left|Y_{opt}\right|^2$ is proportional to the square frequency. Let us consider again NF_{50} (1) which has a frequency independent term $(1+R_n.G_0)$ while the other one $\frac{R_n}{G_0}\left(2.G_0.G_{cor} + \left|Y_{opt}\right|^2 \right)$ is varying as a function of the square frequency. One can conclude that the noise figure with a source impedance equal to *50 Ω is linear as a function of the square frequency*. From the above analysis, it is clear that the equivalent noise resistance R_n or $\overline{i_d}^2$ can be determined accurately using a simple extrapolation of NF_{50} at zero frequency. Since G_{cor} is known, the modulus of Y_{opt} can be deduced also from the variations of NF_{50} versus frequency.

Obviously, the NF_{50} measured data are fluctuating due to uncertainties measurements and, to determine R_n and the modulus of Y_{opt}, a linear regression using the NF_{50} data (plotted versus the square frequency) is required. At this step, one may highlight that, due to the specific nature of a MOSFET (e.g. the particular frequency variations of the noise sources $\overline{i_g^2}$, $\overline{i_d^2}$ and their correlation $\overline{i_g.i_d^*}$ and of the Y parameters), only *one information* is missing in order to obtain the four noise parameters *(*for $F_{min} = 1+2.R_n.(G_{opt}+G_{cor})$ using the NF_{50} data versus frequency. To obtain this information, we consider using a representation with an input gate noise voltage and an output drain noise current (Fig. 2), the noise sources to be uncorrelated [2]. This is equivalent to have, in a current-current representation (Fig. 1), to have the correlation coefficient $C = \frac{\overline{i_g.i_d^*}}{\sqrt{\overline{ig^2}.\overline{id^2}.}} = j.\frac{|Y_{21}|}{|Y_{11}|}.\sqrt{\frac{\overline{ig^2}}{\overline{id^2}}}$. Thus, R_n provides $\overline{i_d^2}$; introducing the expression of $\overline{i_g.i_d^*}$ (from C) in (5) provides $\overline{i_g^2}$ which yields $\overline{i_g.i_d^*}$. From the knowledge of $\overline{i_d^2}$, $\overline{i_g^2}$, $\overline{i_g.i_d^*}$ and of the Y parameters, the four noise parameters are readily obtained. Note that an alternative consists in working directly with a voltage-current representation, in such a case, T_{in}, the input noise temperature is set to the room temperature and T_{out}, the output noise temperature, is the only temperature to extract [2].

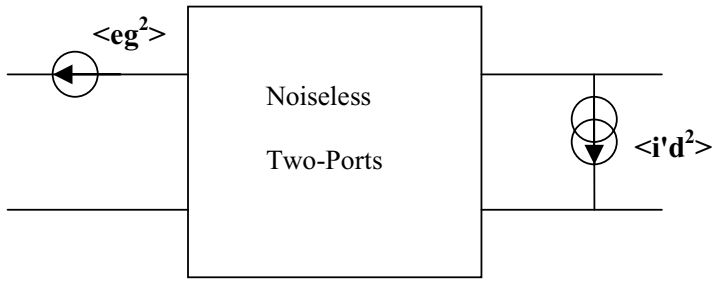

Figure. 2. Noise representation of a Two-Ports Device using a voltage-current representation

The method has been widely used in order to perform noise sources extraction of MOSFETs and some results can be found in [3]. We will pay more attention in the following to several critical points related to the method. The first point is related to the fact that the noise sources extraction method lies on physical considerations, e.g. the fact that in a voltage-current

representation, the noise sources are uncorrelated. The second point is related to the high frequency noise measurements, performed in a *50 Ω* environment, on low resistivity silicon wafers. Such environment requires the use of specific calibrations and de-embedding procedure. We will address these points in the following section.

2. Discussion

2.1. Voltage-Current noise representation : uncorrelated sources

In order to evaluate the assumption made for the extractions, we have used a physical noise modeling. The approach uses a active line (Fig. 3) to represent the MOSFET's channel under the oxide and allows basically to perform the calculation of the noise correlation matrix in any representation. The results issued from this noise modeling are widely described in [4], for that reason, we won't go into details.

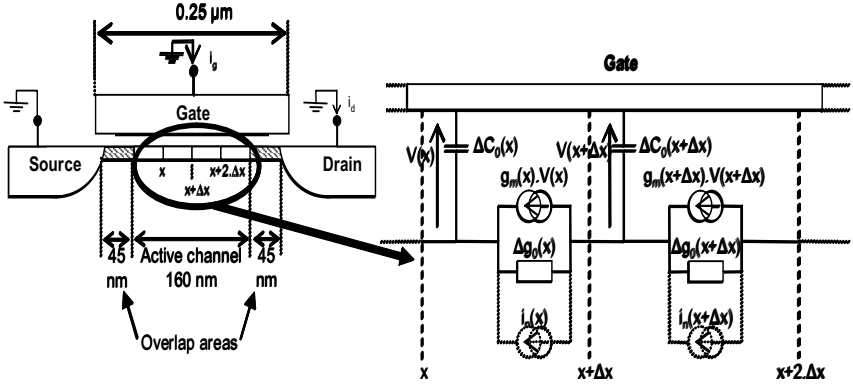

Figure 3. MOS SOI Channel in active line representation.

We will focus mainly on a representation corresponding to an input noise voltage and an output noise current (Fig. 2), for which we have assumed the noise sources to be uncorrelated in Section 1. In Fig. 4 are plotted the real and imaginary part of the complex correlation coefficient $C' = \frac{< e_g . i_d'^{*} >}{\sqrt{< e_g^2 > . < i_d'^2 >}}$. It is found that the imaginary part is almost equal to zero while the real part is not strictly equal to zero, but is very small (lower that *0.2* over the all range of biasing conditions, from small to strong inversion). This result confirms the specific noise behavior of MOSFET's

and of FET's in general [2], and justifies the usefulness of NF_{50} method to extract the noise source correlation matrix of such devices.

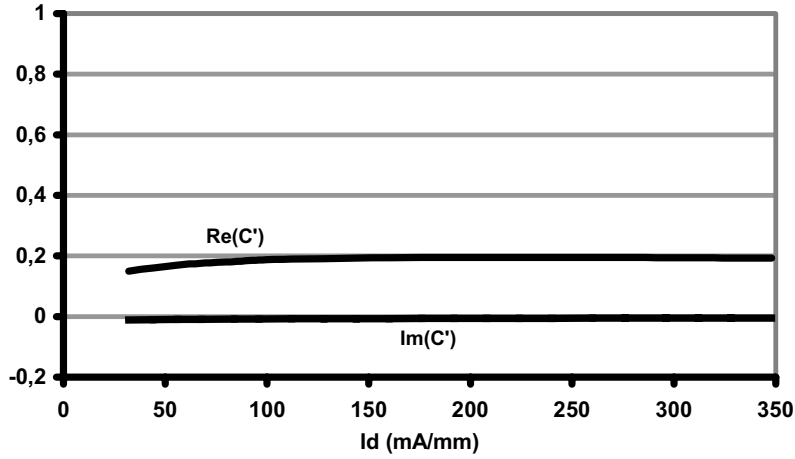

Figure. 4. Variations of the real and imaginary parts of the correlation coefficient using a voltage-current representation

2.2. Noise Figure in *50 Ω* environment on low resistivity Silicon Wafers

2.2.1. Determination of Y parameters of the MOSFET (Y_{DUT})

As shown in part 1, the noise extraction requires an accurate knowledge of the Y parameters, and in the microwave range, it is obvious that one will measure the scattering parameters S. A standard procedure is first used to determine the S parameters of Quad 1 and Quad 2 (Fig. 5), which are required to make later the appropriate de-embedding (both to determine the S parameters of the DUT -S_{DUT}- but also to obtain the noise figure of the DUT).

Once Quad 1 and Quad 2 are perfectly known, then we can perform the measurement of the S_{DUT}. We proceed first by making an *Off*-Wafer LRM Calibration (Ref Planes are probe tips) using a standard kit on Alumine. Then, we proceed to a specific *On*-Wafer de-embedding procedure using an Open Structure, that is associated to each transistor present of the Si Wafer (same geometry). The method lies first in the measurement of the S parameters of the DUT, that will provide a first set of [Y] parameters ($[Y_1]$). Then, it is followed by S parameters measurement of the Open Structure,

that will provide a second set of [Y] parameters ([Y_2]). Finally, the right admittance parameters of the DUT are simply given by : [Y_{DUT}]= [Y_1]– [Y_2].

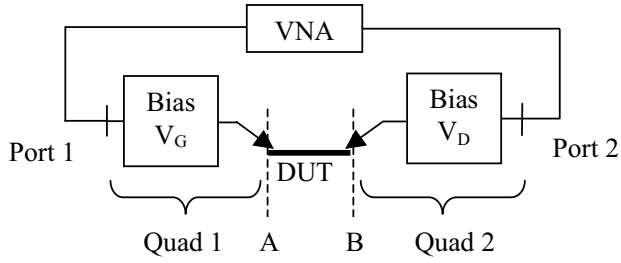

Figure 5. Schematic of the measurement bench to perform the S parameters measurement of the DUT

2.2.2. Problems related to shielded pad

In a *50 Ω* low resistivity Si Wafer environment, other problems may occur. In fact, all transistors are inserted between two *50* Ω TFMS lines of *70* µm long each (minus the finger width of the transistor) added to the shielded pads (around 400 µm for the whole structure). This shielded pad may present strong capacitance value (up to *150* fF) which will modify strongly the impedance presented to the transistor (e.g. the impedance is no longer equal to *50* Ω). So the *measured* noise figure will be given by :

$$NF_{50} = \left(1 + R_n G_0\right) + \frac{R_n}{G_0}\left[2G_{cor}G_0 + \left|Y_{opt}\right|^2 + \omega^2 C_{pad}{}^2 + 2\omega C_{pad} B_{opt}\right] \qquad (6)$$

The noise parameters R_n, $|Y_{opt}|^2$ and B_{opt} correspond to the intrinsic ones and their frequency variations have been previously described. From (6), it is clear that the expression of NF_{50} keeps on varying as a function of the square frequency, when taking account of the shielding capacitance C_{pad} and consequently, the above experimental extraction procedure is still valid, providing the adequate de-embedding is made.

References

[1] G. Dambrine, H. Happy, F. Danneville, A. Cappy, « A New Method for on Wafer Noise Measurement », IEEE Transactions on Microwave Theory and Techniques, Vol. 41, n. 3, pp. 375-381, March 1993

[2] M. W. Pospieszalski, "Modeling of noise parameters of MESFET's and MODFET's and their frequency and temperature dependence", IEEE Trans. Microwave Techn. Theory, Vol. 37, pp. 1340-1350, 1989.

[3] G.Dambrine, C. Raynaud, M. Vanmackelberg, F. Danneville, S. Lepilliet, "Impact of down scaling on high frequency noise performance of bulk and SOI MOSFETs", SPIE, Fluctuations and Noise Conference, Santa Fe, June 2003, Vol. 5113-08, pp. 178-193.

[4] Pailloncy G., G. Dambrine, F. Danneville, B. Iniguez, J.P. Raskin "Noise Modelling in 0.25 µm Fully Depleted SOI MOSFETs", 17th International Conference on Noise and Fluctuations, August 2003, 18-22, Prague.

INFORMATIVE "PASSPORT DATA" OF SURFACE NANO- AND MICROSTRUCTURES

S. F. Timashev[1]
L.Ya. Karpov Institute of Physical Chemistry,
Vorontsovo pole Street 10, Moscow, 105064
Russia

A. B. Solovieva[2]
N.N. Semenov Institute of Chemical Physics, Russian Academy of Science,
Kosygina Street 4, Moscow, 119991
Russia

G. V. Vstovsky[3]
N.N. Semenov Institute of Chemical Physics, Russian Academy of Science,
Kosygina Street 4, Moscow, 119991
Russia

[1] serget@mail.ru
[2] anna@polymer.chph.ras.ru
[3] vstovsky@polymer.chph.ras.ru

Abstract A general phenomenological approach – Flicker Noise Spectroscopy (FNS)- for revelation of information valuable parameters characterizing the arbitrary chaotic surfaces was developed to distinguish their patterns and describe quantitatively their functional properties. The method developed was applied to revelation of effects of a shungit filling agent in polypropylen matrix on the composite properties, revelation of hydrogen treatment effects on the cleavage surfaces of LiF monocrystals after their dissolution in water with quantitative evaluations of their anisotropy, analysis of activity of vacuum deposited porphyrins layers in a photosensibilized generation of singlet oxygen into gaseous phase. The approach elaborated can be used for developing the new control tools for processing scanning probe microscopy (SPM) data in nanotechnologies, microelectronics, production of polymeric materials with specific surface properties, and others.

Keywords: Atomic Force Microscopy, roughness profiles, digitized data processing, structure irregularities, Flicker-Noise Spectroscopy, polymeric composites, dissolution surfaces, deposited layers.

J. Sikula and M. Levinshtein (eds.),
Advanced Experimental Methods for Noise Research in Nanoscale Electronic Devices (177 - 186)

1. Introduction

Usually, scanning probe microscopy (SPM) based analysis of surface structure uses the methods of processing digitized "roughness profiles" obtained by scanning the studied surface fragment with characteristic sizes from several nm to tens of μm. As a rule, the results are presented in the form of images of individual surface fragments (for example, of molecular aggregates) or the images of general surface morphology under the conditions of "model enlightening". The view of obtained images can essentially depend on the localization of model enlightening, and very different images of the same surface fragment for different enlightening chosen by an operator can be obtained. So far there exist no standard and conventional method of digitized data processing to obtain cumulative parameters characterizing the features of a surface under study in general. The pure statistical processing methods giving the mean roughness values with corresponding dispersion and cumulants are not used in practice as they do not give information about a very important property of the structures to be self-correlated in their space fragments organization on different space scales. The use of Flicker-Noise Spectroscopy (FNS) on the base of concept of information essence of real structure irregularities on different space scales gives new opportunities in quantitative description of real chaotic surfaces [1-6]. The main parameters of FNS methodology used in this work are introduced below.

2. Main equations

In accordance with FNS method, the main information hidden in chaotic signals is formed by irregularities of the chaotic series under consideration. They can be considered as the only markers of the evolution process. The FNS method [4-6] with reference to handling the temporal and spatial series (as the digitized sequences of numbers with an equal pitch on temporal or spatial coordinate) consists in an evaluation of the so-called structural functions (difference moments) and Fourier power spectra which are parameterized then on the basis of nonlinear trends (parametrically specified curves). The Fourier spectra were calculated as usual with a reference to surfaces profiles with a zero medial $\langle h'(x,y)\rangle=0$, $h'(x,y)=h(x,y)-\langle h(x,y)\rangle$, where $h(x,y)$ is a reference altitude of a profile. For example, for a profile specified discretely in heights h'_i at the points $x_i = i\Delta x$ (Δx is a sampling pitch) along coordinate x the power spectra were calculated by the formulas

$$S(k) = U^2(k) + V^2(k), \tag{1}$$

$$U(k) = \frac{1}{N}\sum_{i=0}^{N-1} h'_i \cos(x_{i+1} 2\pi k),\ V(k) = \frac{1}{N}\sum_{i=0}^{N-1} h'_i \sin(x_{i+1} 2\pi k),$$

where the magnitude of a wave vector k varies within the limits $[1/(N\Delta x), 1/(2\Delta x)]$, N = 1000, for example, - number of points. In Refs. [4-6] it is proposed to approximate the power spectrum by a model

$$S(k) = \frac{S_0}{1 + (L_0 \cdot k)^n} + D_0. \tag{2a}$$

An automatic choice of parameters of this model is a nontrivial problem. As the calculations were carried out for wave numbers satisfying a condition $(L_0 k)^n >> 1$, in this work a simplified model was used

$$S(k) = \frac{S_0}{(L_0 \cdot k)^n} \tag{2b}$$

where parameter L_0 to be calculated by formula

$$L_0 = \frac{1}{k_1}\left(\frac{S_0}{S(k_1)}\right)^{1/n} \tag{3}$$

using other parameters determined by the processed data. Though such way of calculation of parameter L_0 does not give true value of correlation length. Parameters S_0 were calculated by special algorithm for the same values of maximal and minimum k_1 harmonics for all the profiles processed (see below). Parameter n was calculated by least square method as a declination in double logarithmic coordinates.

The difference moment of the pth order

$$\Phi_{(p)}(\Delta) = \left\langle \left| h(x) - h(x+\Delta) \right|^p \right\rangle \tag{4}$$

[the brackets mean an average, immediate, over all series $h(x)$] in accordance with Refs. [1, 2] was approximated by formula

$$\Phi_{(p)}(\Delta) \approx G_1(p) \cdot \sigma^p \cdot \left[1 - \Gamma(H, \Delta / L_1)/\Gamma(H)\right]^p, \tag{5}$$

where $\Gamma(\alpha)$ and $\Gamma(\alpha, s)$ are gamma function and incomplete gamma function (the first one), respectively; $G_1(p)$ is a numerical coefficient (for the second order moment, p=2, its theoretical value is $G_1(2)$=2), σ is the standard deviation of the chaotic series under consideration. For the small values of difference moments lag, i.e. $\Delta/L_1 << 1$, we have:

$$\Phi_{(p)}(\Delta) \propto \left(\frac{\Delta}{L_1}\right)^{Hp} . \qquad (6)$$

Linear regression in the double logarithmic axes of the $\Phi_{(p)}(\Delta)$ dependence, i.e. the $\ln[\Phi_{(p)}(\Delta)] - \ln[\Delta]$, for a small number of the first points, for example, three, gives declination value pH. Determing this declination and deviding it by the structural function order p, we obtain the Hurst parameter H. Usually, the structural functions of the 2nd order were calculated. The parameter L_1 was calculated by a special algorithm.

For a quantitative description of surfaces the following parameters were used: the average height of a surface roughness h, and corresponding standard deviation σ, lengths of correlation L_0 and L_1, for the most sharp types of surface irregularities – "spikes" and "jumps", respectively [1-6], and also dimensionless parameters n and H. Correlation lengths describe the presence of some memory in the sequences of "spikes (bursts)" and "jumps" modeling surface roughness, n and H describe the extent of memory loss in these sequences. In Fig. 1 the calculated curves and selected parameters are schematically shown. The specificity of "two dimensional" objects, such as surface relief, is that they consist of a great number of series in two (as a minimum) independent directions. For handling such objects the original procedure was developed [4, 5] which is as follows.

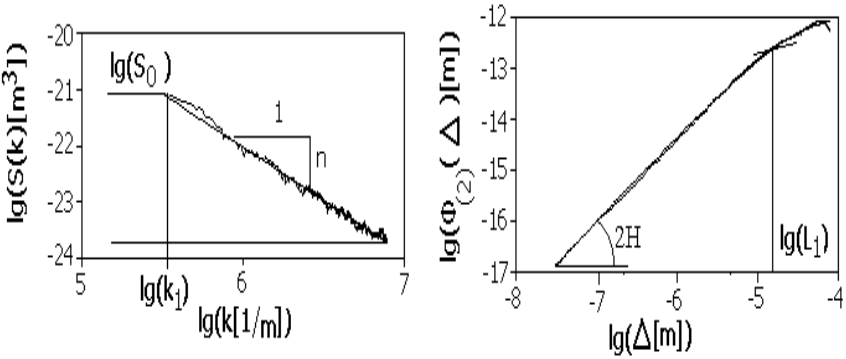

Figure 1. Scheme of parameterization of the power spectra and difference moments.

A given number (for example, 100) of profiles in a given direction was randomly picked up from each relief. Their parameterization was carried out through averaging their parameters that was conducted in two ways, Fig. 2. The average parameters of profiles in two perpendicular directions may be

essentially different. When number of picked up profiles increased from 20 up to 100 the values of obtained parameters varied by 2-5%. This value can be accepted as an estimation error of the obtained parameters.

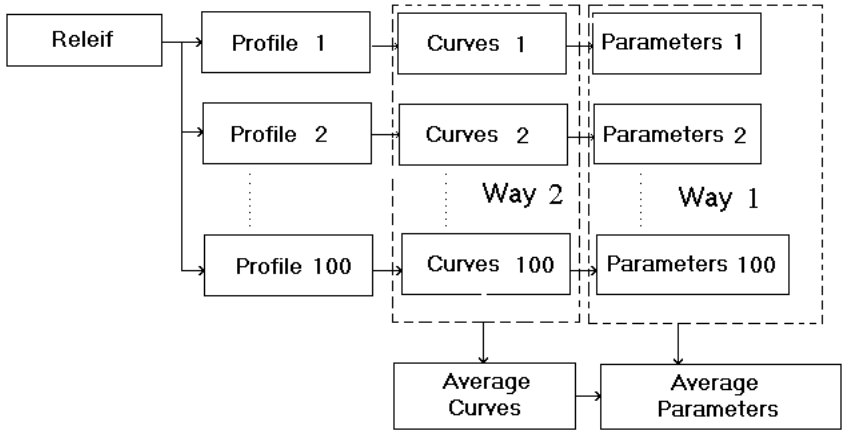

Figure 2. Two ways of parameters averaging.

All calculations were carried out using a specially designed program FNSTV for Windows 95 and higher environment for the same "cutting" parameters for the spectra and difference moments. The program can process the data in sm2 format (up to 1024x1024 points, Scanning Probe Microscope «Solver P-47», NT-MDT Corporation, Zelenograd City), reformat the data in sf2 format for a faster loading, draw the relief views at different view angles and save the pictures on the disk, draw individual profiles and the double logarithmic plots of power spectra and difference moments of required order (from one to ten) of the individual profiles in required direction and the curves averaged over the required number of picked up profiles for set cutting parameters (maximum and minimum spectral harmonics, maximum and minimum delay, smoothing parameters of power spectra, etc.), save the plots on the disk, accumulate the parameters of fitted (interpolated) curves via the formulas (2)-(6) in figure tables on the screen, process the relief by a list of file names at identical "cuttings" parameters of spectrums and difference moments, accumulate the calculated averaged (in two ways by the choice) parameters into text file of tables for further processing by text and electronic tables editors.

3. Effects of shungit filling agent in polypropylene matrix on the composite properties

In recent years, ground shungite rocks came into use as fillers in electro- and thermoconducting polymeric composites. The major components of shungites are amorphous carbon and silicon dioxide. Their ratio varies in a wide range. The characteristic properties of the structure of filled polypropylene (PP) can manifest themselves in the special features of the surface of the samples which, like a bulk volume, exhibits characteristic heterogeneity on various spatial scales. We present results of a quantitative analysis of the micro-roughness of the surfaces of PPS samples revealed in studying the corresponding relief obtained by atomic-force microscopy [4] where experimental conditions are described in details. For shungites-1 and -3, the size of surface regions was 7x7 mcm, and for PP and composite mixtures, this size was 50 x 50 mcm. For each sample, 3-4 such regions were analyzed. Their analysis allowed to extract information about the surfaces. The obtained parameters additionally averaged over regions are listed in Tab. 1.

Table 1. Structural-dynamic parameters of initial components and PP-shungite-1 composites obtained by FNS processing of atomic-force spectroscopy scans (I and II are for 5 and 30 vol % shungite-1 in PP, respectively)

Parameter	Schungite-1	Schungite-3	PP	I	Π
1	2	3	4	5	6
H, mcm	1.15	0.78	0.12	0.32	0.75
σ, nm	293	280	32	60	278
S_0, nm^2 mcm	256	84	213	370	2216
n	1.82	1.82	2.54	2.45	1.95
L_0, mcm	0.44	0.36	3.57	3.54	3.97
G_1	2.79	3.52	2.65	2.51	4.20
H	0.96	0.97	0.94	0.93	0.90
L_1, mcm	1.15	1.38	3.33	3.55	12.64

As follows from the data obtained, the most of the parameters are sensitive to the presence of the shungite phase, and some of them (h, σ, S_0, n, and L^1) are sensitive to its concentration. PPS system is characterized by more “correlated” structural-dynamic parameters (that is, by a greater degree of long-range order) than both its components. The formation of such a structure with a high degree of internal organization is evidence of the important role played by interphase interactions in PPS melts during composite preparation. This conclusion corresponds to the earlier observed phenomenon of an increase in the degree of crystallinity of shungite-filled PP as compared with the initial isotactic PP sample.

4. Formation of anisotropic fractal structures during dissolution of LiF monocrystals

The LiF monocrystals are of broad applications as detectors in different radiometric devices and are used in other areas of physics, chemistry and materials science. To study dissolution surface structure [5] the AFM patterns of an identical size 50x50 mcm (1000x1000 points) were taken out. Each specimen was presented by 3-5 patterns. The values of calculated parameters after an additional averaging over AFM patterns are given in the Tab. 2 for different dissolution temperatures. The numerals X and Y indicate perpendicular directions on dissolution surfaces: X is for profiles predominantly perpendicularly to "stairs\crests", Y is lengthways. In Tab. 2 the differences (between these directions) of correlation lengths and parameters reflecting the correlations loss rates (the lg-lg power spectrums declinations n and Hurst parameters H) are given also.

Table 2. Flicker-noise parameters of reference specimens, averaged by the first way, see *Figure 2*.

T, °C	X/Y	h, mcm	σ, mcm	S_0, nm^2·mcm	n	L_0, mcm	H	L_1, mcm
25	X	0,29	0,10	399	3,62	1,13	0,93	1,08
	Y	0,29	0,09	532	2,56	1,25	0,62	1,43
	|X-Y|				1,06	0,12	0,31	0,35
30	X	0,33	0,08	299	3,62	1,14	0,93	0,99
	Y	0,32	0,10	385	2,61	1,28	0,68	2,43
	|X-Y|				1,02	0,14	0,25	1,44
40	X	0,31	0,10	432	3,73	1,18	0,94	0,86
	Y	0,31	0,11	640	2,38	1,33	0,60	2,06
	|X-Y|				1,35	0,16	0,35	1,20

The dissolution surfaces have greater correlation lengths along local band structure as contrasted to ones across band structure. The formation of local band structure can be explained by the presence of dislocations introduced in a monocrystal when cracking the bar into tablets and cracking the tablets into pair with mirror surfaces. Though in a described model case an anisotropy origin is due to dislocations, the proposed approach can be used for detection of anisotropy of random surfaces, when the anisotropy origin is unknown beforehand. The authors do not know the standard methods which would allow to reflect the presence of anisotropy of random surfaces quantitatively. The FNS method together with atomic-force microscopy gives a unique opportunity to do this that can find applications in different engineering technologies.

5. Effect of porphyrin supramolecular structure on singlet oxygen photogeneration

The new abilities of nanotechnologies can be related to the polymolecular layers formed in the conditions of self-assembly when supramolecular organization of such layers on the scales from nm to fractions of μm is determined by the structure of corresponding molecules and their intermolecular interactions. Here the results of investigations of the vacuum deposited tetraphenylporphyrin (TPP) layers structure by the AFM method are described for their surface concentration range $N_{tot} \sim 10^{-11}$–10^{-9} mol/cm^2 [6]. Such layers turned out to be active in singlet oxygen $^1O_2$ generation into gas phase under photosensitized excitation of adsorbed molecular oxygen $^3O_2$, the generation rate being dependent on the parameters of deposited layers structure on the scales up to the fractions of μm.

It was shown [6] that there is a downfall of the observed singlet oxygen generation rate into gas phase for N_{tot} grows in the range 10^{-10}–10^{-9} mol/cm^2.

The analysis of AFM-images of deposited TPP layers surfaces by using Solver-P47 (NT-MDT, Zelenograd) instrument, shows that their reliefs are changing as the deposited porphyrin concentration grows. The values of the parameters obtained are given in Tab. 3.

Tab. 3 shows how the parameters L_1 and n depend on the overall porphyrin surface concentration N_{tot}. The parameters characterize on nanometer scales the structural organization of porphyrin molecular crystals formed due to deposition on a quartz support. In particular, decrease in correlation length L_1 as well as increase in the parameter n due to increase in N_{tot} in the range of "solidness" of porphyrin layers reflect a loss of correlation links in the structure of the layers when porphyrin surface concentration increases. This circumstance can be the reason for the drop of the singlet oxygen generation rate in the range of high surface concentrations $N_{tot}>10^{-9}$ mol/cm^2.

Table 3. FNS parameters of deposited TPP layers investigated by AFM method.

N_{tot}, mol/cm^2	L_1, mcm	n	h, mcm
$5.2 \cdot 10^{-11}$	0.33	2.8	0.018
$1.3 \cdot 10^{-9}$	0.19	2.9	0.024
$2.4 \cdot 10^{-9}$	0.06	3.3	0.032

6. Conclusion

Recently, nanotechnologies have been developed on the base of molecular assemblies of functional systems. The devices elaborated by now enable not only to view the structures appearing on the atomic and subatomic scale, but to transfer and localize the molecules on a solid surface. These abilities are due to elaboration of SPM and its different types: scanning tunneling microscopy (STM), AFM, scanning magnetic microscopy (SMM), and others. The FNS method of chaotic surfaces parameterization offers a new quantitative tool to control the nanotechnological structures and processes.

Acknowledgements

This work was supported by the Russian Foundation for Basic Research Grants (No.01-05-64379; 02-05-64340).

References

[1] S.F. Timashev, Flicker-Noise spectroscopy as a tool for analysis of fluctuations in physical systems. In: G. Bosman, Ed. Noise in Physical Systems and 1/f Fluctuations – ICNF 2001. World Scientific. New Jersey-London. 2001. P.775-778.

[2] S.F. Timashev and G.V. Vstovsky, Flicker-noise spectroscopy for analyzing chaotic time series of dynamic variables: problem of signal-to-noise relation, Russian Journal of Electrochemistry, 39(2003) 141-153.

[3] S.F. Timashev, D.G. Bessarabov, R.D. Sanderson, S. Marais, S.G. Lakeev, Description of non-regular membrane structures: a novel phenomenological approach, Journal of Membrane Science, 170(2000) 191-197

[4] G.V. Vstovsky, A.B. Solovieva, N.F. Kedrina, V.A. Timofeeva, Yu.K. Kalinin, N.N. Rozhkova, An atomic-force microscopy in the analysis of composites structure, Russian Journal of Physical Chemistry, 75(2001) 1963-1967

[5] A.F. Letnikova, G.V. Vstovsky, S.F. Timashev, Formation of Anisotropic Fractal Structures During Dissolution of LiF Monocrystals, Materials Science (Kaunas), **7**(2001) 98-103

[6] A.B. Solovieva, S.L. Kotova, P.S. Timashev, S.A. Zav'yalov, N.N. Glagolev, G.V. Vstovsky, Photosensitized singlet oxygen generation by deposited tetraporphyrin layers, Russian Journal of Physical Chemistry, 77(2003) 104-112

III. NOISE MEASUREMENT TECHNIQUE

NOISE MEASUREMENT TECHNIQUES

L.K.J. Vandamme
Eindhoven University of Technology/ Department of El .Engineering (EH 9.13)
5600 MB Eindhoven
The Netherlands
L.K.J.Vandamme@tue.nl

Abstract The following topics will be considered:
Noise characterisation of voltage amplifiers in series.
Noise measuring set-up with dc excitation and single ended ac-amplifier or differential amplifier in a bridge configuration. Bias and sample criteria to observe 1/*f* noise in homogeneous samples submitted to homogeneous fields.
Criteria for highest S_V value and highest corner frequency f_c between 1/*f* and thermal noise.
Eddy current shielding (on wafer level measurements).
Calculation of S_R from S_V or current spectra S_I in different bias circuits.
Contact noise reduction in a four probe configuration, by good sample design
Noise correlation measurements

Keywords: Equivalent noise resistance, Shielding, short-circuited current noise, Open-circuit voltage noise, Resistance noise, Correlation measurement, Coherence

1. Noise characteristics of preamplifiers in series

Here voltage amplifiers in series will be discussed where the internal noise of each amplifier can be represented by an external voltage noise source at the input of a noise free amplifier. An input-referred noise of *2 nV/*$\sqrt{\text{Hz}}$ or less at 1 kHz means that the amplifier with a voltage gain G and its input shortened shows $S_v = G^2(2\times10^{-9} V/\sqrt{Hz})^2 = G^2(4\times10^{-18} V^2/Hz)$ at the output. It also means that the thermal noise of a source resistance at the input of the amplifier at 290 K of $(2\text{nV}/\sqrt{\text{Hz}})^2/4\text{kT} = 250\ \Omega$ will double the S_V-value at the output of the amplifier at least if that resistance is much smaller than the input resistance of the amplifier. Hence, the noise of an amplifier is often expressed in terms of an equivalent noise resistance.

J. Sikula and M. Levinshtein (eds.),
Advanced Experimental Methods for Noise Research in Nanoscale Electronic Devices (189 - 202)

The equivalent noise resistance and noise source of the voltage amplifier is defined from the voltage noise at the output S_V with a short-circuited input:

$$R_{eq}(f) = \frac{S_{v\ output}}{G^2\, 4kT} \text{ and } \overline{e_n^2} = 4kTR_{eq} \tag{1}$$

4kT is often taken as 0.1 eV = 1.6×10-20 joule, which corresponds to an ambient temperature of 290 K.
What happens with the overall noise characteristics of an ultra low noise amplifier in series with a second low noise amplifier? The ultra low noise amplifier A is characterised by its equivalent input noise resistance R_{eqA} and gain-factor A. The low noise amplifier B is characterised by R_{eqB} and its gain B. The two amplifiers are in series as shown in Fig.1 and with a short-circuited input we obtain at the output of amplifier B a noise signal in spectral values (V^2/Hz) given by

$$S_{V_{AB}} = 4kT(A^2 \cdot R_{eqA} + R_{eqB})B^2 \tag{2}$$

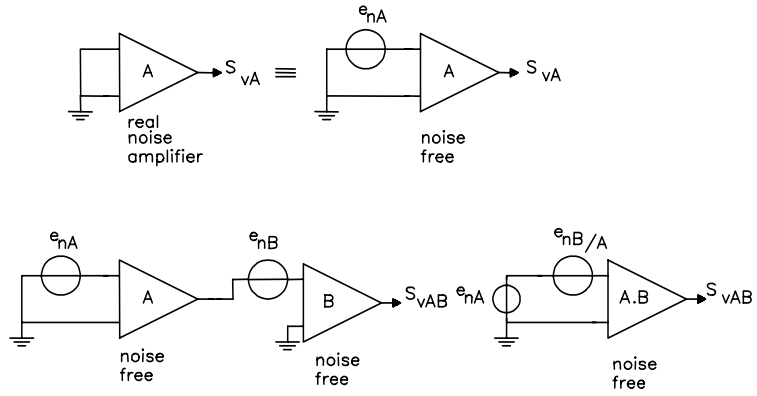

Figure 1. The equivalent input noise source of two amplifiers A and B in series with equivalent noise resistance $R_{eqAB} = R_{eqA} + R_{eqB} / A^2$.

For the two amplifiers in series a new overall equivalent input noise resistance can be defined as R_{eqAB} at the input of a new amplifier with a gain AB. Hence $R_{eq_{AB}} = S_{V_{AB}} / A^2 B^2 4kT$ becomes:

$$R_{eqAB} = (R_{eqA} + R_{eqB} / A^2) \text{ with } \overline{e_{n\ AB}^2} = 4kT(R_{eqA} + R_{eqB} / A^2) \tag{3}$$

The gain of the second amplifier is not important considering the worsening of the overall noise. Only the noise of the second amplifier divided by the gain squared of the first amplifier must be kept lower than the noise contribution of the first amplifier. The criterion to select first amplifier A followed by amplifier B for the lowest total noise is fulfilled when:

$$R_{eqA}(1-1/B^2) < R_{eqB}(1-1/A^2) \tag{4}$$

If the first amplifier A is a buffer amplifier (A=1) the above criterion is never fulfilled, and $R_{eqAB} = R_{eqA} + R_{eqB}$.

Low noise amplifiers in general suffer from 1/*f* noise and white noise. The equivalent input noise resistance is given by an empirical expression

$$R_{eq} = R_{eq\infty}(1+f_c/f) \tag{5}$$

The values often are in between 10 Ω < $R_{eq\infty}$ < 10 kΩ and 3 Hz < f_c <3 KHz. A transformer amplifier can have a $R_{eq\infty}$ as low as 0.5Ω, but the input impedance is strongly depending on frequency and the transfer function depends on source impedance and frequency [1]. The 1/*f* noise of the amplifier often makes an analysis at $f < f_c$ in critical conditions useless.

2. Noise measuring set-up, bias criteria and shielding

The block diagram of a straightforward electrical measuring set-up with one sample and a low noise voltage amplifier is given in Fig.2

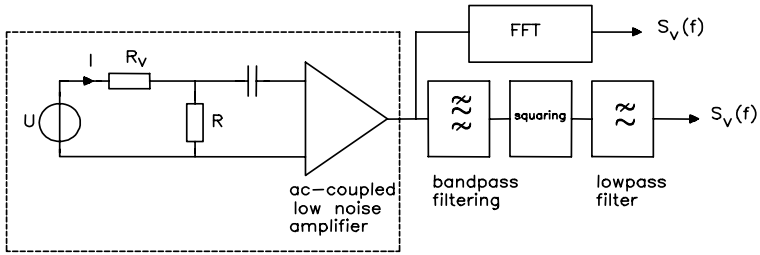

Figure 2. Diagram of a conventional noise measurement set-up (analogue or FFT)

A noise free current *I* is passed through the sample *R* derived from a fresh lead acid battery (*I* > 30 mA) or dry cells in series (*I* < 30 mA) with a quality metal film resistor R_v free from resistance fluctuations. Quality resistors are wire-wounded or metal film but certainly not carbon

composition resistors. For $R_v >> R$ the so-called open circuit voltage noise is measured with an *ac* coupled low noise voltage amplifier. By replacing the sample with a wire-wound resistor of the same value as the sample resistance, it can be checked whether or not the current is noiseless. The amplified noise is then passed through a real time spectrum analyser, which consists of a set of band-pass filter with the inputs in parallel and a constant relative bandwidth between 0.1 and 1 in order to reduce measuring time. Nowadays a digital Fast Fourier Transform (FFT) analyser is used more often. The central frequency f_0 often is in the range of 1 Hz to 1 MHz. The investigations with f_0 < 1Hz become time consuming and often cumbersome because for a long observation time we need a stable sample, constant temperature and stable current supply over a long period of time.

For a homogeneous ohmic resistor with length l and $R >> R_{eq}$ holds a corner frequency at which the $1/f$ noise equals the thermal noise [2].

$$f_c = \frac{\alpha q \mu V^2}{4kTl^2} = \frac{\alpha q \mu E^2}{4kT} \tag{6}$$

α is a $1/f$ noise parameter often between $3\text{x}10^{-7}$ and $3\text{x}10^{-4}$, q elementary charge, μ mobility, V is the average voltage across the sample, $E = V/\ell$ is the electric field, ℓ is the distance between contacts, T temperature and k the Boltzmann constant. The criterion to observe $1/f$ noise at $f < f_c$ is expressed in power density as:

$$\rho J^2 > 4kTfn/\alpha \tag{7}$$

with ρ, J and n: the resistivity, the current density and the free carrier concentration, respectively. Eq. (6) and (7) are independent of sample dimensions and total number of carriers N. Due to the low mobility in dielectrics, the $1/f$ noise is hard to detect for $f > 1$ Hz at an electrical field below breakdown (6).

For homogeneous samples with a resistance R larger than R_{eq} holds a rule of thumb for detecting $1/f$ fluctuations above thermal noise under reasonable bias conditions, the total number of free carriers in the sample N, must be less than 10^{14}. This criterion is calculated from Eq. (7) by multiplying both sides of the equation with the volume of the sample which results in

$$N < \frac{\alpha P}{4kTf}, \tag{8}$$

where P is the power dissipation in the sample and f is the frequency at which the $1/f$ noise must be detectable. For real laboratory conditions with P = 200 mW, $\alpha = 10^{-3}$, $f = 10^2$ Hz, and $4\text{kT} = 1.6\times10^{-20}$ Joule, it holds that

$N \leq 10^{14}$. For modern sub-micron MOS transistors biased in saturation f_c is beyond 1 MHz and given by [3]

$$f_c = \frac{3\alpha q \mu V_G^{*2}}{16kTl^2} \tag{9}$$

where V_G^* is the effective gate voltage. For μ = 200 cm^2/Vs, α=10^{-6}, 4kT/q = 0.1 V, V_G^* = 1 V and ℓ = 0.12 μm, we find $f_c \approx 10^7$ Hz. For a thin metal film holds a maximum power dissipation density of 10^8 watt/cm^3 in order to avoid damage. From Eq. (7) follows that at room temperature with α =10^{-4} , metals will display 1/*f* noise only for *f* < 250 Hz.

The measuring set-up shown in Fig. 3 is less sensitive to fluctuations in environment variables such as temperature and supply voltage and 50 Hz pick up, than the set-up in Fig. 2 due to a good common mode rejection of the balanced bridge and the differential amplifier.

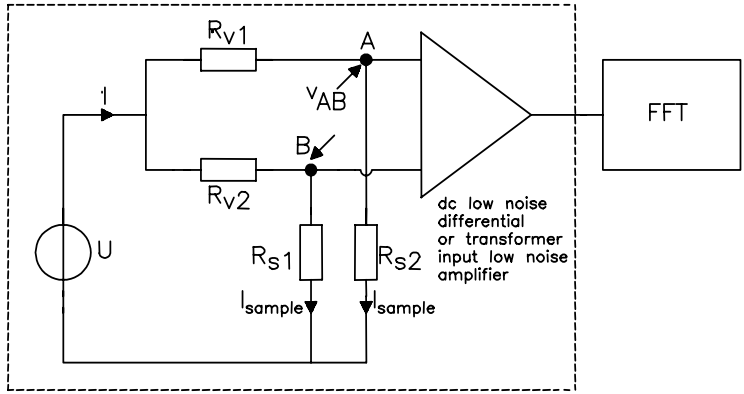

Figure 3. Balanced bridge measurement set up suppresses common mode disturbances stemming from temperature fluctuation affecting all elements of the bridge [4, 5, 6]

For sample impedance below 10 Ω a transformer amplifier can be used in a balanced bridge without coupling capacitors at A, B in Fig. 3. An *ac* balanced bridge technique for measuring low frequency resistance fluctuation spectra can improve the sensitivity over *dc* methods, avoiding the 1/*f* noise range of the amplifier by using a carrier frequency above f_c of R_{eq} (*f*). The low frequency fluctuations at e.g., f_L in the sample resistances R_{s1} and R_{s2} are transformed into voltage fluctuations at $f_{carrier} \pm f_L$ which can be chosen away from the 1/*f* noise range of the amplifier and its low pass

cut-off frequency. Between the output of the amplifier and the FFT analyser a lock-in amplifier is used as a demodulator of the amplitude modulated carrier ($I_{ac}\Delta R$) [6].

Does it help to put n samples with R and S_R given by $S_R / R^2 = C / f$ in series or in parallel in order to improve the f_c value? The answer is no! Using a perfect current source I_m for samples in series, or nI_m for n samples in parallel will result in a corner frequency f_c between $1/f$ and thermal noise floor, given by ($R >> R_{eq}$):

$$f_c = I_m^2 RC / 4kT \,. \tag{10}$$

This holds for one single resistance, n samples in series, or n in parallel provided that each resistor is submitted to a power dissipation of $I_m^2 R$. For two samples in a half bridge as in Fig. 3 with $R_V >> R_S$ also holds Eq. (10). Samples in parallel connection result in a lower thermal noise floor and needs higher supply current levels. The series connection will increase the thermal noise and the needed voltage supply U. The best strategy is the bias condition for which the total sample impedance is well above the equivalent noise resistance of the preamplifier.

The dotted lines in Figs. 2 and 3 represent the cage of Faraday. It is a shielding case to keep out 50 Hz magnetic field disturbances and other unwanted and spurious signals. For eddy current shielding the attenuation of the incoming wave improves with wall thickness d, the radius r of the cage, and is inversely proportional to the skin depth δ of the material used.

A rule of thumb for a good eddy current shielding is derived from [4]

$$r \cdot d \; > \; \delta^2 \text{ with } \delta = (2\rho / \omega \mu_0 \mu_r)^{1/2} \tag{11}$$

r is the radius of the shielding sphere, ρ is the resistivity, μ_r the relative permeability of the shielding material (μ_r = 5000 for transformer steel) and $\mu_0 = 4\pi \times 10^{-7}$ H/m the magnetic permeability of vacuum. The 50 Hz magnetic field disturbances are much better shielded by high permeability material like transformer steel than by the often used copper or aluminium boxes.

Rules of thumb for a reliable noise measurement even on wafer level:

- Short shielded coax cables; no loops for magnetically induced pick-up
- Bias from battery and metal film resistors for a noise free current
- Sample (with probe station); bias box; and preamplifier inside iron cage of Faraday at earth potential.
- Spectrum analyzer and monitor oscilloscope outside cage of Faraday.
- Avoid currents induced by man-made fields: power supply transformers are magnetic field radiators, and are placed at distance outside the cage.

- Low noise current amplifiers in series with high impedance samples are less sensitive for oscillations and EMC.
- Ultra low impedances with very low noise are better measured in a bridge circuit, with a low noise transformer voltage amplifier at the detector side, in order to reduce spurious common mode “noise” due to temperature and bias drift as shown in Fig.3.
- The main noise source in a three- terminal device is found easier by a coherence measurement.
- Make the correct choice of low noise amplifiers. Current amplifier if R is comparable to the input impedance of the voltage amplifier. When using a voltage amplifier choose a reasonable bandwidth and $R_{eq} < R_S$. A double channel coherence measurement is the best choice for $R_{eq} > R_S$

3. Calculated spectra S_R from measured S_V or S_I

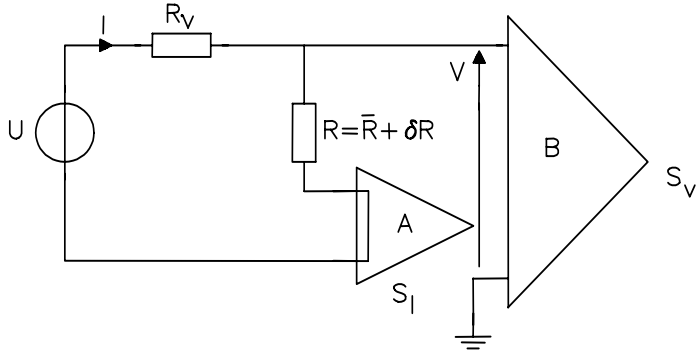

Figure 4. Bias circuit for measuring the spectrum of resistance fluctuation S_R of R with an ideal noise free voltage amplifier B and an ideal noise free current amplifier A.

Consider a sample with fluctuating resistance $R = \overline{R} + \delta R(t)$ with two contacts only in a circuit as in Fig. 4 and biased by a noise free battery U and a series resistance R_v that has thermal noise only. We observe the voltage noise S_v by an ideal voltage amplifier B and the current noise S_I by an ideal current amplifier A in series with the sample. The influence of input resistance of the voltage and current amplifiers can be ignored. Hence, $I = U/(R + R_v)$ and $V = IR = UR/(R + R_v)$. Sample resistance fluctuations result in opposite (fully correlated with different sign) fluctuations in current and voltage as given by relative values

$$\frac{dI}{I} = -\frac{dR}{R+R_v} \text{ and } \frac{dV}{V} = +\frac{dR}{R}\left(\frac{R_v}{R+R_v}\right) \tag{12}$$

These relations hold for quasi-static changes in R around its average value, but also in the frequency domain after band-pass filtering, squaring and averaging. Hence, for the spectral values of $\delta R(t)$, $dI(t)$ and $dV(t)$ holds:

$$\frac{S_I}{I^2} = \frac{S_R}{R^2}\left(\frac{R}{R+R_v}\right)^2 \text{ and } \frac{S_V}{V^2} = \frac{S_R}{R^2}\left(\frac{R_v}{R+R_v}\right)^2 \tag{13}$$

If R_v tends to zero the highest value for S_I is observed and S_v tends to zero. This is in the so-called short circuit limit and only current fluctuations can be observed. For $R_v \to \infty$ and keeping $U/(R+R_v)$ constant ($R_v >> R$), $S_I \to 0$, then we are in the so-called open circuit limit. Only voltage fluctuations are observed. Hence we have for short circuit or open circuit, respectively:

$$\frac{S_I}{I^2} = \frac{S_R}{R^2} \text{ or } \frac{S_V}{V^2} = \frac{S_R}{R^2} \tag{14}$$

The maximum value for S_v at fixed battery voltage is calculated from:

$$S_V = \frac{U^2 R_v^2}{(R+R_v)^4} S_R \text{ and } dS_v / dR_v = 0 \text{ for } R_v = \overline{R} \tag{15}$$

For the calculated relative resistance noise from measured S_V holds:

$$\frac{S_R}{R^2} = \frac{S_V}{U^2}\left(2 + \frac{R_V}{R} + \frac{R}{R_V}\right)^2 \tag{16}$$

The thermal noise of the bias resistor R_v and the sample R will always be the dominant source at higher frequencies. Hence for calibration purposes we must find:

$$S_{Vth} = \frac{4kTR_vR}{R+R_v} \text{ and } S_I = \frac{4kT}{R+R_v} \tag{17}$$

The corner frequency for the voltage amplifier, f_{cV}, and the current amplifier f_{cI} are different. The values are calculated as:

$$f_{cV} = \frac{U^2 R_v RC}{(R+R_v)^3 4kT} \text{ and } f_{cI} = \frac{U^2 R^2 C}{(R+R_v)^3 4kT} \tag{18}$$

The maximum values for f_{cV} occurs for $df_c / dR_v = 0$ which results in a bias condition of $R_v = R/2$. This results in a corner frequency f_{cVmax}, which

is a factor 32/27 higher than f_{cV} for $R_v = R$ leading to the highest S_V. With R_v = 0 in Fig. 4 and a current amplifier only it follows that an ideal current amplifier is always a better choice then an ideal voltage amplifier to study conductance noise considering the value of f_c

$$f_{cV}\,4kT/U^2C = R_V R/(R_V + R)^3 < f_{cI}\,4kT/U^2C = 1/R \qquad (19)$$

Ideal current amplifiers always have a corner frequency of at least 27/4 times higher than the ideal voltage amplifier solution. Current amplifiers are in general the best choice when the sample resistance is of the same order of magnitude or larger than the input impedance of the voltage amplifier.
The input resistance of the voltage amplifier cannot always be ignored. Then the observed voltage noise in Fig. 4 due to resistance fluctuations will be:

$$S_V = \frac{I^2 S_R}{(1 + R/R_i + R/R_v)^2} \qquad (20)$$

The maximum for S_V will be reached not for $R_v = R$, but for $R_V < R$ given by:

$$R_V = R\sqrt{\frac{1}{1 + R/R_i}} \qquad (21)$$

The thermal noise will be given by $S_{Vth} = 4kT(R_v // R // R_i)$ where $(R_v // R // R_i)$ represents the equivalent resistor of R_v, R and R_i in parallel.
For the balanced bridge measurement set-up as shown in Fig. 3 we assume samples which are equal in average value and in statistical properties. Hence, $R_{s1} \approx R_{s2} = R_s$ and $S_{R_{s1}} \approx S_{R_{s2}} \approx S_R$. We assume a constant current through the samples $(R_{v1} \approx R_{v2} = R_v >> R_s)$. This results in a thermal noise at the contacts AB of $S_V = 4kT(2R_s)$. The voltage noise S_{VAB} stemming from uncorrelated fluctuations in R_{s1} and R_{s2} is given by:

$$S_{VAB} = 2I^2_{sample} \cdot S_R \qquad (22)$$

If the balanced bridge contains n $(1 \le n \le 4)$ fluctuating resistances R with noise S_R and $(4-n)$ bias resistors $R_V = \overline{R}$ with $S_{Rv} = 0$ then the noise between A and B in Fig. 3 becomes:

$$S_{VAB} = \frac{n}{4} I^2_{sample} \cdot S_R \tag{23}$$

4. How to suppress contact noise

The noise is often contaminated by an excess noise contribution at the contacts while we are interested in the bulk noise. The contact noise at the driver contacts [7] can be suppressed in a sample provided with a pair of current contacts and a pair of voltage sensing contacts if placed at side arms on a rectangular bar in a field free area [8]. Only then the network as in Fig. 5 is applicable. If the input resistance of the amplifier $R_i >> R//(R_v + r_1 + r_2)$, and defining $R_t = R_v + r_1 + r_2 + R$ we find:

$$S_V = \frac{I^2 S_R}{(1 + R/(R_t - R))^2} + \frac{I^2 S_{r1}}{(1 + (R_t - R)/R)^2} + \frac{I^2 S_{r2}}{(1 + (R_t - R)/R)^2} \tag{24}$$

$$\frac{S_V}{V^2} = \frac{S_R}{R^2}\left(\frac{R_t - R}{R_t}\right)^2 + \frac{S_{r1}}{R_t^2} + \frac{S_{r2}}{R_t^2} \tag{25}$$

S_R represents the resistance fluctuations between the sensing contacts Q_1 and Q_2, S_{r1} and S_{r2} is the uncorrelated contact noise between the driver and sensor contacts D_1Q_1 and D_2Q_2 respectively. Normally we wish to suppress S_{r1} and S_{r2}. In the variable R_v –method we keep the same current I and increase the supply voltage U and R_v. Then the contact contributions can be reduced (24) (25). However, this does not mean that a noise contribution of the sensor contacts Q_1 and Q_2 is excluded! Although the sensor contacts Q_1, Q_2 do not pass an external current towards the amplifier in Fig. 5, there can be a current through this contact entering and leaving at the rims and not going external. This contact noise cannot be suppressed by a four-point probe analysis with the variable R_V -method. The best way to avoid noise

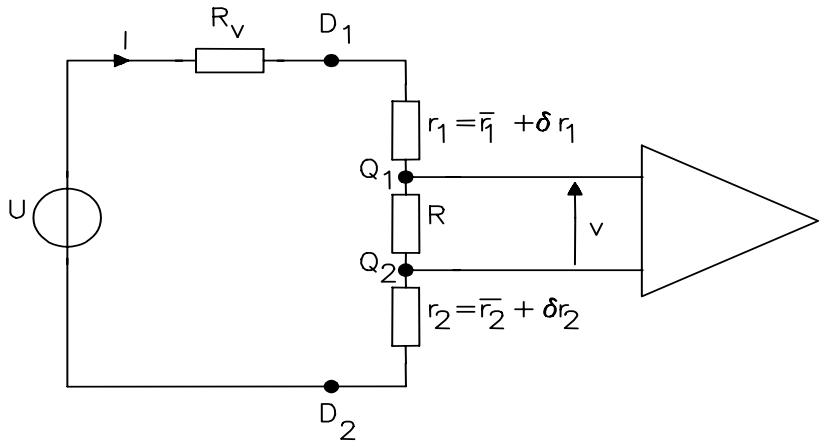

Figure 5. A four-probe configuration with a pair of noisy driver (D_1 D_2) and a pair of sensor contacts (Q1 Q_2).

contributions from the contacts D_1, D_2, Q_1, Q_2 is to put Q_1, Q_2 in a field and current density free area of the sample and not in a current path. A cross-shaped sample as shown in [8] or a rectangular sample with side arms are a nice compromise between a good suppression of the contact noise at D_1, D_2, and Q_1, Q_2 and an increase of thermal noise at the sensors by too long contact arms.

5. Noise measurement of levels lower than the amplifier background-noise

How to measure sample noise buried in the noise of the amplifier? Noise measurements are not only used to characterise devices but can also be used as an effective reliability screening tool [9]. Abnormal high amounts tend to indicate defects in the material. Making noise measurements with a dual channel system outlined in Fig. 6, offers the advantage of an increased sensitivity down to a factor 40 below R_{eq} of one single amplifier.

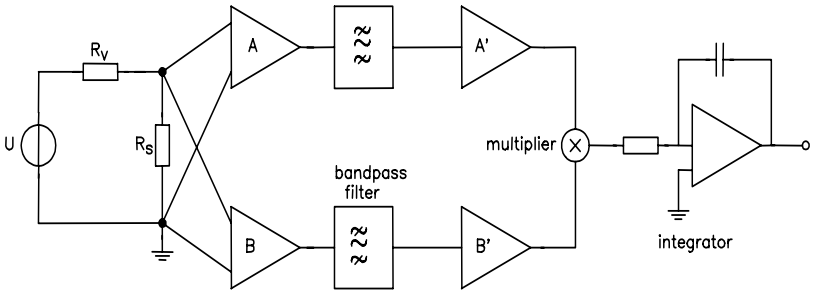

Figure 6. Analogue correlation measurement set-up

The following conditions are important. The cross talk between the amplifiers and the filters must be low. There is only an equivalent voltage noise source at the input of the amplifiers (no current noise source) in the considered frequency range. The multiplication and the integration in an analogue system have no *dc* offset and are drift free. The DUT noise feeds into similar channel A and B. Each channel output consists of both amplified DUT noise and amplifier noise. We can write N_{DUT} (t) + N_A (t) and N_{DUT} (t) + N_B (t) for channel A and B, respectively. After band-pass filtering multiplying and averaging we obtain in the ideal case the cross spectral density S_{AB} *(f)* = *AB* S_{DUT} *(f)*. Uncorrelated fluctuations of amplifier A and B are after multiplying as often positive as negative and the correlated contribution in both channels stemming from DUT are after multiplying always positive and can dominate over the uncorrelated contributions after long integration times.

The most convenient way to calibrate the system is by measuring the thermal noise of the DUT or a calibration network. With the T-network shown in Fig. 7, the correlation system can be calibrated on the thermal noise of R_1, R_2 and R_3. At amplifier A and B, we will observe a noise referred to the input as $(R_{eqA} + R_1 + R_3)$ and $(R_{eqB} + R_2 + R_3)$, respectively. The cross correlation spectrum of the noise common to both channels is proportional to R_3. The coherence function γ^2 is defined by:

$$\gamma^2 = \frac{S_{vAB}^2}{S_{vA} \cdot S_{vB}} = \frac{R_3^2}{(R_{eqA} + R_1 + R_3)(R_{eqB} + R_2 + R_3)} \qquad (26)$$

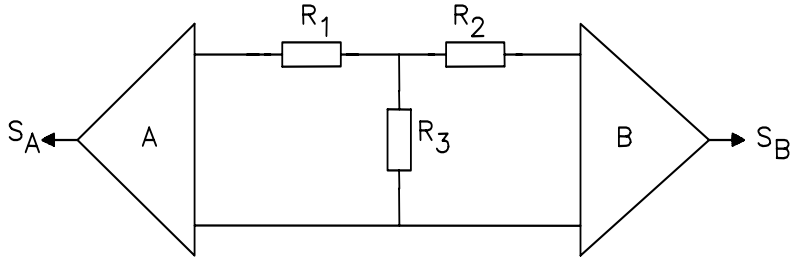

Figure 7. Calibration network for correlation measurements

If we are facing a situation where the noise is 40 times lower than the background noise of the two identical amplifiers then $\gamma^2 \approx 5.95\text{x}10^{-4}$. For a reliable result in S_{vAB} with a dual channel FFT analyser, averaging over a minimum number of time blocks is needed. This is given by [10]:

$$N_{AV} \geq 1/\gamma^2 \tag{27}$$

This means that for a noise level that is 40 times lower than the background, ($\gamma^2 \approx 5.95\text{x}10^{-4}$), $N_{AV} \approx 1700$. For a spectrum starting at 1Hz with a resolution of 1Hz the measuring time is at least half an hour. Another limiting factor is the cross talk between the channels. The cross talk between channels is often given by a factor x. If channel A and B are excited by the noise signals a and b which are completely uncorrelated then the minimum valve γ^2 is calculated for the signals $(a + bx)$ in channel A and $(b + ax)$ in channel B. The minimum value of γ^2 is often 5×10^{-4} depending on the cross talk value x which means that we need at least 2×10^3 averages to detect this floor. A higher amount of averages will not improve the results for situations where the hidden noise is a factor 50 or more below the background noise.

Acknowledgements

The NATO programme Science for Peace (SfP 973799) financially supported part of this work.

References

[1] Suppliers of low noise amplifiers:
EG&G Instruments / Princeton Applied Research.www. egginc.com
NF circuit design LTD. www. Nfcorp.co.jp/english/cprofile.html
DL Instruments, LLC.www.dlinstruments.com
Stanford Research System, Inc. www.srsys.com

[2] L.K.J. Vandamme and G. Trefan, "1/f noise in homogeneous and inhomogeneous media", IEE Proc.-Circuits Devices Syst. **149** (2002) 3-12

[3] L.K.J. Vandamme and R.G.M. Penning de Vries, Correlation between MOST 1/f noise and CCD transfer inefficiency, Solid-State Electr. **28** (1985) 1049-1056

[4] F.M. Tesche, M.V. Ianoz and T. Karlsson, EMC analysis methods and computational Models J. Wiley & Sons Inc. (1997)

[5] H. Kaden, Wirbelströme und Schirmung in der Nachrichten Technik 2nd ed. Berlin Springer-Verlag (1959) 85-87

[6] J.H. Scofield: Rev. Sci. Instrum. **58** (1987) 985

[7] J.J. Brophy, Physical Review **106** (1957) 675-678

[8] L.K.J. Vandamme and A.H. de Kuijper, Conductance noise investigations on symmetrical planar resistors with finite contacts, Solid-State Electronics **22** (1979) 981-986

[9] L.K.J. Vandamme, Noise as a Diagnostic Tool for Quality and Reliability of Electronic Devices , IEEE Trans on Electron Devices **41 (**1994) 2176-2187

[10] J. Briaire and L.K.J. Vandamme, J. Appl. Phys. **84** (1998) 4370-4373

TECHNIQUES FOR HIGH-SENSITIVITY MEASUREMENTS OF SHOT NOISE IN NANOSTRUCTURES

B. Pellegrini, G. Basso, M. Macucci
Dipartimento di Ingegneria dell'Informazione
Università degli Studi di Pisa
Via Diotisalvi, 2 I-56122 Pisa
Italy
b.pellegrini@iet.unipi.it

Abstract Recent theoretical and experimental findings have raised interest in the issue of shot noise suppression and enhancement in nanostructures. Several theoretical predictions have already been confirmed by means of sophisticated experiments, but further work is needed to improve the achievable sensitivity of noise measurements.

We have been working on the integration of several different noise reduction techniques, with the objective of being able to measure the shot noise levels associated with currents of less than a picoampere. We combine the usage of correlation amplifiers, cryogenic cooling of the active elements and feedback resistors, correction techniques based on the substitution impedance method, and the precise evaluation of the transfer function of the amplifiers.

Keywords: Shot noise, noise amplifier, correlation amplifier, nanostructures.

1. Introduction

In the last decade shot noise suppression and enhancement in nanostructures has received growing attention, in the wake of pioneering theoretical predictions that have then found experimental confirmation. Shot noise deviates from the predictions of Schottky's theorem, i.e. a power spectral density equal to $2qI$, where q is the electron charge and I is the average value of the current, whenever the charge carriers do not cross the device with a Poissonian distribution (i.e. independently from one another). Negative correlations between charge transfer events lead to shot noise suppression, while positive correlations lead to shot noise enhancement. Therefore shot noise measurements

J. Sikula and M. Levinshtein (eds.),
Advanced Experimental Methods for Noise Research in Nanoscale Electronic Devices (203 - 210)

can provide a deeper insight into device behavior and physics than standard transport measurements. Currents in nanostructures are often very small, of the order of nanoamperes or picoamperes, thus it is necessary to develop specific equipment for performing reliable measurements of the shot noise power spectral density. In this contribution we present the most recent version of a cryogenic correlation amplifier that we have been developing specifically for the investigation of noise in nanoscale devices.

2. Noise reduction techniques

When performing shot noise measurements, a limit to the minimum measurable noise level is given, in conventional instrumentation, by the amplifier noise contribution, which has to be kept lower than the noise to be measured by at least a factor of 10. Thus a transimpedance amplifier (see Fig. 1) with a feedback resistor in the gigaohm range, will have a sensitivity limited by the thermal noise of such a resistor, and, even if implemented with an operational amplifier with negligible noise contribution, will allow measurement of the shot noise power spectral density associated to currents no smaller than a few hundreds of picoamperes. A partial solution to such a problem consists in lowering the temperature of the feedback resistor: for instance by means of liquid nitrogen, thus achieving a minimum measurable power spectral density which is lower by about a factor of four with respect to room temperature. A better improvement can be achieved if the feedback resistor is operated at liquid helium temperature.

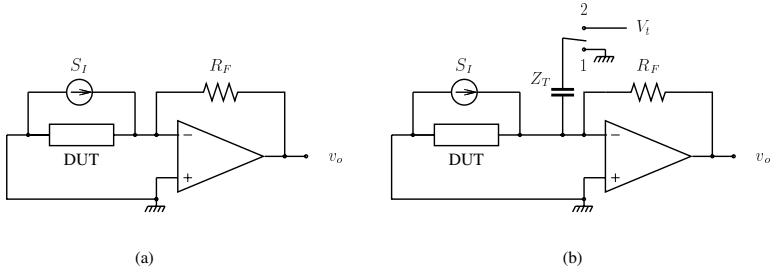

Figure 1. Transimpedance amplifier (a) and schematics of the measurement procedure for the evaluation of the amplifier transimpedance (b).

One further improvement may consist in the subtraction of the power spectral density due to the system (i.e. the one due to the amplifier, to its power supply, and to the bias network) from the result of the measurement. To this purpose, it is necessary to know the value of such a spurious noise power spectral density with great accuracy, in the actual measurement conditions: this

means that its dependence on the differential impedance of the device under test (DUT) has to be taken into account. Therefore a correction procedure can be put into practice, consisting in the evaluation of the system noise by substituting the DUT with a proper impedance, equivalent (in both the real and the imaginary parts) to the one of the DUT itself in the measurement conditions (bias, temperature, etc.) and with a known noise behavior. A new measurement is performed and the subtraction of the known noise of the impedance from the obtained result yields the contribution from stray sources, that can in turn be subtracted from the result of the measurement on the DUT.

Further improvement of the sensitivity can be achieved by means of the accurate measurement of the amplifier transimpedance with respect to the input current noise source, evaluated in the actual measurement configuration, rather than simply relying on a standard measurement of its transfer function. This can be accomplished by means of the circuit arrangement sketched in Fig. 1(b).

The noise amplifier is provided with a test impedance Z_T which can be either connected in parallel to the amplifier input (switch S in position 1) or used in order to drive the amplifier with a known noise generator V_t. With S in position 1 the total noise power spectrum S_o at the amplifier output is measured; then with S in position 2 the frequency response $F(f)$ between the signal source V_t and the amplifier output is measured. Finally, by means of simple calculations [1], it is possible to obtain the current noise power spectrum S_I as

$$S_I = \frac{S_o}{|F|^2 Z_T^2} \,. \tag{1}$$

The impedance Z_T can, in principle, be of any type: we have chosen a capacitor C_T as test impedance, because it does not contribute to the system noise and, in addition, has a quasi-ideal behavior over a wide frequency range. As apparent from Eq. (1), it is necessary to know the exact value of the test impedance Z_T; for this reason C_T has to be chosen large enough with respect to other (stray) capacitances which could affect the result of the evaluation of Eq. (1).

Such a procedure can be automated using a programmable signal analyzer, which performs both the measurements (S_o and $F(f)$) and the calculations finally leading to the current power spectrum S_I. The above described procedures were used in conjunction [2], allowing an over 10 dB improvement in sensitivity.

The system noise can be further reduced by making use of two noise amplifiers, with the application of cross correlation techniques. The principle of operation is conceptually simple (see Fig. 2): the same current noise S_{In} is fed into the two noise amplifiers, and the cross-correlation of the two output signals is evaluated. Since the noise contributions due to the equivalent input current noise sources of the amplifiers are uncorrelated, they are averaged out

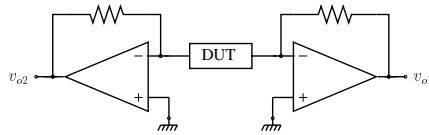

Figure 2. Correlation amplifier

in the procedure: in this way only contributions from the noise source S_{In} and from the sum of the power spectral densities associated with the equivalent input voltage noise sources are present in the final result [3]. If the contribution of the equivalent input voltage noise sources is negligible (as in the case of a DUT impedance much larger than the input impedance of the amplifiers), the result of the procedure is substantially coincident with the device noise power spectral density, with the spurious contributions removed.

3. Correlation amplifier

In order to take advantage of such noise reduction and measurement techniques, a correlation noise amplifier, to be operated with DUT and feedback resistors at liquid nitrogen or helium temperature, has been designed, realized and tested.

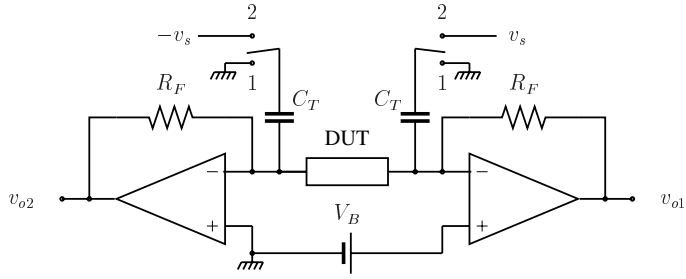

Figure 3. Schematic of the correlation noise amplifier.

The schematic diagram of the correlation amplifier is shown in Fig. 3. It is based on a TLC072 dual operational amplifier, characterized by a very low input current noise (0.6 fA/$\sqrt{\text{Hz}}$ at 1 kHz) and an input voltage noise of 7 nV/$\sqrt{\text{Hz}}$ at 1 kHz and beyond (12 nV at 100 Hz).

Due to the requirements of short wiring to the sample and of low-temperature operation the whole amplifier must be located inside a stainless steel pipe with a diameter of about 30 mm, which, in turn, has to be fitted to a dewar vessel containing the cryogenic liquid. For this reason, the amplifier components (the

op-amps, the feedback resistors, the test capacitance C_T) had to be arranged in such a way as to minimize space occupancy.

Moreover, since proper operation of the op-amps is not guaranteed at very low temperatures, they must be kept at a distance from the cryogenic liquid, whereas the DUT and the feedback resistors have to be kept close to the liquid itself, to warrant the lowest possible temperature. For such reasons, the printed circuit board containing the two operational amplifiers can be moved up to about 50 cm away from the one supporting the feedback resistors, the test capacitances and the device under test.

In addition, particular care has to be taken in preventing the sample holder from coming into contact with the surface of the cryogenic liquid, as its ebullition introduces additional noise, particularly at low frequencies.

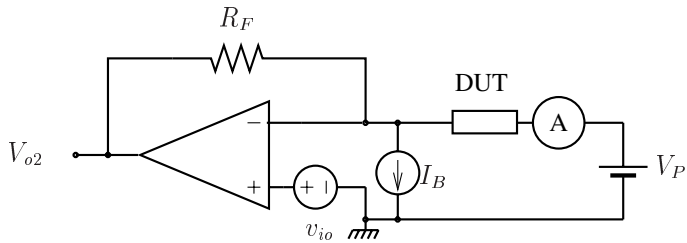

Figure 4. Calibration procedure.

The DUT can be biased by means of a voltage V_B, applied between the noninverting inputs of the two operational amplifiers. In many cases (for instance, when measuring shot noise) one is interested in knowing with very good accuracy the value of the current through the device under test: this can be achieved by measuring the DC voltage V_{o2} at the output of one of the two op-amps. However, especially for very low current levels, such a measurement may be affected by sources of nonideality, such as the operational amplifier bias current and offset voltage: a calibration procedure is therefore necessary. To perform such a calibration (Fig. 4), one of the two operational amplifiers is disconnected, the DUT is biased and the current flowing through it is directly measured by means of a picoammeter for several values of the bias voltage V_P. Then a calibration chart is obtained, listing the values of the output voltage V_{o2} as a function of the measured current through the device. This chart is then used during noise measurements (when both operational amplifiers are connected and the current cannot be directly measured), to obtain the value of the bias current from the measurement of the output voltage.

4. Measurement procedure and experimental results

4.1. Thermal noise

In order to test the correlation amplifier, it was first used for thermal noise measurements on several resistor as DUTs; the value of the feedback resistors has been raised up to $3\,\mathrm{G}\Omega$, which allows higher sensitivity of the amplifier with respect to previous versions [4].

The procedure for thermal noise measurements requires, first of all, the evaluation of the cross spectrum S_{v1v2} of the voltage outputs of the amplifiers. Such a result is obtained by means of a two-channel digital signal analyzer (SR785) by Stanford Research Systems.

Then the same instrument allows the measurement of the transimpedance of the amplifier with respect to the two output ports. For this purpose, a known signal v_s (see Fig. 2) is injected into one of the two amplifiers, and an opposite signal $-v_s$, obtained from the first by means of a unit gain inverting amplifier, into the other one. With such a setup, the transfer function $A_1(f)$ from the input v_s to the output v_{o1} is measured. Then the input signals are interchanged and the second transfer function, $A_2(f)$ from the input v_s to the output v_{o2} is measured.

Finally, the noise current power spectral density is obtained as

$$S_I(f) = \frac{S_{v1v2}}{A_1(f)A_2^*(f)Z_T^2} = \frac{-4S_{v1v2}\pi^2 f^2 C_T^2}{A_1(f)A_2^*(f)} \tag{2}$$

where $A_2^*(f)$ is the complex conjugate of $A_2(f)$. The relationship in Eq. (2) represents the extension of Eq. (1) for the correlation amplifier.

As an example, the result obtained for a resistor $R = 3\,\mathrm{G}\Omega$ as a DUT and (as it has already been stated) with $3\,\mathrm{G}\Omega$ feedback resistors, is shown in Fig. 5; the measurement was performed at a temperature $T = 92.4\,\mathrm{K}$. The theoretical value is indicated with a thin line, for comparison.

It is worth noting that, in order to obtain the best results from the correlation technique, it is necessary to average the cross spectrum over a large number of measurements. Due to the fact that the narrower the measurement frequency band, the longer the time necessary for for the time record acquisition is, such a result requires a total data acquisition time of a few hours.

4.2. Shot noise in p-n junctions

Further tests on the correlation amplifier were performed by means of shot noise measurements on a Ga-As p-n junction. In this case, a bias voltage V_B for the DUT has to be applied between the noninverting inputs of the operational amplifiers (Fig. 3).

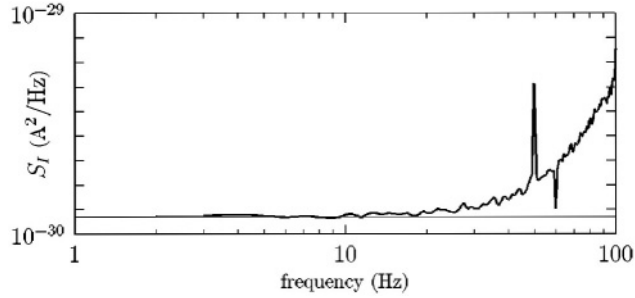

Figure 5. Thermal noise power spectrum for a resistor $R = 3\,\mathrm{G}\Omega$ at $T = 92.4\,\mathrm{K}$: measured value (thick line) and theoretical value (thin line).

After performing the previously described calibration procedure, the actual bias current through the device can be inferred from a measurement of the output DC voltage V_{o2}. The same feedback resistors $R_F = 3\,\mathrm{G}\Omega$ as before were used in this case, in order to obtain the highest possible sensitivity.

The measurement procedure requires, also for shot noise measurements, first the evaluation of the cross spectrum S_{v1v2}, then the measurement of the two transfer functions $A_1(f)$ and $A_2(f)$, and finally the calculation of the noise current power spectral density, by means of Eq. (2).

In Fig. 6 results obtained from such measurements are reported. In particular, the power spectral densities for the bias currents $I_B = 5\,\mathrm{pA}$, $I_B = 800\,\mathrm{fA}$ and $I_B = 190\,\mathrm{fA}$ (thick lines) are shown and compared to theoretical values (thin lines).

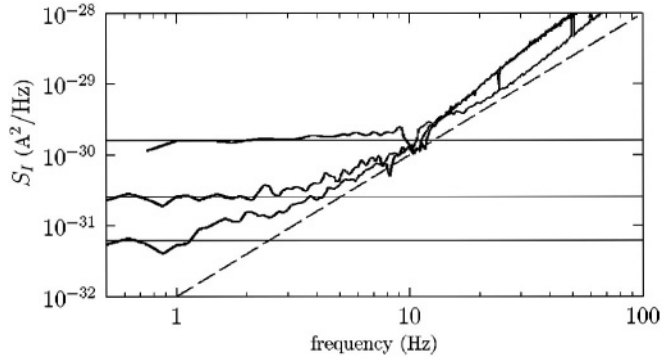

Figure 6. Measured shot noise power spectra at currents $I_B = 5$ pA (upper thick line), $I_B = 800$ fA, and $I_B = 190$ fA (lower thick line), compared with theoretical values (thin lines).

5. Conclusions

We have presented results obtained with a cryogenic correlation amplifier for measurements of thermal noise and of shot noise at very low current levels. Thanks to the application of the correlation technique, of a procedure for the precise evaluation of the transimpedance, and of cryogenic cooling of the feedback resistors, it has been possible to measure reliably the shot noise power spectral density associated with a current of 0.19 pA. We plan further improvements, consisting in the reduction of stray capacitances in order to increase the bandwidth over which measurements can be performed and in further suppression of mechanical noise on the sample holder, with the aim of reaching an even better sensitivity.

Acknowledgments

We gratefully acknowledge financial support from the Italian CNR (National Research Council) through the "5% Nanotecnologie" project and from the cofunding program of the University of Pisa.

References

[1] M. Macucci and B. Pellegrini, Very Sensitive Measurement Method of Electron Device Current Noise, IEEE Trans. Instrum. Meas. 40 (1991) 7-12.

[2] G. Lombardi, M. Macucci, R. Giannetti, and B. Pellegrini, Cryogenic amplification system for ultra-low noise measurements, J. Phys. IV France 8, (1998) Pr3-185-188.

[3] M. Sampietro, L. Fasoli, and G. Ferrari, Spectrum analyzer with noise reduction by cross-correlation technique on two channels, Rev. Sci. Instrum. 70 (1999) 2520-2525. 2520 (1999).

[4] G. Basso, M. Macucci, M. Casarin, and B. Pellegrini, Ultra low-noise cryogenic correlation amplifier for shot noise measurements, Proc. of the 16^{th} International Conference on "Noise in Physical Systems and 1/f Fluctuations" (2001) 697-700.

CORRELATION SPECTRUM ANALYZER: PRINCIPLES AND LIMITS IN NOISE MEASUREMENTS

G. Ferrari and M. Sampietro

Dipartimento di Elettronica e Informazione, Politecnico di Milano
P.za L. da Vinci 32, 20133 Milano
Italy

Marco.Sampietro@polimi.it

Abstract The paper describes the principles of operation and the expected performance of correlation spectrum analyzers in the detection and measurement of stationary noise produced by passive or active devices under test (DUT). It is shown that a sensitivity of few pV/√Hz in voltage noise measurements and of few fA/√Hz in current noise measurements may be reached with a properly long measurement time rarely exceeding few hours. The paper highlights the role of the DUT impedance and of the amplifiers noise sources in setting the sensitivity limit of the instrument as given by the generation of spurious correlated signals that feed both channels.

Keywords: Spectrum analyzer, Noise measurements, Correlation technique, High sensitivity measurements

1. Introduction

Beside setting the performance of newly conceived devices, noise has revealed itself to be an extraordinarily powerful tool to investigate the properties of transport phenomena at a very basic level. Single carrier trapping and detrapping, carriers diffusion in solids, fractionally charged quasiparticles in quantum Hall systems or many others, have all found a clear explanation through a noise approach [1-4]. Very recently, also new field of research, like protein dynamics and molecular transport, are posing new important questions that may find an answer from noise measurements. The challenge for the experimenter is to track this evolution and to conceive

J. Sikula and M. Levinshtein (eds.),
Advanced Experimental Methods for Noise Research in Nanoscale Electronic Devices (211 - 218)

measuring tools with constantly better sensitivity and flexibility to adapt to an increasingly vast field of applications.

When the noise to be measured is stationary, the cross-correlation technique has proven to be effective to overcome the limitations imposed by the electronic noise of the instrument amplifier and to extend the sensitivity of noise measurements to very good values. An instrument using this technique, which we call a correlation spectrum analyzer, is based on the processing of signals from two independent channels operated in parallel and takes advantage of the uncorrelated properties of the noises of the two input stages. This class of analyzers is effectively becoming more and more popular in the research activities as the need of very low noise measurements is increasing [5-8].

2. Description of the instrument

2.1. Principles of operation

Fig. 1 shows a basic scheme of the Correlation Spectrum Analyzer [9,10]. The signal from the DUT is fed to two distinct and independent input amplifiers operated in parallel, followed by a frequency selector circuit and a correlation stage that multiplies each component of the two channels. An integrator stage averages with time the result. Besides the input amplifiers, the other functions may be performed by a digital processor using sampled values of the two input amplifiers outputs.

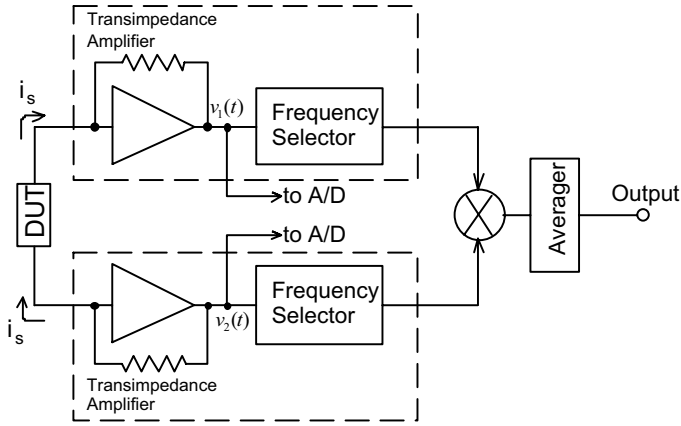

Figure 1. Schematics of the building blocks of the Correlation Spectrum Analyzer.

The signal to be measured from the DUT is therefore processed in phase by the two channels and multiplied frequency by frequency to give at the output a signal with mean value proportional to the DUT input signal at each selected frequency. In the case of DUT noise measurements, this will produce the DUT noise power density. The noise components of the two input amplifiers, instead, are uncorrelated each other (out of phase) and give at the output of the multiplier a signal with zero mean value and standard deviation equal to the input amplifier noise power density at each frequency.

The standard deviation $\sigma_{S_{DUT}}$ of the fluctuations around the DUT power density value at the output of the instrument can be written [9] as

$$\sigma_{S_{DUT}} = \overline{s_n^2} \cdot \frac{1}{\sqrt{2 \cdot RBW \cdot T_m}} \tag{1}$$

where RBW is the resolution bandwidth of the spectrum. In the case of N samples taken at a sampling frequency f_s, the resolution bandwidth is equal to $RBW=f_s/N$. Equation (1) gives the equivalent input noise of the instrument after a measuring time T_m. Few minutes measuring time are in general sufficient to improve sensitivity by an order of magnitude, and few days give another factor of ten.

The time needed to obtain a given sensitivity can be traded with the resolution bandwidth RBW, as indicated by Eq.(1): a frequency resolution relaxed by a factor of 10 would need 10 times faster measurement for the same noise sensitivity. This, of course, implies that the low frequency section of a DUT spectrum would require a proportionally long measurement time.

2.2. Effect of channel non-uniformity

The instrument is relatively insensitive to nonuniformity in gain and phase between the two channels. A phase difference $\Delta\varphi$ between the two channels results in a product between correlated signals reduced by a factor $cos(\Delta\varphi)$, while leaving unaffected the uncorrelated noise components. The consequence of a phase difference is therefore to reduce the useful output signal (gain) without modifying the superimposed uncorrelated noise and can be recovered by a slight extension of the measuring time. Different gains in the two channels affect correlated and uncorrelated signals in the same way and therefore do not play any role in setting the instrument sensitivity. The precision in the calculation of the system gain and of its frequency response will set the accuracy of the measurement.

2.3. Quantisation noise

The peculiarity of the Correlation Spectrum Analyzer to measure DUT signals much smaller than the instrument noise implies that the dynamic range of the A/D converters should be set in accordance to the instrument noise and that the DUT signal may, in some cases, be comparable to the least significant bit (LSB). This extreme situation does not introduce, however, quantisation errors nor prevent the measurement to be performed correctly. This is because the small DUT signal is summed in the same direction to both the large uncorrelated instrumental noises of the two channels. The large instrumental noise shifts the small DUT signal randomly across almost the full dynamic range of the A/D converter. The correlation procedure performed by the instrument sorts out the small DUT signal common to both channels. In addition, thanks to the random sweep across the ADC dinamics, the differential nonlinearities of the converter are averaged down by the number of quantisation levels covered by the instrumental noise [11] and do not produce spurious effects.

3. Limits in noise measurements

The level of fluctuation given by Eq.(1) defines the minimum DUT signal that can be ideally measured. In practice, the ultimate performance of the instrument in term of sensitivity is set by the amount of correlated spurious signals generated by those sources of noise in the input preamplifiers that produce a signal exactly in parallel to the one produced directly by the DUT. Fig. 2 shows the noise sources and the electrical connections that are responsible for these correlated spurious signals in the case of a current sensitive set-up (Fig.2a) and of a voltage sensitive set-up (Fig.2b). These correlated components are read by the two channels of the instrument the same way as the DUT component and can therefore not be removed.

3.1. Current sensitive set-up

For what concerns current noise measurements with the set-up of Fig.2a, the correlated component is produced by the noise voltage sources $\overline{e_n^2}$ and sets the minimum DUT signal that can be measured by the instrument as:

$$\overline{i_{corr}^2} = 2 \cdot \overline{e_n^2} \left[\frac{1}{R_D} \left(\frac{1}{R_F} + \frac{1}{R_D} \right) + \omega^2 C_D \left(C_D + C_{stray} \right) \right] \qquad (2)$$

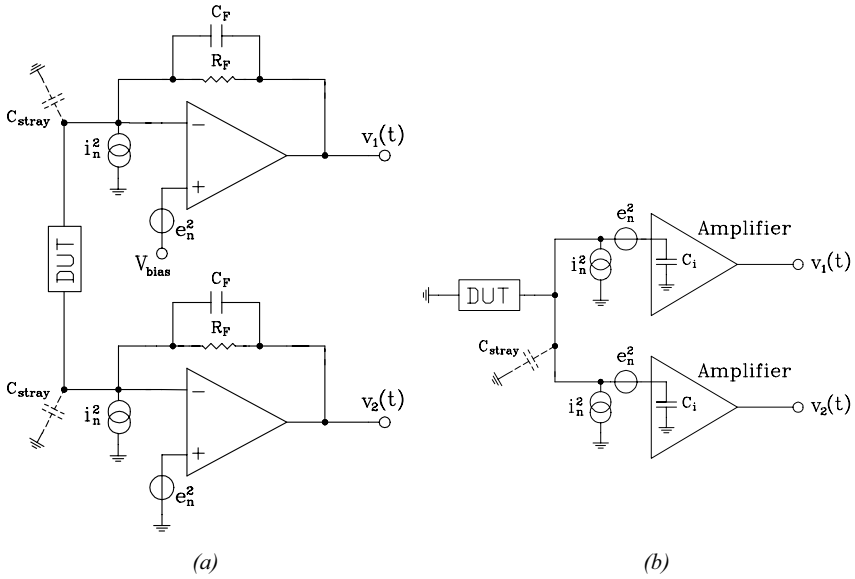

Figure 2. Schematics of instrument input stage for the case of a current sensitive set-up (a) and of a voltage sensitive set-up (b). Main noise sources, parasitic capacitances and DUT impedance are indicated to help in the evaluation of the spurious correlated signal that set a lower limit in the instrument sensitivity.

where R_D and C_D are the equivalent resistance and capacitance of the DUT and C_{stray} is the stray capacitance of the connection. We have assumed that both amplifiers and connections are exactly equal. The limits predicted by Eq.(2) are function of the frequency and of the impedance of the DUT.

Note that at low frequencies the 1/f noise component of $\overline{e_n^2}$ may be the limiting factor. Special care should therefore be taken when designing the transimpedance amplifier by choosing low 1/f noise components for the input stage.

At high frequencies, the second term in Eq.(2) increases and becomes the limiting factor when the impedance of the DUT is particularly large. This is unavoidable and practically sets the effective bandwidth of the instrument, when measuring very low noise levels, to less than 1MHz. It is evident from Eq.(2) that a DUT with a large resistance R_D and a small capacitance C_D would fully exploit the capability of the instrument reaching noise levels well below the femtoAmperes/√Hz.

3.2. Voltage sensitive set-up

For what concerns voltage noise measurements with the set-up of Fig.2b, the correlated noise can be summarized by the equivalent voltage noise source, $\overline{v_{corr}^2}$ whose value

$$\overline{v_{corr}^2} = 2 \cdot i_n^2 R_D^2 + 2 \cdot e_n^2 \omega^2 R_D^2 (C_D + C_{stray} + C_i) C_i \qquad (3)$$

can be directly compared to the noise $\overline{v_{DUT}^2}$ produced by the DUT. The first term in the sum reduces to a negligible value thanks to the very small value of $\overline{i_n^2}$ of amplifiers with a JFET input transistor. The second term, which increases with frequency, becomes significant only when the DUT resistance is high, in our instrument for example only when R_D is higher than about 100Ω.

4. Current versus voltage measurements

As most of the primary physical noise sources in electronic devices are in the form of current, the current-sensitive scheme is often preferred as closer to physical intuition. It has practical advantages in term of simplicity of connection and biasing of the device directly through the instrument and, by avoiding voltage conversion, often simplifies the measuring set-up leading to an improvement of the overall performance. Nevertheless, the clue to make the choice between current-sensitive or voltage-sensitive set-up stands on the DUT impedance.

To compare the sensitivity of the voltage and the current scheme, we can refer to Fig. 3 where the noise temperature of the instruments is reported as a function of the DUT resistance. The dashed lines indicate the sensitivity limit in the measurement of devices with no bias applied. The Current correlation scheme should be chosen whenever the DUT resistance is larger then about 300kΩ.

The range of applicability of the current scheme extends further to lower DUT resistances when a bias is applied to the DUT. The continuous curves in Fig. 3 report the instrument best performance in the case of a biasing network of 100kΩ resistance, showing that the current scheme is already advantageous at 10kΩ DUT resistance.

With a commercial single-channel spectrum analyzers, the performance of the measurement would be the one indicated by the dots.

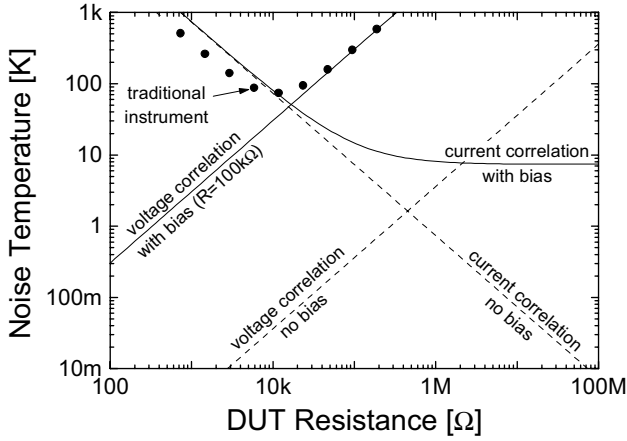

Figure 3. Comparison between the current-sensitive scheme and the voltage-sensitive scheme in term of Noise temperature of the correlation spectrum analyzer. The dashed line indicates the sensitivity without bias applied, whereas the continuous line reports the case with bias. The dots indicate the sensitivity of a traditional single channel analyzer

5. Comparison with standard spectrum analyzer

In a comparison with a standard spectrum analyzer, a correlation-based instrument shows not only a significant advantage in term of sensitivity, but also advantages in term of dynamic range, bandwidth and immunity to stray capacitance. To understand this point consider for example the current sensitive set-up of Fig. 2a in which the feedback resistance R_F of the transimpedance amplifier may be chosen low enough to manage the standing current from the DUT and/or to extend the bandwidth of the instrument (inversely proportional to R_F) as required (or imposed) by the application. The sensitivity of the measurement would not be affected by this reduction of R_F as long as a correspondingly longer measuring time is used. Conversely, if only one transimpedance amplifier is used, as it is the case in a standard analyzer, the reduction of R_F to satisfy dynamic range or bandwidth would reduce sensitivity correspondingly.

By considering the effect of a stray capacitance, in a standard analyzer the signal produced by the input voltage noise through the stray input capacitance sums directly to the DUT signal and reduces the instrument sensitivity. In a correlated instrument, the signal generated on the stray capacitance tends to flow on a single channel (depending on the DUT impedance) and therefore may be reduced by proper averaging time. Only

the fraction that flows trough the DUT is correlated on the two channels and sets the sensitivity limit of the instrument.

Acknowledgements

Authors would like to thank E.Gatti and D.Natali for the many interesting discussions. Work supported by italian CNR and INFN.

References

[1] *Noise and Fluctuations Control in Electronic Devices*, edited by A.A. Balandin, Los Angeles, USA: American Scientific Publishers, 2002.

[2] L. K. J. Vandamme, IEEE Trans. Electron Devices **41** (1994), 2176.

[3] J.Sikula and L. Štourač, Proc. 23rd Int. Conf. on Microelectronics (2002), 767.

[4] G. Gomila and L. Reggiani, Phys. Rev. B **62** (2000), 8068.

[5] L.Saminadayar, D.C.Gattli, Y.Jin and B.Etienne, Phys.Rev.Lett.**79** (1997), 2526.

[6] D.C.Gattli, P.Jacques, A.Kumar, P.Pari and L.Saminadayar, J.Appl.Phys. **81** (1997), 7350.

[7] G.Basso, M.Casarin, M.Macucci, B.Pellegrini, in Proceedings of the 16th ICNF 2001 (2001), 697.

[8] M.Sampietro, G.Ferrari and G.Bertuccio, J.Appl.Phys., **87** (2000), 7583.

[9] M.Sampietro, L.Fasoli and G.Ferrari, Rev.Sci. Instrum. **70** (1999), 2520.

[10] G.Ferrari and M.Sampietro, Rev. Sci. Instr. **73** (2002), 2717.

[11] C. Cottini, E. Gatti, V. Svelto. Nucl. Instr. And Meth. **24** (1963), 241.

MEASUREMENT AND ANALYSIS METHODS FOR RANDOM TELEGRAPH SIGNALS

Z. Çelik-Butler

University of Texas at Arlington, Electrical Engineering Department / Nanofab
Box 19072, Arlington, TX 76019
USA

zbutler@uta.edu

Abstract Large-area device noise models are based on ensemble averaging techniques. Typically, the physical mechanisms leading to fluctuations of microscopic entities, such as charge carrier number or mobility can be modeled by connecting these fluctuations to noise in a measurable device parameter, such as voltage or current. In the process, ensemble averaging of independent (or some times dependent) fluctuators is done to obtain an "average" power spectral density function that agrees with the experimentally measured one. This procedure breaks down in small area devices where the observed noise is basically a single electron phenomenon. Small devices can be manufactured with a single defect which in time domain show only two level switching signals known as burst noise and/or Random Telegraph Signal (RTS) noise. The RTS noise in sub-micron MOSFETs usually dominates over all the other noise sources and becomes a major noise generator for low frequency region of spectrum. With usual oxide and interface trap densities in the order of 10^{10} eV cm^{-2}, active traps being located only within a few k_BT around the Fermi level, a sub-micron MOSFET of 1.0×0.15 μm dimensions will have only 78% chance of having an active electron trapping site. Therefore, it will be a hit or miss situation to observe RTS in the signal. It is essential to be able to perform accurate measurements of RTS both in time and frequency domains, not only to be able to understand, analyze and model the noise in these advanced devices, but also to use RTS measurements as a characterization tool for the interface and bulk traps responsible for these RTS events.

Keywords: Random Telegraph Signals, Noise, MOSFETs, Noise Measurements

1. Introduction

RTS or Random Telegraph Signals are fluctuations in the current or voltage with random discrete pulses of equal heights. RTS due to several

J. Sikula and M. Levinshtein (eds.),
Advanced Experimental Methods for Noise Research in Nanoscale Electronic Devices (219 - 226)

trapping centers can produce multi-level amplitude fluctuations superimposed on each other, thus provide a complicated noise behavior. A simple two level RTS can be seen in various types of semiconductor devices such as bipolar junction transistors (BJT), and metal-oxide-semiconductor field effect transistors (MOSFET). A systematic analysis of two level RTS can be made to obtain information about the physical location and energy of the defect center causing the RTS. There are hundreds of active traps in large area devices causing superposition of single RTS's leading to Lorentzian or $1/f$ noise spectra depending on the distribution of the capture and emission time constants associated with these traps. It is expected that as the devices continue to scale down, there will be an increased need to understand and model the role of RTS in noise.

In this workshop, we present the methods of measurement and analysis for RTS. The experimental setups are described. Two RTS measurement methods, time and frequency domains, are explained. The techniques presented here would be applicable to any nanoscale device exhibiting two-level RTS. In the last section, we discuss the method of analysis to obtain the RTS characteristics, capture and emission times and RTS amplitude using both time and frequency domain data.

In addition to simple two-level RTS, there also have been reports of complex RTS showing three or more levels, rapidly switching RTS modulated by an envelope of the same amplitude as well as RTS with various anomalous behavior. Although a complete physical explanation of these complex switching phenomena has not been made yet, plausible hypotheses have been offered, involving trapping configurations that exist in two or more metastable states and multi-electron trapping by the same site. Explanation of complex RTS is perhaps the single most outstanding issue in switching phenomena observed in microstructures.

Through careful time and frequency domain analysis, the effect of each trap on complex RTS can be de-coupled.

2. Measurement Methods

The RTS obtained at different biasing conditions can be analyzed in time domain and frequency domain. In time domain analysis, we use the data obtained from a digital oscilloscope as shown in Fig. 1. The frequency domain analysis is done using the data obtained from a signal analyzer. The noise power spectrum shows a Lorentzian form due to the RTS with two level switching. As an example, the voltage noise power spectrum of a MOSFET as a function of frequency obtained at V_{gs}=1.3 V and V_{ds}=0.05 V is shown in Fig. 2 with a Lorentzian fitting.

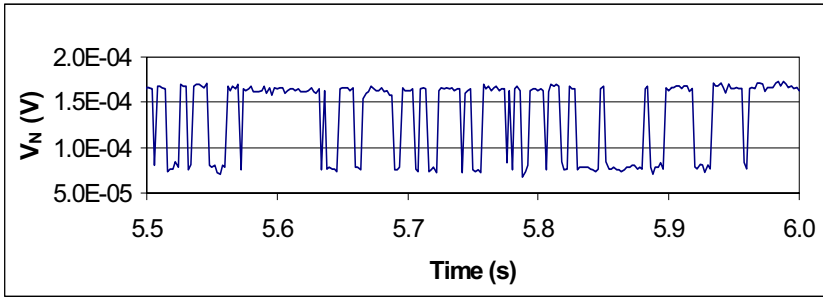

Figure 1. A sample RTS in time domain, showing two-level switching.

In a MOSFET, if $\bar{\tau}_1$ is the mean-time that the drain voltage spends in state 1 and $\bar{\tau}_0$ is the mean-time in state 0, then it can be shown that the probability of a transition from 0 to 1 is given by $1/\bar{\tau}_0$, and the probability of a transition from 1 to 0 is given by $1/\bar{\tau}_1$ [1]. Depending on the type of the trap involved (acceptor or donor) and the type of the carrier, the states 1 and 0 can be identified as capture τ_c and emission τ_e of the carrier from and to the relevant band by the trap.

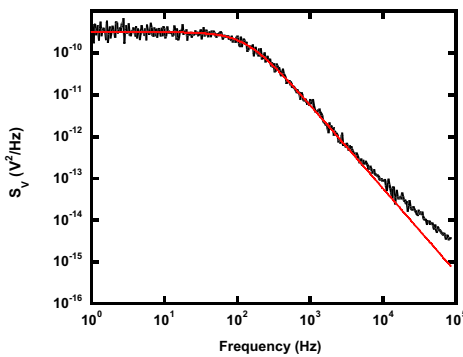

Figure 2. RTS in frequency domain with Lorentzian fitting.

2.1. Time Domain Measurements and Analysis

In time domain, the RTS data is obtained from a digital oscilloscope, preferably interfaced to a computer. Window size of the sampled data is an important aspect of the time domain observations. There are two factors that

need to be considered: resolution and number of transitions. Fast sampling rate (or high resolution) is desired so that no transitions (pulses) are missed in the data. However, a large enough window is also needed that contains at least 200 transitions for a meaningful statistical average. Defining a voltage level between the maximum and minimum voltage levels in the RTS time domain data, one can compute times that wave form spends above and below that defined level and hence calculate $\bar{\tau}_c$ and $\bar{\tau}_e$.

If there are sufficient number of transitions between those two levels, using Poisson analysis, more accurate values for $\bar{\tau}_c$ and $\bar{\tau}_e$ can be obtained. According to Kirton and Uren [1], in order to have a less than 10% error, there must be at least 200 transitions within at least 20,000 data points. Here $\bar{\tau}_c$ and $\bar{\tau}_e$ are obtained by fitting a curve to the distribution of capture and emission times separately. Using the noise data obtained from a digitizing oscilloscope, mean capture and emission times can be calculated by a graphical method. In this method, we define a voltage level in between the minimum and maximum voltage levels in the graph of drain voltage noise versus time as shown in Fig. 1**.** Every voltage above this defined level is classified as a "1" and every voltage equal to or below this level is classified as a "0". A single set of time domain data contains about 20,000 data points. Multiplying the "1"s and "0"s by sampling rate and averaging, the mean value of the time spent above the level which is called $\bar{\tau}_1$, and the mean time spent below the level which is called $\bar{\tau}_0$ can be obtained. This method works best when there are only two discrete voltage levels, a clear "1" and "0". If it becomes difficult to determine such a level without getting false readings, e.g. a "1" mistakenly classified as a "0" and vice versa, it is better to rely on an alternate method of analysis such as the spectral analysis, or the Poisson analysis.

The amount of time spent in either the "1" or "0" state follows a Poisson distribution. If there are enough transitions with well-distributed capture and emission times, we can use the Poisson method of analysis and expect reasonable values for $\bar{\tau}_1$ and $\bar{\tau}_0$. In this method, the total time is broken into small intervals, and then the number of pulses in each interval that have a width that falls into each time interval is counted. A plot of the frequency of pulses for each time width should follow a Poisson distribution, $p_0 e^{-t_0(t)}$. As an example, this distribution obtained from our actual data is shown in Fig. 3. $\bar{\tau}_1$ and $\bar{\tau}_0$ are then calculated using the equation:

$$\tau_{1/0} = \frac{\sum_i (t_i) p_0 e^{-t_0(t_i)}}{\sum_i p_0 e^{-t_0(t_i)}} \qquad (1)$$

The parameter t_0 and p_0 can be obtained as fitting parameters. If the values for $\bar{\tau}_1$ and $\bar{\tau}_0$ calculated from the Poisson analysis are close to those calculated from the time analysis, then this indicates a good data set with a Poisson distribution and enough transitions for minimal error.

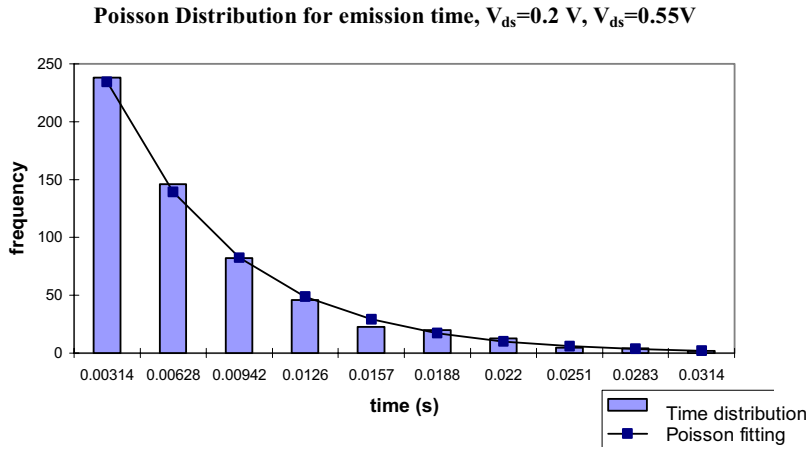

Figure 3. Distribution of emission times for a RTS with a Poisson distribution fitting.

The amplitude is another important parameter in RTS. Based on the correlation theory of $1/f$ noise where current (or voltage) fluctuation due to a single electron capture and emission by a defect at or near the semiconductor – dielectric interface can be interpreted mathematically in terms of number and mobility fluctuations as [1]:

$$\frac{\Delta I_d}{I_d} = \frac{1}{W \times L}\left(\frac{1}{N}\frac{\partial N}{\partial N_t} \pm \frac{1}{\mu}\frac{\partial \mu}{\partial N_t}\right) \qquad (2)$$

where, N_t is the number of occupied traps per unit area, N is the number of carriers per unit area, W is the channel width, L is the channel length, and μ is the carrier mobility. The expression above is written for the drain current of a MOSFET. Similar expressions can be written for other advanced devices. The sign in front of the mobility term depends on the trap type, accepter or donor. The term $\partial N / \partial N_t$ is approximately equal to –1 when the number of carriers per unit area, N, is greater than 10^{11} cm^{-2}. According to Matthiessen's rule as $1/\mu = 1/\mu_n + 1/\mu_{ox} = 1/\mu_n + \alpha N_t$. Here, α is the carrier scattering coefficient, μ_{ox} is the mobility limited by oxide charge scattering.

μ_n is the mobility limited by other scattering mechanisms. Therefore, Eq. (2) can be rewritten as:

$$\frac{\Delta I_d}{I_d} = -\frac{1}{W \times L}\left(\frac{1}{N} \pm \alpha\mu\right) \tag{3}$$

This is the basic expression for drain current fluctuation due to RTS in small scale MOSFETs. In deep sub-micron devices, as the device dimensions approach to electron mean free path, quantum effects become more significant. In highly doped deep sub-micron MOSFETs, a triangular potential well can be created with a high enough electric field in the inversion layer. If the width of this potential well is small compared to the wavelength of the carriers, the conduction band is quantized into discrete energy levels. Although RTS have been studied extensively, the quantization effect on the main parameters of RTS: capture and emission times and the RTS amplitude, has not been fully understood.

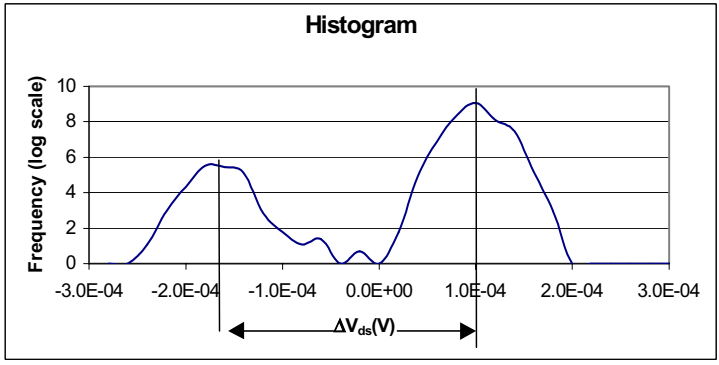

Figure 4. Histogram of the time-domain data. The distance between the two maxima corresponds to the RTS amplitude.

The RTS amplitude can be calculated by the noise data obtained in the time domain. In order to do this, statistical methods can be used either numerically or graphically. In both schemes, the voltage (or current) vs. time data is used. In order to extract the value for RTS amplitude numerically, a voltage between higher and lower voltage levels is selected and the hence average upper and lower voltage levels are statistically calculated. In graphical scheme, the time domain data is displayed in a histogram as shown in the Fig. 4. The distance between two maxima provides the RTS amplitude.

2.2. Frequency Domain Measurements and Analysis:

A typical frequency domain measurement system consists of biasing circuitry, device under test (DUT), a pre-amplifier in AC mode (preferably differential), and a signal analyzer. In the case of a voltage noise spectral density measurement, the resistance in series with the DUT is made large enough to minimize the contribution to fluctuations from the circuitry. The biasing circuit is preferably battery operated to avoid ac/line pick-up at 60 (or 50) Hz and its harmonics. For the same reason, a shielded room or at least an enclosure is required, made of a high-permeability metal that will shield against planar and magnetic waves down to low frequencies. Metal-film or wire-wound resistors and potentiometers are used. The background noise of the system is measured separately and subtracted from the total noise measured with the device biased.

The voltage power spectral density of an RTS is given by [2]:

$$S_V(f) = \frac{4\Delta V_{ds}^2}{(\bar{\tau}_1 + \bar{\tau}_0)\cdot\left[\left(\frac{1}{\bar{\tau}_0} + \frac{1}{\bar{\tau}_1}\right)^2 + (2\pi f)^2\right]} \tag{4}$$

where ΔV_{ds} is the RTS amplitude, in other words, the average drain voltage difference between the level 1and 0. Let

$$\frac{1}{\tau} = \frac{1}{\bar{\tau}_0} + \frac{1}{\bar{\tau}_1} \Rightarrow \tau = \frac{\bar{\tau}_0 \bar{\tau}_1}{\bar{\tau}_0 + \bar{\tau}_1} \tag{5}$$

and

$$f_0 = \frac{1}{2\pi\tau}, \quad k = \frac{4\tau^2 \Delta V_{ds}{}^2}{\tau_0 + \tau_1} \tag{6}$$

then

$$\bar{\tau}_{0/1} = \frac{2\tau^2 \Delta V_{ds}{}^2}{k}\left[1 \pm \sqrt{1 - \frac{k}{\tau \Delta V_{ds}{}^2}}\right] \tag{7}$$

These $\bar{\tau}_0$ and $\bar{\tau}_1$ are distinguished by the + or – sign in Eq. (7) and they correspond to mean capture and emission times of the RTS depending on the trap type, acceptor or donor. One can use Eqs. (6) and (7) to rewrite the Eq. (4) as:

$$S_V(f) = \frac{k}{1 + (f/f_0)^2} \tag{8}$$

Using curve fitting tools, the knee frequency f_0 and the corresponding power spectral value k can be calculated (Fig. 2). From k, f_0, and ΔV (calculated

from time domain analysis), $\bar{\tau}_1$ and $\bar{\tau}_0$ can be obtained utilizing Eq. (7). Since, in most cases, we can find more than one trap active close to the interface in a certain gate voltage range, better fitting can be obtained if we sum up contributions of different traps.

3. Summary

A brief description of experimental techniques has been provided for analysis and measurements of random telegraph signals. Unlike most other noise measurements systems, where a frequency domain analysis such as power spectral density is sufficient, RTS requires both time and frequency domain measurements and analysis.

Acknowledgements

I would like to acknowledge the contributions of my post-doctoral associates and students over the years to this research.

References

[1] M. J. Kirton and M. J. Uren, Noise in Solid-State Microstructures: A New Perspective on Individual Defects, Interface States, and Low-Frequency Noise, Advances in Phys., **38** (1989) 367

[2] K. K. Hung, P. K. Ko, C. Hu and Y. C. Cheng, Random Telegraph Noise of Deep Submicrometer MOSFETs, IEEE Tran. Electron Devices Letters, **11** (1990) 90.

RTS IN QUANTUM DOTS AND MOSFETS: EXPERIMENTAL SET-UP WITH LONG-TIME STABILITY AND MAGNETIC FIELD COMPENSATION

J. Sikula[1] and J. Pavelka

Czech Noise Research Laboratory, Brno University of Technology
Technicka 8, 616 00 Brno
CzechRepublic

M. Tacano*, S. Hashiguchi** and M. Toita***

**Department of Electrical Engineering, Meisei University, Hino 191 8506, Toky, Japan*
***Department of Electrical Engineering, University of Yamanashi,Kofu 400 851, Japan*
****Asahi Kasei, Nobeoka, Miyazak, Japan*

[1] sikula@feec.vutbr.cz

Abstract This paper investigates the emission and capture kinetics of random telegraph signals (RTS) in Quantum dots and submicron MOSFET structures. Emphasis is laid on the signals showing a capture process which deviates from the standard Shockley-Read-Hall kinetics. The proposed model distinguishes between primary processes consisting in quantum transitions of electrons between traps and the conduction or valence band and secondary processes, consisting in current modulation. If the RTS noise sources are quantum transitions of electrons between a shallow trap and the conduction band then the primary process is one-dimensional and it coincides with the secondary process – current modulation. For deep traps the primary process is a two dimensional g - r process. It is shown in this paper how to distinguish experimentally between the one or two-dimensional primary processes by measuring the probability density of the occupation time in both current states. These long-time measurements require a very stable power source and active shielding of low frequency magnetic fields.

Keywords: RTS noise, Burst noise, Quantum Dots, MOSFETs, Noise measurements

1. Introduction

Quantum dot (QD) structures have attracted much attention because of interest in not only the relevance of low-dimensional electron gas physics

J. Sikula and M. Levinshtein (eds.),
Advanced Experimental Methods for Noise Research in Nanoscale Electronic Devices (227 - 236)

but also of future applications. RTS as being observed in short- and narrow-channel FETs makes direct evidence of a single charge capture and emission. Awano et al. [2] fabricated an AlGaAs/InGaAs heterojunction field-effect transistor (FET) memory cell in a tetrahedral-shaped recess (TSR) structure.

An analysis of RTS presented in their paper explains quantitatively the details of hole trapping processes in the TSR QD. RTS was observed in the saturated current region and the RTS signal showed pure Lorentzian power spectrum. This process is thermally activated with the activation energy of hole capture and emission as 260 and 190 meV, respectively, as is shown in Fig. 1.

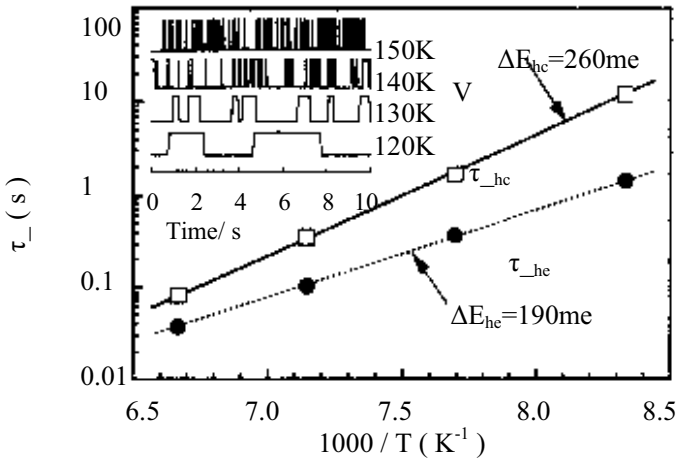

Figure 1. Temperature dependence of average hole capture and emission time

From experiments carried out on submicron MOSFETs it is known that the capture and emission rates are thermally activated [3, 4]. Taking account of the exhaustive published data, it is rather unlikely that there exists a universal type of RTS behaviour and consequently a model.

Nevertheless some interesting properties have been revealed, which extend the insight in the mechanisms underlying the interaction between traps and free carriers. It has been proved that Coulomb interaction might play an important role in the capture and emission processes. In some devices the capture time τ_c is inversely proportional to the square of the drain current I_D (see Fig. 2). We suppose that the standard Shockley-Read-Hall theory and Machlup model [1] are acceptable to describe RTS noise in special cases only.

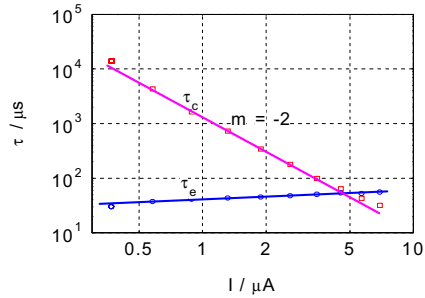

Figure 2. Capture τ_c and emission τ_e time constants of a submicron Si n-MOSFET

2. Primary and secondary processes

There are more mechanisms, which are the sources of bistable RTS current fluctuation. We will distinguish the primary processes as an ensemble of quantum transitions of electrons between the trap and the conduction or valence band from the secondary process, which is the current modulation. The primary process can be a one or more dimensional stochastic Markowian process. If the RTS noise sources are quantum transitions of electrons between shallow traps and the conduction band then we can describe this primary process by means of a one dimensional stochastic process and in this case the secondary process – current modulation – will coincide with the primary process. Such model was described by Machlup [1]. For deep traps there are possible quantum transitions of electrons between the trap and the conduction or valence band. In this case the primary process X(t) is in general a two dimensional g - r process. The respective secondary process Y(t) is represented by the current modulation. It is a one-dimensional stochastic process featuring two discrete states (α, β). In this case, two states of the X(t) process are transformed into one state of the measurable secondary Y(t) process. It is possible to distinguish experimentally between the two or three state primary processes by measuring the probability density and the dispersion time in the β state. These long-time measurements however have to use a highly stable power source and active shielding of low frequency magnetic fields to decrease the background noise level.

3. Transition probability intensities

This model supposes for the system: (i) to be Markowian, (ii) to be near equilibrium, (iii) generation and recombination processes may take place between the interface trap energy level and one band only. We assume that

the process of the trap occupation has two states, being stationary with a constant transition probability intensity μ_{ij} defined by

$$\mu_{ij} = \lim_{t \to s} \frac{p_{ij}(s, t)}{t - s}, \tag{1}$$

where p_{ij} is the transition probability at time s from the i-state to the j-state at time t. There are two measurable quantities: the pulse duration in the lower and the upper states. They are inversely proportional to the transition probability intensities μ_{ij}. In terms of the Shockley-Read-Hall model, one gets the matrix elements of transition probability intensities:

$$\mu_{10} = c_n n = 1/\tau_c \tag{2}$$

and

$$\mu_{01} = c_n n_1 = 1/\tau_e \tag{3}$$

where μ_{01} is the transition probability intensity for the carrier emission and μ_{10} - for capture.

4. One dimensional G-R process

In the special case, where the source of RTS noise are quantum transitions of electrons between a shallow trap and conduction band, we can describe this primary process by one dimensional stochastic process, which coincides with the secondary process – current modulation [4]. This model is the same as that of Machlup [1] and we will follow this derivation to show how the more general two-dimensional process can be described.

The probabilities $p_{ij}(t)$ of the transition from the state i into the state j is found by solving the Kolmogorov differential equations

$$\frac{dp_{ij}(t)}{dt} = \sum_{k \in I} \mu_{ik} p_{kj}(t), \tag{4}$$

for $I = (0, 1)$, $i, j = 0, 1$, with the conditions $p_{ii}(0) = 1, p_{ij}(0) = 0$, for $i \neq j$.

The absolute probability distribution Π_i is given by solving Kolmogorov equation in the form

$$\sum_{i \in I} \Pi_i \mu_{ik} = O, \tag{5}$$

We have

$$\Pi_0 = 1/(1 + \mu_{01}/\mu_{10}) = f_{pt} \tag{6}$$

and

$$\Pi_1 = 1/(1 + \mu_{10}/\mu_{01}) = f_t \tag{7}$$

The absolute probability distributions Π_0 and Π_1 correspond in thermodynamic equilibrium to Fermi – Dirac statistics for the trap to be free and occupied by an electron, respectively.

The dispersion of the current modulation process is then

$$D\{Y(t)\} = \Delta I^2 \Pi_0 \Pi_1 = \Delta I^2 x/(1+x)^2. \tag{8}$$

where ΔI is the RTS noise amplitude (see Fig. 3.) and $x = \mu_{10} / \mu_{01}$.

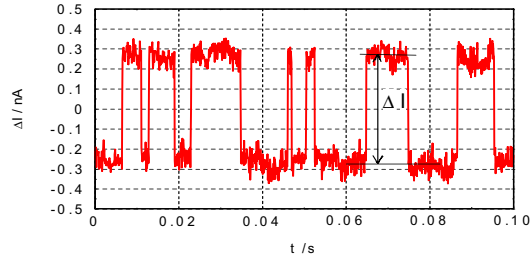

Figure 3. RTS noise in time domain

The correlation function is

$$B_Y(t) = D\{Y(t)\}\exp(-\mu.t) \tag{9}$$

where $\mu = \mu_{01} + \mu_{10}$

Similarly, we find the spectral density

$$S_Y(\omega) = \frac{2D\{Y(t)\}}{\pi} \cdot \frac{\tau}{1+\omega^2\tau^2}, \tag{10}$$

where $\tau = 1/\mu$

The RTS noise current spectral density as a function of frequency f is given by $S_I(f) = 2\pi . S_I(\omega)$ and then we have

$$S_I(f) = \frac{4\Delta I^2}{\mu_{01}} \cdot \frac{x}{(1+x)^3} \cdot \frac{1}{1+\omega^2\tau^2} \tag{11}$$

Experimental results obtained for a submicron MOSFET made by Asahi Kasei are shown in Fig. 4.

The probability density of the occupation time in state α is given by

$$g_\alpha = \frac{1}{\tau_\alpha}\exp(-t/\tau_\alpha), \tag{12}$$

where τ_α corresponds to the emission or capture constant. The probability density distribution (see Fig.5) is exponential with the resultant time constant τ = 0.52 ms, which is in good agreement with the time

constant corresponding to the cut-off frequency of the Lorentzian type spectral density (see Fig. 4).

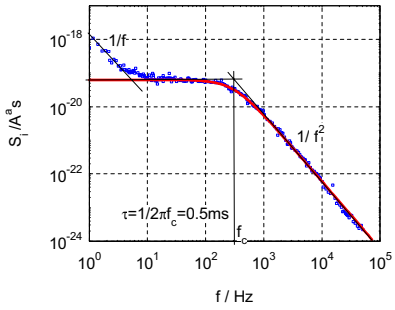

Figure 4. The current noise spectral density vs. frequency for sample N32

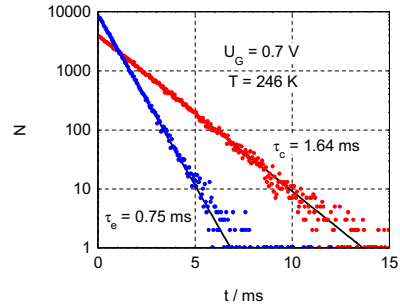

Figure 5. Histogram of τ_c and τ_e for sample N32

In this case the one-dimensional process or the model of Machlup [1] can be used to describe RTS noise kinetics. It applies to shallow traps, low temperatures and traps located near the silicon-oxide interface.

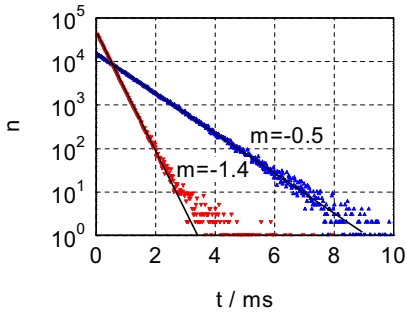

Figure 6. Histogram of τ_c and τ_e for sample N32 with $7x10^5$ pulses

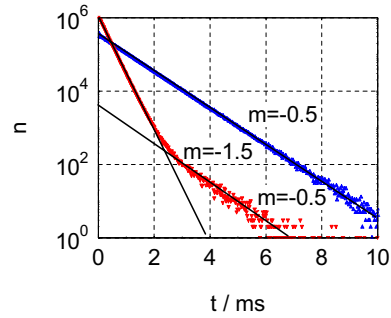

Figure 7. Histogram of τ_c and τ_e for sample N32 with $15x10^6$ pulses

Long-time measurements on submicron MOSFETs show that the probability density of occupation time for emission is given by a superposition of two exponential dependencies given by

$$g_\beta = A\exp(-t/\tau_1) + B\exp(-t/\tau_2) \tag{13}$$

Histograms for submicron MOSFET made by Asahi Kasei sample N31 at temperature 256 K and drain current 2.6 μA are in Fig. 6. for $7x10^5$ pulses and in Fig. 7. for $15x10^6$ pulses. It is important that capture time constant does not depend on the number of the pulses being measured.

To obtain more accurate information on the role of quantum transitions of charge carries in the kinetics of RTS process, the measuring set-up must

be able to guarantee stable conditions (temperature, voltage supply and magnetic field) for long-time data acquisition.

5. Fully computer-controlled battery power source

Many of the rectified power sources could supply current or voltage through the software program, but they do not always come without minute residual line noise. This becomes a serious problem in highly sensitive low-signal devices working in the μV/nV ranges [5].

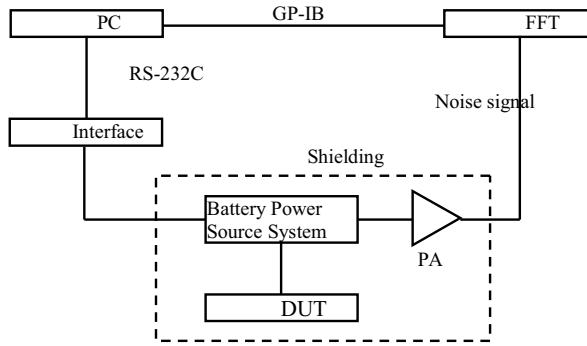

Figure 8. Block diagram of fully automatic battery power source

An automated power system was reported recently by Jonker and Vandamme [7] for low frequency noise measurements of low-Ohmic samples and magnetic sensors. They used a fixed battery and relayed fixed resistors to control the current through the DUT to obtain an equivalent noise resistance R_{eq} of 10 Ohm using two pre-amplifiers connected in parallel.

We describe here a fully computer-controlled battery power source with following features: it is able to measure the resistance of the DUT, set the current through or the voltage across the DUT, communicate with the computer through optical TX/RX interfaces and reject circuit noise by switching off the power of the internal circuit when starting the measurement, and charge up the battery automatically when low. This power source makes therefore the ultimate quiescent power source without any line noise.

The block diagram of the new fully automated power supply system, which consists of a personal computer, an interface controller, a battery power source system, the DUT and measuring instruments, is shown in Fig. 8. The personal computer and the interface controller are connected through the control signal line enabling either parallel or serial two-way communication. Personal-computer-controlled microcomputer units (MCUs) and an AD converter installed in a shielding box together with batteries and

optical connection from outside make it possible to set automatically the DC power source for low-frequency noise measurements without any spurious line noise. After the resistance of the device under test is measured automatically at 1 mA, the voltage across or the current through the sample is set to equal the required value given by the external PC. The power sources for the MCU and the AD converter in the shielding box are automatically switched off in order to minimize the noise induced from the electronic circuit. This power source substantially improves the low-frequency noise measurement technology. Low-frequency noise measurements and noise figure measurements of the devices are the most sensitive cases where the superimposed line noise must be entirely eliminated from the measuring set-up. This power source substantially improves the low-frequency noise measurement technology.

6. Active shielding for low-frequency magnetic field

When handling very low noise signals at low frequencies, magnetically induced noise is sometimes difficult to avoid by conventional shielding. The main sources of such interfering magnetic noise fields are the commercial power lines and apparatuses utilizing motors and transformers. The noise voltage induced in a one-turn coil of $1cm^2$ cross-section by such a field sometimes becomes about 0.1 μV/Hz, which corresponds to a magnetic field of 3 $\mu Wb/m^2$ at 50 Hz. We report here a method to reduce such interfering magnetic fields by applying an inverted magnetic field generated by a negative feedback system [6].

The configuration of the system is shown in Fig. 9. The system consists of a pickup coil L_p, two low-noise pre-amplifiers (A_{p1}, A_{p2}), two driving amplifiers (A_{d1}, A_{d2}), and a driving coil L_d. This symmetrical push-pull configuration is adopted to reject the interference through capacitive coupling. The voltage induced in the pickup coil by the interfering magnetic field is amplified and fed to the driving coil. The driving coil is arranged so as to cancel the existing magnetic field. The system is designed to reduce the 50 Hz magnetic field of around $1\mu Wb/m^2$ by 40 dB.

The spectra of the inducing magnetic field before and after the application of the negative feedback system are shown in Fig. 10. where 0 dB of the vertical axis corresponds to a magnetic field induction of 8 mWb/m^2. The upper trace is an example of the induced magnetic field in a laboratory room. In addition to spikes at harmonic frequencies of 50 Hz, there is a spike at 20 Hz. The lower trace shows the magnetic field when the negative feedback system is applied. The spike at 50 Hz is reduced by 35 dB and the most of the other spikes are suppressed to the background level (−165 dB/Hz).

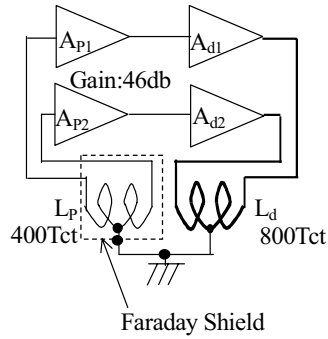

Figure 9. Magnetic negative feedback system

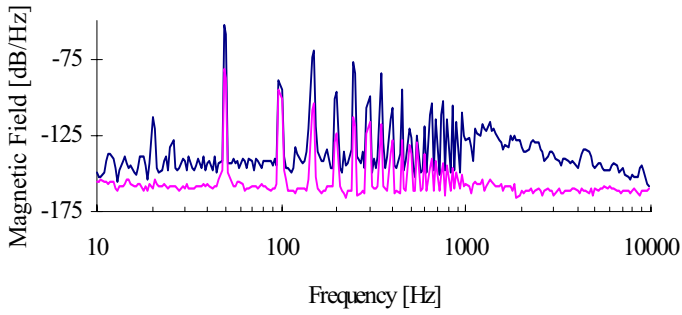

Figure 10. Effect of magnetic negative feedback. Upper trace: original field, lower trace: reduced field.

7. Conclusion

The standard Shockley-Read-Hall theory and the model of Machlup [1] are acceptable in describing the RTS kinetics in special cases only, where the RTS noise sources are quantum transitions of electrons between shallow traps and the conduction or valence band only. If there are possible quantum transition of electrons between the trap and the conduction or valence band, the primary process X(t) is in general a two dimensional g - r process. A secondary process Y(t) is represented by the current modulation. It is a one-dimensional stochastic process with two discrete states (α, β). In this case two states of the X(t) process are transformed into one state of the measurable secondary Y(t) process. It is possible to distinguish experimentally between the one or two-dimensional primary processes by measuring the probability density and the dispersion time in the β state. To

obtain more accurate information on the role of quantum transitions of charge carries in the kinetics of RTS process, the measuring set-up must be able to guarantee stable conditions (temperature, voltage supply and magnetic field) for long-time data acquisition.

References

[1] S. Machlup, J. appl. Phys., **25,** 341, (1954)

[2] Y.Awano, M. Shima, Y. Sakuma, Y. Sugiyama, N. Yokoyama and M. Tacano, Temperature controlled RTS noise from a single InGaAs quantum dot, Proc. of the Int. Conf. "Noise in Physical Systems and 1/f Fluctuations", ed. by G. Bosman, Gainesville, FL, USA (2001) p.359

[3] M. J. Kirton and M. J. Uren, Noise in Solid-State Microstructures: A New Perspective on Individual Defects, Interface States, and Low-Frequency Noise, Advances in Phys., **38** (1989) 367

[3] Z. Celik – Butler and N.V. Amarasinnghe, Random Telegraph Signals in Deep Submicron Metal–Oxide–Semiconductor Field-Effect Transistors,Noise and Fluctuation Control in Electronic Devices, ed. by A. A. Balandin pp.187 – 199, American Scientific Publisher (2002)

[4] J.Sikula , M. Sikulova , P. Vasina , B. Koktavy : Burst Noise in Diodes. Proc. of the 6th Int. Conf. on Noise in Physical Systems and 1/f Fluctuations, eds.by P. H. E. Meijer, R. D. Mountain and R.J.Soulen, pp. 100 - 104, NBS Washington DC, (1981)

[5] S.Yokokura, N. Tanuma, M. Tacano,S. Hashiguchi and J. Sikula, Fully computer-controlled battery power source for low-frequency noise measurements, Proc. of the Int. Conf. "Noise in Physical Systems and 1/f Fluctuations", ed. by G. Bosman, Gainesville, FL, USA (2001) p.

[6] S. Hashiguchi, C. Taki, A. Kitahara, M. Ohki, M. Tacano and J. Sikula, Active shielding for low frequency magnetic field, Proc. of Int.Workshop Noise and Non-Linearity Testing of Modern Electronic Components, September 12 – 13, 2001,Brno, Czech Republic (2001) pp. 44-47.

[7] R.J.W. Jonker, J. Briaire and L.K.J. Vandamme: “Automated System for Noise-Measurements on Low-Ohmic Samples and Magnetic Sensors”, IEEE Trans. IM, **48**(1999) 730.

SOME CONSIDERATIONS FOR THE CONSTRUCTION OF LOW-NOISE AMPLIFIERS IN VERY LOW FREQUENCY REGION

J. Sikula[1]
Czech Noise Research Laboratory, Brno University of Technology
Technicka 8, 616 00 Brno
CzechRepublic

S. Hashiguchi[2] and M. Ohki
Department of Electrical Engineering, University of Yamanashi,
Kofu 400 8511
Japan

M. Tacano[3]
Department of Electrical Engineering, Meisei University
Hino 191 8506, Tokyo
Japan

[1] sikula@feec.vutbr.cz
[2] has@es.yamanashi.ac.jp
[3] tacano@ee.meisei-u.ac.jp

Abstract Important points in designing a low noise amplifier in very low frequency region such as around 1mHz are to avoid the coupling capacitor at the front end, and to suppress the thermal drift. Practical examples are described.

Keywords: very low frequency, low noise amplifier, thermal feedback

1. Introduction

The fundamental requirement on the amplifier for noise measurements is that the noise level referred to the input should be below the noise to be measured by more than 20 db. This requirement is not difficult to fulfill in audio frequency region, and it is possible to make the white noise level of the system referred to the input less than -190 dbV/Hz. In the very low

J. Sikula and M. Levinshtein (eds.),
Advanced Experimental Methods for Noise Research in Nanoscale Electronic Devices (237 - 244)

frequency range extending to sub-milli-Hz there are several difficulties. Those are the problems concerning to the coupling capacitors, the excess noise in amplifying devices, the effects of the ambient temperature variation, and so on.

The capacitance necessary for the lower cutoff frequency of 0.1 mHz is 16 mF for the input resistance of 100 kΩ. The electrolytic capacitors are the exclusive selection for such a value of capacitance, and the electrolytic capacitors accompany a considerable amount of leakage current causing additional noise. In addition, the coupling capacitor presents high signal source impedance for the amplifying device. For example, the impedance of 16 mF is 10 kΩ at 1 mHz, and this enhances the contribution of the input current noise of active devices. The coupling capacitor also causes the long transient when the power supply of the amplifier is switched on.

The active devices for the first stage amplifiers are selected by checking the values of the equivalent input noise level and the trans-conductance. The offset voltage and its drift are serious in a direct-coupled amplifier. The offset is cancelled by inserting a combination of small batteries, and the drift is suppressed by the thermal feedback stabilization. As the measurements are performed over a long time, for a week for example, the power supply voltage should be stable enough over this duration.

2. The First Stage

2.1. Amplifying device

A junction FET is better for the first stage device than a bipolar transistor because the gate biasing circuit is simpler. The device should be selected by checking the input equivalent noise voltage at 10 Hz in the catalogue data. One of the best devices at present is 2SK369 JFET (supplied by Toshiba[1]) whose equivalent input noise is -175 dbV/Hz (typ.) at 10 Hz for the drain current I_D=3 mA.

A bipolar transistor is preferable when the impedance R_g of the signal source (sample under test) is low. The bipolar transistor pair 2SA1316/2SC3329 is recommended for such cases. Its input noise voltage is -177.5 dbV/Hz for the collector current I_C=10 mA as indicated in Table 1 [1].

Table 1. Equivalent input noise of 2SA1316/2SC3329

I_C(mA)	NF(db)	R_s(Ω)	S_n(10Hz)(dbV/Hz)
0.1	8	100	-170.5
1	8	30	-175.8
10	8	20	-177.5

The values in Table 1 are computed with Eq.(1) using the data from the catalogue which says that NF=8 db for R_g=100 Ω at I_c=0.1 mA, for 30 Ω at 1mA, and for 20 Ω at 10 mA, respectively.

$$\begin{aligned} S_n &= 10\log < e_n^{\,2} > = 10\log 4kTR_g + 10\log(10^{\frac{NF}{10}} - 1) \\ &= -197.8 + 10\log R_g + 10\log(10^{\frac{NF}{10}} - 1) \ @300\text{K} \end{aligned} \tag{1}$$

Parallel connection of n pieces of FETs and n pieces of the load resistors, shown in Fig.1, reduces the input noise voltage to $1/\sqrt{n}$, maintaining the voltage amplification unchanged, as shown in Eq.(2).

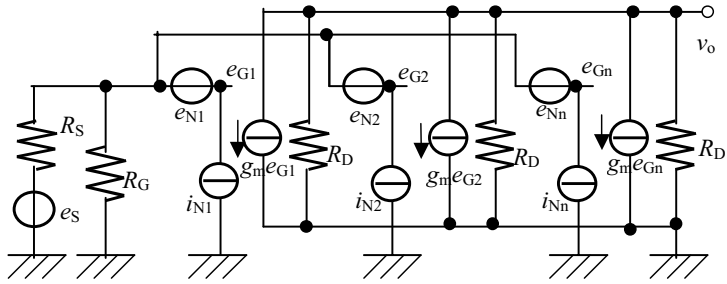

Figure 1. Noise equivalent circuit of paralleled JFET.

$$v_o = -g_m \frac{R_D}{n}\sum_i^n (e_s + e_{Ni} + R_G i_{Ni}) = -g_m R_D (e_s + \sum_i^n \frac{e_{Ni} + R_G i_{Ni}}{n})$$

$$< v_o^{\,2} > = (g_m R_D)^2 \{< e_s^{\,2} > + \frac{n < e_N^{\,2} > + nR_G^{\,2} < i_N^{\,2} >}{n^2}\}$$

$$= (g_m R_D)^2 \{< e_s^{\,2} > + \frac{< e_N^{\,2} > + R_G^{\,2} < i_N^{\,2} >}{n}\},$$

if

$$< e_{N1}^{\,2} > = < e_{N2}^{\,2} > = \ldots\ldots\ldots = < e_{Nn}^{\,2} > = < e_N^{\,2} > \tag{2}$$

and

$$< i_{N1}^{\,2} > = < i_{N2}^{\,2} > = \ldots\ldots\ldots = < i_{Nn}^{\,2} > = < i_N^{\,2} > .$$

2.2. Circuit configuration

The first stage FET is to operate at zero bias (0 ~ -50 mV) in the common source configuration as shown in Fig.2. This is to obtain the lower

gate noise voltage at the higher drain current, and to avoid noise generated in the resistors for biasing. The operating point of FETs with higher I_{DSS} is less sensitive for the variation in the gate bias of 50 mV. The sample under test and the gate of the FET is directly connected when the dc voltage V_S of the SUT output is between 0 and -50 mV, else a bank of batteries of V_{BC}(V) is inserted between the output of SUT and the gate of the first stage FET as shown in Fig.3 to make the gate voltage between 0 and -50 mV. The bank of batteries consists of series connection, in forward and reverse direction, of such batteries as shown in Table 2. The obtainable value of V_{BC} is with a step of 50 mV.

The voltage gain A_1 of the first stage must be higher than the ratio of the input noise of the second stage to that of the first stage. One of the best candidates for the second stage is a low noise linear IC amplifier such as μPC815C (NEC)[2]. As the input noise level of μPC815C is -171 dbV/Hz at 10 Hz, A_1 must be higher than 10 db. and A_1 = 30 db is reasonable.

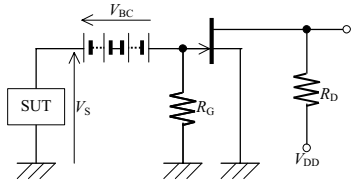

Figure 2. First stage circuit

Table 2 Small-sized batteries

type	voltage(V)
NiMH	1.2
PR	1.4
LR	1.5
SR	1.55
CR	3.0
ER	3.6

2.3 Passive suppression of temperature fluctuation

Temperature fluctuation is reduced by applying thermal insulation to the FET and/or by attaching heat sinks to the FET. Fig. 3 shows the effects of thermal insulation [3]. The upper trace is the noise output of a FET (2SK117) when it is bare, while the lower trace is that when it is thermally insulated with an enclosure of a few millimeter thick foam polystyrene. This thermal insulation is effective below 0.5 Hz, and the fluctuation level is reduced by 30 db below 0.1 Hz.

Fig. 4 shows the effect of attaching heat sinks. The shapes and the sizes of the heat sinks are shown in Fig.5, and the thermal parameters are shown in Table 3. The thermal resistance is computed from the measured values of thermal time constants. As is seen in Fig.3 the heat sinks #2 and #3, both attached to the leads of the FET, are very effective below 0.3 Hz. The humps at 0.05 Hz on the traces (c) and (d) are smoothed out by additional heat sink #1 to the head (plastic part) of the FET. The thermal time constants of such thermal insulation and heat sinks are limited by the size of the amplifier and may not be so effective below 0.01Hz.

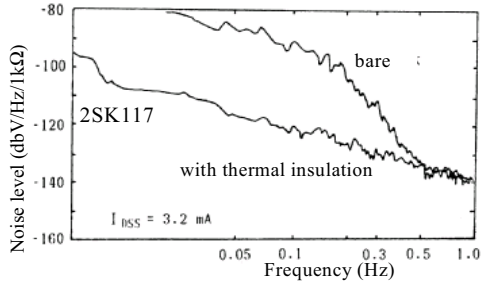

Figure 3. Effect of thermal insulation

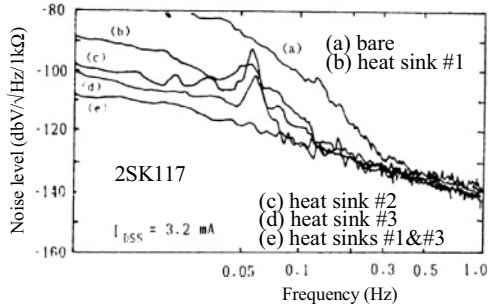

Figure 4. Effect of heat sinks

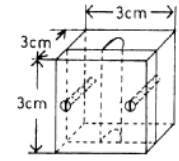

heat sink #1
Aluminum 71gwt
for attaching to the head

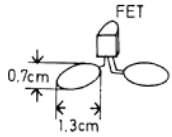

heat sink #2
Lead 1.9gwt 2pcs
for attaching to the legs

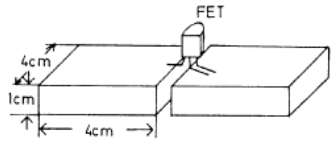

heat sink #3
Brass 140gwt 2pcs
for attaching to the feet

Figure 5. Heat sinks

Table 3 Thermal parameters of heat sinks

name	time constant (s)	heat capasity (J/K)	thermal resistance (Ks/J)
#1(2parts)	1200	62.4	19.2
#2(2pcs)	12	0.48	25
#3(2pcs)	1300	104	12.5

2.4 Active suppression of temperature fluctuation

Temperature fluctuation below 0.01 Hz is reduced by the local temperature stabilization applied to the first stage devices [4]. The system consists of two amplifying paths with identical circuit configuration as shown in Fig.6. The amplifier with less noise is put in the signal amplifier, and the other is in the feedback path for stabilizer. The first stage FETs in both paths are thermally coupled to the collector plate of the heater transistor, which generates heat to set the FETs at some raised temperature about 320 K. The voltage across the heater transistor is controlled by the offset voltage of the feedback path so as to maintain the temperature of the FETs at the assigned value around 320 K.

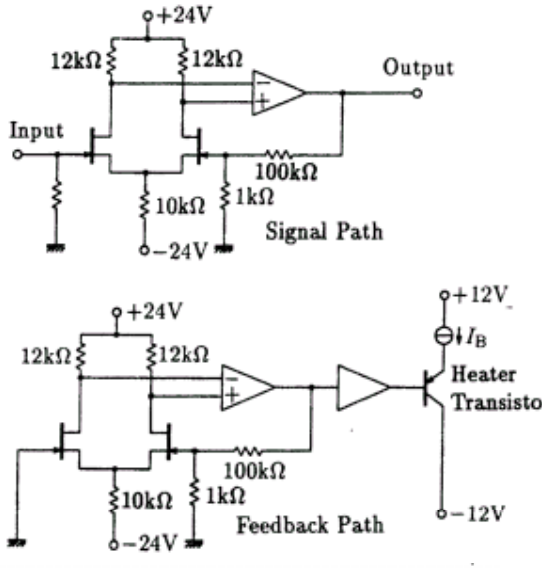

Figure 6. Circuit configuration of the thermal feedback system

Fig. 7 shows the static characteristics of the thermal feedback system. The suppression effect is more than 40 db. The temperature sensitivity is reduced from 36.5 μV/K to 0.36 μV/K.

Fig. 8 shows the dynamic response of the system. The upper and lower traces are the spectra of the offset voltage when the ambient temperature varies stepwise with the period of 3600 s (0.28 mHz) and 1800 s (0.56 mHz), respectively. It is seen that the system is effective below 1 mHz. The span of the effective frequency range can be extended by reducing the heat capacity

of the assemble consisting of the heater transistor and the FETs. It is also extended by reducing the distance from the heat generating portion to the pellets of FETs.

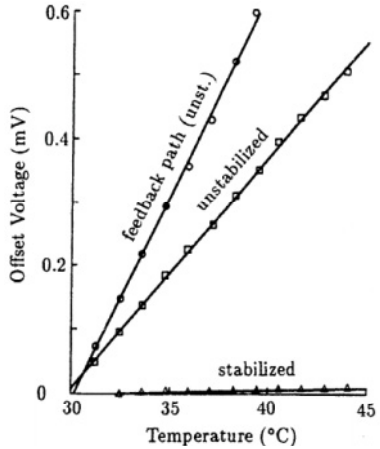

Figure 7. Stabilizing effect of thermal feedback system

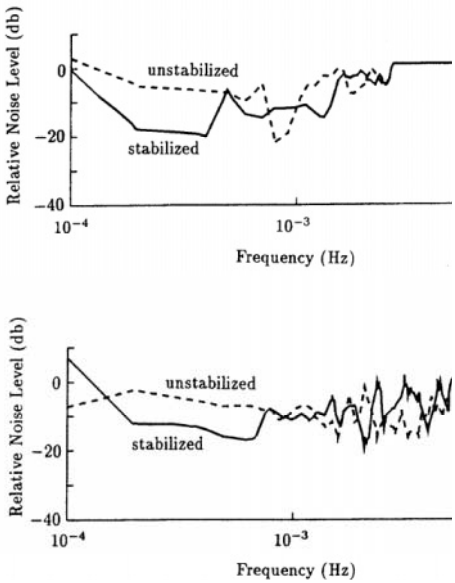

Figure 8. Dynamic characteristics of the thermal feedback system

2.5 Power supply

Lead-acid batteries are good selection for low noise power supply when they are fresh and fully charged. The ambient temperature of the batteries should be stabilized at around 300 K, for example. In order to reject the effect of terminal voltage drop according to discharge, multiple units of large sized cells are connected in parallel. Voltage stabilizers consist of low noise transistors are, in some cases, inserted between the batteries and the circuit.

3. Conclusion

Practically important points are described to realize a noise measuring system in mHz and sub-mHz regions. The most important and difficult point is to reduce the effect of temperature fluctuation.

References

[1] http://www.semicon.toshiba.co.jp/ja/bucat_3/bucat_0/bucat_4/td_24/TD.pdf

[2] http://www.ic.nec.co.jp/image/IC-2120A.pdf

[3] S. Hashiguchi, F.Ito, K.Kurita, Low Frequency Fluctuation in FETs, Res. Rpt., Faculty of Engineering, Yamanashi Univ., **35**(1984), 93-96, (in Japanese)

[4] S. Iino, T. Sanada, S. Hashiguchi, A Low-Drift dc Amplifier Utilizing Thermal Feedback, Trans. IECEJ, **J69-C(**1986**),**1031-1038, (in Japanese)

MEASUREMENTS OF LOW FREQUENCY NOISE IN NANO-GRAINED RuO_2+GLASS FILMS BELOW 1 K

A. Kolek

Department of Electronics Fundamentals, Rzeszów University of Technology
Wincentego Pola 2, 35-959 Rzeszów
Poland

akoleknd@prz.rzeszow.pl

Abstract Measurements of low-frequency noise in RuO_2+glass thick films at subkelvin temperatures are presented. Films were prepared by a standard "high temperature" process: 20 nm sized crystalline RuO_2 powder was mixed with 0.5 μm granular lead-borosilikate glass and organic solvent to give a paste, which was screen printed onto alumina substrates (with pre-fired AuPd contacts) and fired in a tunnel furnace. Noise measurements reveal that below liquid helium temperature and for low biasing voltages the low frequency excess noise is a pure resistance noise. At larger voltages its power spectral density depends sublinearly on voltage square. In the liner regime noise increases with decreasing temperature, approximately as $T^{-2.3}$. Up to 4 T no dependence of noise intensity on magnetic field has been observed. These effects are discussed in terms of possible conduction mechanisms in the RuO_2+glass thick films: hopping, thermally activated tunneling and weak localization.

Keywords: Ruthenium based thick films, 1/f noise, thick film resistors

1. Introduction

One of the possible applications of RuO_2+glass films is cryogenic thermometry. This is because they exhibit large temperature sensitivity and very low magnetoresistance at low temperatures. Very few papers report on noise versus temperature measurements [1-3] in such films. So far, noise properties below liquid helium temperature have not been the subject of any research. Our measurements show that as $T \rightarrow 0$ the noise level of RuO_2+glass films increases significantly and noise becomes a factor limiting

J. Sikula and M. Levinshtein (eds.),
Advanced Experimental Methods for Noise Research in Nanoscale Electronic Devices (245 - 252)

the resolution of these temperature sensors. The data presented in this paper are also important for studies of conduction mechanism in RuO_2+glass thick films which is still unknown (see e.g. ref. [4-6]).

2. Experimental

RuO_2+glass thick films are prepared by screen-printing of a suitable paste onto a ceramic substrate and firing at approximately 850° C. The paste is composed of ruthenium dioxide and glass powders and organic solvent. RuO_2 powder we have used had grains as small as 13.7 nm (X-ray peaks broadening) or 25 nm (BET or electron microscope). The glass frit consisted of 65% PbO, 10% B_2O_3, 25% SiO_2 by weight. Pastes of volume fraction υ = 0.10, 0.12, and 0.16 of conducting component (RuO_2) were prepared. After firing the average thickness of the films was 10 μm. The samples were 1 mm wide and 6 mm long with two side contacts (2 mm apart) along one of its edges. A pair of such samples was used in ac noise measurements setup [7]. The total volume involved in noise detection was 8×10^{-11} m^3. The room temperature sheet resistances of the films were 3.82, 2.86 and 0.48 kΩ for υ = 0.10, 0.12, and 0.16, respectively.

Noise measurements were made with ac technique with a carrier frequency of 325 Hz [8, 9]. A pair of specimens with approximately equal resistance $\cong \frac{1}{2}R$ was placed in bottom arms of the bridge and biased through ballast resistors of resistance $\cong \frac{1}{2}R_B$ ($R_B \gg R$). The signal from bridge diagonal was amplified and demodulated in 5105 lock-in amplifier. Power spectral densities S_V were calculated in HP 35660A signal analyzer in a frequency range of 0 - 25 Hz for several ac voltages across the sample. For V = 0 the spectrum $S_{V=0}$ (background noise) was flat in the whole frequency range. In Fig. 1a $S_{V=0}$ averaged ($\langle\,\rangle$) over the band Δf = 0.0625-3 Hz is plotted versus temperature T. After initial decreasing with decreasing temperature, $S_{V=0}$ increases for T below 2 K. The explanation of this unusual behavior is easy. The films under measurements are kept at temperature T whereas the ballast resistors are at 300 K. For $R_B \gg R$ we shall have

$$S_{V=0} \cong 4kTR + 4k(300\,\mathrm{K})R_B\left(\frac{R}{R+R_B}\right)^2 + S_{amp}\,. \qquad (1)$$

where S_{amp} is the preamplifier's noise. Experimental data in Fig. 1a follow the theoretical lines of Eq. (1) very closely. This agreement makes us sure that measurement setup was thoroughly calibrated.

At low temperatures the second component in Eq. (1), which comes from Johnson's noise of the ballast resistors increases due to the increasing resistance R of the RuO_2+glass film (see Fig. 1b). Fortunately, the

contribution of this component can be dumped by increasing R_B. It is demonstrated in Fig. 2a, where data for two different R_B's are shown. This experiment shows, however, that low temperatures make requirements for the ratio R_B/R much stronger. Usually $R_B/R \geq 10$ is recommended to make contact noise and fluctuations of biasing voltage sufficiently suppressed. It follows from Fig. 2a that to make the contribution of the second term in Eq. (1) unimportant (i.e. « S_{amp}), even $R_B/R \cong 100$ could be too small.

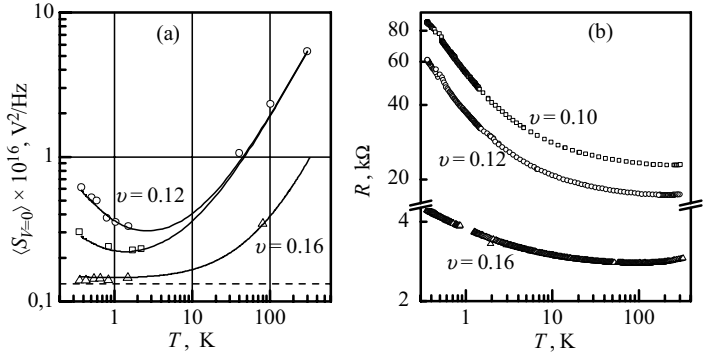

Figure 1. *a)* Background noise measured for sample $\upsilon = 0.12$ with two different values of R_B (1 MΩ – circles, 4 MΩ - squares) and for sample $\upsilon = 0.16$ (triangles) measured with $R_B \cong$ 0.2 MΩ. Solid lines are drawn according to Eq. (1). Dashed line shows preamplifier's noise, S_{amp} *b)* Resistance versus temperature for the samples $\upsilon = 0.10$, 0.12 and 0.16.

3. Results

Spectra of excess noise $S_{Vex} \equiv S_V - S_{V=0}$ were measured at selected temperatures. As it is shown in *Fig. 2a*, they behave in 1/f manner. So, $\langle f \cdot S_{Vex} \rangle$ was used as a measure of noise intensity. Squared voltage scaling of $\langle f \cdot S_{Vex} \rangle$ was found only in $V \to 0$ limit. Fig. 2b shows that at low temperature and above a certain voltage the dependence of S_V on V^2 becomes sub-linear. This nonlinearity is associated only with very small curvature on I-V characteristic and cannot be explained as resulting from selfheating of the films by the driving current. The current densities used at the lowest temperatures were smaller than 10^{-2} A/cm^2 and the total dissipated power was less than 100 nW. These values indeed lead to a small drop in the resistance but the drop in noise intensity is too large to be interpreted as caused by the increase of either lattice or the electron temperature [10]. This is clearly evident in Fig. 3a where relative noise versus resistance follows different traces depending on whether R is changed by temperature or voltage. In Fig. 3b the normalized resistance noise $S \equiv \langle f \cdot S_{Vex} \rangle / V^2$ measured in the limit $V \to 0$ is plotted versus temperature. One can see that below 4 K

S increases significantly with decreasing temperature. This is new observation, since other studies explore different temperature range [1-3].

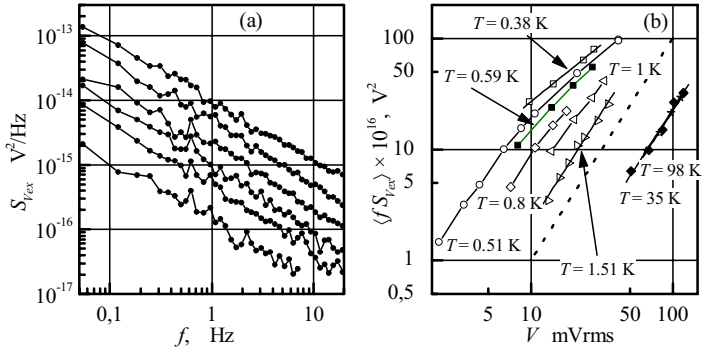

Figure 2. *a)* Power spectral densities of excess noise S_{Vex} measured at T = 0.51 K for several voltages V across the sample υ = 0.12 *b)* Dependence of noise intensity $\langle f \cdot S_{Vex} \rangle$ on voltage at selected temperatures measured for sample υ = 0.12. Dashed line has the slope of 2.

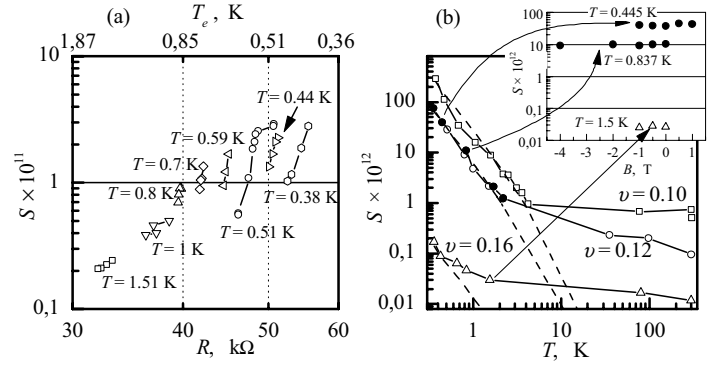

Figure 3. *a)* Normalized noise plotted as a function of resistance (or electron temperature) for sample υ = 0.12 at different (lattice) temperatures. For subsequent series the resistance drops a little due to selfheating caused by the increasing voltage. *b)* Normalized noise at $V \rightarrow 0$ plotted as a function of temperature. Filled and empty symbols for υ = 0.12 series refer to different values of R_B used in the measurements (contact noise eliminated). The inset shows how at fixed temperature S depends on magnetic field B. Dashed lines are drawn according to Eq. (6).

Measurements in magnetic field were performed for samples υ = 0.12 and υ = 0.16 [9]. They are illustrated in Fig. 3b inset. As one can see, S does not depend on magnetic field B. This conclusion holds at least in the range from –4 T to +1 T, in which the measurements were performed. It should be noted for completeness that the whole S_V versus V dependencies, including nonlinear effects at larger voltages are independent of B.

4. Discussion and summary

Since conduction mechanism in RuO_2+glass films is still unknown, we start discussion from qualifying the samples as either metallic or insulating. $R(T)$ and $S(T)$ dependencies are insufficient to distinguish between those two because both weak localization and hopping predict increase of resistance and relative noise as the temperature is lowered [11-15]. Weak localization, however, requires ½ noise suppression by the magnetic field [11]. As it is not the case, our samples are on insulating side of MIT. As for the hopping, the theories are not consistent [12-15]. For those which predict increase of noise with lowering temperature, the expected dependence is either exponential [12] or of power law, $S \sim T^{-\alpha}$, with $\alpha \cong 3.4$ for Efros-Shklovskii hopping or $\alpha \cong 1.7$ for Mott hopping in 3D [13, 14]. The divergence in Fig. 3b is weaker than exponential. The exponent $\alpha \cong 2.3$ found for our films is different from both the above values. The possible interpretation is that the samples are in the crossover region and/or percolation-like morphology of the films changes exponents. In such a case one has to argue about common objection arising when scaling $\ln R$ vs $(T_0/T)^{1/n}$ for RuO_2+glass films, namely that the quantities extracted from T_0 are unphysical and temperature range does not satisfy the condition $T \ll T_0$ [6]. Leaving these questions open we propose another scenario which takes into account the specific granular nature of our films.

For granular metals and thin films it is believed that conduction is due thermally activated tunneling between neighboring metallic grains. Inter-grain resistances are

$$r_{ij} = r_0 \exp(2s_{ij}/a + E_{ij}/kT), \qquad (2)$$

where s_{ij} is the intergrain separation, a is the localization length and E_{ij} is the charging energy. These resistors form a regular network through which current flows along a variable, temperature dependent path. For RuO_2+glass films the typical values of E_{ij} extracted from Arrhenius plots (from few μeV to several hundreds μeV) are too small to be interpreted as arising from charging the grains. On the other hand the well-known fact is that Ru (RuO_2) diffuses into the glass and large density of dopants exists in the barrier insulator [5, 16]. E_{ij} may then have the meaning of energy required to activate a trap-assisted-tunneling channel. A slightly different approach gives a graded barrier model of ref. [6]. Here the conduction in RuO_2+glass films results from parallel flow of tunneling currents and thermally activated emissions over graded (i.e. of variable heights) barriers between neighboring grains. Yet another picture can be adopted from the model proposed recently by Meir [17]: transport between nanometer grains occurs via quantum point contacts, each characterized by its energy E_{ij}. Those with $E_{ij} > \mu$, μ is the chemical potential, are insulating and for them $r_{ij} \sim \exp(E_{ij}/kT)$. In any of the

above cases at low temperatures resistances r_{ij} that build up the network take on values from an exponentially wide range. The total resistance of such a network is described by the critical resistance R_c

$$R \cong R_c = R_0 \exp(\xi_c) \sim R_0 \exp(E_c(T)/kT). \tag{3}$$

For 3D regular network the correlation length L_c and relative noise S scale as $L_c \sim (\xi_c)^{\nu} \sim \ln^{\nu}(R/R_0)$, and

$$S \sim L_c^3 S_c \sim \xi_c^m S_c, \quad m = 3\nu, \tag{4}$$

where $\nu \cong 0.9$ is the percolation correlation length exponent and S_c is the relative noise of critical resistance [18]. Assuming that two-level systems (TLS) couples to R_c via barrier height fluctuations we get

$$\langle \delta R_c^2 \rangle = R_c^2 \langle \delta E_c^2 \rangle / (kT)^2 \sim R_c^2 n_{\mathrm{TLS}} / (kT)^2, \tag{5}$$

where n_{TLS} is the density of TLS. As $n_{\mathrm{TLS}} \sim kT$ we eventually get

$$S \sim \frac{1}{T} [\ln(R / R_0)]^m, \ m \cong 2.7 \ \text{in 3D}. \tag{6}$$

In Fig. 3b the dependence of Eq. (6) is drawn assuming $R_0 = R(300\ \mathrm{K})$. The only adjusting parameter was scaling coefficient of 1.3×10^{-11} for $\upsilon = 0.12$, 4.8×10^{-11} for $\upsilon = 0.10$, and 5.4×10^{-13} for $\upsilon = 0.16$. The agreement is quite good justifying that assumptions in our picture were quite reasonable. The result of Eq. (6) agrees qualitatively with numerical simulations of ref. [19] where the increase of noise at low temperatures was also found in 2D network of resistances described by Eq. (2). It could also refer to experimental data of refs. [20, 21] where the increase of noise with decreasing temperature as well as sublinear S vs V^2 dependence at large voltages were found for granular metals.

The picture above can be extended further assuming that the heights of intergrain barriers depend on the electric field applied to the junctions, $E_{ij} = E_{ij}(eV)$. The critical barrier E_c is then also field dependent $E_c = E_c(kT, eV)$. Assuming that the fluctuation δE_{c1} caused by the change of state of a single TLS is homogeneous function of both variables $\delta E_{c1} = \lambda^p \varphi(kT/\lambda, eV/\lambda^{\beta})$ the relative noise can be described by the following scaling form

$$S \sim \frac{1}{kT} [\ln(R / R_0)]^m \Phi(eV / (kT)^{\beta}). \tag{7}$$

Exponent $p \cong 0$ was found from scaling S in $V \to 0$ limit. Exponent $\beta \cong 1.6$ was found from the scaling plot of *Fig. 4*.

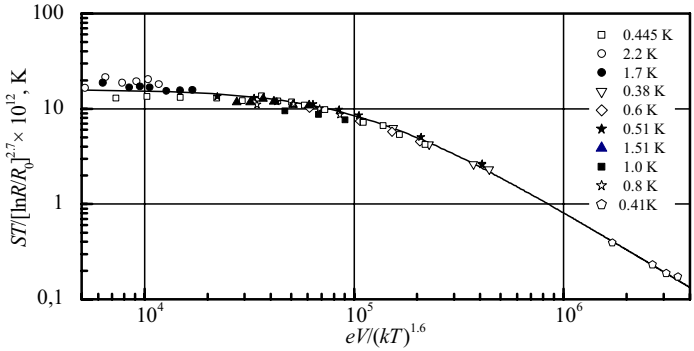

Figure 4. Scaling plot of Eq. (7) made for sample $\upsilon = 0.12$ (eV and kT on horizontal axis are in eV). Symbols refer to different temperatures. Line shows the shape of function Φ.

In summary measurements of low-frequency noise in nano-grained RuO_2+glass films can be interpreted as arising from the fluctuations of voltage dependent barriers in thermally activated transitions between neighboring RuO_2 grains.

Acknowledgements

The work was supported by Rzeszów Univ. Technol. projects U-6180/BW and U-6179/DS. NATO is gratefully thanked for reimbursing the costs of author's attendance at ARW in Brno.

References

[1] A. Masoero *et al*, Excess noise and its temperature dependence in thick-film resistors, J. Phys. D: Appl. Phys. **16** (1983) 669-674.

[2] T. M. Chen, S. F. Su, D. Smith: 1/f noise in Ru-based thick-film resistors, Solid State Electronics **25** (1982) 821-827.

[3] B. Pellegrini, $1/f^{\gamma}$ noise in thick film resistors as an effect of tunnel and thermally activated emissions, from measures versus frequency and temperature, Phys. Rev. B **27** (1983) 1233-1243.

[4] M. Affronte *et al*, Low temperature electronic transport in RuO_2-based cermet resistors, J. Low Temp. Phys. **109** (1997) 461-475.

[5] G. E. Pike and C. H. Seager, Electrical properties and conduction mechanisms of Ru-based thick-film (cermet) resistors, J. Appl. Phys. **48** (1977) 5152-5169.

[6] K. Flachbart *et al*, Conduction mechanism in RuO_2-based thick films, Phys. Stat. Solidi (b) **205** (1998) 399-404.

[7] J. H. Scofield, ac method for measuring low-frequency resistance fluctuation spectra, Rev. Sci. Instrum. **58** (1987) 985-993.

[8] A. Kolek *et al*, Low temperature nonlinear 1/f noise in RuO_2 based thick film resistors, Proc. 25th Int. Spring Sem. on Electronics Technol., ISSE 2002, Prague, Czech Rep. (2002) 142-146.

[9] P. Ptak *et al*, 1/f noise versus magnetic field in RuO_2 based thick film resistors, Proc. 26th Int. Spring Sem. on Electronics Technol., ISSE 2003, Stara Leśna, Slovak Rep. (2003) 196-201.

[10] D. McCammon *et al*, 1/f noise and hot electron effects in variable range hopping conduction, Phys. Stat. Solidi (b) **230** (2002) 197-204.

[11] N. Birge, B. Golding, W. Haemmerle, Electron quantum interference and 1/f noise in bismuth, Phys. Rev. Lett. **62** (1989) 195-198.

[12] B. I. Shklovskii, 1/*f* noise in variable range hopping conduction, Phys. Rev. B **67** (2003) 045201 1-6.

[13] V. I. Kozub, Low-frequency noise due to site energy fluctuations in hopping conductivity, Solid St. Comm. **97** (1996) 843-846.

[14] V. Ya. Pokrovskii *et al*, Modulation origin of 1/f noise in two-dimensional hopping, Phys. Rev. B **64** (2001) 201318 1-4.

[15] K. Shtengel, C. C. Yu, 1/f noise in Coulomb glass, Phys. Rev. B **67** (2003) 165106 1-8.

[16] T. Yamaguchi, Y. Nakamura, Sol-gel processing and conduction mechanism of RuO_2-glass thick film resistors, J. Am. Ceram. Soc. **78** (1995) 1372-1374.

[17] Y. Meir, Percolation-type description of metal-insulator transition in two-dimensions, Phys. Rev. Lett. **83** (1999) 3506-3509.

[18] A. Kolek, A. A. Snarskii, A. Morozovskii, Structure of the percolation cluster and excess 1/*f* noise in systems with an exponentially broad spectrum of resistances, Sov. JETP **81** (1995) 490-495.

[19] D. Lubin, I. Goldhirsch, Y Gefen, Temperature dependence of resistance noise in metal-insulator mixtures below the percolation threshold, Phys. Rev. B **38** (1988) 5899-5905.

[20] J. V. Mantese *et al*, Excess low frequency conduction noise in granular composite, Solid St. Comm. **37** (1981) 353-357.

[21] J. V. Mantese, W. Webb, 1/f noise of granular metal-insulator composites, Phys. Rev. Lett. **55** (1985) 2212-2215.

TECHNIQUE FOR INVESTIGATION OF NON-GAUSSIAN AND NON-STATIONARY PROPERTIES OF LF NOISE IN NANOSCALE SEMICONDUCTOR DEVICES

A. Yakimov, A. Belyakov, S. Medvedev, A. Moryashin and M. Perov

Nizhni Novgorod State University, Radiophysics Faculty

Gagarin Avenue 23, Nizhni Novgorod 603950

Russia

yakimov@rf.unn.ru

Abstract We investigated known methods of the LF (1/f) noise Gaussianity test. These are measurements of: (a) high order semi–invariants, (b) the histogram as the estimate of the probability density function, (c) the accuracy in the measurement of the noise intensity at the output of bandpass filter, (d) the correlation between intensities of the noise at outputs of non–overlapped filters, and (e) the complex bispectrum of the noise. These methods are sensitive to the non–stationarity of the noise as well. A special computer–aided setup was designed for these measurements. Tests were performed for quantum well laser diodes manufactured in Nizhni Novgorod State University. We have found that the voltage noise in the diodes is non–Gaussian and seems to be non–stationary. Our results may be used for the check of radiation defects in semiconductor devices and for the investigation of the 1/f noise nature.

Keywords: Semiconductors, nanoscale devices, 1/f noise, non-Gaussianity, bispectrum, non-stationarity

1. Introduction

The research of the 1/f noise non–Gaussian and non–stationary behaviors may give a new information on its nature and, thus, to find new ways for improving of semiconductor devices. M.B.Weissman [1] published in 1988 the comprehensive review on the non-Gaussianity problem and results obtained, some investigations were made later (see, e.g., [2]). But the problem is open for discussions until now. The problem of the noise non–stationarity detection is not investigated in detail as yet.

J.Sikula and M.Levinshtein (eds.),
Advanced Experimental Methods for Noise Research in Nanoscale Electronic Devices (253 - 260)

We report results of the investigation of the LF (1/f) voltage noise in laser diodes on $In_{0.2}Ga_{0.8}As/GaAs/InGaP$ quantum well. The diodes were manufactured in Nizhni Novgorod State University (Dr. B.Zvonkov's laboratory). Both "traditional" tests and a new one were used. A special computer–aided setup was designed for these measurements [3]. We have done all measurements in the laboratory by Prof. L.K.J.Vandamme (Eindhoven University of Technology, the Netherlands).

High–order semi–invariants, and the histogram as the estimate of the probability density function were measured. The accuracy in the measurement of the noise intensity at the bandpass filter output (**accuracy test**), and the correlation between intensities of the noise at outputs of non-overlapped filters (**correlation test**) were estimated experimentally as well. These so called "traditional" tests were supported by the standard spectral analysis.

It seems, the complex bispectrum of the 1/f noise was measured and investigated for the first time. It is quite surprising because the use of the bispectrum for the noise analysis is well described [4, 5].

Methods tested here have different sensitivity to the non–Gaussianity, and are sensitive to the non–stationarity of the noise. We have found that the voltage noise in the diodes is non–Gaussian and seems to be non–stationary.

Our results may be used for the check of radiation defects in semiconductor devices and for the investigation of the 1/f noise nature.

2. Experimental results

Amplified voltage noise was sampled (N=10^6 points for every selected current I_d through the laser diode) and recorded onto hard disk of PC as the binary file. We have used the analogue input/output 24-bit module ADS224x48 (Instrumental Systems Corporation, Moscow, Russia) with sampling frequency 48 kHz. Each record takes nearly 21 sec. Such records were used for further noise analysis.

The voltage noise spectrum from one of lasers is shown in Fig. 1a for different currents. The **lowest curve** shows the noise floor of the measuring setup. Three first spectra (from the top) correspond to I_d = 0.47, 0.85, 2.4 mA. That is a "dark" mode, without light emission. Spontaneous light emission (SE) starts at 4.2 mA in this diode. The following three spectra correspond to SE–mode, I_d = 12, 45, 208 mA. These spectra have the 1/f type, and are characterized by the Hooge's parameter of the order $\alpha \sim 10^{-3}$. The laser emission (LE) starts at I_d >290 mA. That yields considerable flattening of the spectrum, see last three curves obtained at I_d = 410, 540, 610 mA. We have no explanation for this effect as yet.

In Fig. 1b the dependences on the current at two frequencies are shown. The behavior in the "dark" mode may be explained by the noise in the leakage current. It should be noted that the leakage was seen in the I-V characteristic only at currents less than 10^4 A. The noise in SE–mode, and at the beginning of LE–mode, corresponds to the Kleinpenning's approach for ordinary *p–n* diodes [6].

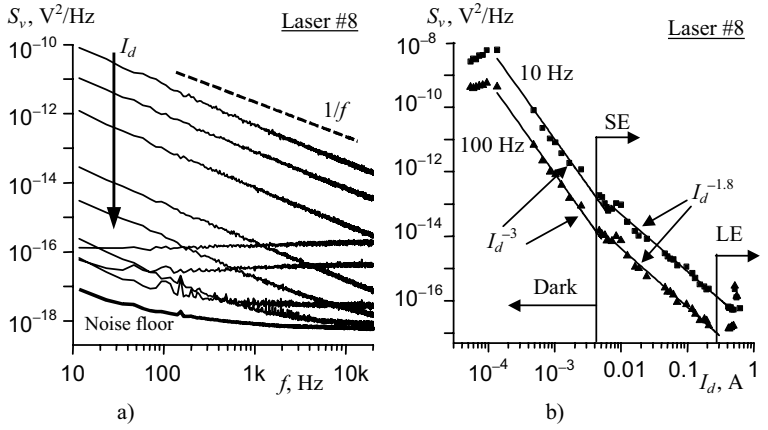

Figure 1. The voltage noise spectrum for laser #8. (a) The frequency dependence at different currents through the diode. (b) The current dependence at two different frequencies.

2.1. One-dimensional statistical characteristics

Semi–invariants and *pdf* being one–dimensional statistical characteristics were measured at the first. Results are presented in Fig. 2.

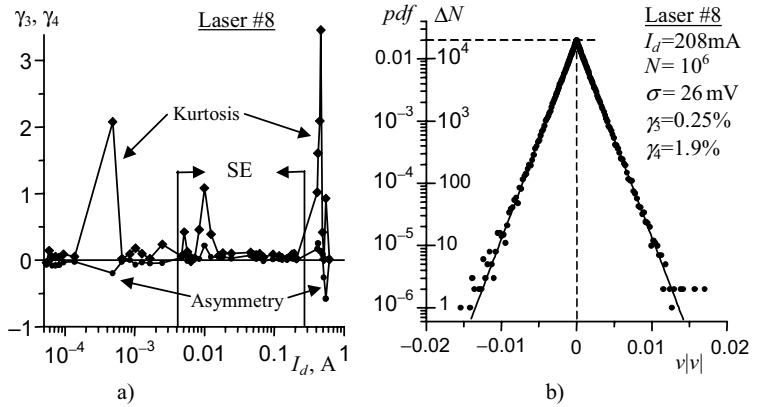

Figure 2. One-dimensional statistical characteristics for laser #8. (a) The dependence of asymmetry and kurtosis on the current through the diode. (b) The *pdf* at I_d=208 mA.

To estimate the asymmetry γ_3 and kurtosis γ_4 we have measured the standard σ together with the third and fourth semi–invariants $\kappa_{3,4}$. Then we calculated $\gamma_3=\kappa_3/\sigma^3$, and $\gamma_4=\kappa_4/\sigma^4$. This procedure is characterized by large statistical error, but is useful due to its simplicity. Fig. 2a shows the dependence of γ_3 and γ_4 on the current I_d. Large excursions are obviously seen in the kurtosis while the asymmetry is close to the zero as it should be for the Gaussian noise. Perhaps, such a sharp dependence of γ_4 on I_d may be explained rather by the non–stationarity than the non–Gaussianity of the noise.

The *pdf* of the noise at current 208 mA is shown in Fig. 2b. The Gaussian reference frame is used here. This function was calculated on the usual way, $pdf=\Delta N/N$. Here $\Delta N=\Delta N(v)$ is the quantity of data points that falls into the discriminator interval $[v; v+\Delta v]$. The relative error for the *pdf* is $\varepsilon_{pdf}=1/\sqrt{\Delta N}$. It is of the order 1% at the peak and reaches 100% at the tails. It can be concluded that the shown *pdf* corresponds to the Gauss law.

2.2. The accuracy test

The researched noise is subjected to the Fast Fourier Transform. Then the sum of intensities of spectral components, which fall into selected interval of frequencies, is calculated. The number of samples N_{FFT} for used FFT is previously set. The total quantity $N_a=N/N_{FFT}$ of intensity estimates for the filtered noise is obtained in this way. The estimate with number n_a (here $n_a \le N_a$) is calculated by the averaging of n_a accumulated data. The array of obtained intensity estimates is used for the experimental evaluation of current accuracy of the measurement $\varepsilon_{exp}=\varepsilon_{exp}(n_a)$. Certainly, the value ε_{exp} is random; therefore a confidence interval is to be determined for it.

The aim of the present investigation is the check of so-called "zero hypothesis" (ZH) on the Gaussianity and stationarity of the noise. The calculation of the confidence interval for ZH is made, for example, in [2] for the probability to fall into the interval being $P_c=95\%$. If approximately 5% of the data are outside of the interval, ZH is fulfilled. Otherwise, at least, one condition is not true – the Gaussianity, or stationarity of the noise.

With accuracy sufficient for experiments it is possible to take the half-width of the confidence interval equal $\Delta H_a \approx 4.3\varepsilon_{th}$, where $\varepsilon_{th}=1/\sqrt{(t\cdot\Delta f_a)}$. Here t is the duration of a treated part of the noise record, $t \le 21$sec; Δf_a – effective width of the filtered noise spectrum.

Fig. 3a shows results of the accuracy test for laser #8 at current $I_d=208$ mA. Here the total number of estimates is $N_a=10^6/2048=488$, that yields the theoretical accuracy $\varepsilon_{th}\approx 0.9\%$. The shadow region shows the 95% confidence interval. It is seen that 54% of the estimates are out of the interval. Thus, the ZH is not fulfilled here. Note, that one-dimensional

statistical characteristics did not reveal any remarkable deviation from the zero hypothesis for the noise at this current, see Fig. 2. The trend of data in Fig. 3a suggests that the noise is non–stationary.

Relative amount of estimated accuracies found outside of the confidence interval, versus the current through the diode, is presented in Fig. 3b. As it can be seen the ZH is not fulfilled for most currents.

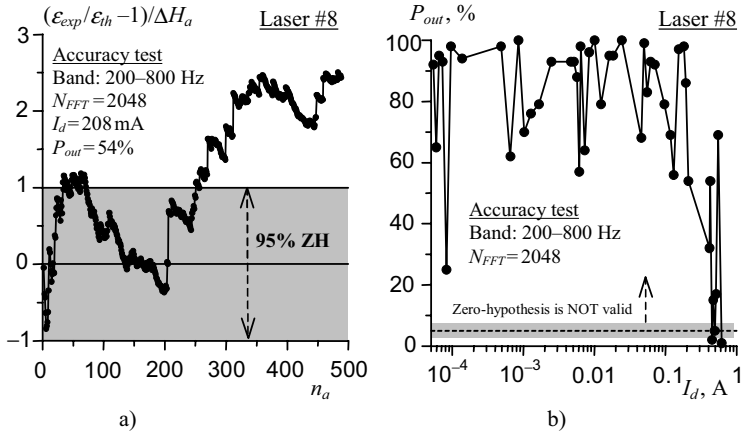

Figure 3. Accuracy test for laser #8. (a) Data as compared with 95% confidence interval at I_d=208 mA. (b) Amount of accuracies found outside of the confidence interval, versus I_d.

2.3. The correlation test

The procedure of array of intensity estimates obtaining is similar to that one used in the accuracy test. The difference is two non-overlapped filters were used. Another difference is less N_{FFT} was used for the correlation test. It was made so because the accuracy of this test is $\varepsilon_R=1/\sqrt{n_R}$. Here n_R, similar to n_a, is the number of the record treated piece, $n_R \le N_R = N/N_{FFT}$.

The correlation factor $R=R(n_R)$ between intensities of the noise at outputs of the filters was measured. If these intensities are fully correlated, then R=1. In the case of stationary Gaussian input noise R=0. The ZH 95% confidence interval half-width is $\Delta H_R \approx 2\varepsilon_R$.

Fig. 4a shows results of the correlation test for laser #8 at current I_d=208 mA. Here the total number of estimates is $N_R=10^6/512\approx1953$, that yields $\Delta H_R \approx 4.5\%$. It is seen that nearly half of the estimates are out of the interval. Thus, the ZH is not fulfilled here. The same trend of data as in Fig. 3a suggests that the noise is non–stationary.

Dependence of the correlation factor on the current through the diode at different treated lengths n_R is presented in Fig. 4b. It again can be seen the ZH is not fulfilled for most currents.

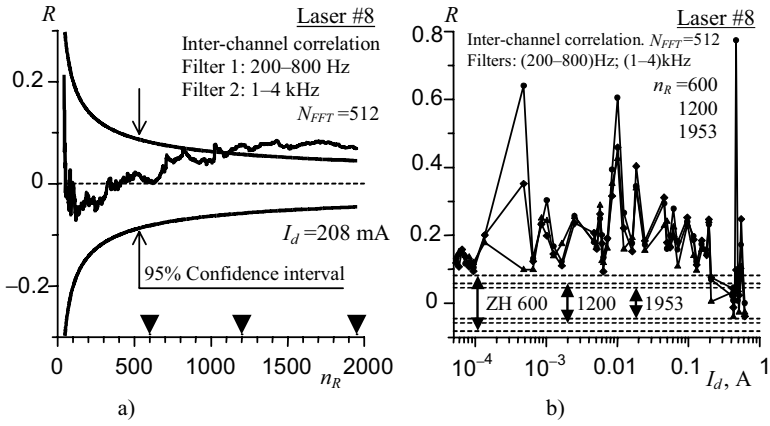

Figure 4. Correlation test for laser #8. (a) Data as compared with 95% confidence interval at I_d=208 mA. Magnitudes of n_R are marked, which are used in Fig. 4b. (b) Inter–channel correlation versus I_d at different n_R.

3. The bispectrum

The bispectrum $B_v(f_1, f_2)$ being a complex function determined on the frequency plain $0f_1f_2$ is estimated as follows.

$$B_v(f_1, f_2) = \frac{1}{N_B T_B} \sum_{n=1}^{N_B} \chi_n(f_1)\chi_n(f_2)\chi_n^*(f_1 + f_2). \qquad (1)$$

In the difference with the estimation of the spectrum $S_v(f)$ the product of three Fourier transforms $\chi_n(f)$ of noise $v(t)$ is used here. Each transform is calculated over the time block $[t_s+(n–1)T_B;\ t_s+nT_B]$, $n\in[1;\ N_B]$. Value t_s is the time of the recording start, product $N_B{\cdot}T_B$ is the total duration of the analyzed noise record, while treating it is divided onto $N_B=N/N_{FFT}$ pieces.

Fig. 5a shows estimates of the bispectrum absolute value measured along the bisector of the frequency plain. The same currents as in Fig. 1a are selected. It should be noted that the effect of the "whitening" of the noise in LE–mode obtained from the spectrum is much more pronounced here. In other words, the laser light emission yields the increase of the non–Gaussianity of the voltage noise.

In Fig. 5b the dependence of the bispectrum absolute value at the point (375Hz, 375Hz) versus the current through the diode is shown. Two smooth lines present limits of 95% confidence interval for the zero hypothesis. To determine this interval we have used relation found from [5] for the variance of the complex bispectrum at the bisector of frequency plain. That yields the

following result for the variance σ_1^2 of single component (real or imaginary) of the bispectrum estimate in point (f,f):

$$\sigma_1^2 = \frac{S_v^2(f)\cdot S_v(2f)}{N_B \cdot T_B \cdot (\Delta f)^2}. \qquad (2)$$

In our experiment $N_B \cdot T_B = 21$ sec, and frequency resolution $\Delta f = 93.75$Hz. If the input noise is Gaussian (the ZH is fulfilled) then, due to the Central Limit Theorem, estimates of real and imaginary parts of the bispectrum may be considered to be Gaussian, with the zero mean value, and variance (2). This yields the distribution of the bispectrum absolute value of the Reyleigh type with the maximum at σ_1. To find the 95% confidence interval we take the probabilities of excursions out of the bottom and top limits to be equal to 2.5% each. Results obtained are drawn in Fig. 5b by smooth lines. It is obviously seen that the most part of estimates lay over the confidence interval. Thus, we can conclude that the noise is non–Gaussian.

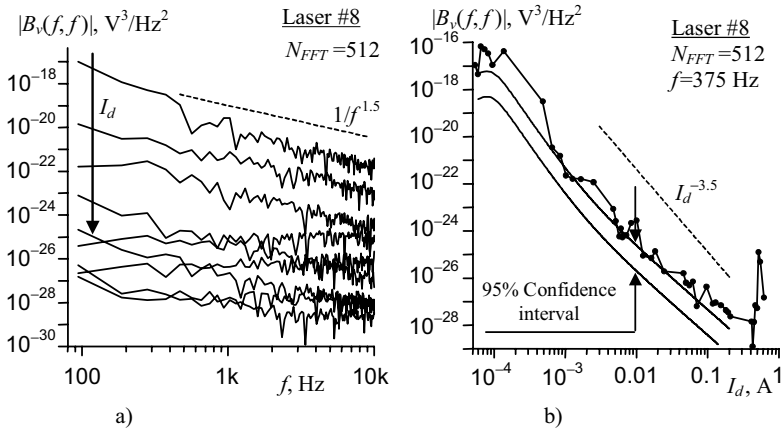

Figure 5. The bispectrum absolute value at the bisector for laser #8. (a) The frequency dependence at different currents through the diode. (b) Data as compared with 95% confidence interval versus I_d.

4. Conclusions

In addition to "traditional" methods of the Gaussianity check the bispectrum $B_v(f_1, f_2)$ of the 1/f voltage noise in laser diodes on $In_{0.2}Ga_{0.8}As/GaAs/InGaP$ quantum wells was measured for the first time. This method may be considered as an additional one for the investigation of the 1/f noise nature.

The estimates of asymmetry and kurtosis suggest that the noise is non–stationary. The same result follows from accuracy and correlation tests.

If results of our measurements are reliable, we can conclude that the 1/f noise in investigated laser diodes is non–Gaussian random process. It also seems that the noise is non–stationary, but to prove this feature additional investigations are necessary.

Acknowledgements

This work was supported by the NATO in the framework of the "Science for Peace" Project SfP–973799 "Semiconductors" with the universities of Eindhoven (co–director Prof. L.K.J.Vandamme) and Nizhni Novgorod (co–director Prof. A.Yakimov) as partners. The work was also supported by grants of RFBR 01–02–16666, 02–02–06298, and NSh–1729.2003.2 (Scientific School).

References

[1] M. B. Weissman, 1/f Noise and other slow, nonexponentional kinetics in condensed matter, Rev. Mod. Phys. **60** (1988) 537–571.

[2] A. V. Yakimov, and F. N. Hooge, A simple test of the Gaussian character of noise, Physica B **291** (2000) 97–104.

[3] A. A. Andronov, A. V. Belyakov, V. A. Guryev, and A. V. Yakimov, The interactive visual development of applications of automation scientific and industrial measuring and control systems by means of LabVIEW 6i National Instruments, Proc. NATO Project SfP–973799 Semiconductors 2nd Workshop "Design of radiation-hard semiconductor devices for communication systems and precision measurements using noise analysis", TALAM–Press, Nizhni Novgorod, 2002, 38–46; http://www.rf.unn.ru/NATO/index.html.

[4] C. L. Nikias and M. R. Raghuveer, Bispectrum estimation: a digital signal processing framework, Proc. IEEE **75** (1987) 869–891.

[5] G. N. Bochkov, K. V. Gorokhov, and I. R. Konnov, On the accuracy of spectral and bispectral measurements, Techn. Phys. Lett. **20** (1994) 319–321.

[6] T. G. M. Kleinpenning, 1/f noise in p-n diodes, Physica **98B+C** (1980) 289–299.

THE NOISE BACKGROUND SUPPRESSION OF NOISE MEASURING SET-UP

P. Hruska[1]
Brno University of Technology, Department of Physics
Technicka 8, 616 00 Brno
Czech Republic

K. Hajek[2]
Military Academy, Department of Electronics
Kounicova 65, 612 00 Brno
Czech Republic

[1] hruskap@feec.vutbr.cz
[2] karel.hajek@vabo.cz

Abstract Preamplifier noise reduction in the view of varying source impedance, as in AE sensors, is discussed. First, the relation of the preamplifier noise and the source resistor is treated. Further, the input capacitance and the internal source capacitance influence are discussed. Eventually, the influence of preamplifier AC coupling on the noise is shown and analyzed.

Keywords: Low noise, dynamic range, current noise, voltage noise, charge amplifier.

1. Introduction

The noise background of a preamplifier is mainly determined by the preamplifier actual noise. Nevertheless, the output noise of the preamplifier is an involved phenomenon, which depends on several terms. The basic noise properties of the preamplifier are given by its circuit design, by the source output parameters and the way of the preamplifier - source circuit connection. The optimum solution of this complex problem lies in the preamplifier – source impedance matching.

J. Sikula and M. Levinshtein (eds.),
Advanced Experimental Methods for Noise Research in Nanoscale Electronic Devices (261- 270)

The basic model of the signal source and the preamplifier connection is shown in Fig. 1. In the model analysis we have to take into consideration:

- noise properties of preamplifier
- input impedance of preamplifier
- output impedance of source
- total gain
- AC coupling (if necessary)

These model parameters are mutually connected and therefore the solution is not elementary.

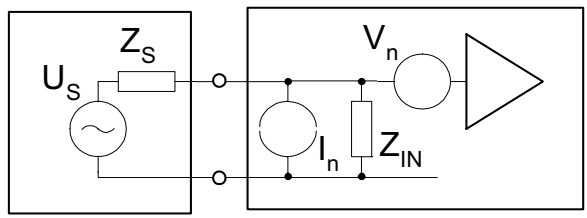

Figure 1. A simple noise and impedance model of the connection of a signal source and a preamplifier.

2. Equivalent input noise of the preamplifier

The basic noise model of a preamplifier is shown in Fig. 2. We can see several sources of the noise. The external resistors R_i are sources of thermal noise. Their values V_{nRi} are related to the internal resistance of the signal source. The equivalent voltage noise and two input current sources of the preamplifier are also indicated. Considering the case A>>1 (A= - R_2/R_1 or A= 1+ R_2/R_1), the equivalent output noise can be expressed as

$$V_{nOUT} = AV_{neq} = A\sqrt{V_n^2 + V_{In+}^2 + V_{In-}^2 + V_{nR1}^2 + V_{nR2}^2 / A^2 + V_{nR3}^2} \tag{1}$$

where particular noise sources can be expressed as:

$$V_{In+} = I_{n+}R_3 \tag{2}$$

$$V_{In-} = I_{n-}(R_1 // R_2) \tag{3}$$

$$V_{nR1} = \sqrt{4kTBR_1} \tag{4}$$

$$V_{nR2} = \sqrt{4kTBR_2} \tag{5}$$

$$V_{nR3} = \sqrt{4kTBR_3} \tag{6}$$

with $B = \Delta f$, the frequency range

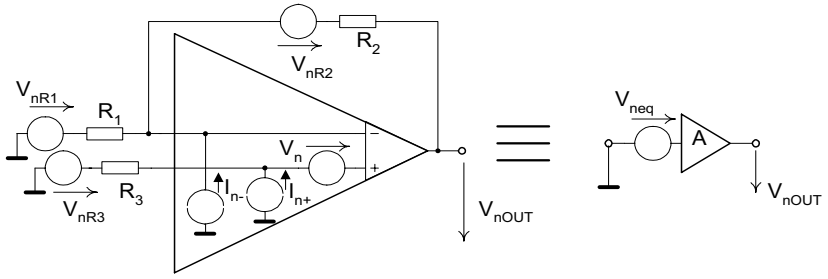

Figure 2. A basic noise model of the preamplifier.

The discussion of equations (1-6) offers the following practical conclusions from the point of view of resistors (or impedances) values:

$$V_{neq} \approx \sqrt{(I_{n\pm}R)^2 + 4kTBR} \quad \left(V_{neq} \approx \sqrt{(I_{n\pm}Z)^2 + 4kTBR}\right) \tag{7}$$

thermal noise - $V_{neq} \approx \sqrt{R}$ (8)

current noise - $V_{neq} \approx R$ (resp. $V_{neq} \approx Z$) (9)

Accordingly, the equivalent input noise is determined by the voltage noise source V_n for low resistor values and by the current noise sources I_{n+} and I_{n-} for high resistor (or impedance) values, respectively. It is necessary to consider a generation of voltage noise by multiplying the current noise I_n by the impedance Z. For example, the capacitive internal impedance of source generates noise by the current noise action.

The influence of both noise sources is shown in Fig. 3. The thermal noise of the resistor is expressed by line "thermal noise of R". The growth of the preamplifier actual noise is caused by the voltage noise - for low value of R, and by the current noise - for high value of R, resp. The voltage noise can be expressed in terms of the equivalent noise resistor R_{neq}. Typical value of R_{neq} for a good amplifier with bipolar input is approximately 100 Ω. As we can see, the minimum of a noise rise in comparison with thermal resistor noise is in the middle of the curve, approximately for the value 10 kΩ.

We have two practical possibilities of the preamplifier realization, one with bipolar transistor input and the other with unipolar transistor input. Since the current noise dominates in the bipolar input (approximately 1 pA /√Hz, 1 nV/√Hz), while the voltage noise prevails in the unipolar input

(approximately 10 fA /√Hz, 10 nV/√Hz), we can choose the type of realization according to the rule:

- for R<<10 kΩ the bipolar transistor input is used
- for R>>10 kΩ the unipolar transistor input is used
- for R is about 10 kΩ both the transistors can be used

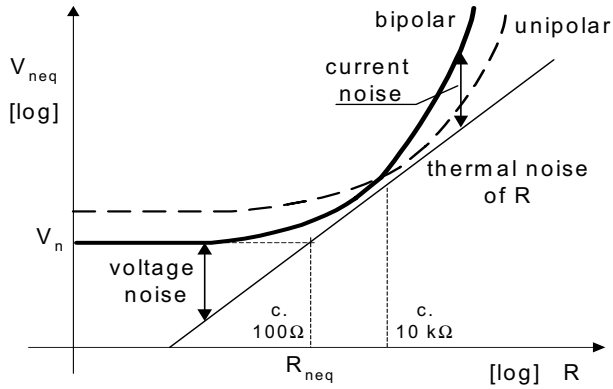

Figure 3. The equivalent amplifier voltage noise as a function of equivalent source resistance (solid line - bipolar input, dashed line – unipolar input).

This solution is optimum for the medium frequency, where the spectral density of the voltage and the current noise are frequency-independent, as in the case of thermal noise. We have to consider growth of the noise for both types of inputs for lower frequencies. Typical examples of these dependencies are shown in Fig. 4.

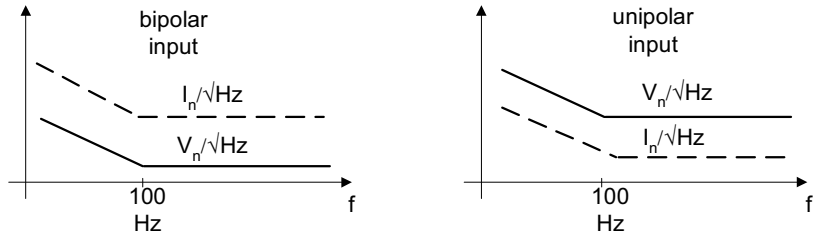

Figure 4. Examples of the voltage and current spectral density of amplifiers with bipolar transistor input and unipolar transistor input.

The above-mentioned conclusions show that the solution of the preamplifier design for an arbitrary value of the input resistance is very difficult. One way, how to solve the problem, is the use of the special input unipolar transistors with low V_n. Nevertheless, this transistor has disadvantage of a higher input capacitance, which is a limiting factor for high impedance sources at higher frequencies.

3. Input capacitance influence

Previous text introduces the question of input capacitance. It is connected with the noise through the signal/noise ratio. Therefore its analysis is very important for the practical use of preamplifiers, particularly for high source resistance. The basic model of this effect is shown in Fig. 5. The total transfer function can be expressed as

$$H = \frac{Z_{IN}}{R_S + Z_{IN}} A, \tag{10}$$

where Z_{in} is the parallel combination of R_{IN} and C_{IN}. Solving (10), we obtain the cut-off frequency

$$f_C = \frac{1}{2\pi R C_{IN}}, \tag{11}$$

where R is the parallel combination of R_S and R_{IN}. This effect is very strong for high source resistance. Typical example is illustrated in Fig. 5. The solution of this problem consists in minimization of the input capacitance C_{IN}. One may use low input resistance (using the resistive divider R_S/R_{IN} as shown in Fig. 5, case b) with a consequent decrease of gain and, unfortunately, with a lowering of the signal/noise ratio.

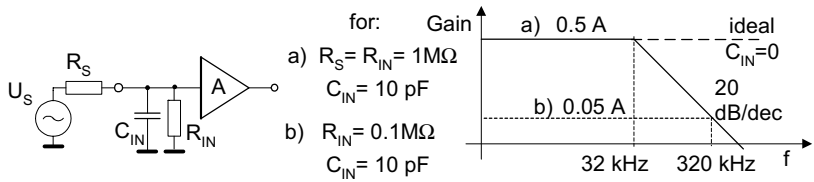

Figure 5. Basic model and example for input capacitance effect. The magnitude response for resistive dividing is shown for two values of input resistance.

4. Influence of output source impedance

Let us consider the case of capacitive impedance of the output source. The impedance of AE sensors is a typical example. Two types of amplifiers can be used in this case, see Fig. 6. Beyond a typical voltage amplifier, we can use the charge amplifier. We have to divide this problem into two basic cases before we make comparison of the solutions. The main criterion is the operating frequency range. Consider the following ranges:

a) low frequency – $f_s < 1$ kHz
b) high frequency – $f_s > 100$ kHz
c) medium frequency – 1 kHz $< f_s <$ 100 kHz

Nevertheless, in all cases, these amplifiers work as high-pas filters of cutoff frequency f_c as shown in Fig. 7.a.

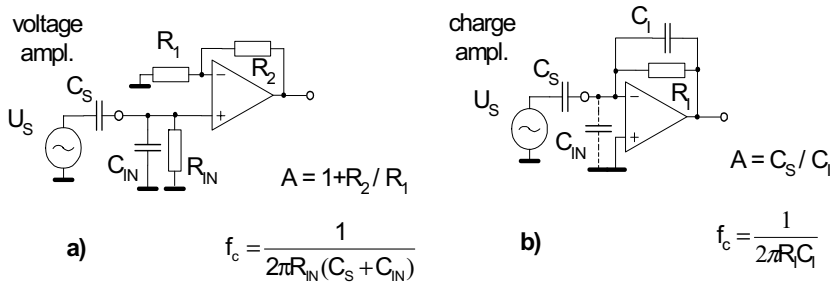

Figure 6. Preamplifiers for source with capacitive output impedance a) basic model of voltage preamplifier, b) basic model of charge preamplifier.

The first case, the low frequency region, opens a basic problem of the cutoff frequency minimization by the use of maximum resistance R_I (R_{IN}). It is necessary to consider this factor in the noise analysis. The noise signal is generated in two major ways. First, let us focus attention on the thermal noise of resistors R_{IN} and R_I. The voltage amplifier exhibits higher noise, since the thermal noise of the resistor R_{IN} is amplified (with gain A), while the charge amplifier doesn't amplify that of R_I. On the other hand, the gain A and the same cutoff frequency requires lower value of capacitance C_I and higher value of R_I, which rises the value of the noise by in root of A, see Fig. 7.b.

The current noise is higher than the thermal noise of resistor R_{IN} or R_I. Therefore it is necessary to compare the impedance of equivalent input circuit for both types of amplifiers and to compare the transfer of the mentioned noise into the amplifier output.

At first glance, the impedance is approximately unchanged. The voltage amplifier transfer of the current noise I_n*Z to output is A times higher. Nevertheless, if we consider the same cut-off frequency, obtained by A times higher R_I value, the output noise is the same in both cases. Therefore, we can use (in this frequency range) both types of amplifier without any substantial difference, see Fig. 7.c.

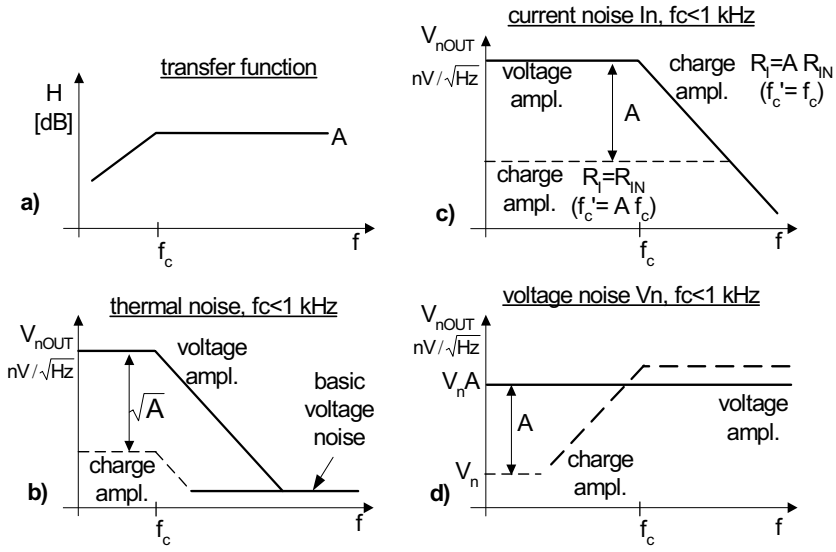

Figure 7. Properties of the voltage and charge amplifiers form Fig. 6: a) basic transfer function; Voltage spectral density b) for low frequency and thermal noise, c) for low frequency and current noise, d) for high frequency and voltage noise.

The voltage noise is the dominant noise effect in the second case, the higher frequency region. The voltage amplifier transfers the voltage noise of the amplifier with gain A without any frequency distortion:

$$V_{nOUT} = V_{neq} A \tag{12}$$

On the other hand, the charge amplifier introduces an output noise

$$V_{nOUT} = V_{neq} \frac{s\dfrac{C_S + C_{IN} + C_I}{C_S} + \dfrac{1}{C_I R_I}}{s + \dfrac{1}{C_I R_I}} = V_{neq} \frac{s\left(A + 1 + \dfrac{C_{IN}}{C_S}\right) + \dfrac{1}{C_I R_I}}{s + \dfrac{1}{C_I R_I}} \tag{13}$$

which brings unit gain for the low frequency region and a slightly higher gain for the frequency region up to the cut-off frequency, compared to the

voltage amplifier, see Fig. 7.d. If we consider typically attenuated noise band below the cutoff frequency by next ordered high-pass filter, the charge amplifier has usually higher output noise in comparison with the voltage amplifier in this frequency region.

In the case of the mid frequency band (approximately 1 kHz – 100 kHz), it is necessary to consider simultaneously the effect of the current and voltage noise of the amplifier. As we can see, the use of the charge preamplifiers for the AE sensors is debatable, with a need of more criterions. We believe, that the voltage amplifier and the charge amplifier have practically very similar noise properties in the low frequency region. At this point, we would like to point out, that the above statement is not a widely known piece of information.

5. AC coupling influence

We have to consider this effect in the case of AC coupling with DC source, see Fig. 8. In the case of high input resistance of R_{IN} of universal preamplifier A and low internal resistance R_S of the source, we observe an effect of the noise growth in the frequency range below f_2. The frequencies can be expressed as

$$f_1 = 1/(2\pi R_{IN} C_C)\,, \tag{14}$$

$$f_2 = 1/(2\pi R_S C_C)\,. \tag{15}$$

It is caused by time constants $C_C R_{IN,}$ $C_C R_S$ and corresponding R_{IN} thermal noise. The use of the maximum value of coupling capacity C_C in this case can minimize this effect. The use of high-pass filter in the next stage is not entire solution of this problem because it brings the same problem as in previous case. The voltage spectral density for current noise effect brings the same frequency dependence, but in the power value. Therefore it is more important.

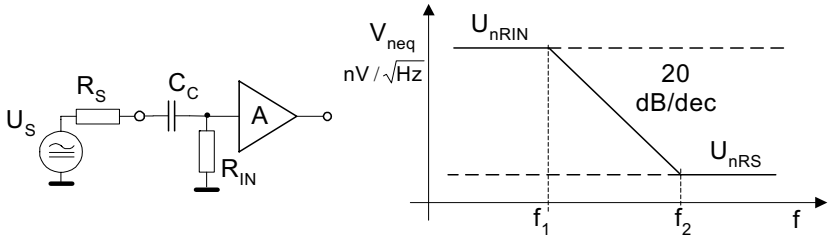

Figure 8. Preamplifiers with capacitive coupling of source: a) basic model, b) noise spectral density response.

Conclusions

The paper deals with selected problems of the preamplifier noise background minimization. As we have seen, the solutions under consideration are not unambiguous and the need of more conditions discussion arises. Therefore, the design and application of the versatile preamplifiers is rather a complicated problem.

In general, it is advisable to consider the following basic recommendations:

- choose the optimum type of the input preamplifier (unipolar or bipolar), depending on the magnitude of the source resistance,
- minimize the noise by standard classical ways (parallel connection of preamplifiers, etc.)
- minimize the amplifier input capacitance for high values of the source resistance
- in the case of capacitive impedance of sensors:
  - use an HP filter in the subsequent block
  - recall, that in the higher frequency range (f > 100 kHz), the voltage amplifier has rather low noise
  - use freely either voltage or charge amplifier in the lower frequency range
- in the case of AC coupling use maximum value of coupling capacitance C_C.

Acknowledgement

This paper is based on the research supported by the project MSM 262200022 and by the grant GACR 102/03/1811.

References

[1] K. Hajek, J. Sikula. M. Tacano, S. Hashiguchi: Signal to Noise Ratio and Preamplifier Noise of AE Measuring Systems. Proc. of EWGAE'02, Prague, August 2002, p. 111-118.

[2] K. Hajek, J. Sikula: Electrical Filters for AE Ultra-Low Noise Amplifier. Proc. of ECNDT'02, Barcelona, June 2002. p. 246.

[3] Analog Devices,: Datasheets, http://www.analog.com.
[4] Linear Technology: Datasheets, http://www.linear-tech.com.
numbered.

ACCURACY OF NOISE MEASUREMENTS FOR 1/*f* AND GR NOISE

I. Slaidiņš

Riga Technical University, Faculty of Electronics and Telecommunications, Department of Radio Systems

Azenes 12, LV-1048, Riga

Latvia

slaidins@rsf.rtu.lv

Abstract High accuracy of an experimental investigation of noise features of semiconductor devices and materials in low frequency region is very important for reaching deep understanding of noise features It will enable precise extracting of essential noise parameters and modelling noise behaviour of real devices.

In this paper measurement accuracy of 1/f and GR noise in semiconductor devices, as well as data processing for parameter extraction will be discussed. Theory of random process parameter estimation gives us a basis for evaluation of measurement errors. General analysis of statistical accuracy of noise measurement is made. From this analysis practical recommendations and formulas for accuracy evaluation are derived. Differences in 1/f and GR noise characteristics must be taken into account in measurement. Choice of the most appropriate measurement conditions for particular kind of noise is discussed.

Another source of measurement error could be contribution of other interfering signal sources. As a rule 1/f and GR noise are present simultaneously and a task is to evaluate their parameters separately. In the measurement and data processing process discrimination of particular noise sources and subtraction of other background noise sources must be provided.

Keywords: Noise measurement, 1/f and GR noise, measurement accuracy

1. Introduction

Semiconductor device technology has reached a very high level of sophistication but low frequency noise parameters still can not be theoretically predicted with a needed accuracy. Only very focused and

J.Sikula and M.Levinshtein (eds.),
Advanced Experimental Methods for Noise Research in Nanoscale Electronic Devices (271 - 278)

accurate experimental research can lead to deeper understanding of noise features in real devices.

Current and voltage fluctuations in semiconductor devices are random processes. Measurement methodology of noise source parameters is based on estimation theory of parameters of random processes and is well developed. Less attention is devoted to evaluation of measurement accuracy from the statistics point of view. Insight in this problem and basic analysis was given already in [1].

There are several noise sources in every device and we are observing a combined contribution of all these sources at the output. Research interest is to discriminate contribution of particular source enabling extraction particular parameters [2].

High measurement accuracy and appropriate data processing methodology is needed for precise extracting of essential noise parameters. Detailed analysis of device model with location of noise source, appropriate choice of measurement circuit configuration and measurement conditions, as well as appropriate data processing and subtraction of background are all important procedures to obtain high accuracy of results.

In this paper main focus is on statistical accuracy of noise measurement. Other aspects of measurement and data processing accuracy will be just shortly discussed and are treated in more detail elsewhere [3].

2. Statistical Accuracy of Noise Measurement

Theory of random process parameter estimation gives us a basis for evaluation of measurement errors. Let us consider that both 1/f and GR noise are measured in a limited frequency band and are ergodic stationary stochastic processes with Gaussian probability density function and zero mean. Based on these assumptions general analysis of statistical accuracy of noise measurement is made.

2.1. Analog measurement

Noise is usually measured as a power estimate of random process or estimate of variance σ_x^2. For stationary ergodic process *x(t)* with zero mean we can use following algorithm for measurement of the estimate of variance as a time-average

$$\hat{\sigma}_x^2 = \frac{1}{T}\int_0^T x^2(t)dt\,, \tag{1}$$

where T - measurement time.

According to Eq. (1) instantaneous values of time function of noise have to be squared (square-law detector) and then applied to integrator circuit. Linear detector is also often used for noise measurement. Measurement accuracy analysis and, in particular, for linear detector is presented in [1].

To obtain good accuracy measurement time T must be much larger than correlation time τ_k of random process $x^2(t)$. Correlation time is a parameter derived from the autocorrelation function $K_x(\tau)$

$$\tau_k = \frac{1}{\sigma_x^4} \int_0^\infty K_x^2(\tau) d\tau . \tag{2}$$

Variance of the estimate of variance could be determined by formula [4]

$$D(\hat{\sigma}_x^2) = \frac{4}{T} \int_0^T K_x^2(\tau) d\tau = \frac{4\tau_k}{T} \sigma_x^4 . \tag{3}$$

Statistical error of measurement could be determined as a relative variation of the estimate of variance

$$\varepsilon^2 = \frac{D(\hat{\sigma}_x^2)}{\sigma_x^4} = \frac{4\tau_k}{T} . \tag{4}$$

We can not determine accuracy of each particular measurement. Just we can state that with confidence probability 0.68 relative variation of estimate of variance will be in limits $\pm\varepsilon^2$. Result could be expressed in percents as well.

Width of autocorrelation function and accordingly τ_k depends on how rapidly are changing instantaneous values of the process. To determine τ_k analytically autocorrelation function must be absolutely integrable that is not always a case. As temporal and spectral characteristics are inter-linked it is reasonable to use spectral characteristics in the cases when appropriate.

Let us use power spectral density (PSD) of the process in the following format:

$$G_x(f) = 2S_x(f) = 2 \int_{-\infty}^{\infty} K_x(\tau) \exp(-2\pi j f \tau) d\tau . \tag{5}$$

Then applying Parssevals's theorem we can obtain following equality between temporal and spectral characteristics:

$$\int_0^\infty K_x^2(\tau) d\tau = \frac{1}{4} \int_0^\infty G_x^2(f) df . \tag{6}$$

Using Eq. (2) to substitute left part of Eq. (6) we will arrive at

$$\tau_k = \frac{1}{4\sigma_x^4}\int_0^{\infty} G_x^2(f)df\,. \tag{7}$$

Finally, we will obtain formula for calculation of relative variation of the estimate of variance from PSD:

$$\varepsilon^2 = \frac{\frac{1}{T}\int_{-\infty}^{\infty} G_x^2(f)df}{\left[\int_0^{\infty} G_x(f)df\right]^2}. \tag{8}$$

If we consider that measurement system has a filtering ability with frequency response *H(f)* then noise spectral and temporal characteristics will be affected. It must be taken into account in evaluation of measurement accuracy as well.

2.2. Measurement with discrete sampling

Previous analysis was based on consideration that noise is measured with analog measurement devices. The same analysis could be transformed to case of discrete sampling. Considering N independent samples x_i of ergodic stationary stochastic process with Gaussian probability density function and zero mean, unbiased estimate of variance could be determined by well known formula

$$\hat{\sigma}_x^2 = \frac{1}{N-1}\sum_{i=1}^{N} x_i^2\,. \tag{9}$$

Estimate of variance is a random value and has Pierson's probability distribution with $\nu = N-1$ states of freedom. For such case variance of the estimate of variance according to [5] is

$$D(\hat{\sigma}_x^2) = \frac{1}{N}\left(\mu_4 - \frac{N-3}{N-1}\sigma_x^4\right), \tag{10}$$

where μ_4 - is a 4th central moment.

For $N > 30$ Pierson's distribution is converging to Gaussian distribution with $\mu_4 = 3\sigma_x^4$ and it leads to simpler version of Eq. (10)

$$D(\hat{\sigma}_x^2) = \frac{2}{N-1}\sigma_x^4\,. \tag{11}$$

Statistical error of discrete sample measurement as before could be determined as a relative variation of the estimate of variance:

$$\varepsilon^2 = \frac{2}{N-1}. \tag{12}$$

As we see from (12) statistical accuracy is steadily improving with increasing number of independent samples. To determine conditions when samples could be considered statistically independent we can compare Eq. (4) and (12) to get formula for calculation of equivalent number of independent samples N in noise time function of length T:

$$N = \frac{T}{2\tau_k} + 1, \tag{13}$$

From (13) we can easily determine a minimum sampling interval T_s for maintaining statistically independent samples:

$$T_S = 2\tau_k. \tag{14}$$

Formula looks similar to Nyquist sampling interval in digital signal processing which state that sampling rate must be 2 times higher than the highest frequency in the time function. Still correlation time τ_k have no relation to the highest frequency, but to low frequency components of random time function.

2.3. Practical examples

Combining different noise varieties existing in semiconductor device we obtain complex PSD

$$G(f) = G_E + \frac{G_\mathrm{F}}{f^\gamma} + \sum_{i=1}^{N} \frac{G_\mathrm{i}}{1 + (f/f_\mathrm{i})^2}, \tag{15}$$

where G_E - PSD of thermal and/or shot noise component, G_F - $1/f^\gamma$ noise PSD value at f = 1 Hz, G_i – PSD value of GR noise components, γ - parameter of 1/f noise (usually γ = 1).

Analysis of this complex PSD shows that there are 3 typical frequency dependencies. One is representing thermal noise, shot noise and low frequency part of GR noise. This is an even PSD with frequency non-dependent constant value. Another component is representing $1/f^\gamma$ noise with corresponding frequency dependence. For simplicity let us assume $\gamma = 1$ for this part of PSD. The third typical part is another $1/f^\gamma$ but with $\gamma = 2$. It is typical for GR noise.

Analysis of measurement accuracy can be provided for these 3 typical parts of spectra using the same equation at 3 different values of $\gamma = 0; 1; 2$

$$G(f) = \frac{G_0}{f^{\gamma}}. \tag{16}$$

For limited frequency band $f_1 \le f \le f_2$ and $\gamma = 0$ from Eq. (8) we can obtain

$$\varepsilon^2 = \frac{1}{T(f_2 - f_1)} = \frac{1}{TB}, \tag{17}$$

where $B = f_2 - f_1$.

This well-known formula is valid for evaluation of noise measurement accuracy in even part of PSD using an ideal rectangular band-pass filter. Accuracy will increase as measurement time and/or bandwidth increases.

Combining Eq. (4) and (17) we can get relation between B and correlation time τ_k

$$\tau_k = \frac{1}{4B}. \tag{18}$$

Taking into account (18) from (14) we can get formula for calculation of sampling intervals for discrete measurement

$$T_s = \frac{1}{2B}. \tag{19}$$

For $1/f^{\gamma}$ noise with $\gamma = 1$ from Eq. (8) we will get

$$\varepsilon^2 = \frac{\frac{1}{f_1} - \frac{1}{f_2}}{T \ln^2 \frac{f_2}{f_1}}. \tag{20}$$

Measurement accuracy again depends on the measurement time in the same way as before, but dependence on filter bandwidth is complex. On decreasing the bandwidth the formula (20) is converging to the same result as Eg. (17). Increasing the bandwidth in $1/f^{\gamma}$ variance measurement first leads to improvement of accuracy but after reaching some optimum point accuracy is again decreasing with further increase of bandwidth. The optimum ratio of frequencies for the best accuracy is

$$\left(\frac{f_2}{f_1}\right)_{opt.} = 4.92\,. \qquad (21)$$

Optimum frequency ratio is quite large. For example, it could be frequency range from 400 Hz up to 2000 Hz. Then we can get $\varepsilon^2 = 0.0077$ or 8.8% for measurement time T = 0.1 sec. At the same time if, as usually, we choose bandwidth of 100 Hz around 1 kHz, then calculation gives $\varepsilon^2 = 0.1$ or 32% for the same measurement time.

Optimum bandwidth measurement could be successfully applied in automated low frequency noise testers for semiconductor device production, but could not be used for experimental determination of noise PSD for research purposes. Then we must use higher spectral resolution and large measurement time.

3. Noise Parameter Extraction

Noise power spectral density at the output of semiconductor device contains contributions of all noise sources with different weight depending on circuit transfer function. Total PSD presented by Eq. (15) contains several coefficients. Still each one of these coefficients could be representing several noise sources. For example, G_E is representing total contribution of all thermal and shot noise sources in the device. Task is to extract parameters of one particular noise source from such complex measurement data. As 1/f and GR noises are present simultaneously then a task could be to evaluate their parameters separately.

From analysis of noise source location in the model of the device we can determine the most appropriate measurement circuit configuration. Then the most appropriate measurement conditions in terms of DC bias, temperature and frequency must be chosen to enhance contribution of wanted noise source in total PSD. For discrimination of 1/f and GR noise sources different behaviour of noise parameters versus frequency and temperature could be used.

Important stage in determination of noise parameters is processing of measured raw data. Data processing include:

- Filtering of measured noise power spectral density to avoid such interfering components as 50 Hz with harmonics and other.
- Subtraction of unwanted noise spectra components (for example, thermal and shot noise).
- Determination of specific parameters in noise model, for example, G_F, and γ for 1/f noise.

All these procedures introduce some error and can lead to false interpretation of results. Therefore it is reasonable to simulate noise measurement/extraction for different measurement circuits and different complexity of transistor model and evaluate possible errors [3].

4. Conclusion

Evaluation of measurement accuracy is important to obtain confident experimental evidence on values of noise parameters. Formulas are obtained for calculation of statistical accuracy of low frequency noise parameter measurement and practical recommendations given. Both temporal (autocorrelation function) and spectral (PSD) noise characteristics could be used for accuracy evaluation. Minimum sampling interval in discrete measurement is determined to provide statisticaly independent samples.

Extraction of noise parameters from measurement data is a complex task because other noise sources contribute to the output noise of the device being tested. The most appropriate configuration of measurement circuit and measurement conditions must be chosen to enhance contribution of wanted noise source in measured value. For discrimination of 1/f and GR noise sources different behavior of noise parameters versus frequency and temperature could be used.

References

[1] I. Slaidiņš, J. Šikula and P. Vašina, Noise Measurement: Technique and Accuracy, Elektrotechn. Časopis, 43 (1992) 299-303.

[2] M. Heiningen., E. Vandamme, L. Deferm and L. Vandamme, Modeling 1/f Noise and Extraction of the Spice Noise Parameters Using a New Extraction Procedure, http://www.imec.be/design/pdf/mixsig/essderc98_heijningen%5B1%5D.pdf

[3] M. Zeltins and I. Slaidins. Measurement Circuits and Data Processing for Transistor 1/f Noise Parameter Extraction, Sc. Proc. of RTU, Series 7, Telecommunications and Electronics, **2** (2002) 17–22. http://www.rsf.rtu.lv/Anglu%20lapa/proceedings/proc_.htm

[4] V. S. Pugachev. Theory of Random Functions and its Applications, Fizmatgiz, Moscow, (1962). (In Russian)

[5] G. A. Korn and T. M. Korn, Mathematical Handbook for Scientists and Engineers, McGraw-Hill (1968).

RADIOFREQUENCY AND MICROWAVE NOISE METROLOGY

E. Rubiola⋆ V. Giordano◇
⋆ *Université Henri Poincaré* - ESSTIN & LPMIA
2 r. Jean Lamour, F-54519 Nancy, France
◇ *Laboratoire de Physique et Metrologie des Oscillateurs*
32 av. de l'Observatoire, F-25044 Besançon, France
rubiola@esstin.uhp-nancy.fr
giordano@lpmo.edu

Abstract The radiofrequency interferometer, as compared to other methods for the measurement of amplitude noise and phase noise, shows higher sensitivity. In favorble onditions the background noise can be as low as -180 $\mathrm{dB[rad^2]/Hz}$ at $f = 1$ Hz off the carrier, up to microwaves (10 GHz) for real-time measurements. Exploiting correlation and averaging, a white noise floor of -204 $\mathrm{dB[rad^2]/Hz}$ has been observed, not limited by the thermal energy $k_B T_0$ referred to the carroer power P_0. This article reports on the method, on the recent developments, and on the measurement of low-noise hard-to-measure devices.

Keywords: Phase noise, amplitude noise, parametric noise, low-noise oscillators.

1. Basic Interferometric Measurements

The output signal of a two-port device under test (DUT) crossed by a sinusoidal signal can be represented as

$$x(t) = V_0[1 + \alpha(t)] \cos[\omega_0 t + \varphi(t)] \tag{1}$$

where $\varphi(t)$ and $\alpha(t)$ are the random phase and the random normalized amplitude fluctuation of the DUT, respectively. AM and PM noise is usually described in term of the cross spectrum densities $S_\varphi(f)$ and $S_\alpha(f)$. We find more useful the Cartesian representation

$$x(t) = V_0 \cos(\omega_0 t) + n_c(t) \cos(\omega_0 t) - n_s(t) \sin(\omega_0 t) \quad . \tag{2}$$

J. Sikula and M. Levinshtein (eds.),
Advanced Experimental Methods for Noise Research in Nanoscale Electronic Devices (279 - 286)

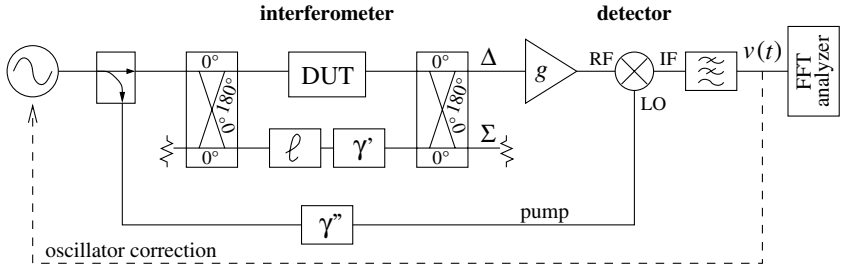

Figure 1. Interferometric measurement system.

In low-noise conditions, (2) is equivalent to (1) with

$$\alpha(t) = \frac{n_c(t)}{V_0} \qquad \text{and} \qquad \varphi(t) = \frac{n_s(t)}{V_0} \ . \tag{3}$$

Figure 1 shows the interferometric system used to measure $n_c(t)$ and $n_s(t)$, thus $\alpha(t)$ and $\varphi(t)$ and their spectra. The scheme derives from [1, 2]. Recent applications [3] have been reported, and [4] provides insight and design rules.

The instrument works as an impedance-matched null bridge followed by a synchronous detector. AM and PM noise reside entirely in the sidebands, hence advantages arise from removing the carrier signal and detecting the noise alone. Accordingly, ℓ and γ' are adjusted for the carrier to be suppressed ad the amplifier input (Δ output of the interferometer). The detector can be regarded as a part of lock-in amplifier [5] or of a phase-coherent receiver [6, 7]. By inspection on Fig. 1, we find the output voltage

$$v(t) = \sqrt{\frac{gR_0P_0}{2\ell_m}}\ \alpha(t) \qquad \text{or} \qquad v(t) = \sqrt{\frac{gR_0P_0}{2\ell_m}}\ \varphi(t), \tag{4}$$

depending on the phase γ''. g is the amplifier power gain, R_0 is the characteristic impedance of the whole ciruit, P_0 is the power at the DUT output, and ℓ_m is the single sideband (SSB) loss of the mixer. The background white noise is

$$S_{\varphi\,0} = S_{\alpha\,0} = \frac{2Fk_BT_0}{P_0} \ , \tag{5}$$

where F is the amplifier noise figure and k_BT_0 the thermal energy at room temperature. Eq. (5) derives from the equivalent noise Fk_BT_0 at the amplifier input, processed in the same way as the DUT noise.

The interferometer shows advantages versus the saturated mixer, which is the common approach, namely:

- **Low noise floor.** The noise floor is due to Fk_BT_0 at the amplifier input. The noise of a saturated mixer is higher because saturation takes place at the input, before converting.

- **Low flicker.** The amplifier can not flicker around the carrier frequency because there is no sufficient power to up-convert the near-dc noise by nonlinearity. The passive components of the interferometer are less noisy than the amplifier, while detection takes place after amplification.
- **Low sensitivity to ac magnetic fields.** Amplification takes place at the carrier frequency, where ac magnetic fields from the mains have little or no effect.
- **Wide power range.** The interferometer works at low P_0 (10^{-3} to 10^{-6} W, or less). In the same condition a saturated mixer would require amplification, which flickers. The interferometer performs well at high P_0 (1 W or more), where the noise floor (5) is not limited by saturation.

Finally, the real-time measure of $\varphi(t)$ makes possible to correct the noise of an oscillator, or to lock an oscillator to a frequency discriminator (dashed path of Fig. 1, inserting a discriminator as the DUT).

2. Vector Detection Interferometer

The vector detection interferometer [8] is shown in Fig. 2. The multistage carrier suppression provides low background flicker, while correlation and averaging reduces the noise floor.

The matrix $R = BG$ processes the signal at the I-Q output. G corrects the orthogonality error and the amplitude asymmetry of the I-Q detector. It is obtained with the Gram-Schmidt process. B rotates the detection frame of the I-Q. It can be set for $w_1(t) = k\alpha(t)$ and $w_1(t) = k\varphi(t)$, where k is the instrument gain, or for any desired combination of $\alpha(t)$ and $\varphi(t)$ at the output. The phase of the I-Q pump signal can be let arbitrary.

The I-Q modulator provides automatic suppression of the carrier through a dual integrator and the matrix D. The system works in Cartesian coordinates on the phasor plane. The diagonalization matrix D turns the system into two separate subsistems. It compensates for the arbitrary LO phase of the I-Q detector and of the I-Q modulator, and corrects the amplitude and orthogonality error of both.

2.1. Reduction of the Background Flicker

Common sense suggests that the flicker noise of the interferometer is due the mechanical instability of the variable elements ℓ and γ and of their contacts, rather than to the instability of the semirigid cables, connectors, couplers, etc. Of course, lower flicker is expected from by-step attenuators and phase shifters, and even lower flicker is expected if these components can be of a fixed value. Thus we use by-step or fixed-value components in the inner interferometer, and

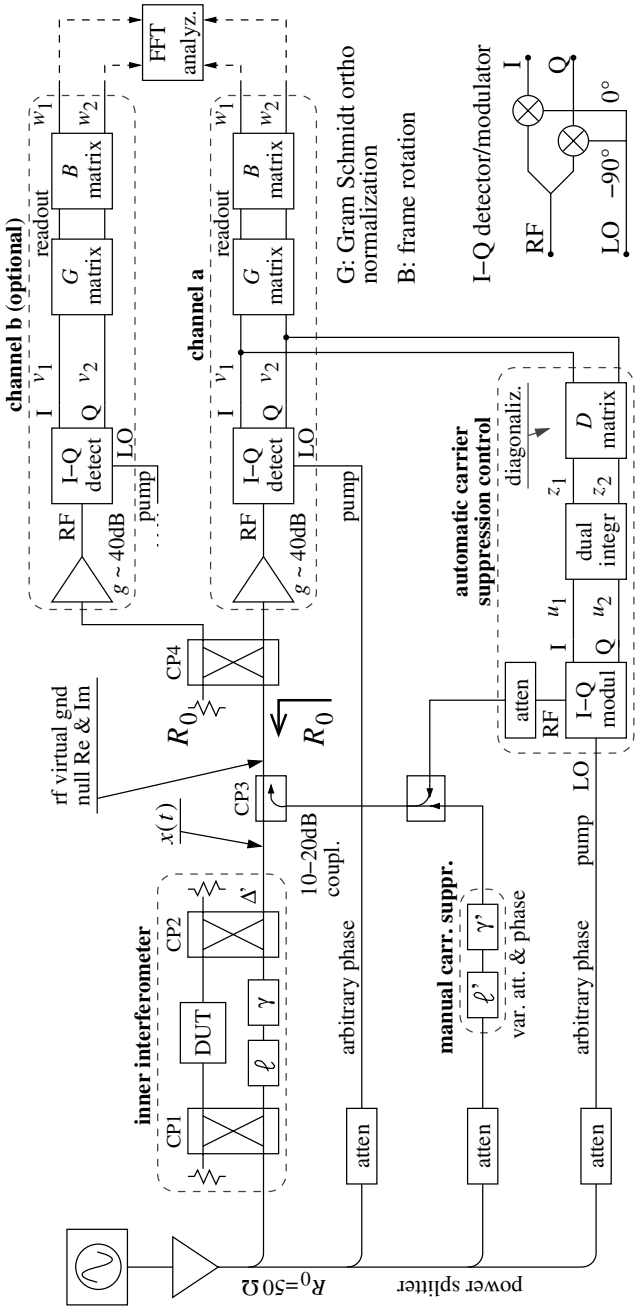

Figure 2. Interferometric measurement system.

we add an interpolating signal [9]. Due to the low weight of the latter, higher noise can be tolerated.

2.2. Correlation

In the traditional mode, the FFT anlyzer measures the cross spectrum $S_\varphi(f)$, or $S_\alpha(f)$, correlating the output of the two radiofrequency channels. The matrices B are set for the two channel frames to be parallel, thus $w_1(t) = k' n_c(t)$ and $w_2(t) = k' n_s(t)$, with k' a constant. Let $n_1(t)$ and $n_2(t)$ the input signals of the coupler CP4, and $a = (n_2 + n_1)/\sqrt{2}$ and $b = (n_2 - n_1)/\sqrt{2}$ the output signals. CP4 sees an impedance equal to R_0 at both inputs. In the presence of thermal noise only, the cross spectrum is $S_{ab}(f) = \frac{1}{2}\,[S_{n_2}(f) - S_{n_2}(f)]$, which means $S_{ab}(f) = 0$ if temperature is uniform. Consequently, the instrument rejects the thermal noise. The DUT noise present in the two channels is fully correlated, hence it is measured. The correlation enhancement of sensitivity is of common use in radioastronomy [10], radiometry [11], and thermometry [12]. It was introduced in phase noise metrology long time ago [13, 14], but the rejection of thermal noise was understood only recently [15].

In the $\pm 45^\circ$ mode, FFT anlyzer measures the cross spectrum of the two ouputs of a single radiofrquency channel; the other channel is not used. The matrix B is set for the instrument to detect at $+45^\circ$ and -45° off the carrier phase. With random noise, $n_c(t)$ and $n_s(t)$ of Eq. (2) are uncorrelated, thus the cross spectrum is zero. Based on this property, the instrument rejects thermal noise and the noise of the amplifier, despite a single amplifier is shared. The assumption of temperature uniformity is not needed. The measured cross spectrum is proportional to $S_\alpha(f) - S_\varphi(f)$. Fortunately, parametric noise phenomena tend to privilege PM noise or AM noise, which can be measured. Of course, the a-priori knowledge of the DUT physics is needed. This method was invented to measure the resistance fluctuations of metal films at low frequencies [16], and then introduced in phase noise metrology [17].

3. Experimental Results

Figure 3 summarizes the sensitivity obtained with the different processing methods, compared the saturated mixer. The white noise floor is limited by the averaging capability ($m = 2^{15}$) of the available FFT analyzer; it is expectd to be lower as m increases. The interferometric instruments have been used to measure the $1/f$ noise of low-noise devices, as shown below.

Variable attenuators and delay lines (100 MHz and 9 GHz). A few devices have been tested at $P_0 \approx 10$ dBm. Phase noise was of -145 to -165

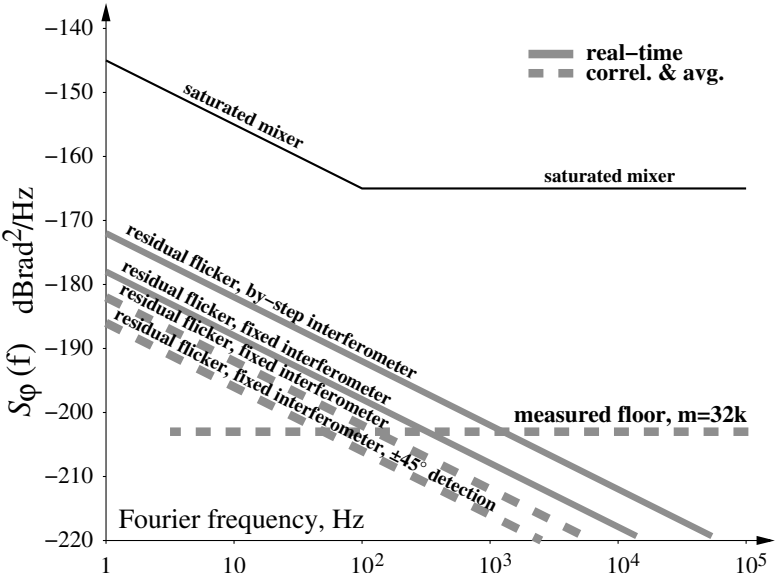

Figure 3. Sensitivity of the interferometric measurement instruments.

dBrad^2/Hz at $f = 1$ Hz. Using a microwave delay line at 100 MHz instead of a VHF device hoping for lower noise proved to be useless.

Precision by-step attenuators (100 MHz). Four devices have been tested, at $P_0 = 14$ dBm. In all cases the flicker noise is close to -170 dB[rad]^2/Hz, with little or no difference between amplitude and phase noise.

Amplifier in low-power conditions (100 MHz). Some amplifiers have been tested $P_0 = 0$ dBm; the devices are specified for a compression point $P_{1\,\mathrm{dB}} \geq 14$ dBm. Flicker phase noise is of some -140 dBrad^2/Hz at $f = 1$ Hz. Interestingly, if the amplifier is used at higher power there is little or no difference in $1/f$ noise.

Hybrid junctions (5–100 MHz). Four devices have been tested, at $P_0 \approx 15$ dBm. Flicker noise is close to -170 dBrad^2/Hz at $f = 1$ Hz, with a difference between amplitude and phase noise within 3 dB. The $1/f$ noise originates in the magnetic core of the internal transformers. For the highest sensitivity we built our own hybrid junctions, based on $\lambda/4$ coaxial lines. The $1/f$ noise of these custom devices is lower than the background noise, which is of -180 dBrad^2/Hz.

Microwave Circulators (9 GHz). Six devices have been tested in isolation mode, at $P_0 = 19$ dBm. The 1 Hz flicker is between -160 and -172 dB[rad]^2/Hz, with a maximum difference of 5.5 dB between AM and PM [18]. Noise is clearly of magnetic origin, through some mechanism still not understood.

Quartz Resonators (10 MHz). Six high-stability resonators have been measured at a dissipated power P_d from -25 to -7 dBm [19]. The $1/f$ phase noise, turned into a fluctuation of the resonant frequency, has been further converted into the two-sample (Allan) deviation $\sigma_y(\tau)$ of the fractional frequency y. Flicker of phase turns into a floor of σ_y. The observed σ_y is between 7.5×10^{-14} and 3.5×10^{-13}, depending on the resonator and on P_d. The instrument noise is of 6×10^{-14} to 1×10^{-14}, depending on P_d and on the resonator merit factor Q.

Noise Corrected Oscillator. The interferometer has been used to improve the stability of a mirowave oscillator through the reduction of the $1/f$ noise of the amplifier in closed loop. A stability improvement of 40 dB has been achieved, still limted by the control loop. Two room-temperature prototypes have been implemented, and the extension to cryogenic oscillators is in progress.

References

[1] K. H. Sann, *The measurement of near-carrier noise in microwave amplifiers*, IEEE Trans. Microw. Theory Tech. **9** (1968), 761–766.

[2] F. Labaar, *New discriminator boosts phase noise testing*, Microwaves **21** (1982), no. 3, 65–69.

[3] E. N. Ivanov, M. E. Tobar, and R. A. Woode, *Microwave interferometry: Application to precision measurements and noise reduction techniques*, IEEE Trans. Ultras. Ferroel. and Freq. Contr. **45** (1998), no. 6, 1526–1535.

[4] E. Rubiola, V. Giordano, and J. Groslambert, *Very high frequency and microwave interferometric PM and AM noise measurements*, Rev. Sci. Instr. **70** (1999), no. 1, 220–225.

[5] M. L. Meade, *Lock-in amplifiers: Principle and applications*, IEE, London, 1983.

[6] W. C. Lindsey and M. K. Simon, *Telecommunication systems engineering*, Prentice-Hall, Englewood Cliffs, NJ, 1973, (Reprinted by Dover Publications, 1991).

[7] A. J. Viterbi, *Principles of coherent communication*, McGraw Hill, New York, 1966.

[8] E. Rubiola and V. Giordano, *Advanced interferometric phase and amplitude noise measurements*, Rev. Sci. Instr. **73** (2002), no. 6, 2445–2457.

[9] ———, *A low-flicker scheme for the real-time measurement of phase noise*, IEEE Trans. Ultras. Ferroel. and Freq. Contr. **49** (2002), no. 4, 501–507.

[10] R. Hanbury Brown, R. C. Jennison, and M. K. Das Gupta, *Apparent angular sizes of discrete radio sources*, Nature **170** (1952), no. 4338, 1061–1063.

[11] C. M. Allred, *A precision noise spectral density comparator*, J. Res. NBS **66C** (1962), 323–330.

[12] D. R. White, R. Galleano, A. Actis, H. Brixy, M. De Groot, J. Dubbeldam, A. L. Reesink, F. Edler, H. Sakurai, R. L. Shepard, and G. J. C., *The status of Johnson noise thermometry*, Metrologia **33** (1996), 325–335.

[13] R. F. C. Vessot, R. F. Mueller, and J. Vanier, *A cross-correlation technique for measuring the short-term properties of stable oscillators*, Proc. IEEE-NASA Symposium on Short Term Frequency Stability (Greenbelt, MD, USA), November 23-24 1964, pp. 111–118.

[14] F. L. Walls, S. R. Stain, J. E. Gray, and D. J. Glaze, *Design considerations in state-of-the-art signal processing and phase noise measurement systems*, Proc. Freq. Contr. Symp. (Atlantic City, NJ, USA), EIA, Washington, DC, 1965, June 2-4 1976, pp. 269–274.

[15] E. Rubiola and V. Giordano, *Correlation-based phase noise measurements*, Rev. Sci. Instr. **71** (2000), no. 8, 3085–3091.

[16] A. H. Verbruggen, H. Stoll, K. Heeck, and R. H. Koch, *A novel technique for measuring resistance fluctuations independently of background noise*, Applied Physics A **48** (1989), 233–236.

[17] E. Rubiola, V. Giordano, and H. Stoll, *The* $\pm 45^\circ$ *interferometer as a means to measure phase noise of parametric origin*, IEEE Trans. Instrum. Meas. **52** (2003), no. 1, 182–188.

[18] E. Rubiola, Y. Gruson, and V. Giordano, *The measurement of the flicker noise of circulators*, Proc. 17th European Frequency and Time Forum / 2003 Frequency Control Symposium (Tampa, FL, USA), May 5–8, 2003, In print.

[19] E. Rubiola, J. Groslambert, M. Brunet, and V. Giordano, *Flicker noise measurement of HF quartz resonators*, IEEE Trans. Ultras. Ferroel. and Freq. Contr. **47** (2000), no. 2, 361–368.

TREATMENT OF NOISE DATA IN LAPLACE PLANE

B. M.Grafov
A.N.Frumkin, Institute of Electrochemistry of Russian Academy of Sciences
31 Leninskii prospekt, Bld. 5, Moscow 119071
Russia
vek@elchem.ac.ru

Abstract It is shown that there is a wavelet technique that allows one to estimate the power spectral density of random noise in Laplace plane.

Keywords: Noise spectral density, Laplace plane.

1. Introduction

Spectral analysis is a powerful and elegant tool for investigation of noise processes and random time series [1-3]. Windowed Fourier transforms unite wavelet and Fourier analysis. However, physical interpretation of the wavelet spectral density is still open to question [4]. We found [5-7] that the Laguerre wavelet spectral density of the noise process possesses quite a clear physical interpretation. The above quantity coincides with the Laplace transform of covariance function and can be called the operational power spectral density. In the case of random discrete time series the Meixner wavelet transforms [8] play role of the Laguerre wavelet transforms.

The aim of this report is to give a short review of the basic results in the field of the operational analysis of random noise processes.

2. Notations

We use the notations as follows: $y(t)$ is zero mean stationary random process, t is time, $y(t) = e(t)$ for voltage noise, $y(t) = i(t)$ for current noise, $< y(0)y(t) >$ is covariance function, $< y_{\omega}^2 >$ is power spectral

J. Sikula and M. Levinshtein (eds.),
Advanced Experimental Methods for Noise Research in Nanoscale Electronic Devices (287 - 292)

density, ω is frequency of the Fourier analysis, $h^E(t)$ is voltage linear response function, $h^I(t)$ is current linear response function, Z_ω is small-signal impedance, G_ω is small-signal admittance, Z_p is small-signal operational impedance, G_p is small-signal operational admittance, p is the Laplace frequency, the angular brackets <...> denote averaging over ensemble of realizations, k_B is the Boltzmann constant, T is temperature.

3. Operational Power Spectral Density

It is well known that there exist the following relationships between the linear response functions $h^E(t)$ and $h^I(t)$ and linear impedance Z_ω and linear admittance G_ω:

$$Z_\omega = \int_0^\infty dt \exp(-j\omega t) h^E(t), G_\omega = \int_0^\infty dt \exp(-j\omega t) h^I(t) \tag{1}$$

where j is imaginary unit. The definition of operational impedance and operational admittance is given in following equations:

$$Z_p = \int_0^\infty dt \exp(-pt) h^E(t), \; G_p = \int_0^\infty dt \exp(-pt) h^I(t) \tag{2}$$

Eqs. (2) show clearly the way for definition of the operational power spectral density of random process:

$$< y_p^2 > /4 = \int_0^\infty dt \exp(-pt) < y(0) y(t) > \tag{3}$$

where the Laplace frequency p is a positive value. If the Laplace frequency has an imaginary part ($p = \sigma + j\omega$; $\sigma > 0$) the definition of the operational power spectral density is slightly changed:

$$< y_p^2 > /4 = \mathrm{Re} \int_0^\infty dt \exp(-pt) < y(0) y(t) > \tag{4}$$

In the case of equilibrium systems one can use the Nyquist fluctuation-dissipation theorem in the following form:

$$< e(0) e(t) > = k_B T h^E(t); \; < i(0) i(t) > = k_B T h^I(t) \tag{5}$$

On this basis it is possible to write for equilibrium operational power spectral density:

$$< e_p^2 > = 4k_B T r_p \,, < i_p^2 > = 4k_B T g_p \tag{6}$$

where $r_p = \mathrm{Re}\, Z_p$ and $g_p = \mathrm{Re}\, G_p$ .Therefore for the equilibrium RCL-circuit one can predict the following equation for the voltage operational power spectral density:

$$< e_p^2 > /(4k_B T) = R + \sigma C^{-1} / (\sigma^2 + \omega^2) + \sigma L \tag{7}$$

It is seen that capacitance as well inductance makes a source of the operational noise.

Let us consider the linear (in kinetic relation) system showing the voltage flicker noise behavior [1,2]:

$$< e_\omega^2 > = A / f \tag{8}$$

where $f = \omega / 2\pi$ and A is a constant with respect to frequency f . Use of the electrochemical $1/f$ noise model [9] allows one to predict the following operational power spectral density expression:

$$< e_p^2 > /4 = A\, \mathrm{Re} \frac{\ln(p / \omega_0)}{p} \tag{9}$$

where ω_0 is the frequency that characterizes the diffusion-like inner relaxation process.

4. Wavelet Transforms Providing the Operational Power Spectral Density

4.1. The Laplace transform

It is possible to show that one can calculate the operational power spectral density by using following equation (with $p > 0$):

$$< y_p^2 > /4 = p < Y_p^2 > \tag{10}$$

where Y_p stands for the Laplace transform of the stationary random process:

$$Y_p = \int_0^\infty dt \exp(-pt) y(t) \tag{11}$$

For complex Laplace frequency ($p = \sigma + j\omega$) one can use Eq. (12) instead of Eq. (10):

$$< y_p^2 > /4 = \sigma < Y_p Y_p^* > \tag{12}$$

where the asterisk denotes a complex conjugate quantity.

4.2. The Laguerre transforms

It is an interesting fact that there exists an ensemble of the wavelet transforms each of which delivers the operational power spectral density in line with following equation:

$$< y_p^2 > /4 = \sigma < Y_p^{(n)} Y_p^{(n)*} > \tag{13}$$

where $Y_p^{(n)}$ is the Laguerre transform of the random process $y(t)$:

$$Y_p^{(n)} = \int_0^\infty dt \exp(-pt) \mathrm{L}_n(2\sigma t) y(t) \tag{14}$$

In Eq. (14) symbol $\mathrm{L}_n(x)$ stands for the Laguerre polynomial in x of the n-th order. It is suitable to remind that

$$\mathrm{L}_0(x) = 1;\ \mathrm{L}_1(x) = 1 - x;\ \mathrm{L}_2(x) = 1 - 2x + x^2/2 \tag{15}$$

It is seen from Eq. (13) that it is possible to organize the multi-channel estimator of the operational power spectral density. Input of each channel is random process $y(t)$. Output of each channel is operational power spectral density $< y_p^2 >$.

It should be noted that multi-channel estimator of the operational power spectral density was successfully applied to the analysis of micro-seismic low-frequency noise [10].

5. Conclusions

1. Operational power spectral density (i.e. the Laplace transform of the covariance function) may be introduced for the treatment of stationary noise.
2. Due to fast decay of the exponential function the finite time interval of realization can be considered infinite.

3. The estimation of the operational power spectral density can be performed by direct way without prior estimation of the covariance function as a function of time.
4. It is possible to create a multi-channel estimator of the operational power spectral density.
5. In the case of continuous time each Laguerre wavelet transform can be used for constructing the operational power spectral density estimator.
6. In the case of discrete random time series each Meixner wavelet transform can be used for the construction of the discrete operational power spectral density estimator.
7. Analysis of an $1/f$ noise system in Laplace plane allows one to estimate the inner frequency of the diffusion-like random process.
8. Capacitance as well inductance is the source of the operational noise.
9. The operational power spectral density technique was successfully applied inside the micro-seismic low-frequency noise method for searching oil and gas deposits.
10. It is of importance to be aware of the opportunity to use the high order operational spectrum technique.

Acknowledgments

This work was supported by Russian Foundation for Basic Research (project No.02-03-32114).

References

[1] Sh.Kogan, Electronic Noise and Fluctuations in Solids, Cambridge University Press, London, 1996

[2] M.B.Weissman, $1/f$ noise and other slow, non-exponential kinetics in condensed matter, Reviews Modern Physics **60** (1988) 537-671.

[3] M.B.Priestley, Spectral Analysis and Time Series, Academic Press, London, 1996.

[4] M.B.Priestley,Wavelets and time-dependent spectral analysis, J. Time Series Analysis **17** (1996) 85-103.

[5] B.M.Grafov, The Laplace transformation for description of noise signals from electrochemical sensors, Russian J. Electrochemistry **29** (1993) 1290-1291.

[6] B.M.Grafov, I.B.Grafova, Theory of the wavelet analysis for electrochemical noise by use of Laguerre functions, Electrochemistry Communications **2** (2000) 386-389.

[7] B.M.Grafov, I.B.Grafova, Discrete Laplace transformation as a wavelet tool to analyse the electrochemical random time series, J. Electroanalytical Chemistry **502** (2001) 47-50.

[8] I.B.Grafova, B.M.Grafov, Meixner wavelet transform: a tool for studying stationary discrete-time stochastic processes, Russian J. Electrochemistry **39** (2003) 130-133.

[9] B.M.Grafov, Flicker noise in the Laplace space, Russian J. Electrochemistry **34** (1998) 1149-1153.

[10] Yu.V.Sirotinskii, S.L.Arutyunov, B.M.Grafov, A.E.Suntsov, Comparative calibration of electrochemical geophones in the acoustic low-frequency oil and gas prospecting, Russian J. Electrochemistry **35** (1999) 596-598.

MEASUREMENT OF NOISE PARAMETER SET IN THE LOW FREQUENCY RANGE: REQUIREMENTS AND INSTRUMENTATION

L. Hasse

Gdańsk University of Technology, Department of Measuring Instrumentation Narutowicza str. 11/12, 80-952 Gdańsk

Poland

lhasse@pg.gda.pl

Abstract Two basic metrological noise models of a two-port: with noise sources at the input and with noise short-circuit currents, have been described. Noise parameters describing the models including a correlation between currents and/or voltages are measured using indirect and direct methods. Some noise reduction techniques are reported. Two-channel noise measurement system with computer-controlled biasing of a measured device using the LabVIEW software and noise signal processing procedures has been presented.

Keywords: noise parameter set, noise measurement, instrumentation

1. Introduction

Low frequency noise measurement and modelling is a useful tool for the evaluation of the production process, localization and analysis of phenomena mechanisms and the characterization of the device quality and reliability. The investigation of the most frequent failure mechanisms by noise measurements seems to be especially advantageous for the ultra large scale integrated circuits and nanoscopic devices – noise level scales inversely with the size of the elements containing noise sources. Besides, in scaled devices fluctuations are often comparable to the dc currents or voltages.

Noise characterization of a Two-port Under Test (TUT), eg. a bipolar or field effect transistor, can be accomplished by the measurement of four noise parameter set fully describing its noise properties. The relationship between measured input and/or output noise parameters is expressed by the correlation factor or the coherence function. To accurate measure the noise parameters having often very low values the appropriate system is necessary.

J.Sikula and M.Levinshtein (eds.),
Advanced Experimental Methods for Noise Research in Nanoscale Electronic Devices (293 - 302)

2. Metrological Noise Models of a Two-port

The equivalent noise sources may be located at different sites on a noise-free two-port. Two uncontrolled noise generators (not independent generally) are required to characterize a two-port noise and their relationship may be expressed by the complex correlation factor $c(f)$ between them (by two data). Therefore there is four parameter set characterizing noise properties of a linear two-port.

Two basic noise representations are commonly used: in terms of spectral densities of equivalent input voltage $S_E(f)$ and current $S_I(f)$ noise sources (Fig. 1a) or in terms of spectral densities of input $S_{I_i}(f)$ and output $S_{I_o}(f)$ short-circuit current noise sources (Fig. 1b).

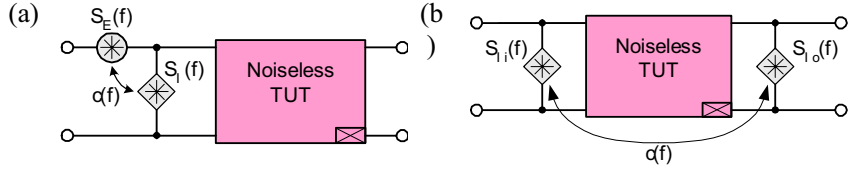

$$c(f) = \frac{S_{EI^*}(f)}{\sqrt{S_E(f) S_I(f)}} \qquad c(f) = \frac{S_{I_i I_o^*}(f)}{\sqrt{S_{I_i}(f) S_{I_o}(f)}}$$

Figure 1. Equivalent circuits of a Two-port Under Test (TUT) with two noise sources at input port (a) and with noise current sources at each port (b)

2.1. Measurement of input equivalent noise sources

A measurement of noise parameters from Fig. 1a requires an usage of multi-impedance measurement technique - the noise measurement at the output of TUT at several input terminal loads and then the data processing to estimate the noise parameters. It is a more general method and is commonly used in the high frequency range, however very sophisticated statistical procedures should be used to estimate four noise parameter set with an appropriate accuracy [1].

2.2. Measurement of input and output noise current sources

Using the direct technique one can measure the short-circuit input and output current noise spectra and their correlation (Fig. 1b) directly at the TUT input and output. An input port load does not change during noise waveforms acquisition, therefore the measurement process is much faster and can be easily remote controlled during the data acquisition.

Instead of the correlation factor it is often sufficient to calculate the magnitude-squared coherence $\gamma^2(f) = \frac{\left|S_{I_i I_o^*}(f)\right|^2}{S_{I_i}(f) \cdot S_{I_o}(f)}$. The correlated spectrum in the nominator is calculated through a multiplication in the frequency domain between the complex Fourier transforms of two measured independently noise signals. The coherence $\gamma^2(f)$ supply in a very efficient and accurate way a good estimation of the output noise signal energy entity exclusively due to the input noise.

The measurement technique can be based on the measurement of noise voltages across series resistors R_S and R_L (for a bipolar transistor in the emitter or base along with the collector terminal) in the input and output circuits of a TUT, respectively (Fig. 2). However, the current noise $S_{I_i}(f)$ and $S_{I_o}(f)$ can be also measured directly for a wide range of source resistance R_S using transimpedance amplifiers T_i and T_o as the impedance of the measured TUT is larger than input impedance of the current amplifiers T_i and T_o. This enables measurements of both current noise simultaneously and also direct calculation of the coherence between noise currents. The influence of inherent noise of a measurement system is much more critical for the direct method.

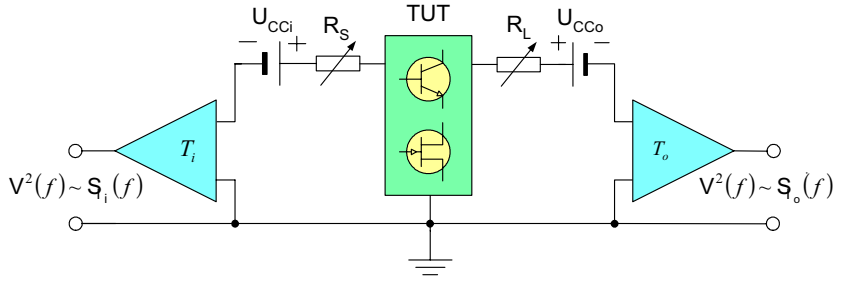

Figure 2. Simplified setup for short-circuit input (base, gate) and output (collector, drain) noise currents measurement

3. Two-Channel Noise Measurement System

The sensitivity of noise measurement system depends on the inherent noise of the measurement system, mainly on its first stages (preamplifiers). Depending on TUT and on direct or indirect measurement method used,

different types of low-noise voltage and transimpedance preamplifiers can be included in the front-end part of the system [2].

3.1. Low-noise preamplifiers

For ultra-low noise voltage preamplifiers parallel connection of several low-noise devices decreasing the noise optimal resistance R_{S0} is preferable. For low values of R_S the dominant influence on noise level have an equivalent input noise voltage of used devices and for N devices it enables to increase signal-to-noise ratio $\sqrt{N}$ times. For example, three pairs of low-noise transistors MAT-03 PMI lowers the equivalent input noise voltage $S_E(f)$ of the preamplifier to $\cong 0.32\ nV/\sqrt{Hz}$ at $1\ kHz$ at rather high collector currents ($I_C = 2\ mA$) reducing shot noise components. A little better result confirmed by the simulation analysis in NOISE program has been achieved for eight LT1028AM/AC Linear Technology op-amps.

In transimpedance amplifiers the main noise contribution usually comes from the high value feedback resistor. For low noise transimpedance amplifiers the op-amps with very low equivalent input current noise should be selected. However, a high value of the feedback resistor can easier saturate the output for dc coupling the TUT and limit the bandwidth (parallel to parasitic capacitance). Using differential connection of the TUT with the inputs of two identical transimpedance amplifiers (so called *dual sensing structure*) an equivalent reduction of a factor 2 can be obtained in the level of background noise of a system [3].

For example, FETs noise measurements in the gate channel require an ultra low-noise I/V converter with the appropriate conversion factor (the gate current noise level for MESFETs equals often only a few nA). For the OP 128 as the transimpedance amplifier the equivalent input noise current is equal $I_{ni} \approx 41\ fA/\sqrt{Hz}$ for the feedback resistor of the converter having the resistance 10 $M\Omega$. The results of the noise analysis were confirmed also using the PSICE simulator and were verified experimentally.

Other type of transimpedance amplifiers facilitates internal voltage bias of TUT with a high resolution and can be easily controlled by a computer. However these internal noise sources induce much higher noise level into the measurement setup. External voltage sources (in biasing circuits) with variable alternate current impedances realized on batteries enables a higher amplification factor of transimpedance amplifiers (they do not need to sink the direct current).

3.2. Block diagram of the two-channel system

General block diagram of the whole measurement system with two data acquisition channels controlled by LabVIEW software is shown in Fig. 3.

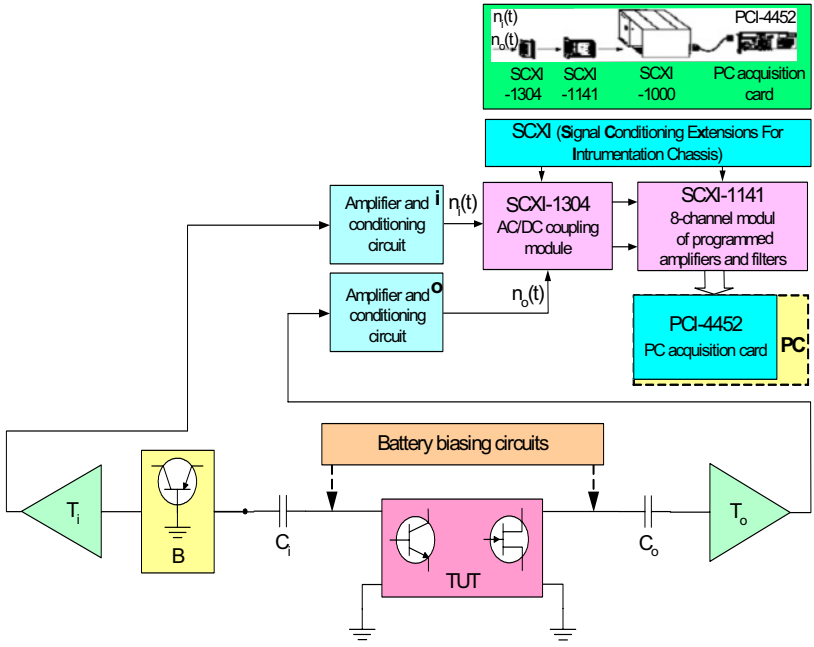

Figure 3. General block diagram of two-channel measurement system

The antialiasing filters (software-controlled input channels with the software-selectable cut-off frequency $f_a = 100/m \ \ kHz$, where m is an integer - $m \geq 4$) give an output signal range ±5 V. The low noise Dynamic Signal Acquisition Board PCI-4452) simultaneously digitises input signals (within the range from ±10 mV to ±42.4 V) by means of a 16-bit resolution, 64-times oversampling, delta-sigma ADC over a bandwidth 95 kHz. The data can be next processed on-line or stored on a disk as time series with a required number of samples according to the accuracy of noise parameters and characteristics estimation. In the calibration phase the inherent noise and the main electrical parameters of the particular sub-assemblies of the system can be measured and subtracted from the results of the noise measurements. External interferences should be reduced or completely removed by proper shielding and grounding.

3.3. Measurement of coherence

The measurement of the coherence between the input and output noise currents of a TUT operating as an amplifier is a critical task - all noise sources associated with the input amplifier T_i can give a significant contribution to the output noise current and hence to the coherence [4]. To improve accuracy for low values of source resistance R_S (when the measured coherence between $S_{i_1}(f)$ and $S_{i_2}(f)$ is systematically too low) the low noise voltage preamplifier with passive input can be used in the additional step of the measurement (with sufficiently high value of R_S) mainly to accurately calculate the coherence [5]. It is especially recommended for the bipolar transistors.

Two-channel noise measurements enables to localize noise sources in measured devices and to verify mechanisms of noise generation [Jon]. Very often a common noise source causes both 1/f noise in the base current and in the emitter series resistance but as experiments showed these two noise sources are not fully correlated.

In Fig. 4 the coherence measured of GaAs MESFET [6] is shown. The maximum of coherence function γ^2 occurs at the frequency $f \approx 700$ Hz and is associated with the presence of a generation-recombination trap (g-r noise component appearing in the spectrum $S_{i_1}(f)$). The traps were identified by the presence of Lorentzians in the measured noise spectra and also by the higher value of the coherence function at some frequency ranges.

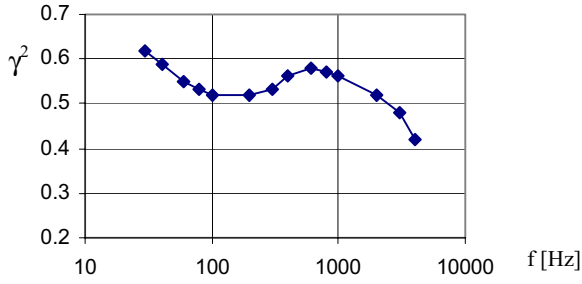

Figure 4. Coherence function of measured GaAs MESFET

The obtained results suggest that for the measured transistor the most influential noise source at the output is related to the surface leakage between gate and source [7]. This fact can be associated with the existence of g-r centre and very noisy processes in this region. Thus a coherence

measurement can be used as an additional diagnostic tool for MESFET and MODFET reliability studies.

3.4. System noise reduction techniques

To measure properly all noise parameters directly with transimpedance amplifiers the input voltage noise source of the T_i should be separated from the input of TUT without degradation of the T_i noise properties and not introducing an attenuation into the ultra low level stage of the measurement system. These requirements can be fulfilled by insertion a low noise buffer amplifier B (Fig. 3) with a very small reverse gain between the T_i and the input port of TUT. It can be the buffer with a common base bipolar junction transistor with properly selected bias conditions (a compromise between the lowest output noise of the buffer amplifier B and the as low small-signal input impedance as possible). Its noise properties have no major effects on the system noise background but it effectively isolates the T_i input voltage noise source from the TUT input.

To evaluate and subtract the background noise of the system some correlation method can be used enabling the estimation of the TUT noise power spectral density much lower than the inherent noise of the measurement system.

3.5. Computer-controlled biasing system

A low noise programmable computer-controlled biasing system make it possible automated noise measurements. The fraction of the system for automatic polarisation of the measured devices consists of (Fig. 5): CPU (μP), ADC, DAC1 up to 10.24V and DAC2 up to 5.12 V enclosed in the very carefully shielded and grounded mechanical modules [8].

All major system functions are programmable and executed by means of the local controller. Coupling to μP effects of stray capacitance were minimised by keeping digital lines far from analog components. Two separate modules for the gate (base) bias DAC1 and for the drain (collector) bias DAC2 on PCM1702P Burr-Brown (20 bits, ultra low distortion plus noise: -96 dB with a full-scale output) were implemented. Suitable filtering of the inherent system noise at the output (giving only -140 dB of background noise) for biasing separately the base (gate) and the collector (drain) of the measured transistor was provided. The resolution of biasing current setting of 10 points per decade in the range $10^{-9} \div 10^{-5}$ A for base or gate current and $10^{-7} \div 10^{-2}$ A for collector or drain current brings a complete flexibility and automation for the required polarisation. To minimise

interference separate batteries for all main modules and optoisolation between analogue and digital part of the system have been provided

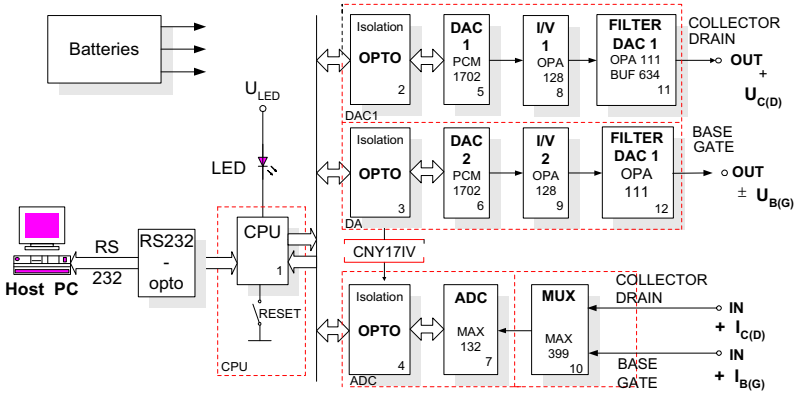

Figure 5. Automatic setting of TUT polarisation controlled under the LabVIEW

.

4. Noise Parameter Estimation Procedures

A special attention should be paid for the appropriate averaging procedures during coherence estimation to achieve a low value of the random component of mean square error. The precision and resolution of the spectral estimate depends on the choice of the number of data samples and the window size, respectively.

A LabVIEW virtual instrument provides the computation and display of coherence function in conjunction with the output noise power spectrum to allow an efficient comparison between the coherence function variations and the related base (gate) and collector (drain) noise spectra components. The estimator of coherence uses the cross spectrum function with an adequate level of linear averaging. If k is the number of records used (often $k = 124 \div 516$), a signal to noise ratio improvement equals $10 \cdot \lg(k)\,[dB]$.

Values of $\gamma^2(f)$ are less than 1 if both noise signal are uncorrelated, exists additional noise source in the input noise signal (e.g. not negligible inherent noise of T_i), TUT should be treated as non-linear [9] or error leakage is not reduced with windowing during data processing (resolution bias errors are present in the spectral estimates). The variance of the coherence function can be used as a measure of the accuracy of the spectral analysis. For different amounts of window overlap (referring to segmented spectral analysis) the variance of the coherence function is reduced as more averages are taken. A suitable value for overlap can be around 60%.

5. Conclusions

The measurement system with transimpedance amplifiers can be used to measure directly noise parameters of two-ports (transistors) including the coherence function. To improve the accuracy of coherence measurement an additional voltage preamplifier can be used at the input terminal of the measured transistor. Another way to achieve a reduction of inherent noise influence is to separate the input transimpedance amplifier from the measured TUT by means of the buffer amplifier reducing the T_i noise influence on the output of measured transistor.

From the coherence measurement for different source resistance a dominant noise source in a transistor can be established.

References

[1] J. Cichosz, L. Hasse, L. Spiralski, D. Godyń., A genetic algorithm application for the estimation of four noise parameter set of a linear twoport, Kleinheubacher Berichte **40** (1996) 566-568.

[2] L. Hasse, L. Spiralski, J. Sikula, Noise magnitudes for twoports and the accuracy of their measurement and estimation, XI Inter. Conf. Brno, Czech Republic, 1999, Sec. C2, 99-102.

[3] R. M. Howard, Dual sensing receiver structure for halving the amplifier contribution to the input equivalent noise of an opto-electronic receiver, IEE Proc.-Optoelectron. **146** (1999) 189-200

[4] L. Hasse, Measurement of coherence function between noise currents of transistors, 12th IMEKO TC4 Inter. Symposium: Electrical Measur. and Instrum., Zagreb, Croatia, 2002, 29-32.

[5] S. Bruce, L. K. J. Vandamme, A. Rydberg, Improved correlation measurements using voltage and transimpedance amplifiers in low-frequency noise characterization of bipolar transistors, IEEE Trans. Electron Devices **47** (2000) 1772-1773.

[6] A. Konczakowska, J. Cichosz, L. Hasse *et al*., The 1/f noise in GaAs MESFET transistors, Proc. 14th ICNF, Loeuven, Belgium, 1997, 59-62.

[7] B. K. Jones, C. Graham, A. Konczakowska, L. Hasse, The coherence of the gate and drain noise in stressed AlGaAs-InAlGaAs PHEMTs, Microelectronics and Reliability **41** (2001) 87-97.

[8] A. Konczakowska, L. Hasse, L. Spiralski, Ultra-low noise two -channel noise measurement system, XVI IMEKO World Congress, Vienna, Austria, 2000, vol. 4, 161-165.

[9] L. Hasse, Frequency domain analysis of nonlinear twoport using two -channel noise measurements. Kleinheubacher Berichte **43** (2000) 67-73.

TECHNIQUES OF INTERFERENCE REDUCTION IN PROBE SYSTEM FOR WAFER LEVEL NOISE MEASUREMENTS OF SUBMICRON SEMICONDUCTOR DEVICES

L. Spiralski, A. Szewczyk and L. Hasse

Gdańsk University of Technology, Department of Measuring Instrumentation Narutowicza str. 11/12, 80-952 Gdańsk

Poland

lhasse@pg.gda.pl

Abstract A probe system for wafer level noise measurements of submicron structures has been briefly presented. Significant influences on probe measurement have interference and inherent noise of the system, especially high level interference introduced by probes (contact resistance probe to wafer area fluctuations caused by vibrations and mechanical shocks in the measurement environment) and electromagnetic (EM) surroundings. Periodical interference caused by vibrations and EM fields can be separated from measured noise. The waveforms are recorded as a sequence of time series with duration being the multiple of the interference period and coherently summed up and finally subtracted from the registered data. It enables to analyse random and periodical components of the signal separately.

Keywords: wafer level noise, system for noise measurement, interference reduction

1. Introduction

The measurements on semiconductor device structures are often curried out in order to evaluate the quality of material composition and technology processes. Nowadays the point-probe measurements are also used to determine the device noise level.

Usually the inherent noise level of polarised submicron microelectronic devices is comparable with the thermal noise level and sometimes even lower than the noise level of the measurement system. For this reason the measurement system requires the special protection against disturbances originating in the system environment.

J.Sikula and M.Levinshtein (eds.),
Advanced Experimental Methods for Noise Research in Nanoscale Electronic Devices (303 - 309)

2. Point-probe noise measurement system

The schematic diagram of the measurement set-up containing a transimpedance amplifier for current noise i_n of bipolar transistor measurement is shown in Fig. 1. The whole system with a point-probe station is presented in Fig. 2.

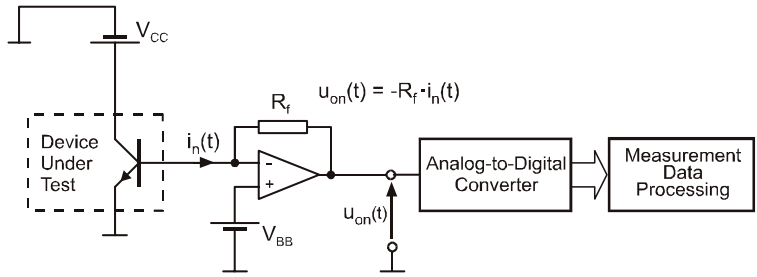

Figure 1. The schematic diagram of the measurement set-up for transistor base current noise measurement

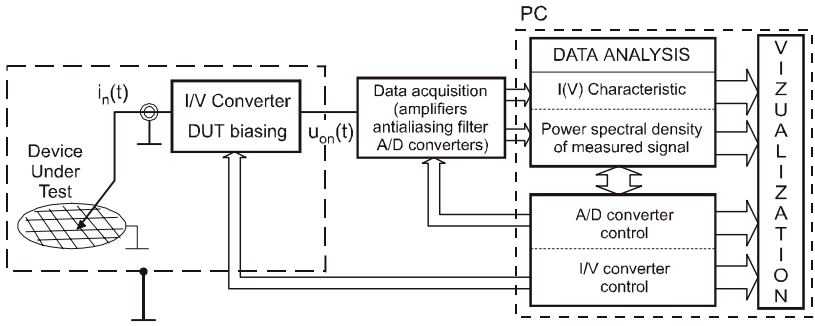

Figure 2. The computer-controlled measurement system with the point-probe station

3. Disturbances in point-probe measurements

Disturbances in the system for point-probe noise measurement on microelectronic devices originate both from external, as vibrations and electromagnetic interference, and internal sources (Fig. 3). Vibrations and shocks cause fluctuation of the contact resistance between a probe and a contact pad. In those fluctuations one can observe both periodical and random components, often having high values [1]. The effective minimisation of the shocks and vibration influence on measurement results can be obtained by using the heavyweight measurement stations.

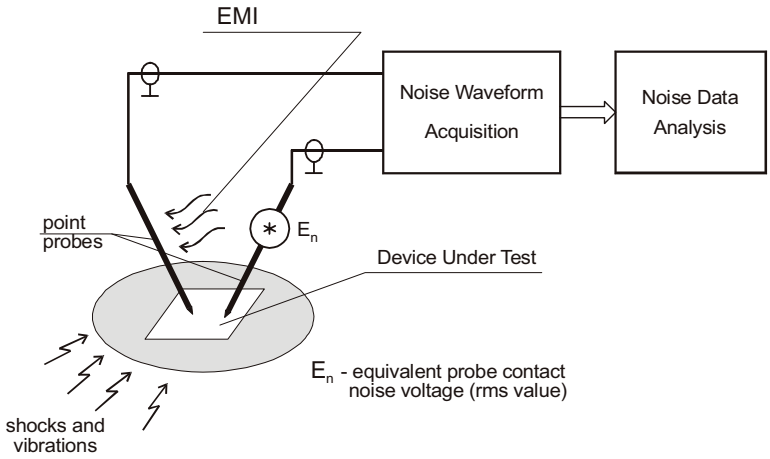

Figure 3. Interference sources in-point probe measurements (EMI – Electromagnetic Interference)

Using the appropriate shield and ground systems one can reduce unwanted influence of the EM field. It's worth to mention that shielding is very effective method of system protection but applied shields change electrical parameters of the object (change the electrical capacitance between the shielded components, induct the high capacitance between the measured object and the shield, decrease the effective induction, increase losses and attenuation - thus the effective frequency bandwidth of the protected object is decreased). Shields increase also the cost of the total system.

The proper grounding of the system has a significant influence on decreasing of the EMI. For noise measurement in the low frequency range, a single point-parallel grounding system should be used for signal lines. The conducted disturbances can be significantly reduced by separation of the measured noise signal, digital circuitry and power lines.

In low-level measurements, the measured signal should be conducted to the transimpedance preamplifier (*I/V* converter, Fig. 1) with the possible shortest cable. Moreover, it should be carefully selected low-noise cables with reduced triboelectric effect.

The analog part of the system (mainly preamplifier) often introduces non-negligible contribution caused by its inherent noise. The predominant noise source of transimpedance amplifier is the thermal noise of the back -loop resistance R_f. For the high R_f values, the thermal noise level can be even higher than the noise level of measured current noise. For example, for R_f = 100 $M\Omega$ the power spectral density of thermal noise is equal $E_n = 1.29\times10^{-6}\ V^2/Hz$ (current noise of op-amp used in the system is $I_n^2 = 1{,}66\times10^{-28}\ A^2/Hz$) for $T = 300\ K$.

However, using lower-value resistance of R_f in order to reduce its thermal noise influence on measurement data, results in decreasing of the current to voltage amplification of the I/V converter and requires the greater amplification (sensitivity) of the next stage in the system.

Calculating the noise level of the transimpedance preamplifier (I/V converter), one has to take into consideration the noise level of the operational amplifier used in the converter circuit. In low-level measurements the amplifier noise is usually significantly lower than the thermal noise level of the R_f resistance, which value should be enough high to ensure the proper I/V conversion value. However for low R_f values, when its thermal noise and the preamplifier noise are comparable, the measured signal is sufficiently high to take no account the influence of both those disturbances. For example, the power spectral density of current noise for operational amplifier OPA128 is $I_n = 0.12\ fA/\sqrt{Hz}$, thus two decades below the thermal noise of the resistance $10^8\ \Omega$.

In noise measurements with the transimpedance preamplifier (I/V converter) its frequency bandwidth should be considered. The frequency characteristic of the preamplifier depends mainly on the value of capacitance connected to the input of the operational amplifier, the parasitic capacitance of the resistor R_f and the parasitic capacity between input and output of the amplifier. There capacitance and the resistance R_f form the low-pass RC filter with the filter time-constant $\tau = R_f C_p$, where C_p is the effective equivalent capacitance connected to the output of the amplifier.

In order to decrease the filter time constant the C_p value should be minimised by using the shortest possible connection cables. Decreasing the R_f value leads to decreasing the system amplification, thus the measurement accuracy.

The most important in data acquisition with the A/D converter is the proper value of sampling frequency and the proper number of samples to be stored. They determine the frequency bandwidth of the estimated power spectral density and the intervals between spectrum bars. When the signal is sampled with the frequency lower than twice the maximum frequency of signal components, the aliasing effect occurs. Using the low-pass filter with the cut-off frequency set accordingly to the usable frequency band in the measured signal can reduce the aliasing. In modern A/D converter cards the anti-aliasing filter cut-off frequency is set automatically, as at least half of the sampling frequency (the 3dB frequency of the filter in NI PCI 4452 card is 0.5 of sampling frequency and the attenuation is 100dB).

4. The method of random and periodic components separation

Disturbances are often not completely eliminated from the measured noise and a processed signal comprises unwanted components, in particular having periodic character (Fig. 4). The latter originates from the power lines (usually 50Hz and harmonics) and computer electronics used for the measurement system control (e.g. screen frame trigger frequencies). The periodic components usually appear as narrow lines at respective frequencies in the power spectral density characteristic. The level of periodic components can be higher than that of the random component and this may results in a degradation of the accuracy of the noise measurement.

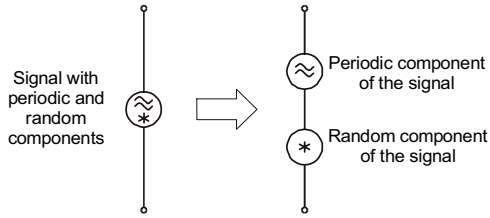

Figure 4. The model of measured signal components: random and periodic, before and after separation

In order to eliminate the impact of the periodic signal on the noise measurement accuracy, the efficient method of separation the noise and periodic components [2,3] can be implemented into the measurement algorithm. The digitised signal $u_x(m)$ is split into K sub-records $u_{x1}(n)$, ..., $u_{xK}(n)$ each having an equal number of samples. For facilitating the further procedures, each sub-record should start with the sample corresponded to the same phase of the periodic component. That requires choosing the appropriate sampling frequency value, corresponding with the frequency of the component, that will be removed before the noise analysis. Next the mean-value record $u_h(n)$ is calculated by coherent adding of sub-records and dividing the result by K. The $u_h(n)$ represents the periodic component of the measurement signal. Subsequently, the $u_h(n)$ is subtracted from the individual sub-records $u_{xk}(n)$. The result is the random component of the measurement signal, which can be used for further analyses.

The algorithm synopsis for the method is shown in Fig. 5. Fig. 6 shows the digital processing procedures.

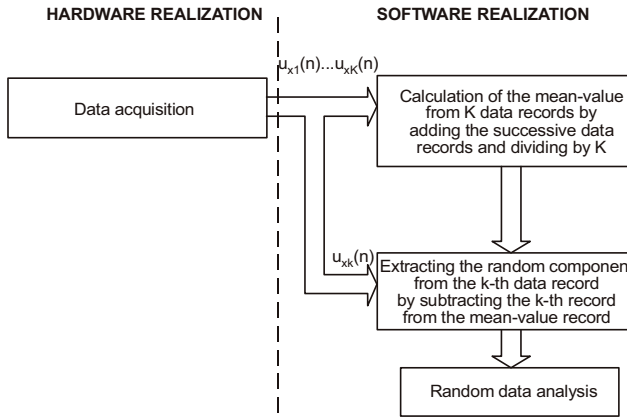

Figure 5. The algorithm for periodic and random signal components separation

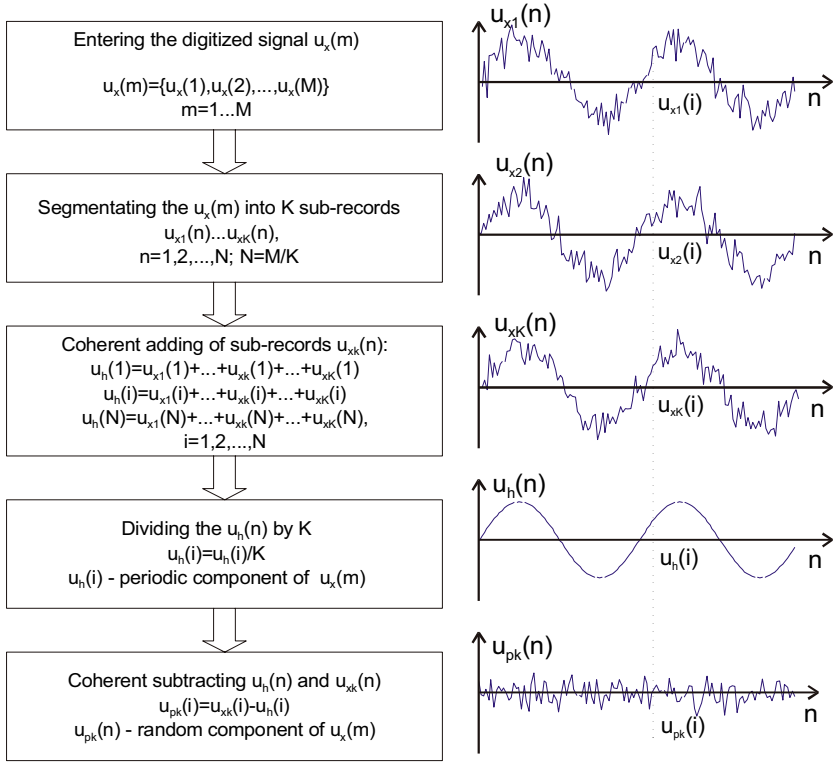

Figure 6. The procedure and illustration of random and periodic components separation

It's worth to mention, that such a procedure is appropriate when the level of the periodic component in the measured signal is comparable or higher than that of the analysed noise component and assuming that these signals are in the same frequency range.

5. Conclusions

The accuracy of noise measurements in submicron semiconductor structures depends mainly on the transimpedance preamplifier used in the system. The preamplifier noise and bandwidth are mainly determined by the resistance value in back-loop of the operational amplifier, especially in low -level signal measurements when its high value is required. Its influence on measurement results can be significant. The great importance for the measurement accuracy in point-probe measurement has also proper isolation of the system from the external interference sources, both mechanical and electromagnetic.

Applying additional methods for reduction of disturbances on the noise measurement results requires of increasing costs for measurement set-up modification. However these costs could be minimised by using the software methods, not requiring the intervention in the hardware part of the measurement system.

References

[1] A. Szewczyk and L. Spiralski, The method of distortion reduction in low frequency noise measurements on wafer-level. Proc. Polish Metrology Congress KKM 2001, 24-27 June 2001, Warsaw, vol. 2 321-324.

[2] B. Pałczyńska, L. Spiralski and J. Turczyński, The new method of interference assessment in low-voltage power supply lines. Proc. 11th IMEKO TC-4 Symposium, 13-14 Sept. 2001, Lisbon, 130-134.

[3] B. Pałczyńska, J. Turczyński, A. Konczakowska and L. Spiralski, Method of parasitic signal measurement in low voltage supply lines in the low and high frequency range, particularly in ship lines, Polish Patent Office, Patent Application No. 140152 (2000).

HOOGE MOBILITY FLUCTUATIONS IN *n-InSb* MAGNETORESISTORS AS A REFERENCE FOR ACCESS RESISTANCE LF–NOISE MEASUREMENTS OF *SiGe* METAMORPHIC HMOS FETs

S. Durov[1], O.A. Mironov[2], M. Myronov and T.E. Whall

Department of Physics, University of Warwick
Gibbet Hill Rd, Coventry CV4 7AL
United Kingdom

V.T. Igumenov, V.M. Konstantinov and V.V. Paramonov

Institute for Electronic Materials
248001 Kaluga
Russia

[1] S.Durov@warwick.ac.uk

[2] O.A.Mironov@warwick.ac.uk

Abstract For the first time, to verify the origin of LF-noise (LFN) in the access resistance of metamorphic SiGe HMOS FETs, we used a thin film *n-InSb* magnetoresistor (MR) as a reference control. Hybrid MRs were fabricated on $NiO{\times}Fe_2O_3$ ferrite substrates from Sn-doped MBE-grown *n-InSb/i-GaAs* heterostructures. The thickness of the *InSb* epilayers lie in the range 1.0-2.0 μm giving a room-temperature Hall mobilities of $\mu = 5.5{\times}10^4$ cm^2/Vs at a carrier densities of $5{\times}10^{16}$ cm^{-3}. The device resistance could be changed by up to 500% in a magnetic field of B = 325 mT. LFN spectra were measured at B = 0 and 31mT. Results show that the current dependence of the PSD for this MR is described by the Hooge mobility fluctuation model, according to $S_I / I^2 = S_R / R^2 = \alpha_H \times \mu\,(eR / fL^2)$. A simple design for a calibrated noise reference is proposed.

Keywords: LF-noise, Magnetoresistor, SiGe MOSFET

J. Sikula and M. Levinshtein (eds.),
Advanced Experimental Methods for Noise Research in Nanoscale Electronic Devices (311 - 318)

1. Introduction

The origin of 1/f noise in the bulk semiconductors [1, 2], thin films / heterostructures [3], and MOSFET devices [4,5,6] is still an open question despite numerous papers published to date and intensive research still in progress. The main question is still whether the noise originates from low frequency (LF) carrier number fluctuations (CNF) or from carrier mobility fluctuations (CMF). Relatively LF noise (LFN) measurements of magnetic effects in thin film *n-GaAs* [7-9] and bulk *n-InSb* [10] magnetoresistors (MRs), of various geometries, most authors concluded that the observed 1/*f* type noise was due to CNF. This is because, a magnetic field dependence in the reduced voltage noise for *GaAs* MRs has not been experimentally observed, and they used assumption that the Hooge parameter is magnetic field independent.

Here, we study the noise for a custom made *n-InSb* thin film MR [11] in order to confirm the Hooge dependence [12,13] of the drive current noise power spectral density (PSD) on current, presented by expression (1) below. We suggest this is an important result in understanding the origin of LFN in the heavily doped contact areas of *Si*, *SiGe* MOSFETs. Such an *n-InSb* epitaxial MR was chosen because its value can be easily controlled over a wide range (197-958Ω) by simple changing the distance between the MR and a small permanent magnet of 325 mT. It is worth mention that almost 500% change of resistance was achieved without affecting the structural properties of the *n-InSb* epilayer.

The influence of magnetic field on the 1/f noise in the *n-InSb* epilayer

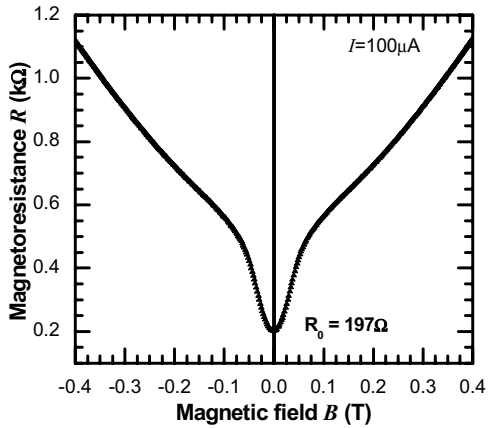

Figure 1. Magnetoresistance for *n-InSB* MR fabricated on $NiO \times Fe_2O_3$ ferrite substrate. Ferrite saturation field is at $B_{sat} \approx 0.1$T.

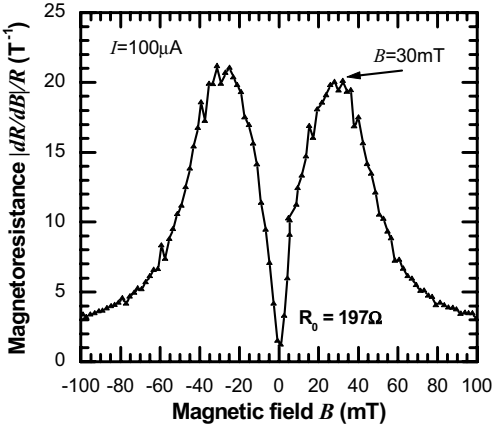

Figure 2. Reduced differential magnetoresistance for *n-InSb* MR.

has also been studied. The magnetic field dependence of reduced 1/*f* noise measured in our *n-InSb* MR can not be explained by the carrier number and mobility fluctuation models published in ref. [7-9]. Unlike the case of *n-GaAs*, there are no published evidence of deep *D*(*X*)-like centres in *n-InSb*, influencing transport properties at room temperature (RT) *T*=293K and normal atmospheric pressure [14], which is important for suppression of the CNF component in 1/f noise. Additionally, our *n-InSb* epilayer was three times over-doped (in comparison with extrinsic concentration at RT) to minimise the temperature fluctuations of carrier concentration. For this reason, we are sure that the CNF mechanism is not responsible for 1/f noise in our *n-InSb* MR and propose an alternative to [7-9] model for the LFN magnetic field dependence.

2. Samples and experimental setup

n-InSb/i-GaAs Sn-doped heterostructures were grown using a vacuum epitaxy method with e-beam evaporators [11]. The thickness of the *InSb* epilayer lies in the range 1.0-2.0 μm giving a RT Hall mobility of 5.5×10^4 cm^2/Vs at a carrier density of 5×10^{16} cm^{-3}. MRs were fabricated by wet etching of a special shaped stripe with metal shorts. The total stripe length and width were respectively $L_{tot} = 5.4$ mm and $W = 140$ μm. The 20 μm length of metal covered parts is equal to the length of metal-free *n-InSb*. The total *n-InSb* effective length of MR-device is $L = L_{tot}/2 = 135 \times 20$ μm $= 2700$ μm. The effective MR width to length ratio is

$W / L = 7$, which is similar to a Corbino disk geometry with strong shorting of the Hall voltage by the metal contact pads. An integrated sandwich was fabricated by placing the MR between two ferrite HH-1000 ($NiO{\times}Fe_2O_3$) concentrators with sizes 1×1×0.5 mm and 2.7×2.7×0.5 mm.

A *SiGe* MOSFET, with gate length 1 μm and gate width 50μm, was fabricated using reduced thermal budget processing at 650 °C on multilayer *SiGe* heterostructures grown by solid-source MBE [6]. Source and drain contacts were fabricated by BF_2^+ implantation at 40keV, with a dose of $4{\times}10^{15}\text{cm}^{-2}$ and activated at 650 °C for 30 sec. The Al gate and Ti/Pt/Au contact metallisation were evaporated at the end of the fabrication process.

The current-voltage (*I-V*) characteristics were measured using an "Agilent" 4156C semiconductor parameter analyser. Magnetoresistance (Fig. 1,2) was measured using a Keithley based DC-kit. LFN was measured with a help of an HP 35670A dynamic signal analyser and a custom-made preamplifier containing LT1028 (Linear Technology) operational amplifier in the first stage [15]. Noise spectra for *n-InSb* MR were extracted from measured data by subtraction of the preamplifier background noise due to the relatively small absolute level of the measured noise signal.

3. Low frequency noise measurements

3.1. Noise of *n-InSb* magnetoresistor

LF noise spectra were measured without magnetic field and at an external field of $B_{ext} = 31$ mT (Fig. 3), which is close to the maximum of the normalized differential MR (Fig. 2) ($\mu B \approx 1$, where $B \approx 5.8{\times}B_{ext}$ is the magnetic field on the *n-InSb* epilayer surface). It was found that the dependence of current noise PSD on current, described by the Hooge relation (Fig. 4) [13]

$$\frac{S_I}{I^2} = \frac{S_R}{R^2} = \alpha_H \frac{1}{Nf} = \alpha_H \frac{\mu e R}{fL^2} \qquad (1)$$

where α_H is the Hooge parameter, N is the total number of carriers in the sample, μ is the carrier mobility, e is the electron charge and R is the sample resistance.

The noise reduced mobility $\alpha_H{\times}\mu$ [16], which acts as a "material fingerprint", is equal to $4.1{\times}10^2\ \text{cm}^2\text{V}^{-1}\text{s}^{-1}$. The Hooge parameter is $\alpha_H = 7{\times}10^{-3}$, which is comparable to bulk n-InSb ($4{\times}10^{-3}$) [2] and the same order of magnitude as in 2DEG InAs quantum wells [3].

If the reduced PSD S_I / I^2 dependence on magnetic field described by the CNF model to satisfy the empirical Hooge relation (1) [7,9]:

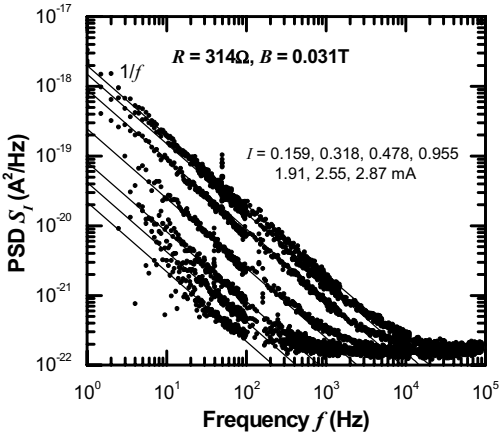

Figure 3. Current noise spectra for *n-InSb* MR at different drive currents in an external magnetic field of 31 mT.

$$\frac{S_N}{N^2} = \frac{S_I}{I^2} = \alpha_H \frac{1}{Nf} \tag{2}$$

where the Hooge parameter α_{H} is independent of carrier number and magnetic field. The total number of carriers N in the device is also independent of magnetic field. So, the reduced current noise should show no magnetic field dependence.

If the 1/f noise is caused by CMF, then the effect of magnetoresistance observable in the 1/f spectrum and current spectrum equation can be written as [7,17]

$$\frac{S_I}{I^2} = \left(\frac{1-\mu^2 B^2}{1+\mu^2 B^2}\right)^2 \frac{S_\mu}{\mu^2} = \left(\frac{1-\mu^2 B^2}{1+\mu^2 B^2}\right)^2 \alpha_H \mu \frac{eR}{fL^2} \tag{3}$$

Here the reduced current noise should decrease with magnetic field for the CMF model, if S_μ / μ^2 is suggested to be magnetic field independent.

However, the results presented in Fig. 4 can be described neither by the CNF nor by the CMF models due to the increase of S_I / I^2 with magnetic field.

If one could suggest that the mobility fluctuation spectrum and Hooge parameter are functions of magnetic field, then:

$$\alpha_H(B) = \left(\frac{1+\mu^2 B^2}{1-\mu^2 B^2}\right)^2 \alpha_H(0) \tag{4}$$

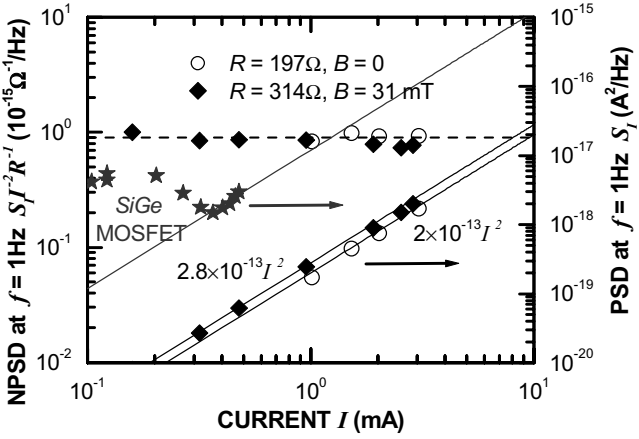

Figure 4. LF-noise power spectral density (PSD) and normalized PSD (NPSD) at f = 1Hz and T = 293K versus DC current through hybrid *n-InSb* MR. PSD current dependence also shown for SiGe p-MOSFET (stars) at f = 1Hz and T = 293K.

$$\frac{S_I}{I^2}=\left[\left(\frac{1-\mu^2B^2}{1+\mu^2B^2}\right)^2\mu\right]\times\left[\left(\frac{1+\mu^2B^2}{1-\mu^2B^2}\right)^2\alpha_H(0)\right]\frac{eR}{fL^2}=\mu\times\alpha_H(0)\frac{eR}{fL^2} \quad (5)$$

The form of expression (5) is very similar to the CNF model, but in fact represents a CMF model.

3.2. Access resistance noise of short channel *SiGe* p-MOSFETs in strong inversion

The drain current noise was measured for 1μm gate length $Si_{0.3}Ge_{0.7}/Si_{0.6}Ge_{0.4}$ p-MOSFET [6] from subthreshold region to strong inversion at a fixed drain-source voltage V_{DS}. The current dependence of PSD is described by a CNF model due to flat band voltage fluctuations at low currents (low gate-overdrive voltages). However, at high currents (high gate-overdrive voltages), the PSD dependence on current can be described neither by the CNF nor by the carrier number with correlated mobility fluctuations or Hooge mobility fluctuations of effective mobility in the channel. Access resistance (through heavily Boron doped contact areas) for SiGe MOSFETs was extracted from the DC characterictics of p-MOSFETs with different gate lengths [18] and found to be comparable with the channel resistance for a 1μm gate length MOSFET in strong inversion. Figure 4 shows that the PSD for SiGe MOSFETs at high currents has the same current dependence ($\sim I^2$) as for *n-InSb* MR. Hence, we can conclude that

drain current noise in p-MOSFETs, with short gate lengths and in strong inversion, is associated with access resistance fluctuations and can be described by the empirical Hooge relation (1).

The normalised noise PSD generated in access resistance of SiGe MOSFET is $S_I/I^2R = 8\times10^{-14}\ \Omega^{-1}\mathrm{Hz}^{-1/2}$. If we estimate the Hooge parameter using $L_{SD} \approx 5\mu\mathrm{m}$ and $\mu_{SD} \approx 10\text{-}100\ \mathrm{cm^2V^{-1}s^{-1}}$, then we obtain the reasonable value $\alpha_H \approx 10^{-2}\text{-}10^{-3}$.

4. Conclusions

It was found that LF noise for *n-InSb* MR can be described by Hooge mobility fluctuations, with the parameter $\mu\alpha_H = 4.1\times10^2\ \mathrm{cm^2V^{-1}s^{-1}}$.

We propose a precision noise reference based on *n-InSb* MR. This noise reference has an extremely wide dynamic range, which is easily controlled by the simple adjustment of a permanent magnet position over the distance of a few millimetres. The current noise value can be easily recalculated from the measured MR value.

The drain current noise of p-MOSFETs, with short gate lengths in strong inversion, is associated with access resistance fluctuations and can be described by an empirical Hooge relation [13].

The question about the origin of magnetic field influence on 1/f noise in semiconductors still requires further investigation.

Acknowledgements

We acknowledge M. Levinshtein, F. Hooge and L.K.J. Vandamme for fruitful discussion and useful notes during the NATO Workshop “Advanced Experimental Methods for Noise Research in Nanoscale Electronic Devices” (Brno, Czech Republic, July 2003). We are also thankful to Adrian Lovejoy and John Reed for technical support and J. Routoure for comments.

References

[1] A.L. McWhorter. 1/f noise and germanium surface properties. In R. H. Kingston, editor, Semiconductor Surface Physics, University of Pennsylvania Press, Philadephia, 1957.

[2] L.K.J. Vandamme, 1/*f* noise in homogeneous single crystals of III-V compounds, Physics Letters **49A** (1974) 233-234.

[3] M. Tacano, M. Ando, I. Shibasaki, S. Hashiguchi, J. Sikula, T. Matsui, Dependence of Hooge parameter of InAs heterostructure on temperature, Microelectronics Reliability **40** (2000) 1921-1924.

[4] L.K.J. Vandamme, L.B. Kiss, O.L.J. Stoelinga, Anomalous behaviour of the current noise in long-narrow channel MOSFETS and its interpretation, Solid-State Electronics. **43** (1999) 697–700.

[5] G. Ghibaudo, T. Boutchcha, Electrical noise and RTS fluctuations in advanced CMOS devices, Microelectronics Reliability, **42** (2002) 573-582.

[6] M. Myronov, S. Durov, O.A. Mironov, T.E. Whall, E.H.C. Parker, Low-frequency noise analysis for buried SiGe channel metamorphic p-MOSFETS with high Ge content, ICNF-17 Proceedings, Prague, 2003, p. 343-346

[7] M.E. Levinshtein and S.L. Rumyantsev, Noise of the 1/*f* type under conditions of a strong geometric magnetoresistance, Soviet Physics - Semiconductors **17** (1983) 1167–1169.

[8] M. Song and H.S. Min, Influence of magnetic field on 1/*f* noise in GaAs Corbino disks, J. Appl. Phys. **58** (1985) 4221–4224.

[9] M.H. Song, A.N.Birbas, A. van der Ziel and A.D. van Rheenen, Influence of magnetic field on 1/*f* noise in GaAs resistors without surface effects, J. Appl. Phys. **64** (1988) 727–728.

[10] P. Vande Voorde, W.F. Love, Magnetic effects on 1/*f* noise in *n*-InSb, Physical Review B **24** (1981) 4781–4786.

[11] O.A. Mironov et al, The sub-micrometer thickness n-InSb/i-GaAs epilayers for magnetoresistor applications at room temperatures of operation, Abstracts NGS−11 Buffalo New York, USA, (June 16-20, 2003) TuP-16.

[12] F. Hooge, 1/*f* noise, Physica B, **83** (1976) 14

[13] F.N. Hooge, T.G. Kleinpenning and L.K.J. Vandamme, Experimental studies on 1/*f* noise, Rep. Prog. Phys. **44** (1981) 479–532.

[14] Z. Wasileski, R.A. Stradling, Magneto-optical investigation of a deep centre in n-InSb, Solid State Communications **57** (1986) 123–127.

[15] S. Durov, O.A. Mironov, Optimised preamplifier for LF-noise MOSFET characterization, in this Proceedings

[16] M.M. Jevtic, Z. Stanimirovic, I. Stanimirovic, Evaluation of thick-film resistor structural parameters based on noise index measurements, Microelectronics Reliability **41** (2001) 59.

[17] H.M.J. Vaes and T.G.M. Kleinpenning, Hall-effect noise in semiconductors, J. Appl. Phys. **48** (1977) 5131–5134.

[18] D. K. Schroder, Semiconductor material and device characterization, Second Edition, A Wiley-Interscience publication, 1998, p. 223-234.

OPTIMISED PREAMPLIFIER FOR LF-NOISE MOSFET CHARACTERIZATION

S. Durov[1] and O.A. Mironov[2]

Department of Physics, University of Warwick
Gibbet Hill Rd, Coventry CV4 7AL
United Kingdom

[1] S.Durov@warwick.ac.uk

[2] O.A.Mironov@warwick.ac.uk

Abstract A modular design of preamplifier for low frequency noise measurements with interchangeable first stage was chosen to improve reliability and to reduce the influence of connection cables on measurement results. In this communication we present the optimised preamplifier modules as the first stages for MOSFETs gate leakage and drain current noise measurements with input impedance 50 Ω - 10^8 Ω in the frequency range 1.0 Hz - 10^5 Hz. The best available commercial operational amplifiers (OPA's) AD549, OPA637 and LT1028A were used for the first stage module at each of the three chosen impedance ranges. The noise characteristics of different OPA's, which have been tested, are also presented.

Keywords: LF noise, ultra-low noise preamplifier, preamplifier optimisation

1. Introduction

Conventional MOSFET characterisation techniques, such as the combination of I-V (current-voltage) and C-V (capacitance-voltage) measurements, are very problematic as device sizes decrease down to the deep sub-μm (DS-μm) scale. "Average per square" characteristic parameters obtained from large-scale devices cannot be suitable for DS-μm MOSFET analysis due to statistical uncertainties in the fabrication technology together with the importance of mesoscopic quantum effects. Low frequency noise measurements could be a powerful diagnostic technique for DS-μm MOSFET characterization in a wide range of device operation regimes [1]. Unfortunately, the commercially available current preamplifiers such as

J.Sikula and M.Levinshtein (eds.),
Advanced Experimental Methods for Noise Research in Nanoscale Electronic Devices (319 - 326)

ITHACO-1211 [2], SR-570 [3], EG&G-181 [4] have been optimised only for limited ranges of device input impedance and their conventional "all-in-one" desktop design also introduces extra problems when long cables are used to connect to the sample test fixture. To overcome all the above problems we present in this communication optimised preamplifier modules as the first stages for gate leakage and drain current noise measurements of MOSFETs with input impedance 50Ω-10^8Ω in the frequency range 1.0 Hz-10^5 Hz.

2. Low frequency noise of current-preamplifier

Background equivalent noise of the amplifier is defined by the equivalent noise of the first stage. Electrical noise of the first stage was described earlier by Hung *et al* [5] and more thoroughly analysed by Vandamme *et al* [6] for the particular case of common-emitter amplifier with BJT input. However, the individual current source introduces additional noise in system, and the first stage here was also used as a current source for device under test (DUT). The equivalent scheme for the first stage of such a preamplifier is shown on Fig. 1.

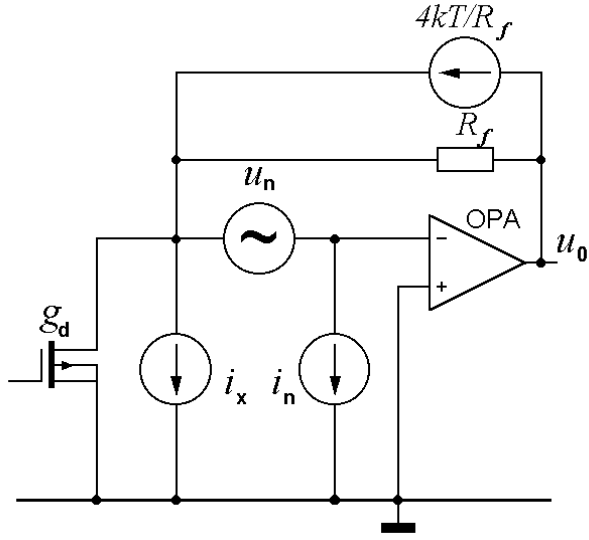

Figure 1. Equivalent scheme for the first stage of the current preamplifier. Sources of current and voltage noise are shown.

According to Fig. 1, output voltage fluctuations of the first stage could be presented as:

$$u_0^2 = R_f^2 \left(i_x^2 + i_n^2 + \frac{4k_B T}{R_f} + u_n^2 \left(\frac{1}{R_f} + g_d \right)^2 \right) \tag{1}$$

where i_n – equivalent input current noise of OPA, u_n – equivalent input voltage noise of OPA, i_x – drain current noise of DUT, R_f – feedback resistance value, g_d – DUT conductance ($g_d = 1/R_{tot}$ in linear regime). At low frequencies (below 10^5Hz), a feedback resistor can introduce extra 1/f noise, which depends on the quality of resistor material and is not described here.

Drain current MOSFET noise could be measured if background noise from the preamplifier is less than (unmasked by) noise from our device:

$$i_x^2 \geq i_n^2 + \frac{4k_B T}{R_f} + u_n^2 \left(\frac{1}{R_f} + g_d \right)^2 \tag{2}$$

The condition for reduced drain current noise can be rewritten as:

$$\frac{i_x^2}{I_D^2} = \frac{i_x^2 R_{tot}^2}{V_{DS}^2} \geq \left(i_n^2 + \frac{4k_B T}{R_f} \right) \frac{R_{tot}^2}{V_{DS}^2} + \frac{u_n^2}{V_{DS}^2} \left(\frac{R_{tot}}{R_f} + 1 \right)^2 \tag{3}$$

We can get optimal resistance and device impedance for each OPA or optimal OPA for defined device impedance, if we could compare preamplifier noise with DUT thermal noise $i_x^2 / I_D^2 = 4k_B T R_{tot} / V_{DS}^2$ and minimise the functional (4) by R_{tot} and R_f variation:

$$F(R_{tot}, R_f) = \left(\left(i_n^2 + \frac{4k_B T}{R_f} \right) \frac{R_{tot}^2}{V_{DS}^2} + \frac{u_n^2}{V_{DS}^2} \left(\frac{R_{tot}}{R_f} + 1 \right)^2 \right) \Bigg/ \frac{4k_B T R_{tot}}{V_{DS}^2} \tag{4}$$

$$\frac{\partial F(R_{tot}, R_f)}{\partial R_{tot}} = 0 \tag{5}$$

$$R_{tot} = \frac{R_f u_n}{\sqrt{i_n^2 R_f^2 + 4k_B T R_f - u_n^2}} \tag{6}$$

If an OPA is used as a current source for a DUT, current through the DUT is limited by supply voltage V_{bat} of OPA and feedback resistance value R_f:

$$I_{max} \approx \frac{V_{bat}}{R_f} \geq \frac{V_{DS}}{R_{tot}} \Rightarrow R_{tot} \geq R_f \frac{V_{DS}}{V_{bat}} \quad (7)$$

So, the choice of feedback resistance and selection of OPA is restricted by the DUT impedance range [6,7]. The optimal feedback resistance for the selected OPA can be chosen using the condition $R_f i_n \approx u_n$. The choice of R_f is also depends on stability of the module designed and maximum input current, which limits the minimum allowed DUT resistance for measurements at fixed drain-source voltage V_{DS}.

3. Preamplifier design

Thorough analysis of currently available commercial OPAs was carried out. Average values and frequency dependence at frequency range 10^0-10^5 Hz of equivalent input current i_n and voltage u_n noise were determined from datasheets and measurements of available samples. The AD549, OPA637 and LT1028A OPAs were chosen to use in the first stage modules at three impedance ranges to obtain the lowest noise at each range. Feedback resistance R_f and i_n , u_n values for used OPA are presented in Table 1.

Table 1. Parameters of operational amplifiers (OPAs) used for preamplifier modules

OPA	Input noise at f = 1 Hz		Input noise at f = 10 kHz	
	i_n (fA×Hz$^{-1/2}$)	u_n (nV×Hz$^{-1/2}$)	i_n (fA×Hz$^{-1/2}$)	u_n (nV×Hz$^{-1/2}$)
LT1028	9000	1.6	1000	0.85
OPA637	2.5	50	2.0	3.7
AD549	0.7	200	0.15	35

OPA	R_f (Ω)	DUT resistance (Ω)	Gain-Bandwidth product (MHz)
LT1028	1×10^4	$(0.05\text{-}5)\times10^3$	75
OPA637	1×10^5	$(0.05\text{-}5)\times10^5$	80
AD549	1×10^7	$(0.05\text{-}9)\times10^7$	1

Functional $F(R_{tot}, R_f)$ for selected OPAs are shown on Fig. 2. Thermal noise of the DUT could be measured, if $F(R_{tot}, R_f) \leq 1$, while $1/f$ noise could be measured at low frequency (1-10Hz) even if $F(R_{tot}, R_f) > 1$.

The feedback resistor was chosen of wired or metal film type to keep preamplifier stability and bandwidth and to reduce 1/f noise introduced by it. Each preamplifier module was placed in a separate small shielded metal box with coaxial connectors. A digital oscilloscope (Tektronix 24678) and dynamic spectral analyser (HP35670A) were used to adjust and calibrate the preamplifier. A modular design was chosen to increase reliability of the amplifier and reduce the influence of connection cables on measurement results. The schematic amplifier circuit diagram is shown on Fig. 3. Preamplifier modules ***A***, ***B*** and ***C*** can be used for drain current noise measurements (connectors 1,2,3). Module ***C*** with AD549 OPA is also suitable for gate leakage current noise measurements (connectors 1,2,4).

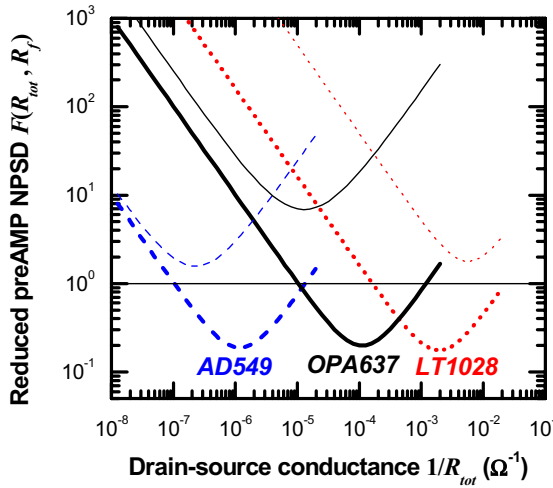

Figure 2. Preamplifier modules background noise normalised on thermal noise of DUT for OPAs AD549 with R_f = 10 MΩ, OPA637 with R_f = 100 kΩ and LT1028 with R_f = 10 kΩ at f = 10 kHz (thick lines) and f = 1 Hz (thin lines).

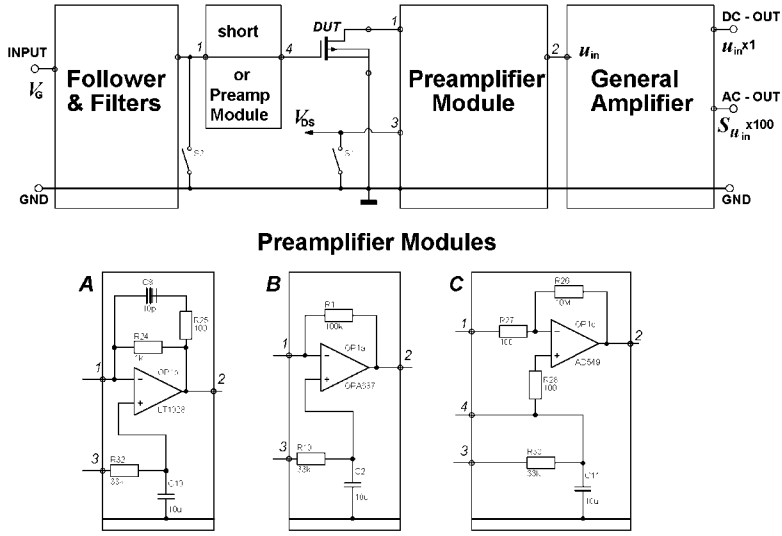

Figure 3. Schematic circuit diagram of the current preamplifier with modular design and interchangeable first stages ***A***, ***B*** and ***C*** for LF-noise measurements.

Three preamplifier modules, a follower with two-pass LF noise filter, a general amplifier module with gain of $G = 100$, Pb-acid batteries and a test fixture or cryostat with DUT were used for further measurements. The preamplifier modules' background noise mixed together with MOSFET's noise measured at $f = 1$Hz and $f = 100$kHz versus DUT conductance are shown on Fig. 4. Normalised drain current power spectral density (NPSD) for MOSFETs at $f = 100$kHz agree with preamplifier noise together with thermal noise NPSD predicted and measured on set of metal film resistors at low and high DUT conductance. Increased values of NPSD for MOSFETs at $f = 100$kHz at intermediate DUT conductance range correspond to 1/f noise. NPSD for MOSFETs at f=1Hz are almost several orders of magnitude higher than preamplifier background noise at chosen conductance ranges.

4. Conclusions

The preamplifier must be specially designed or carefully fitted for measurements of low frequency noise on MOSFETs due to the extremely wide range of its input and output impedances. A modular design with separate first stage should be used to overcome problems with extra noise, extra inductance and capacitance introduced by cables. Individual operational amplifiers (OPA's) must be used for each impedance range or

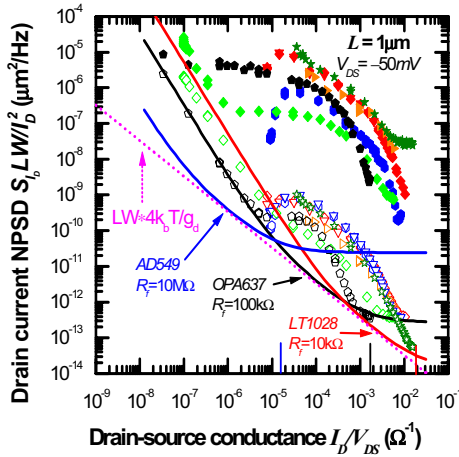

Figure 4. Normalised drain current noise of measured MOSFETs (filled symbols at $f = 1$ Hz and unfilled symbols at $f = 100$ kHz) and background noise of built preamplifier modules at $f = 10$ kHz (solid lines). Thermal noise of devices is also shown for comparison (dotted line).

regime of MOSFET operation. Currently available commercial OPA's could be used for gate leakage and drain current noise measurements of MOSFETs with input impedance 50Ω-10^8Ω in the frequency range 1.0 Hz-10^5 Hz. The AD549, OPA637 and LT1028A OPA's are recommended for use in the first stage modules at each of the three chosen impedance ranges to improve measurement system.

Acknowledgements

SD acknowledges E.H.C. Parker and T.E. Whall for support during his PhD study at Warwick University. We are thankful to Adrian Lovejoy and John Reed for fruitful consultations, useful notes and technical support. We would like to acknowledge also „Analog Devices®" for free OPA samples used during this research. We thank Bruno Guillet and Jean Routoure for discussion and useful comments.

References

[1] G. Ghibaudo, T. Boutchcha, *Electrical noise and RTS fluctuations in advanced CMOS devices*, Microelectronics Reliability, **42** (2002) 573-582.

[2] http://www.dlinstruments.com/products/index.html

[3] http://www.srsys.com/html/sr570.html

[4] http://www.signalrecovery.com/181detai.htm

[5] K. Hung, P. Ko, C. Hu, Y. Cheng, *A physics-based MOSFET noise model for circuit simulators*, IEEE Transactions on Electron Devices **37** (1990) 1323-1333

[6] L.K.J. Vandamme, Gy. Trefan, *A review of 1/f noise in terms of mobility fluctuations and white noise in modern submicron bipolar transistors – BJTs and HBTs*, Fluctuations and Noise Letters, **1** (2001) R175-R199

[7] LT®1115 datasheet (http://www.linear.com/pdf/lt1115fa.pdf)

NET OF YBCO AND LSMO THERMOMETERS FOR BOLOMETRIC APPLICATIONS

B. Guillet[1], L Méchin, F. Yang, J.M. Routoure, G. Le Dem, C. Gunther and D. Robbes

GREYC (UMR 6072),ENSICAEN & University of Caen,
6 Bd Maréchal Juin, 14050 CAEN cedex,
France

R.A. Chakalov

School of Physics and Astronomy, University of Birmingham,
Birmingham B15 2TT
United Kingdom

[1] bguillet@greyc.ismra.fr

Abstract In this work, two types of perovskite oxide materials with high temperature coefficients have been chosen as thermometers for use in bolometric applications: superconducting $YBa_2Cu_3O_{7-\delta}$ (YBCO) and colossal magnetoresistive $La_{2/3}Sr_{1/3}MnO_3$ (LSMO) thin films. Two different temperature ranges are concerned: around 90 K for YBCO, since they were operated at the superconducting-metal transition and around the room temperature for LSMO. The temperature coefficient ratio and the noise were carefully measured. Best NET values of 3×10^{-8} K.Hz$^{-1/2}$ at 1 Hz, 90 K and 5 mA current bias for YBCO and 1.3×10^{-6} K.Hz$^{-1/2}$ at 1 Hz, 300 K and 1.5 mA current bias for LSMO were obtained. Results are compared to literature and, in the case of room temperature applications, to other types of materials such as semiconductors (a-Si, a-Si:H, a-Ge, poly SiGe) and other oxide materials (semiconducting YBCO, VO_x, other manganite compounds). Finally, the possible use of these thermometers with such low NET characteristics for the fabrication of both membrane-type bolometers for mid-infrared detection and antenna coupled bolometers for THz applications is discussed.

Keywords: Low frequency noise, oxide thin film, bolometer

J. Sikula and M. Levinshtein (eds.),
Advanced Experimental Methods for Noise Research in Nanoscale Electronic Devices (327 - 336)

1. Performances of a bolometer

The basic physics and performances of a bolometer with a resistive thermometer are well established [1]. The detector consists of a radiation absorber of absorptivity η (black metal, antenna, cavity, fedhorn, etc...) and a thermometer that are connected to the heat sink via a heat link of thermal conductance G [W·K^{-1}]. The temperature coefficient ratio $\alpha = (1/R) \times (dR/dT)$ in [K^{-1}], the dimensionless slope $A = dln(R)/dln(T)$ and the Noise Equivalent Temperature NET in [K·Hz$^{-1/2}$], which represents the noise over thermometer sensitivity ratio, are usually used to characterize the performance of the resistive thermometer of real impedance R [Ω]. In order to compare thermometers operated at different temperatures T we will use the following expression of the NET:

$$NET(f) = \frac{T}{\sqrt{R} \times A \times \sqrt{P_{el}}} \times \sqrt{S_v(f) + 4k_B TR + e_{nA}^2(f)} \qquad (1)$$

where $S_v(f), 4k_B TR$ and $e_{nA}^2(f)$ are the low frequency excess noise, the Johnson noise of the thermometer and the noise of the amplifying electronics, respectively and P_{el} is the electrical Joule power dissipated in the thermometer. The main figures of merit of bolometers are the Noise Equivalent Power NEP [W·Hz$^{-1/2}$] and the specific detectivity D^* [cm·Hz$^{1/2}$·W^{-1}], which is the area normalized NEP. In the case the photon and the phonon noise $4k_B T^2 G$ are negligible, the NEP can be written as the ratio of the voltage noise over the voltage sensitivity, which gives:

$$NEP(f) = NET(f) \times \eta^{-1} \times G_{eff} \times \left(1 + j2\pi f \tau_{eff}\right) \qquad (2)$$

where G_{eff} is the effective thermal conductance [W·K^{-1}] and $\tau_{eff} = C / G_{eff}$ is the effective thermal constant [s], with C the heat capacity [J·K^{-1}]. The specific detectivity D^* [cm·Hz$^{1/2}$·W^{-1}] is convenient for comparing bolometers with different areas S [cm^2] and will be used hereafter:

$$D^* = S^{1/2} / NEP \qquad (3)$$

A rapid examination of Eq. (1) shows that low NET could be obtained if T and noise are low and A, R and P_{el} are high. T and A are often fixed by the choice of the material. It has to be noted that high A is often related to a narrow operating temperature window and that there is an upper limit in the choice of P_{el} in order to avoid parasitic self heating. Moreover the electrical Joule power P_{el} combined with A induces electrothermal feedback (ETF) [2, 3]. If A>0, as in LSMO and YBCO cases, and in the Constant Current Mode (CCM) we have $Geff = |\alpha| P_{el}$. For stable operation, the feedback coefficient

L, defined as $L=|\alpha|P_{el}/G$ is limited to be around 0.3 (<1) to avoid thermal runaway (positive ETF). In the Constant Voltage Mode (CVM), the negative ETF would allow a less restrictive L range. In this case and with α positive, there would be no limit for the bias voltage, so the bolometer could operate in a strong ETF mode, which additionally decrease the time constant as $\tau_{eff}=\tau/(1+L)$. Active negative electrothermal feedback mode made with an analog electronic feedback control would improve bolometer performances too [4].

The background fluctuations noise-limited D^*_{BLIP} (Background Limited Infrared Photodetector) for an ideal bolometer having an emissivity of unity and viewing an angle of 2π steradians is independant of the receiving area but related to $(T_{bg}^5+T^5)^{-1/2}$ with T_{bg} the background temperature [K]. The highest possible D^*_{BLIP} to be expected from a thermal detector operated at room temperature or at 90 K and viewing a background at the same temperature is 1.8×10^{10} cm·Hz$^{1/2}$·W^{-1} and 3.7×10^{11} cm·Hz$^{1/2}$·W^{-1}, respectively. If the field of view is reduced by cold shielding and the receiving area remains background limited, the D^*_{BLIP} value would inversely depend upon the noise of the half angle of θ, where θ is the included angle of the cold shield [5].

The studied thermometers are envisaged to be used in membrane-type bolometers for detection in the infrared to mid-infrared wavelength range and in antenna-coupled bolometers on membranes for detection around the 100 µm wavelength. In the first case we have to take care of the low frequency noise of the device since the operating frequency can be quite low because of the relatively big volume of the detecting area (tens of microns). At higher wavelength (around 100µm), the active volume is the load of the antenna that has to be much smaller. It can be of nanometric size, thus leading to small C and consequently small τ. The limiting noise would then be the Johnson noise. It has to be noted that in the membrane case because the thermal conductance G is low, the phonon noise $4k_BT^2G$ can be neglected. However further investigations will have to be made in order to clarify whether the noise in nanometric sample scales with classical models.

In the present work we chosed two types of materials with high temperature coefficients as thermometers for bolometric applications: superconducting $YBa_2Cu_3O_{7-\delta}$ (YBCO) and colossal magnetoresistive $La_{2/3}Sr_{1/3}MnO_3$ (LSMO) thin films. Both 200 nm thick layers were deposited by KrF pulsed laser deposition from a stoichiometric target onto (100) $SrTiO_3$ substrates at 700°C and at 780°C in oxygen pressure, respectively. In case of YBCO the use of the very sharp drop of the resistance at the normal to superconducting transition requires operating temperatures close to 90 K whereas LSMO that has a Curie temperature of 350 K, can be operated around room temperature.

Sections 2 and 3 summarize the *NET* values we obtained for LSMO and YBCO thermometers, respectively. Section 4 gives a short analysis of the results compared to literature and makes an evaluation of the performances of both membrane-type bolometers for mid-infrared detection and antenna coupled bolometers for THz applications fabricated with these materials.

2. *NET* of the LSMO thin films

LSMO bridges with 3 different geometries (large: 400µm×96µm; medium: 660µm×35µm and narrow: 660µm×6µm) were patterned by standard UV photolithography. A four-probe noise measurement setup with a voltage white noise level of 1.6 nV·Hz$^{-1/2}$ was used in order to reduce the influence of the contact resistance noise. *R(T)* characteristics of the LSMO films are reported in figure 1 for all the geometries. At 300 K the resistivity of the 200 nm thick layer was in the 5-20 µΩ·m range and the α value was in the 1.2×10^{-2} - 1.4×10^{-2} K^{-1} range, thus giving A values in the 3.6 - 4.2 range.

The noise properties were described more precisely earlier [6]. The sample voltage noise principally consisted of two parts: a white noise part that corresponds to the Johnson noise of the thermometer expressed by $4k_BTR$ and a $1/f^a$ noise part with $0.7<a<1.2$. In normal metals the following Hooge empirical relation is used:

$$\frac{S_V(f)}{R^2I^2} = \frac{\gamma}{n\Omega f} \tag{4}$$

where γ, n, Ω and f are the dimensionless Hooge parameter, the charge carrier density [m^{-3}], the sample volume [m^3] and the measuring frequency [Hz], respectively.

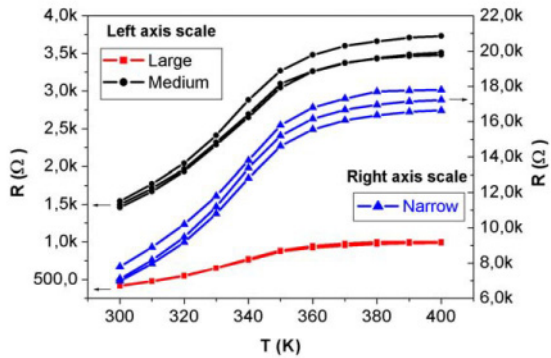

Figure 1. Resistance versus temperature characteristics of LSMO thin films for all the geometries [6]

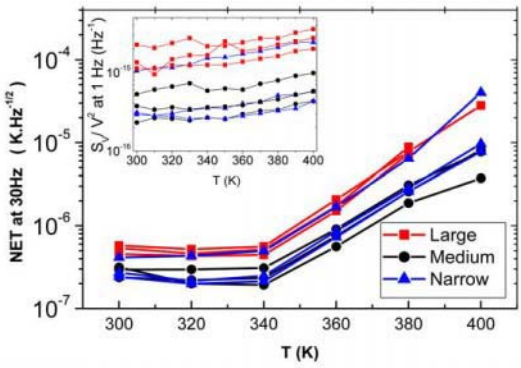

Figure 2. NET at 30Hz and 1.5 mA bias current versus T. Inset shows the normalized S_V/V^2 voltage noise spectral density at 1 Hz as a function of temperature[6]

In our LSMO films we observed that the low frequency noise increased as I^b with $b \sim 1.7$, which does not fully satisfy Eq. (4). A more comprehensive study is in progress in order to measure the dependence of the *1/f* noise on the volume of the sample. However in order to compare the noise level with other materials we assumed that Eq. (4) is valid and we deduced the normalized Hooge parameter γ/n in the 10^{-30}-10^{-29} m^3 range in the whole measured temperature range for all the geometries. These values are among the lowest reported for LSMO thin films [7]. Fig. 2 shows the evolution of the *NET* value at 30 Hz and 1.5 mA as a function of the temperature. At 300 K the lowest measured value was of 2.3×10^{-7} K·Hz$^{-1/2}$ at 30 Hz and 1.3×10^{-6} K·Hz$^{-1/2}$ at 1 Hz.

3. *NET* of the YBCO thin films

The *R(T)* characteristics of the 660 µm×40 µm YBCO bridges with a α coefficient at 90 K of 1.7 K^{-1} (A~160) are shown in Fig. 3. A dedicated read-out electronics was developed for the noise measurements of these low impedance resistive thermometers (<10 kΩ) [8]. The system consists in a highly stable square modulated current source, a low-noise preamplifier and an integrated lock-in amplifier coupled to an optimized analog PID controller. This system was originally designed to monitor an active cavity radiometer operating at 90 K in a liquid nitrogen bath but it is also essential for measurements of YBCO excess noise in the transition region. A high performance temperature controller is indeed required since the resistance

changes drastically as a function of the temperature. The temperature dependence of the excess noise of an YBCO sample in the superconducting transition could then be monitored as a function of the current bias [9].

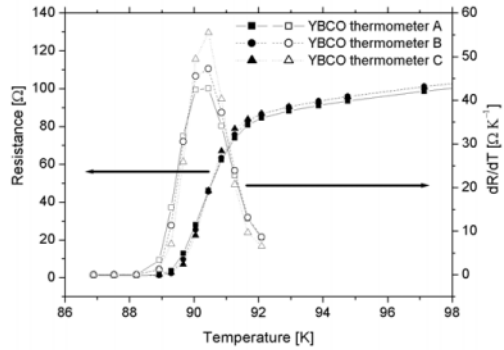

Figure 3. R(T) characteristics of the YBCO thin films[8]

In order to optimize the temperature measurements in our control system, the *NET* has been calculated for each bias current at the temperature where the derivative of the resistance versus temperature is maximum. It decreases with increasing bias current (noise decreases and responsivity increases) (see Fig. 4). At large current bias, the voltage noise spectral density should reach the Johnson noise. A *NET* value of 3×10^{-8} K·Hz$^{-1/2}$ at 1 Hz, 90 K and 5 mA was measured in our YBCO films. These values are among the lowest reported for YBCO thin films [10-11]. It is a very attractive value for our temperature control [8].

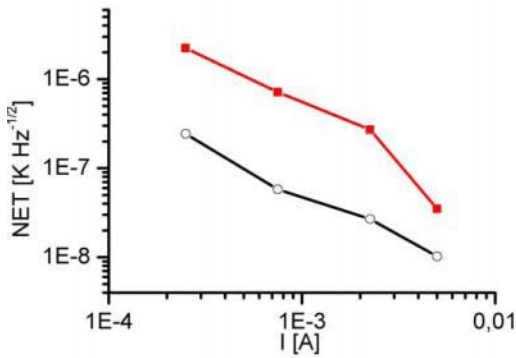

Fiure 4. Measured NET (closed symbols) and calculated NET taking into account the Johnson noise only (open symbols) at 1Hz for the YBCO sample versus current bias [8]

4. Analysis and perspectives of application

Several reviews of heat-sensitive thin-film materials for room temperature thermometers have been published [12-13]. Representative examples for detection in the infrared wavelenght are listed hereafter. Amorphous silicon and amorphous hydrogenated silicon bolometers have shown a value of D^* of 3.2×10^8 cm·Hz$^{1/2}$·W^{-1} for a 70×70 μm^2 detecting area and 1.6×10^8 cm·Hz$^{1/2}$·W^{-1} for a 40×40 μm^2 detecting area, respectively. Amorphous germanium have also been used with D^*=4.7×10^8 cm·Hz$^{1/2}$·W^{-1} for a 70×70 μm^2 detecting area. Polycrystalline SiGe bolometers with optimal geometry are expected to present a specific detectivity of 1.5×10^{10} cm·Hz$^{1/2}$·W^{-1} for a 75×75 μm^2 detecting area [14]. The development of VO_x bolometers have expanded and specific detectivities of 1.9×10^8 cm·Hz$^{1/2}$·W^{-1} at 30 Hz have been obtained for a linear array of eight 10×100 μm^2 elements [15]. Semiconducting YBCO thin film bolometers are also attractive since D^* as high as 1.3×10^8 cm·Hz$^{1/2}$·W^{-1} at 30 Hz was estimated for a 50×50 μm^2 suspended detector area [16]. Compared to manganites the main disadvantages of the above materials are the large excess 1/f noise they present. With a low *NET* value of 2.3×10^{-7} K·Hz$^{-1/2}$ at 30 Hz and using the same membrane type geometry as we previously fabricated [17], we could expect D^* around 10^9 cm·Hz$^{1/2}$·W^{-1} at 300 K and 30 Hz, which is among the best reported results for manganite bolometers [18, 19]. We could also expect D^* around 10^{10} cm·Hz$^{1/2}$·W^{-1} at 90 K and 30 Hz with our YBCO films, coherently to literature data [20]. YBCO thermometers obviously showed better performances but they require nitrogen cooling systems and obviously present a narrow operating window. Room temperature LSMO thermometers are indeed less sensitive but offers smaller sizes, mass and power requirements than cooled YBCO devices.

In case of a detection around or above the 100 μm wavelength, the electromagnetic coupling is made through a metallic antenna (antenna coupled composite bolometers). The incident power of the input wave is then partly transferred to the microload of the antenna, the design of which requiring both a high frequency matching to the antenna impedance and a low frequency matching for the heat exchanges between the microload and its surroundings. The main advantages of these antenna coupled bolometers lies in the heated volume which may be made very small, allowing, in the advanced devices, very large bandwidth, or even mixing properties for THz frequencies. An important drawback is associated to losses in the dielectric and metallic parts of the device, reducing the coupling efficiency to about 20%. This problem can be reduced by membrane technology that minimize dielectric losses and ensure a good thermal insulation of the microload. In

the best case, that is assuming a good high frequency matching between the antenna and the microload, rough estimations of the overall performances would lead to further improvement of the D^* value at a frequency higher than 1 kHz.

5. Conclusion

In conclusion, the presented LSMO and YBCO thin films deposited onto (100) $SrTiO_3$ have shown remarkable low 1/f noise, which could potentially enable the fabrication of high detectivity bolometers at room temperature and 90 K, respectively. YBCO thermometers obviously showed better performances but they require cooling. At last, antenna coupled bolometers are envisaged for wavelength around 100 μm. Further investigations on the noise properties of the nanodevices will have to be made because it is not clear whether its evolution is related to volume according to classical models.

References

[1] P.L. Richards, Bolometers for infrared and millimeters waves, J.Appl. Phys. **76** (1) (1994) 1-24.

[2] K.D. Irwin, An application of electrothermal feedback for high resolution particle detection, Appl. Phys. Lett. **66** (15) (1995) 1998-2000

[3] G.B. Brandao, L.A.L. de Almeida, G.S. Deep, A.M.N. Lima, H. Neff, Stability conditions, nonlinear dynamics, and thermal runaway in microbolometers, J. Appl. Phys. **90** (4) (2001) 1999-2008

[4] I.A. Khrebtov, A.D. Tkachenko, K.V. Ivanov, W. Michalke, Influence of an active electrothermal feedback on noise properties of high-Tc bolometers, to be published in Proc. 17th Int. Conf. On Noise in Physical Systems and 1/f fluctuations (2003), Prague

[5] P. Kruse, Uncooled Thermal Imaging: Arrays, Systems, and Applications, Vol. TT51, SPIE Press (June 2001)

[6] F. Yang, L. Méchin, J.M. Routoure, S. Flament, D. Robbes, R.A. Chakalov, Low 1/f noise in $La_{0.7}Sr_{0.3}MnO_3$ thin films on (100) $SrTiO_3$, to be published in Proc. 17th Int. Conf. On Noise in Physical Systems and 1/f fluctuations (2003), Prague

[7] P. Reutler, A. Bensaid, F. Herbstritt, C. Höfener, A. Marx, R. Gross, Local magnetic order in manganite thin films studied by 1/f noise measurements, Phys. Rev. B **62** (17) (2000) 11619-11625

[8] B. Guillet, D. Robbes, L. Méchin, Low noise temperature control: application to an active cavity radiometer, Rev. Sci. Instrum. **74** (1) (2003) 243-249

[9] B. Guillet, L. Méchin, D. Robbes, High performance temperature controller: application to the excess noise of YBCO thermometers in the transition region, to be published in Proc. 17th Int. Conf. On Noise in Physical Systems and 1/f fluctuations (2003), Prague

[10] H. Neff, I.A. Khrebtov, A.D. Tkatchenko, E. Steinbeiss, W. Michalke, O.K. Semchinova, T. Heidenblut, J. Laukemper, Noise, bolometric performances and aging of thin high Tc superconducting films on silicon membranes,Thin Solid Films **324** (1998) 230-238

[11] D.G Mc Donald, R.J. Phelan, L.R. Vale, R.H. Ono, D.A. Rudman, Passivation, transition width, and noise for YBCO bolometers on silicon, IEEE Trans. Appl. Supercond. **9** (2) (1997) 3087-3090

[12] V.Y. Zerov. and V.G. Malyarov, Heat-sensitive materials for uncooled microbolometers arrays, J. Opt. Technol. **68** (12) (2001) 939-948.

[13] V.G. Malyarov, Uncooled thermal IR arrays, J. Opt. Technol. **69** (10) (2002) 750-760

[14] S. Sedky, P. Fiorini, K. Baert, L. Hermans, R. Mertens, Characterization and optimization of infrared poly SiGe bolometers, IEEE Trans. Electron Dev. **46** (4) (1999) 675-682

[15] C. Chen, X. Yi, J. Zhang, X. Zhao, Linear uncooled microbolometer array based on VOx thin films, Infrared Phys. Technol. **42** (2001) 87-90

[16] M. Almasri, Z. Çelik-Butler, D.P. Butler, A. Yaradanakul, A. Yildiz, Uncooled multimirror broad-band infrared microbolometers, J. Microelectromech. Syst. **11** (5) (2002) 528-535

[17] L. Méchin, J.C. Villégier, G. Rolland, F. Laugier, Double CeO_2 / YSZ buffer layer for the epitaxial growth of $YBa_2Cu_3O_{7-\delta}$ films on Si (100) substrates, Physica C, **269** (1996) 124-130

[18] J.H. Kim, S.I. Khartsev, A.M. Grishin, Epitaxial colossal magnetoresistive $La_{0.67}(Sr,Ca)_{0.33}MnO_3$ films on Si, Appl. Phys. Lett. **82** (24) (2003) 4295-4297

[19] A. Lisauskas, S.I. Khartsev, A. Grishin, Tailoring the colossal magnetoresistivity: $La_{0.7}(Pb_{0.63}Sr_{0.37})_{0.3}MnO_3$ thin-film uncooled bolometer, Appl. Phys. Lett. **77** (5) (2000) 756-758

[20] I.A. Khrebtov, Noise properties of high temperature superconducting bolometers, Fluctuations and Noise Letters, **2** (2) (2002) R51-R70

DIAGNOSTICS OF GaAs LIGHT EMITTING DIODE PN JUNCTIONS

P. Koktavy and B. Koktavy

Brno University of Technology, Fakulty of Electrical Engineering and Communication
Department of Physics
Technicka 8, 616 00 Brno
CzechRrepublic

koktavy@feec.vutbr.cz

Abstract Tracing the bi-stable mechanism of reverse-biased junction conductivity can be used as an efficient tool to study PN junction inhomegeneities. This conductivity mechanism is usually accounted for in terms of crystalline lattice imperfections, dislocations, or metallic precipitates in the PN junction region. Two methods have been suggested for practical application: first, a tentative method to distinguish between the bi-stable and the multi-stable conductivity mechanism, and, second, a noise current rms value versus DC current plot based method.

Keywords:

1. Introduction

The bi-stable mechanism of reverse-biased junction conductivity appears due to crystalline lattice imperfections, dislocations, or metallic precipitates in the PN junction region. Local avalanche breakdowns will thus take place in the neighbourhood of such a defect (microplasma region) at reverse voltages below those required for an avalanche breakdown in a defect-free region of the junction. In consequence of voltage fluctuations across the microplasma region, the electric field intensity may drop below the discharge hold range. The respective current conductivity mechanism would vanish in this case.

J. Sikula and M. Levinshtein (eds.),
Advanced Experimental Methods for Noise Research in Nanoscale Electronic Devices (337 - 344)

2. Microplasma noise vs. time behaviour

Let us consider a diode having a single microplasma region in the PN junction. If the reverse voltage is low, the diode is in a stable state, there are no avalanche breakdowns and the diode current is constant. When the diode voltage is increased, very-low-frequency short-time current impulses will start appearing. Further voltage increase results in increasing both the impulse frequency and width (Fig. 1). After a certain voltage is exceeded, the plasma will be ionized steadily and the diode will be in a stable state again. If there are several microplasma regions in the diode, the above process may occur several times if the voltage is further increased.

Some diodes may feature several microplasma regions, whose bi-stable conductivity mode voltage intervals overlap each other. Multi-level noise (Fig 2) would result in this case.

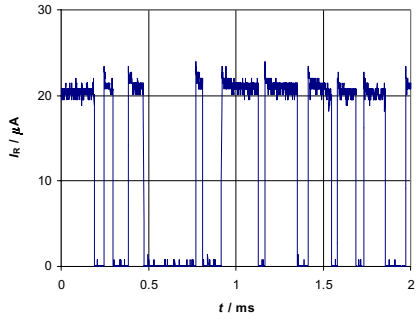

Figure 1. Example of a two-level noise vs. time plot

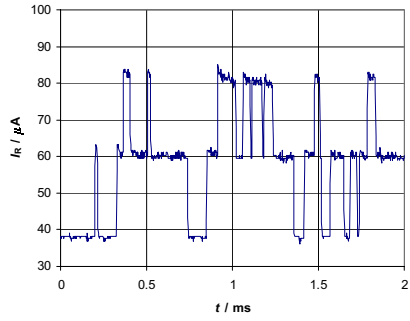

Figure 2. Example of a multi-level noise vs. time plot

3. Diode screening on the basis of microplasma noise vs. time plots

The reverse-biased bi-stable current PN junction characteristics depend on the diode load impedance. Whereas high-accuracy measurements require a load resistance in the order of magnitude of 10^2 Ω, resistances around 10^3 Ω are sufficient for the diode screening process. We used R_L = 1,8 kΩ in our apparatus. Thus it appeared to be possible to dispense with using any low-noise preamplifier when employing a millivolt input range oscilloscope. Otherwise, amplification of the noise voltage by a factor of 10^1 is recommended. Fig. 3 shows a block diagram of the measuring apparatus designed to this purpose.

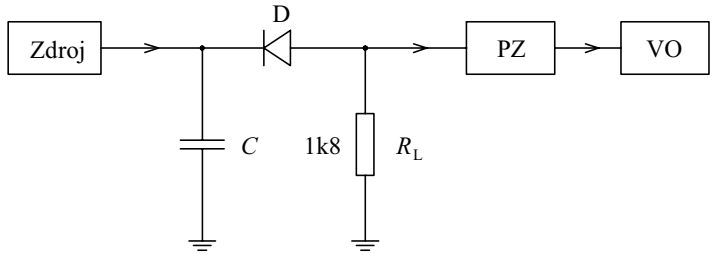

Figure 3. Block diagram of the diode screening device.

A controllable constant-current source is supplying the diode D under test with reverse voltages from 0 to U_{RB}. Being generated by the diode, the noise current produces a noise voltage across the load resistor R_L. This noise voltage is amplified by a pre-amplifier PZ, to be fed into the input of a sampling oscilloscope VO. In the bi-stable behaviour region, the oscilloscope displays random rectangular impulses pertaining to either one or several regions of reverse voltages U_R.

To verify the designed method, we employed following hardware: A BS 554 stabilized power supply 0 to 30 V, C = 22 nF, R_L = 1,8 kΩ, a wide-band pre-amplifier with a voltage gain of 10 and, finally, an HP 54645A oscilloscope.

4. Microplasma noise vs. current behaviour

Reverse biased diodes having no microplasma are expected to generate homogeneous-breakdown avalanche process induced noise only, whereas microplasma diodes will show at lower voltages an additional noise component, corresponding to the bi-stable conductivity due to the individual microplasma regions. The block diagram of the measuring apparatus and the diode measuring circuit is in Fig. 4.

A noise voltage $u_N(t)$ appears across the load resistance R_L through which the noise current $i_N(t)$ is flowing. Being amplified by a narrow-band amplifier and rectified by a full-wave rectifier, the noise voltage is converted into a voltage, whose time average is proportional to the r.m.s. value of U_N in the given frequency band. In this frequency band, the noise current r.m.s. value is

$$I_N = \frac{U_N}{R_L}. \tag{1}$$

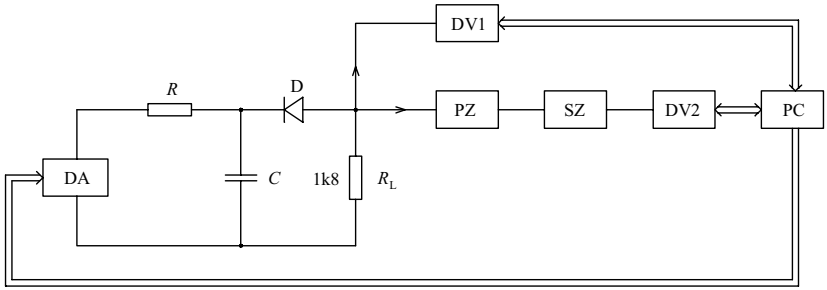

DA – D/A converter
PZ – pre-amplifier
SZ – selective nanovoltmeter
DV1, DV2 – digital voltmeters

Figure 4. Apparatus to measure reverse biased diode noise power spectral density.

The set-point values of the diode reverse current being adjusted by means of a PC-controlled D/A converter, the diagram $I_N = f(I_R)$ shows an I_N versus I_R plot, $I_N = f(I_R)$. Typical plots for M3 diode specimen are shown in Fig. 5 for various band-centre frequencies of Unipan 237 narrow-band frequency filter at a selectivity of 25 dB/oct. Either microplasma region corresponds to a peak, whereas the third region of the curve corresponds to the avalanche breakdown of the junction homogeneous region.

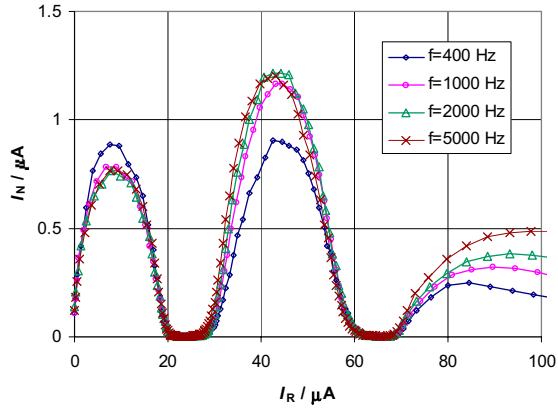

Figure 5. Example of r.m.s. value of noise current I_N versus DC current, specimen M3.

The I_N versus filter band-centre frequency plot has not appeared to be pronounced very much. Therefore, we have chosen $f = 400$ Hz for further measurements.

Under such circumstances, the power spectral density is directly proportional to I_N^2, or U_N^2, and inversely proportional to the filter frequency band equivalent noise band width.

Fig. 6 shows the $I_N = f(I_R)$ plots for a diode with microplasma processes at various temperatures. It can be seen that the noise current r.m.s. value is decreasing with growing temperature, which is in a good agreement with the microplasma related bi-stable current conduction vs. temperature behaviour.

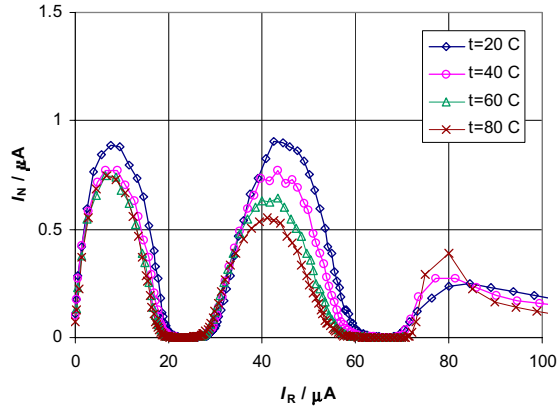

Figure 6. Noise current I_N r.m.s. value versus DC current plot for various temperatures, specimen M3.

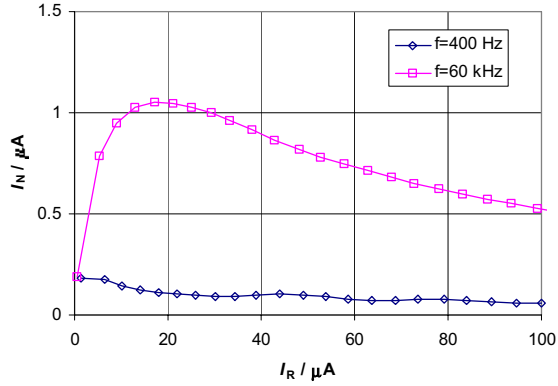

Figure 7. Avalanche breakdown induced noise for diode specimen P1 (with no microplasma).

For the sake of comparison, let us show Fig. 7, in which the noise current I_N vs. *DC* current plots, $I_N = f(I_R)$, for both the diodes showing bi-

stable current conductivity and the diodes showing homogeneous breakdown, are illustrated. It is seen that only homogeneous junction avalanche breakdown induced noise is present in the characteristic in the latter case.

5. Measuring apparatus to study the microplasma noise vs. current behaviour

Fig. 8 shows the block diagram of the measuring apparatus designed to study the noise current (voltage) r.m.s value versus reverse current plots in a given frequency range.

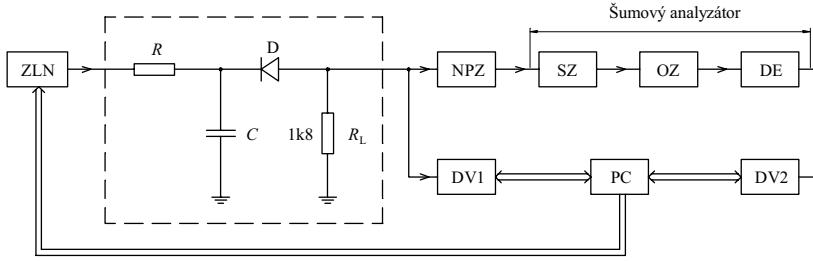

Figure 8. Apparatus to measure reverse biased diode noise current (voltage) spectral density

A dedicated power supply comprising TESLA BM 572 D/A converter is providing a ramp voltage, which is powering the diode D connected in series with a load resistor R_L = 1,8 kΩ. The noise voltage is amplified by a low-noise pre-amplifier featuring an input resistance of about 10^5 Ω and a voltage gain of 10. Further amplification is provided by a narrow-band amplifier with a band centre frequency of 390 Hz and an effective bandwidth of Δf_e = 14.13 Hz. The narrow-band signal is fed, via an insulating amplifier, OZ, into a rectifier whose DC output voltage is measured by an M1T 330 digital voltmeter DV2 (M1T 330). The latter's output is processed in a process-control PC, calculating the r.m.s. value of the noise current I_N passing through the load resistor R_L. The other quantity to be processed is the time-mean value of the impulse noise voltage across the load resistance R_L, which is picked up by another M1T 330 digital voltmeter DV1, from which the mean value of the current I_R is derived.

The noise analyzer shown in Fig. 8 is assembled from functional blocks which have been designed and produced at the Department of Physics especially for noise diagnostics of electronic devices and materials. As an equivalent noise analyzer, a standard narrow-band selective amplifier, such as Unipan 233 or Unipan 237 may also be used.

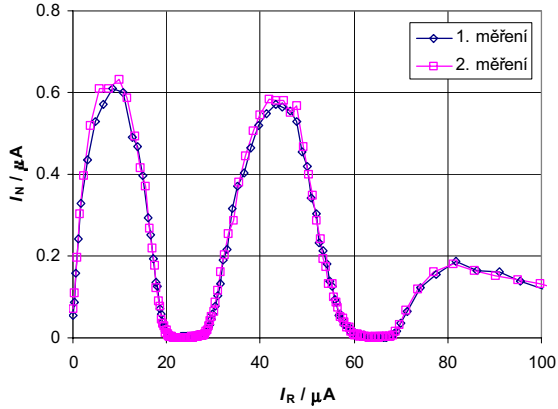

Figure 9. Noise current versus DC current plot for M3 diode.

To demonstrate the results obtained from the above-mentioned measuring apparatus, reverse-biased M3 diode noise is shown. The I_N versus DC current plot is shown in Fig. 9. It can be seen to coincide in shape with that presented in Fig. 6. The deviation in the value of I_N results from different bandwidth values of the narrow-band filter. Therefore, we have calculated the measuring set bandwidths for the case of a Unipan 237 selective nanovoltmeter with a band-centre frequency of 400 Hz and the narrow-band amplifier SZ (made by the Department of Physics) with a band-centre frequency of 390 Hz. The frequency response curves of both apparatuses are shown in Fig. 10. We have calculated the effective band-widths, Δf_e , for both apparatuses (Fig. 1). This being done, the noise current power spectral density may be calculated from the following formula:

$$S_i(I_R) = \frac{I_N^2}{\Delta f_e} \tag{2}$$

The Unipan selective nanovoltmeter features effective noise bandwidths of 49.0 Hz and 9.7 Hz for selectivity settings of 25 dB/octave and 40 dB/octave, respectively, whereas the narrow-band amplifier made by the Physics Department features Δf_e = 14.1 Hz.

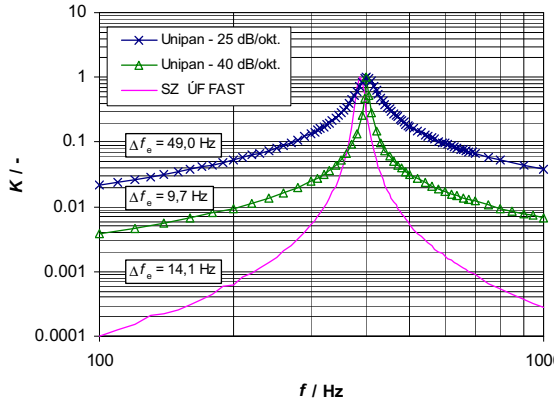

Figure 10. Frequency response curves for Unipan nanovoltmeter and the narrow-band amplifier made by the Department of Physics.

6. Conclusion

The first suggested method for diodes screening is based on tracing the microplasma noise current vs. time behaviour. The reverse-biased bi-stable current PN junction characteristics depend on the reverse voltage, the diode load impedance and the temperature. In the bi-stable behaviour region, the oscilloscope displays random rectangular impulses pertaining to either one or several regions of reverse voltages U_R.

The second method is based on tracing the noise current (voltage) r.m.s value versus reverse current plots. Reverse biased diodes having no microplasma are expected to generate homogeneous-breakdown avalanche process induced noise only. Microplasma diodes will show at lower voltages an additional noise component, corresponding to the bi-stable conductivity due to the individual microplasma regions.

References

[1] K. G. McKay, Avalanche Breakdown in Silicon, Phys. Rev. **94** (1954) 878-884.

[2] Keith S. Champlain, Microplasma Fluctuations in Silicon, J. Appl. Phys. **30** (1959) 1039-1050.

NEW TOOLS FOR FAST AND SENSITIVE NOISE MEASUREMENTS

J. Sikula[1]

Brno University of Technology, Fakulty of Electrical Engineering and Communication
Technicka 8, 616 00 Brno
Czech Republic

M. Tacano[2] and S. Yokokura

Meisei University,
Hino, Tokyo,
Japan

S. Hashiguchi[3]

Yamanasi University,
Kofu, Yamanashi,
Japan

[1] sikula@feec.vutbr.cz
[2] tacano@ee.meisei-u.ac.jp
[3] has@es.yamanashi.ac.jp

Abstract An instrument to improve power spectrum density (PSD) measurements, a highly sensitive preamplifier and a data acquisition unit are designed as well as a programmable power battery source. The preamplifier has 8 junction field effect transistor (JFET) inputs in parallel resulting in an input noise equivalent power of –186 dBV^2/Hz. The data acquisition system consists of a low-pass filter, an A/D converter and a RAM, which transfer the data to the connected PC. The FFT or other signal processing is carried out within the PC. The battery power source is controlled by the PC, enabling us to obtain the device-under-test (DUT) bias DC required by the program.

This measuring system works well at room temperature where the DUT and the power source could be put into a magnetic shielding box to reject spurious line noises. In the case where the DUT is placed in a cryostat to measure the temperature dependence of noise properties, however, the shielding of the DUT from the power line becomes a serious problem. Particularly in order to use a compressor cooling system, spurious noises come into the measuring system through the power lines of the compressor. In such a case the preamplifier must be placed as close as possible to the DUT, and the power line to the compressor is sometimes disconnected from the system.

J. Sikula and M. Levinshtein (eds.),
Advanced Experimental Methods for Noise Research in Nanoscale Electronic Devices (345 - 354)

Keywords: High sensitive preamplifier, programmable battery, power source

1. Introduction

PSD measurements have been carried out using a preamplifier and an FFT analyser together with a battery source and a PC usually to control the FFT as shown in Fig. 1. This measuring system works well at room temperature where the DUT and the power source could be put into a

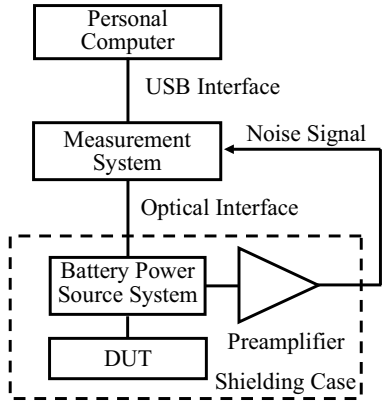

Figure 1. Block Diagram of New Tool for Fast Sensitive Noise Measurements

magnetic shielding box to reject spurious line noises. In the case where the DUT is placed in a cryostat to measure the temperature dependence of noise properties, however, the shielding of the DUT from the power line becomes a serious problem. Particularly in order to use a compressor cooling system, spurious noises come into the measuring system through the power lines of the compressor. In such a case the preamplifier must be put as close as possible to the DUT, and the power line to the compressor is sometimes disconnected from the system.

In order to reject the spurious noise to improve the measuring circumstances, we have developed a new set up with a highly sensitive preamplifier and a data acquisition system instead of the FFT, together with a programmable battery power source system.

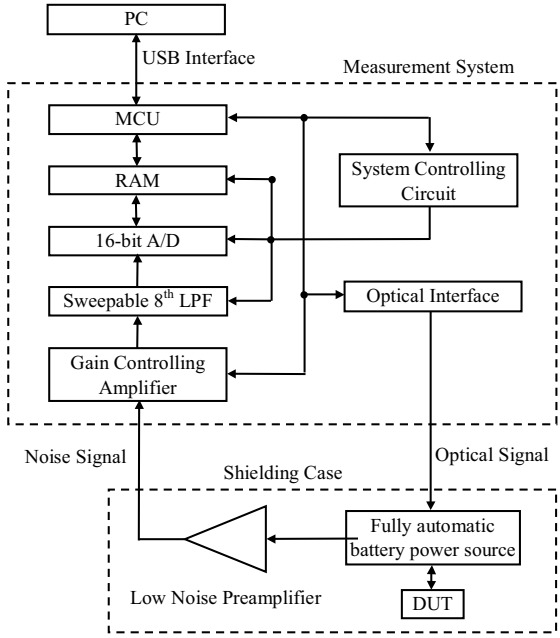

Figure 2. Flow of New Measuring System

An amplifier with an input noise power of below –186 dBV^2/Hz is fabricated by connecting 8 JFETs in parallel followed by operational ampli fiers. The output of the amplifier is connected to the data acquisition system which transfers the time-sequential noise signals to digitized signals through the 16-bit A/D converter and a low-pass filter (LPF). Without using a comer- cially available large instru-ment, we could do the equi-valent work in one simple board, and could attach or install the instrument within a cryogenic system altogether. The data from this acquisition system is transferred to a PC through a USB (Universal Serial Bus) interface, which enables us to connect to every computer without additional cost.

2. PSD measuring system

A block diagram of this new PSD measuring system is shown in Fig. 2. A detailed block diagram of the measuring system is shown in Fig. 3.

The PSD is further amplified by a gain-controlling amplifier, via the 8^{th} LPF (clock sweepable cauer filter) swept by the PC, quantized by a 16-bit A/D converter and stored in the installed RAM.

The data is transferred between the measuring system and PC using the full-speed transfer mode of USB Interface Version 1.1. We do not need any other interface hardware since most PCs have this interface.

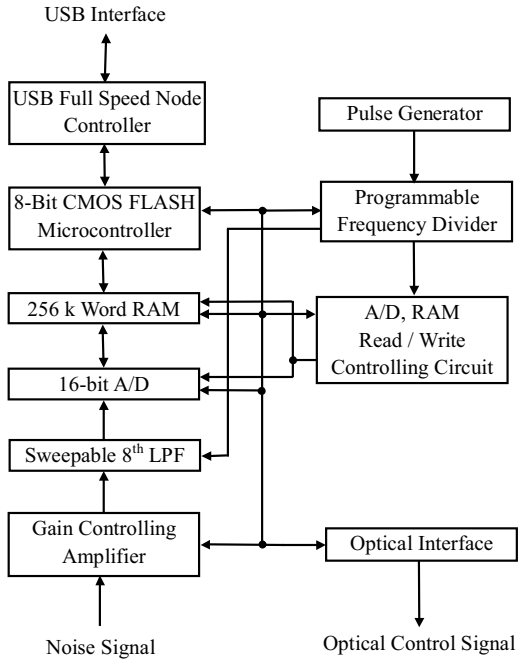

Figure 3. Detailed Block Diagram of Measuring System

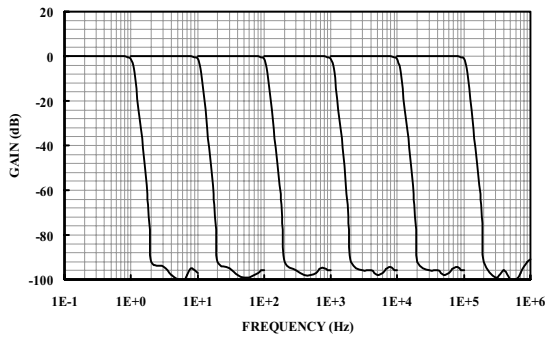

Figure 4. Low-Pass Filter Characteristics

The dynamic range of the system is limited by the anti-aliasing LPF and the A/D. The frequency dependence of this filter is shown in Fig. 4, which shows the dynamic range of the system to be more than 90 dB and the data quantumized by the 16-bit A/D converter. The sampling frequency of the A/D converter is set to be equal to just 4 times that for the LPF set cutoff frequency.

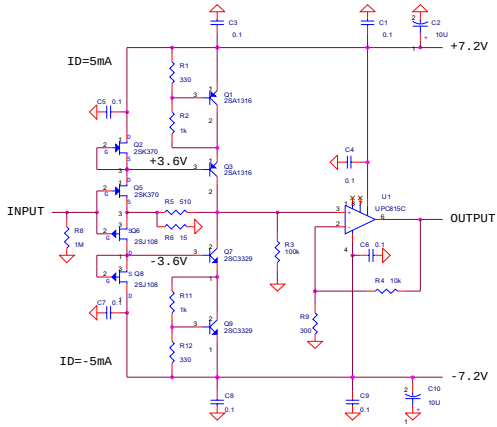

Figure 5. Low-Noise Preamplifier Structure

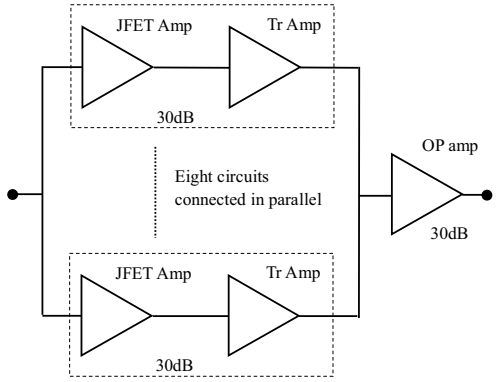

Figure 6. Low-Noise Preamplifier Circuit

In order to measure the frequency range between 100 to 1 kHz, for instance, the cutoff frequency of the LPF and the resolution are set to 1 KHz and 80 per decade, respectively. The sampling frequency of the AD converter is set to 4 KHz, and a word data maximum of 2560 is stored and

transferred to the PC, and undergoes further data transformation, either FFT or real-time RTS analyses. The dynamic range of this system is approximately 90 dB.

3. Preamplifier

We used low-noise JFET devices to reduce the input noise of the amplifier, and also used transistors as the 2nd amplifier and operational amplifiers in the 3rd section. The actual circuit is shown in Fig. 5. Eight JFETs are used in parallel to reduce the input noise of the amplifier, and transistors are also used for the 2nd amplifier and operational amplifiers in the 3rd section. The schematic diagram of the preamplifier is shown in Fig. 6. The 1st and 2nd stages reached an amplification of 30 dB, and the 3rd stage was designed to reach 30 dB in order to obtain the total gain of 60 dB.

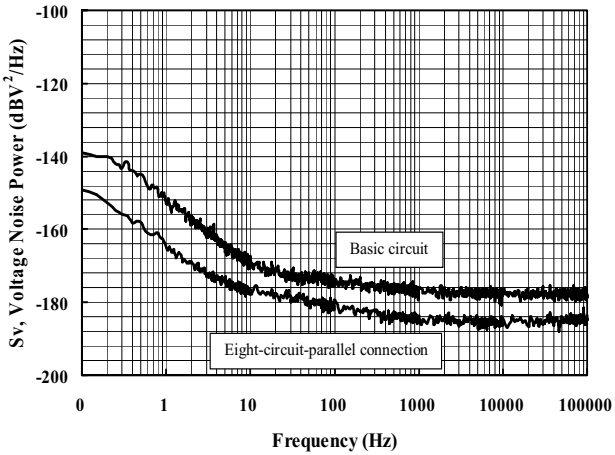

Figure 7. Sensitivity of Completed Amplifier

Figure 7 shows the noise equivalent power of the amplifier with the shorted input. The single JFET amplifier had a maximum sensitivity of –175 dBV^2/Hz, and the 8 devices in parallel had a maximum sensitivity of –186 dBV^2/Hz.

4. Programmable Battery Power Source

A fully automatic battery power source is proposed[1)] to replace the manually controlled power source. Figure 8 shows the block diagram of the

power source system, consisting of a personal computer, an interface controller and a battery power source circuit.

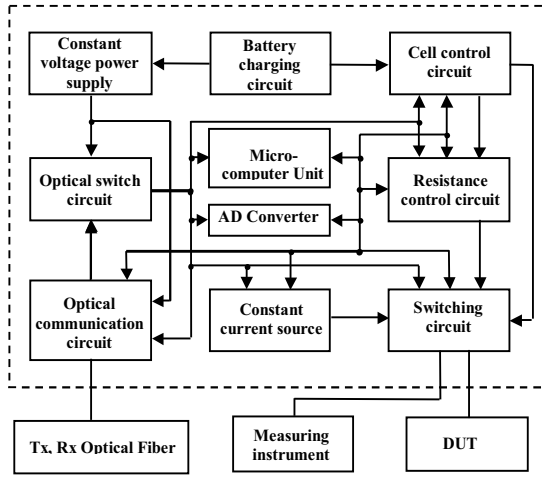

Figure 8. Block Diagram of Programmable Battery Power Source

The personal computer and the interface controller (IFC) are connected via the RS232C control line enabling parallel or serial two-way communication, while the IFC and the battery power source circuit are connected via optical fibers. The IFC transforms the electrical signal from the personal computer into an optical signal and transfers it to the battery power source circuit, while transforming the optical signal from the battery power source circuit and transmitting the corresponding electrical signal to the personal computer. The IFC entirely rejects the line noise superposed on the personal computer and on the battery power source circuit. The personal computer determines the battery voltage and the series resistance calculated for the measured DUT resistance, and transmits the control signal via IFC to the microcomputer within the battery power source circuit. The battery power source circuit measures the DUT resistance, and supplies the required DC power to the DUT while transmitting the control signal to the measuring instruments and receiving the results from them. While the instruments execute the measurements, the microcomputer is switched off in order to minimize the induced noise. The voltage of each battery can be monitored and the batteries are charged if its voltage drops below a threshold. All of these functions are performed by the microcomputer installed in the battery power source circuit. Figure 9 shows the completed power source.

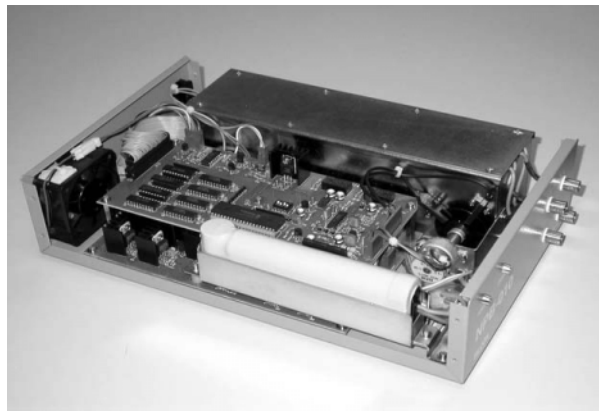

Figure 9. Programmable Battery Power Source

5. Results

The new system, as well as the signal processing, was PC-controlled by Visual Basic ver. 6 of Microsoft.

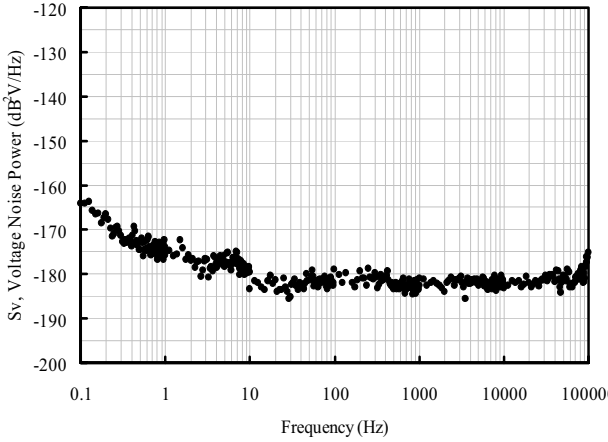

Figure 10. Noise Equivalent Power of New System

The noise equivalent power of the new system with the shorted input terminal is obtained as shown in Fig. 10, indicating the expected maximum sensitivity of –186 dB^2/Hz. The real time signal is also obtained as shown in Fig. 11. The input square wave of 1 kHz 10 nV PP was picked up through the A/D converter with a sampling frequency of 400 kHz and the cut off frequency of the LPF was 100 kHz.

The maximum data transfer rate of our system is about 128 kbyte and is limited by the USB protocol-PC system signal processing time.

These results may certify that the developed system com-pletely works both as a transient analyser and as an FFT analyser.

6. Conclusion

Due to recent advanced signal pro-cessing tools we are able to obtain the noise PSD of devices without using conventional commercial FFTs. It is also possible to fabri-cate a programmable battery power source due to the improved new batteries.

We proposed here a new low-cost instrument for low-frequency noise measurements. Further improvements of the system can be achieved by minimizing the preamplifier and by replacing the digital circuits with a field programmable gate array (FPGA) as well as upgrading the USB to the version 2 interface which will enable the maximum transfer rate of 1 M Word (16 bits/word) at a transfer rate of 5 Mbits. This makes it possible to realize the virtual on-line recording of the RTS signal.

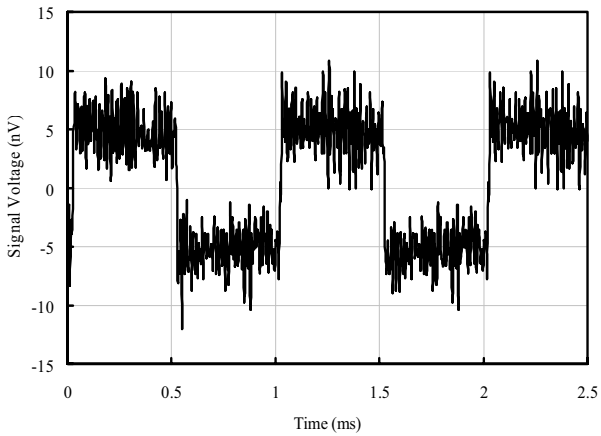

Figure 11. Real time signal trace

References

[1] S. Yokokura et al: Fully Computer-Controlled Battery Power Source for Low Frequency Noise Measurements, Proc. of ICNF p.721, Gainesville (2001)

USING A NOVEL, COMPUTER CONTROLLED AUTOMATIC SYSTEM FOR LF NOISE MEASUREMENTS UNDER POINT PROBES

J.A. Chroboczek[1]
CEA-DRT-LETI/DTS-CEA
17, rue des Martyrs, 38054 Grenoble Cedex 9
France

S. Ferraton[2]
IMEP, UMR CNRS 5130 ENSERG
23, rue des Martyrs, 38016 Grenoble
France

G. Piantino
Synergie-Concept,
7, rue de Prés, 38243 Meylan
France

[1] Jan.chroboczek@cea.fr
[2] ferraton@enserg.fr

Abstract A system for automatic, wafer-level, low frequency, LF, fluctuation measurements on semiconductor devices, involving a novel, programmable biasing amplifier, PBA, is presented. The PBA is computer-controlled and can remotely bias device terminals and measure currents flowing through them to the common ground. Its inputs are traxial with the appropriate guard potentials applied to their inner shields. The system is designed specifically for LF noise measurements on microelectronics structures. It can operate in manual and automatic modes. In the latter, the biasing voltage ranges and their increments are programmable. The program execution is carried out by step-wise biasing voltage variations, followed by measurements of appropriate currents and their fluctuations, with Fourier analysis, completed by the data storage. The program is written in LabView graphical language for a personal computer, equipped with a digital I/O and a data acquisition cards. No additional electronics is needed for the system operation. The system calibration by thermal noise of resistances is proposed. Some measurement results on the state-of-the-art microelectronics devices are discussed.

Keywords: Low frequency noise, microelectronics, current amplifier

J.Sikula and M.Levinshtein (eds.),
Advanced Experimental Methods for Noise Research in Nanoscale Electronic Devices (355 - 362)

1. Introduction

One of the negative consequences of the size reduction of microelectronics devices is the increase in their low frequency noise, LFN. Standard, static characterization of the state-of-the-art microelectronics devices is no longer sufficient and even the most rudimentary device simulation programs, such as SPICE, provide the LFN parameters. Measurements of LFN are delicate and time consuming; that is why the LFN characterization techniques are not more widely used in the electrical characterization and test laboratories, let alone the on-line testing stations. The cutting of the measuring time is only possible if a computer-controlled system is used, both for device biasing and for the LFN measurements. Such a system must not generate electrical noise and be immune to electrical pick-up from the wafer-handling equipment, where the devices are contacted by point probes. This work should be considered as a step towards a realization of an automatic LFN measuring system, capable to operate in the industrial environment.

We present a programmable point-probe noise measuring system, 3PNMS, which, as the name implies, is computer-controlled and can function with point-probe stations. We have not yet approached the problem of automatic wafer handling, nor optimized the measurement speed, both presenting separate engineering problems. However, as compared to the manual procedures, the measurements have been dramatically accelerated. The use of simple and reliable electronics eliminated expensive spectrum analyzers, never used in their full capacity in LFN characterization systems. The essential element of the system, the programmable biasing amplifier, PBA, was designed for biasing each individual contacting probe and for measuring the resulting current, passing through it and the device contact pad, to the system common ground [1]. It requires using coaxial probes (here Cascade Microtech are employed), connected to PBA by traixial leads. Their inner shields are driven, by PBA, at the input potentials, for reducing the leakage currents and suppressing the effective capacitances of the leads.

The PBA and the entire biasing and data acquisition/storage procedure is controlled by a PC, via a program named NOISYS, written in the LabView graphical language, with commands/controls accessible for the user by screen panels of virtual instruments, vi. Digital input/output cards are used for controlling the PBA and the data acquisition procedure. The latter can be run automatically, after inputting the measurement parameters into appropriate vi screen panels. One of such panels is shown in Fig. 1.

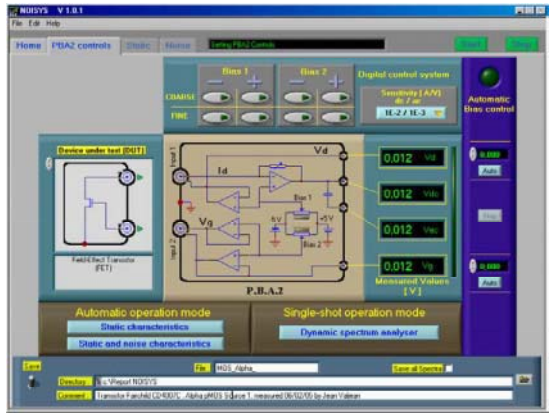

Figure 1. Controls Panel of PBA2, a virtual instrument of the NOISYS program for static and noise measurements for a MOSFET. Bottom part is for the inputting the storage information.

2. The Programmable Biasing Amplifier

We shall discuss here standard LFN measurements on MOSFETs, where the device is biased (drain at V_d and gate at V_g) and just the drain current, I_d, measured. The PBA2, a compact version of the amplifier, is then used. It provides the drain and gate biasing, together with the I_d read-out. Its schematic diagram is shown in Fig. 2. The biasing is provided by stabilized, battery-powered voltage supplies, with digital potentiometers, commanded by TTC signals from a computer, via NOISYS software. The DC gain of the current amplifier is R_f (V/A). The gain values can be changed by NOISYS, by switching an appropriate R_f in the amplifier feed-back loop (cf. Fig. 2).

As known, the voltage generated at the current amplifier output by the current I_d in the input is

$$V_{out} = - I_d R_f \qquad (1)$$

One of the functions of NOISYS software is the maintaining V_{out} below the operational amplifier's saturation voltage. The V_{out} and the corresponding gain are subsequently stored, as couples, for data processing.

.

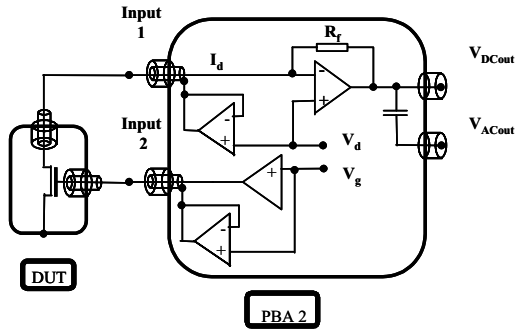

Figure 2. A 2-terminal version of the Programmable Biasing Amplifier, with a single current read-out. The amplifier DC gain is R_f (V/A). Here the device under test, DUT, is a MOSFET

Some characteristics of PBA are listed in Table 1, in particular the open-input V_{out} values at various gains and the corresponding input referred noise. Such values are often referred to as the system noise. The cut off frequencies at various gains are also provided.

Table 1. Some characteristics of the programmable biasing amplifier, PBA

Range [V/A] $\log G_{AC}/\log G_{DC}$	Mean output voltage amplitude [$\mu V_{rms}/\sqrt{Hz}$]	Input referred PSD amplitude [$pA_{rm}/\sqrt{Hz}$]	Pass band f_{max} [kHz]
8/7	6.5	0.065	35
7/6	4.5	0.45	60
6/5	4.0	4	>100
5/4	2.5	25	>100
4/3	2.5	250	>100
3/2	2.5	2500	>100

3. The System Calibration with Resistances

One of the initial steps the user takes after setting up the LFN measuring system, is the determination of the system noise and the calibration of the system, if possible. Thermal noise sources are commonly used for that purpose. Connecting various load resistance R_g in the Input 1 of PBA, we measured the mean output voltage, V_{out}, for various R_f connected in the feedback-loop. The V_{out} values can be calculated by summing up the thermal noise contribution of R_g, amplified by the operational amplifier and the thermal rms voltage of the R_f resistor. We obtain,

$$V_{out}=\sqrt{[4kT\times G_{AC}^2(1/R_f+1/R_g)]},\ [V_{rms}/\sqrt{Hz}] \qquad (2)$$

where G_{AC} is the AC gain (here $G_{AC} = 10G_{DC}$). For a more rigorous derivation of Eq. (2) see refs [2] and [3]. The resulting V_{out} is compared in Fig. 3 with the data. The calculation (surface) and the data (mesh), obtained for a set of R_f and R_g values, both ranging from $10^2\Omega$ to $10^7\Omega$, by decade steps, are seen to account for the measured V_{out}, above the system noise plateau, situated at about –105(±5)dbV/√Hz (or 5 (±1) μV/√Hz). Figure 3 shows that the absolute system calibration by thermal noise of load resistances R_g, is correct in a certain range of R_g and R_f values, where the output noise significantly exceeds the system noise. Note that the system noise plateau in Fig. 3, corresponds to the values listed in Table 1.

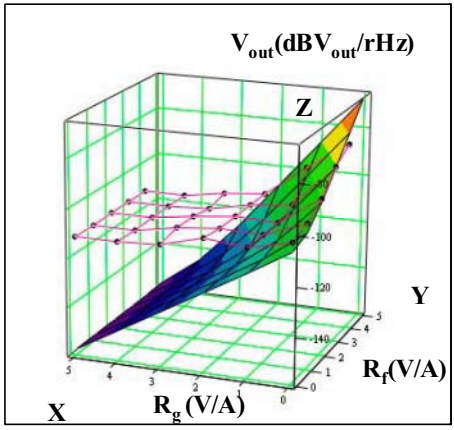

Figure 3. Measured (mesh) and calculated (shaded surface) output voltage of the Programmable Biasing Amplifier, PBA2, plotted on axis Z, for R_f (axis X) and R_g (axis Y) values equal to 10^2, 10^3,10^4, 10^6, $10^7\Omega$, corresponding to numbers 0 to 5, at the axes. Above the system noise, situated at about -100dbV/rHz (~5μV/rHz), the calculation is seen to account for the data.

4. Examples of LFN measurements on MOSFETs

In Fig. 4 we show some results of measurements on a $0.75\mu m^2$ Si MOSFET. In part (A) the values directly measured at the PBA output are shown, with the vertical lines separating V_g regions, where a particular AC gain, G_{AC}, was used. The upper curve was taken with the current (V_d=50mV), the middle, with no current (V_d=0) and the bottom curve represents the calculated (using Eq. 2) thermal noise of the system. Note that at V_d=0 the output voltage PSD contains the system thermal noise and

other unknown contributions, probably generated by electronics. For that reason these data lie above the calculated thermal results. The 1/f component of interest is extracted from the difference of the appropriate values given by the upper and the middle curve. An example of such analysis is shown in part (B) of Fig. 4. As seen, the curves corrected for the system noise, and not, become undistinguishable starting from the threshold voltage of the transistor, where the current becomes easily measurable, i.e. at about 10^{-9}A.

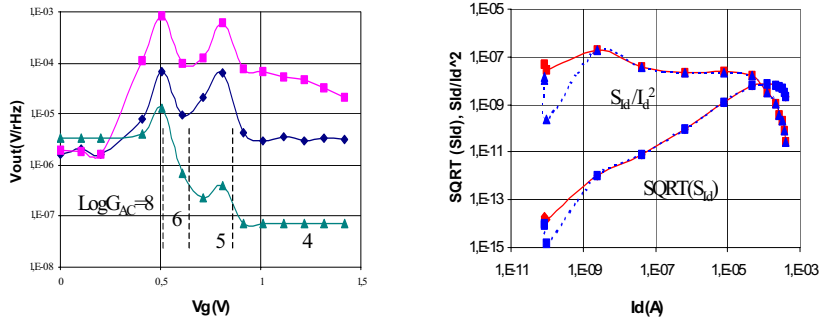

A B

Figure 4. (**A)** The output voltage V^{AC}_{out} [$V_{rms}/\sqrt{Hz}$] measured at V_d=50mv (upper curve) and V_d=0 (middle), *vs* V_g at various AC gain values, G_{AC}, appropriate for the currents measured (regions of the same G_{AC} are separated by vertical dotted lines). The thermal noise contributions of the channel/amplifier system, is presented by the bottom curve. It has been calculated form Eq. (2) with $R_d=V_d/I_d$ replacing R_g. **(B)** The data from (A) converted to $\sqrt{S_{Id}}$ by multiplying by G_{AC} is shown by the lower set of curves; the upper show the PSD data, S_{Id}, normalized by I_d^2. At $I_d<10^{-9}$A the curves representing the total PSD and the 1/f component diverge, indicating that the combined thermal and system noise is non-negligible.

In Fig. 5 we present some data taken on novel devices, with Si-nanocrystals, Si-nc, imbedded in the gate dielectric of MOSFETs, and on control MOSFETs, without the Si-nc's. The results will be discussed in some detail at this Conference [6]. Figure 5 shows the spectra taken in both types of devices using 3PNMS in the automatic data acquisition mode. Note a conspicuous absence of parasitic lines and the smoothness of the ensemble of the data points, plotted as a function of frequency.

The data of Fig. 4 have been shown to be dominated by the number fluctuation LNF and were analyzed as discussed before, cf. [5]. More examples of such analysis is discussed in [2]. We should add at this point, that the set of the data files needed for extracting such parameters as the interface density of noise-generating traps, requiring some 20 spectra, takes

on the average 30 min. A competent operator can, therefore analyze a dozen of devices in a day, an amount impossible to handle if the data were to be taken by traditional equipment. As mentioned, the optimization of the speed of 3PNMS is on the way.

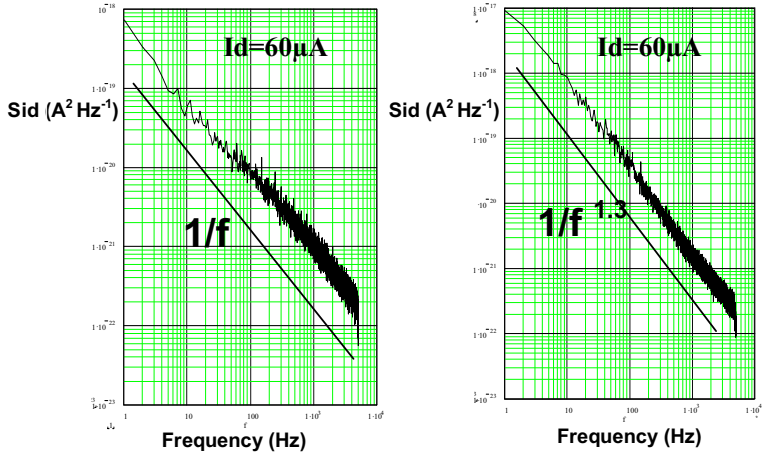

Figure 5. PSD versus frequency measured in the drain current of MOSFETs devices with Si-nanocrystals (right) and without (left), where pure 1/f noise is observed, cf. ref [6].

5. Conclusions

We presented in this contribution some details on the use of a programmable point probe noise measuring system, 3PNMS, designed for the data acquisition on microelectronics devices, on wafer level. The system's performance has been carefully analyzed and a simple method of its absolute calibration by thermal noise of resistances has been proposed and tested. We also discussed some examples of the system functioning on small MOSFETs. It should be emphasized that the system is modular and can be readily adapted for studies on other types of devices and modified to meet novel research requirements.

References

[1] J.A. Chroboczek and G. Piantino, Patent No. 15075, France. Registered in November 1999.

[2] J.A. Chroboczek, G. Reimbold, A. Szewczyk, and G. Piantino, accepted for presentation at the 17th ICNF, Prague, August 18th, 2003.

[3] Zhong Yuan Chang and W. M. C. Sansen, "Low-noise, Wide-band Amplifiers in Bipolar and CMOS Technologies", Kluver, 1991.

[4] A. L. McWhorter, *1/f Noise and Ge Surf. Properties,* p. 207 in *Semicond. Surface Phys.* R.H. Kingston, Edit., Univ. Penn. , 1957.

[5] G. Ghibaudo, Phys. Status Solidi (a) **113**, 223 (1989).

[6] S. Ferraton, L. Montès, I. Ionica, J.A.Chroboczek, and J. Zimmermann, this Conference.

AUTHOR INDEX

SUBJECT INDEX